



**Some pages of this thesis may have been removed for copyright restrictions.**

If you have discovered material in Aston Research Explorer which is unlawful e.g. breaches copyright, (either yours or that of a third party) or any other law, including but not limited to those relating to patent, trademark, confidentiality, data protection, obscenity, defamation, libel, then please read our [Takedown policy](#) and contact the service immediately (openaccess@aston.ac.uk)

# **Bifunctional niobia and zirconia catalysts for 5-hydroxymethylfurfural production from C6 sugars**

Mariano Tapia Reche

Doctor of Philosophy

Aston University

European Bioenergy Research Institute  
(EBRI)

September 2017

©Mariano Tapia Reche, 2017

Mariano Tapia Reche asserts his moral right to be identified as the author of this thesis. This copy of the thesis has been supplied on condition that anyone who consults it is understood to recognise that its copyright belongs to its author and that no quotation from the thesis and no information derived from it may be published without appropriate permission or acknowledgement.

Aston University  
EBRI (European Bioenergy Research Institute)

## **Bifunctional niobia and zirconia catalysts for 5-hydroxymethylfurfural production from C6 sugars**

Mariano Tapia Reche  
Doctor of Philosophy

September 2017

Biomass represents one of the most practical and environmentally friendly options available as an alternative to petroleum derived compounds. Amongst them, 5-hydroxymethylfurfural (HMF) stands as a potential platform chemical for the production of biofuels and other value added chemicals. Although HMF can be selectively produced from mono- and poly-saccharides with the assistance of organic solvents or ionic liquids, its formation in aqueous media under mild conditions remains a challenge due to undesired side reactions.

In this thesis, the conversion of glucose and fructose to HMF has been studied over bulk and SBA-15 supported niobic acid catalysts synthesised through a recently reported peptization procedure which provides high surface area and strong Lewis and Brønsted acid densities. Sintering and crystallization induced by thermal treatment of bulk materials has been proven by XRD, TEM and Raman, provoking a worsening in the textural and acidic properties of the niobia based catalysts. The amorphous phase of nanoparticulate niobic acid is highly active for the aqueous phase isomerisation of glucose to fructose, and subsequent fructose dehydration to 5-HMF under mild reaction conditions, due to an adequate balance of Brønsted-Lewis acid sites.

Additionally, another family of phosphated zirconia bifunctional catalysts has been successfully synthesised, fully characterized and employed for the production of HMF. Tunability of Brønsted-Lewis ratio was possible thanks to a controlled modification of surface acidity by phosphate loading. The presence of phosphate species inhibited the particle growth and crystallization of zirconia, as proved by Raman and XRD, which led to the enhancement of textural and acidic properties. Catalysts with low Brønsted-Lewis ratio and higher basicity show higher activity for glucose isomerization, while catalysts with high Brønsted-Lewis ratio and low basicity proved to be more suitable for the dehydration step to HMF.

**Key words:** Niobic acid, phosphated zirconia, 5-hydroxymethylfurfural, glucose dehydration, bifunctional catalyst

## Dedication

To Lu

*“My face is mine, my hands are mine, my mouth is mine, but I am not. I am yours.”*

## Acknowledgments

First I would like to thank my supervisor Professor Karen Wilson for giving me the opportunity to conduct this PhD and for her excellent guidance, support and patience during the duration of this research. Special thanks also to Professor Adam F. Lee and Dr Marta Granollers Mesa for providing additional supervision, support and advice. They gave me the opportunity to travel and attend to several conferences where I had the chance to grow as a researcher and expand my knowledge of different areas of Green Chemistry. I am also thankful to the EPSRC for the funding of this project; as well as to the European Bioenergy Research Institute (EBRI) at Aston University for providing the wonderful facilities where this research took place.

To the multitude of people who I have met as a member of the Surfaces, Materials and Catalysis (SMAC) research group at Aston University either through temporary or long stay. The multiculturalism of this group has given me the chance to meet people from all around the world, to learn about their culture and habits, which enriched my stay at Aston University. Individually, I would like to thank Dr Christopher Parlett and Dr Lee Durdell for providing the STEM pictures; Dr James Hunns for assisting with XPS analysis; Dr Mark Isaacs for his huge assistance with several analysis techniques such as STEM, XRD, XPS and ICP and for his help with data processing from some of these analyses; Dr Amin Osatiashtiani for his immense patience throughout these years every time I had doubts about anything, and because more than a colleague he became a friend. More friendships were forged with Miss Brunella Barbero and Dr James Andrew Bennett, with whom I had the pleasure of sharing loving moments and countless laughs.

I would like to express my gratitude to my family and friends for their encouragement during my PhD, gracias especialmente a mis hermanos Carmen María Tapia Reche y Juan Javier Tapia Reche, así como a mi padres Mariano Tapia Martínez y Carmen Reche Quiles, porque siempre han sido una inspiración para mí y un ejemplo a seguir como grandísimas personas, por todo el amor y el apoyo que he recibido durante todos mis años académicos, que han hecho posible que haya llegado a este punto. Os quiero.

Last but not least, I have no words to express my eternal gratitude to Miss Lucia Frattini, not only for all the scientific help received during these years, but for being my partner in this British journey that brought us together and for sharing with me the best moments of my life (and a lot more to come!). Probably this thesis would not have been possible without you. I love you babe!

# List of contents

## ***Chapter 1 Introduction***

|     |  |    |
|-----|--|----|
| 1.1 | Introduction   | 20 |
| 1.2 | Green Chemistry and the role of catalysis                  | 21 |
|     | 1.2.1 Principles of catalysis                              | 21 |
|     | 1.2.2 Heterogeneous catalysis                              | 24 |
| 1.3 | Shifting from oil-based products to biomass sources        | 27 |
|     | 1.3.1 Classification of biofuels                           | 27 |
| 1.4 | Production of building blocks from lignocellulosic biomass | 29 |
|     | 1.4.1 Hydrolysis   | 31 |
|     | 1.4.2 Pyrolysis and liquefaction                           | 31 |
|     | 1.4.3 Gasification   | 32 |
| 1.5 | HMF as a platform chemical                                 | 33 |
|     | 1.5.1 HMF derivatives                                      | 34 |
| 1.6 | Glucose and fructose dehydration to HMF                    | 36 |
|     | 1.6.1 Mechanism of glucose to HMF formation                | 36 |
|     | 1.6.2 Production of HMF in different reaction media        | 38 |
|     | 1.6.2.1 Dehydration reactions in aqueous solutions         | 38 |
|     | 1.6.2.2 Dehydration reactions in organic solvents          | 42 |
|     | 1.6.2.3 Dehydration reactions in biphasic systems          | 43 |
|     | 1.6.2.4 Dehydration reactions in ionic liquids             | 44 |
| 1.7 | Thesis aims  | 47 |
| 1.8 | References   | 48 |

## ***Chapter 2 Experimental***

|     |                      |    |
|-----|----------------------|----|
| 2.1 | Catalyst preparation | 58 |
|-----|----------------------|----|

|        |   |    |
|--------|---|----|
| 2.1.1  | Preparation of SBA-15 support   | 58 |
| 2.1.2  | Preparation of bulk precipitated niobic acid  | 58 |
| 2.1.3  | Synthesis of supported niobic acid on SBA-15  | 59 |
| 2.1.4  | Preparation of phosphated zirconia  | 60 |
| 2.2    | Catalyst characterization   | 61 |
| 2.2.1  | Inductively coupled plasma – optical emission spectrometry                                    | 61 |
| 2.2.2  | X-Ray photoelectron spectroscopy  | 62 |
| 2.2.3  | Powder X-Ray diffraction  | 65 |
| 2.2.4  | Nitrogen porosimetry  | 67 |
| 2.2.5  | Transmission electron microscopy  | 71 |
| 2.2.6  | Thermogravimetric analysis  | 72 |
| 2.2.7  | Propylamine chemisorption and temperature programmed desorption                               | 73 |
| 2.2.8  | Diffuse reflection infrared Fourier transform spectroscopy and in situ pyridine chemisorption | 74 |
| 2.2.9  | Carbon dioxide chemisorption  | 76 |
| 2.2.10 | Raman spectroscopy  | 77 |
| 2.3    | Catalytic tests   | 78 |
| 2.3.1  | Glucose and fructose conversion to HMF  | 78 |
| 2.4    | References  | 81 |

### ***Chapter 3 Characterization of niobic acid nanoparticle catalysts***

|         |  |    |
|---------|--|----|
| 3.1     | Introduction                                   | 85 |
| 3.1.1   | Crystallinity                                  | 85 |
| 3.1.2   | Acidity  | 88 |
| 3.2     | Results and discussion                         | 89 |
| 3.2.1   | Characterization of bulk niobic acid catalysts | 89 |
| 3.2.1.1 | Surface and bulk compositional analysis        | 89 |
| 3.2.1.2 | Textural properties                            | 91 |
| 3.2.1.3 | Structure and morphology                       | 93 |

|           |  |     |
|-----------|--|-----|
| 3.2.1.3.1 | Powder X-Ray diffraction   | 94  |
| 3.2.1.3.2 | Scanning transmission electron microscopy  | 96  |
| 3.2.1.3.3 | Thermogravimetric analysis and differential thermal analysis   | 99  |
| 3.2.1.3.4 | Raman spectroscopy   | 100 |
| 3.2.1.4   | Acidity measurement  | 101 |
| 3.2.1.4.1 | Diffuse reflection infrared Fourier transform spectroscopy (DRIFTS) and in situ pyridine chemisorption | 102 |
| 3.2.1.4.2 | Propylamine chemisorption and temperature programmed desorption  | 103 |
| 3.2.2     | Characterization of x%PNA/SBA-15   | 105 |
| 3.2.2.1   | Surface and bulk compositional analysis  | 105 |
| 3.2.2.2   | Textural properties  | 108 |
| 3.2.2.3   | Structure and morphology   | 109 |
| 3.2.2.3.1 | Powder X-Ray diffraction   | 110 |
| 3.2.2.3.2 | Scanning transmission electron microscopy  | 111 |
| 3.2.2.3.3 | Raman spectroscopy   | 113 |
| 3.2.2.4   | Acidity measurement  | 114 |
| 3.2.2.4.1 | Diffuse reflection infrared Fourier transform spectroscopy (DRIFTS) and in situ pyridine chemisorption | 114 |
| 3.2.2.4.2 | Propylamine chemisorption and temperature programmed desorption  | 115 |
| 3.3       | Conclusions  | 117 |
| 3.4       | References   | 118 |

***Chapter 4 Niobic acid nanoparticle catalysts for the transformation of biomass derived sugars to 5-hydroxymethylfurfural***

|         |  |     |
|---------|--|-----|
| 4.1     | Introduction   | 123 |
| 4.2     | Results and discussion   | 125 |
| 4.2.1   | Glucose and fructose conversion to HMF over bulk PNA catalysts | 125 |
| 4.2.1.1 | Effect of catalyst calcination temperature                     | 125 |

|         |  |     |
|---------|--|-----|
| 4.2.1.2 | Effect of reaction temperature                                     | 133 |
| 4.2.1.3 | Effect of reactant concentration                                   | 142 |
| 4.2.1.4 | Effect of solvent (DMSO)   | 149 |
| 4.2.2   | Glucose and fructose conversion to HMF over x%PNA/SBA-15 catalysts | 158 |
| 4.2.2.1 | Glucose conversion   | 158 |
| 4.2.2.2 | Fructose conversion  | 161 |
| 4.2.3   | Comparison between bulk PNA and SBA-15 supported PNA               | 164 |
| 4.3     | Conclusion   | 165 |
| 4.4     | References   | 167 |

***Chapter 5 Bifunctional PO<sub>4</sub>2-/ZrO<sub>2</sub> catalysts for the transformation of biomass derived sugars to 5-hydroxymethylfurfural***

|           |   |     |
|-----------|---|-----|
| 5.1       | Introduction  | 172 |
| 5.1.1     | Crystallinity   | 173 |
| 5.1.2     | Acidity   | 174 |
| 5.1.3     | The application of phosphated zirconia in the production of HMF | 176 |
| 5.2       | Results and discussion  | 177 |
| 5.2.1     | Characterization of phosphated zirconia catalysts               | 177 |
| 5.2.1.1   | Surface and bulk compositional analysis                         | 177 |
| 5.2.1.2   | Textural properties   | 182 |
| 5.2.1.3   | Structure and morphology  | 185 |
| 5.2.1.3.1 | Powder X-Ray diffraction  | 186 |
| 5.2.1.3.2 | Thermogravimetric analysis and differential thermal analysis    | 188 |

|  |  |     |
|--|--|-----|
| 5.2.1.3.3  | Raman spectroscopy   | 190 |
| 5.2.1.4  | Acid and base sites measurement  | 191 |
| 5.2.1.4.1  | Diffuse reflection infrared Fourier transform spectroscopy (DRIFTS) and in situ pyridine chemisorption | 192 |
| 5.2.1.4.2  | Propylamine chemisorption and temperature programmed desorption  | 195 |
| 5.2.1.4.3  | CO <sub>2</sub> titration  | 197 |
| 5.2.2  | Catalytic results  | 198 |
| 5.2.2.1  | Effect of phosphate loading  | 198 |
| 5.2.2.2  | Effect of calcination temperature  | 206 |
| 5.3  | Conclusions  | 212 |
| 5.4  | References   | 214 |
| <b><i>Chapter 6 Concluding remarks and future work</i></b> |  |     |
| 6.1  | Conclusions  | 219 |
| 6.2  | Future work  | 222 |
| 6.3  | References   | 223 |

## List of Abbreviations

- BAS** - Brønsted acid sites
- BET** - Brunauer, Emmett and Teller Adsorption Theory
- BJH** - Barrett, Joyner and Halenda Pore Size Distribution Method
- DRIFTS** - Diffuse reflection infrared Fourier transform spectroscopy
- DSC** - Differential scanning calorimetry
- DTA** - Differential thermal analysis
- EDX** - Energy dispersive X-ray analysis
- HMF** - 5-hydroxymethylfurfural
- ICP-OES** - Inductively coupled plasma optical emission spectroscopy
- LAS** - Lewis acid sites
- PNA** - Precipitated niobic acid
- PZ** - Phosphate zirconia
- rpm** - Revolution per minutes
- STEM** - Scanning transmission electron microscope
- TGA** - Thermogravimetric analysis
- TOF** - Turnover frequency
- TPD** - Temperature programmed desorption
- XPS** - X-ray photoelectron spectroscopy
- XRD** - Powder X-ray diffraction

# List of Equations, Figures, Schemes and Tables

## *Chapter 1 Introduction*

|   |    |
|---|----|
| <b>Figure 1.1</b> World energy consumption by region (1990-2016)  | 20 |
| <b>Figure 1.2</b> The 12 principles of Green Chemistry  | 22 |
| <b>Figure 1.3</b> Energy profile diagram for an uncatalysed (dash line) and catalysed (full line) reaction showing the activation energies of the uncatalysed forward reaction (Ea1), catalysed forward reaction (Ea2), uncatalysed reverse reaction (Ea3) and catalysed reverse reaction (Ea4) | 24 |
| <b>Figure 1.4</b> Extent of total catalytic processes (left) and type of catalysis (right) used in industrial applications (adapted from [17])  | 24 |
| <b>Figure 1.5</b> Composition of lignocellulose   | 30 |
| <b>Figure 1.6</b> 5-hydroxymethylfurfural (HMF)   | 33 |
| <b>Figure 1.7</b> Catalytic conversion of HMF to valuable compounds for the production of biofuels, polymers, building blocks and solvents  | 35 |
| <b>Figure 1.8</b> Proposed cyclic (left) and acyclic (right) mechanisms for glucose conversion to HMF (adapted from [113])  | 38 |

## *Chapter 2 Experimental*

|  |    |
|--|----|
| <b>Equation 2.1</b> Calculation of precursor needed  | 60 |
| <b>Equation 2.2</b> Calculation of precursor solution volume   | 60 |
| <b>Figure 2.1</b> Calibration curve for Nb quantification in ICP-OES                                   | 62 |
| <b>Table 2.1</b> List of scanned elements in XPS   | 63 |
| <b>Figure 2.2</b> Calculated IMFPs for a range of elements spanning Li-Bi as a function of electron KE | 63 |
| <b>Figure 2.3</b> Schematic representation of the photoemission process                                | 64 |
| <b>Equation 2.3</b> Photoelectron kinetic energy   | 64 |
| <b>Equation 2.4</b> Spin orbit coupling effect   | 64 |
| <b>Equation 2.5</b> Bragg's Law  | 66 |
| <b>Equation 2.6</b> Distance between planes in hexagonal (left) and orthorhombic (right) systems       | 66 |
| <b>Equation 2.7</b> Lattice parameter calculation in hexagonal (left) and orthorhombic (right) systems | 66 |
| <b>Figure 2.4</b> Schematic representation of the X-Ray Diffraction instrument                         | 67 |
| <b>Equation 2.8</b> Scherrer equation  | 67 |

|  |    |
|--|----|
| <b>Figure 2.5</b> Classification of adsorption isotherms (left) and type of hysteresis loop (right)  | 69 |
| <b>Equation 2.9</b> Linear BET equation  | 70 |
| <b>Equation 2.10</b> Definition of constant C  | 70 |
| <b>Equation 2.11</b> BET surface area calculation  | 70 |
| <b>Equation 2.12</b> Kelvin equation   | 71 |
| <b>Figure 2.6</b> Schematic view of a TEM [30]   | 72 |
| <b>Equation 2.13</b> Adsorption and reaction of propylamine with the catalyst  | 74 |
| <b>Equation 2.14</b> Kubelka-Munk equation   | 74 |
| <b>Figure 2.7</b> General mechanism of DRIFTS[36]  | 75 |
| <b>Figure 2.8</b> Pyridine adsorption mechanism  | 76 |
| <b>Figure 2.9</b> Adsorption configuration of carbonates   | 77 |
| <b>Figure 2.10</b> Calibration of reactants and potential products in HPLC   | 79 |
| <b>Figure 2.11</b> An example of typical HPLC chromatograms for glucose dehydration in water from DA detector (top) and RI detector (bottom)       | 80 |
| <b>Table 2.2</b> List of compounds calibrated in HPLC  | 80 |
| <b>Equation 2.15</b> Calculation of a) Glucose conversion, b) 5-HMF yield, c) selectivity to HMF, d) fructose yield and e) selectivity to fructose | 81 |

### ***Chapter 3 Characterization of niobic acid nanoparticle catalysts***

|   |    |
|---|----|
| <b>Figure 3.1</b> Basic unit cell of niobic acid in amorphous (A), hexagonal (T) and orthorhombic (TT) form[14]                                       | 87 |
| <b>Figure 3.2</b> XPS of the Nb 3d (left) and O 1s (right) regions for the PNA materials calcined at different temperatures                           | 90 |
| <b>Figure 3.3</b> Oxygen-niobium atomic ratio measured by XPS   | 91 |
| <b>Table 3.1</b> Surface and bulk compositional analysis of as-prepared niobic acid   | 91 |
| <b>Table 3.2</b> Textural properties of PNA materials   | 92 |
| <b>Figure 3.4</b> N <sub>2</sub> porosimetry isotherms (left) and pore size distribution (right) of: PNA (●), 300PNA (▲), 500PNA (■) and 700PNA (◆)   | 93 |
| <b>Figure 3.5</b> Influence of calcination temperature in surface area (●) and pore volume (○)  | 93 |
| <b>Table 3.3</b> XRD reflection positions, Miller index and interplanar distance of the hexagonal structure of PNA obtained from in-situ PNA analysis | 94 |
| <b>Figure 3.6</b> In situ XRD patterns of PNA as a function of calcination temperature  | 94 |

|   |     |
|---|-----|
| <b>Table 3.4</b> XRD reflection positions, Miller index and interplanar distance of the orthorhombic structure of PNA obtained from in-situ PNA analysis                                  | 95  |
| <b>Figure 3.7</b> Orthorhombic structure of Nb <sub>2</sub> O <sub>5</sub> [52]   | 96  |
| <b>Figure 3.8</b> STEM pictures of amorphous PNA and its particle size distribution at the right calculated from 60 particles   | 97  |
| <b>Figure 3.9</b> STEM picture of 300PNA, 500PNA and 700PNA with their particle size distribution at the right calculated from 60-70 particles  | 98  |
| <b>Figure 3.10</b> Differential mass loss of PNA calcined at different temperatures under nitrogen flow; (inset) structural water integration area as function of calcination temperature | 99  |
| <b>Figure 3.11</b> DTA of PNA calcined at different temperatures  | 100 |
| <b>Figure 3.12</b> Raman spectra of thermally treated PNA   | 101 |
| <b>Figure 3.13</b> Representative structure of the Lewis and Brønsted acid sites on niobic acid catalysts   | 102 |
| <b>Figure 3.14</b> In-vacuo DRIFT spectra of pyridine treated PNA (left) and Brønsted : Lewis character of PNA (right) as a function of calcination temperature                           | 103 |
| <b>Table 3.5</b> Acid properties of thermally treated PNA materials   | 104 |
| <b>Figure 3.15</b> Propene desorption for the PNA series  | 105 |
| <b>Table 3.6</b> Surface and bulk composition of PNA/SBA-15 as a function of niobia Loading   | 106 |
| <b>Figure 3.16</b> XPS of the Nb 3d (left) and O 1s (right) regions for the PNA/SBA-15 series   | 106 |
| <b>Figure 3.17</b> Surface versus bulk niobium concentration  | 107 |
| <b>Figure 3.18</b> Nitrogen adsorption-desorption isotherms (left) and BJH pore size distribution of supported niobium materials (right)  | 108 |
| <b>Table 3.7</b> Textural properties of niobic acid supported materials   | 109 |
| <b>Figure 3.19</b> Correlation between niobium mesopore surface area (left) and mesopore pore volume (right) of supported niobium materials   | 109 |
| <b>Figure 3.20</b> Low angle (left) and wide angle (right) X-Ray powder diffraction patterns of the x%PNA/SBA-15 materials  | 110 |
| <b>Table 3.8</b> Unit cell sizes and pore wall thickness calculated from XRD and N <sub>2</sub> adsorption-desorption analyses  | 111 |
| <b>Figure 3.21</b> STEM of 9.1%PNA/SBA-15   | 112 |
| <b>Figure 3.22</b> EDX elemental mapping of 1.8% PNA/SBA-15   | 112 |
| <b>Figure 3.23</b> Raman spectra of x%PNA/SBA-15 samples  | 113 |
| <b>Figure 3.24</b> Schematic diagram of niobia species dispersed on SBA-15 support  | 114 |

|  |     |
|--|-----|
| <b>Figure 3.25</b> In-vacuo DRIFT spectra of pyridine treated x%PNA/SBA-15 as a function of Nb loading | 115 |
| <b>Table 3.9</b> Acid properties of niobic acid supported on SBA-15 materials                          | 116 |
| <b>Figure 3.26</b> Total acid site density of PNA/SBA-15 as a function of Nb loading                   | 116 |
| <b>Figure 3.27</b> Propene desorption for the x%PNA/SBA-15 series obtained by TGA-MS                   | 117 |

#### ***Chapter 4 Niobic acid nanoparticle catalysts for the transformation of biomass derived sugars to 5-hydroxymethylfurfural***

|   |     |
|---|-----|
| <b>Scheme 4.1</b> Simplified pathways for the conversion of glucose to fructose and generation of undesirable side reactions  | 123 |
| <b>Figure 4.1</b> Profiles of glucose conversion and yield of HMF, fructose profiles and other sugars for glucose dehydration after 6 h reaction at 100°C over calcined niobic acid   | 126 |
| <b>Figure 4.2</b> Conversion of glucose over parent niobic acid and corresponding yield (left) and selectivity (right) of HMF, fructose and other sugars as a function of pre-calcination temperature after 6 h reaction at 100°C         | 127 |
| <b>Figure 4.3</b> Turnover frequencies for the aqueous phase conversion of glucose and associated HMF productivity normalised to total acid loading as a function of pre-calcination temperature  | 129 |
| <b>Figure 4.4</b> Profiles of fructose conversion and yield of HMF, glucose and other sugars for fructose dehydration after 6 h reaction over calcined niobic acid at 100°C   | 130 |
| <b>Figure 4.5</b> Conversion of fructose over parent niobic acid and corresponding yields (left) and selectivity (right) of HMF, glucose and other sugars as a function of pre-calcination temperature after 6 h reaction at 100°C        | 131 |
| <b>Figure 4.6</b> Turnover frequencies for the aqueous phase conversion of fructose and associated HMF productivity normalised to total acid loading as a function of pre-calcination temperature   | 133 |
| <b>Figure 4.7</b> Profiles of glucose conversion and yield of HMF, fructose and other sugars for glucose dehydration after 6 h reaction over parent niobic acid at different reaction temperatures  | 134 |
| <b>Figure 4.8</b> Conversion of glucose over parent niobic acid and corresponding yields (left) and selectivity (right) of HMF (white), fructose (black) and other sugars (blue) as a function of reaction temperature after 6 h reaction | 135 |
| <b>Figure 4.9</b> Turnover frequencies for the aqueous phase conversion of glucose and associated HMF productivity normalised to total acid loading as a function of reaction temperature   | 137 |
| <b>Figure 4.10</b> Profiles for fructose conversion and yield of HMF, glucose and other sugars for fructose dehydration after 6 h reaction over parent niobic acid  |     |

|  |     |
|--|-----|
| at different reaction temperatures   | 138 |
| <b>Figure 4.11</b> Conversion of fructose over parent niobic acid and corresponding yields (left) and selectivity (right) of glucose (black), HMF (white) and other sugars (blue) as a function of reaction temperature after 6 h reaction               | 139 |
| <b>Figure 4.12</b> Turnover frequencies for the aqueous phase conversion of fructose over parent niobic acid normalised to Brønsted acid loadings and associated HMF productivity normalised to total acid loading as a function of reaction Temperature | 140 |
| <b>Figure 4.13</b> Determination of the activation energy from Arrhenius equation for the conversion of glucose (red) fructose (blue) (filled symbols), and for the HMF formation (open symbols) from glucose (red) and fructose (blue)                  | 141 |
| <b>Figure 4.14</b> Profiles of glucose conversion and yield of HMF, fructose and other sugars for glucose dehydration after 6 h reaction at 100°C over parent niobic acid at different glucose concentrations  | 143 |
| <b>Figure 4.15</b> Conversion of glucose over parent niobic acid and corresponding yields of fructose (black), HMF (white) and other sugars (blue) after 6 h reaction at 100°C as a function of glucose concentration                                    | 144 |
| <b>Figure 4.16</b> Glucose turnover frequency and HMF productivity over parent niobic acid as a function of glucose concentration  | 145 |
| <b>Figure 4.17</b> Profiles of fructose conversion and yield of HMF, glucose and other sugars for fructose dehydration after 6 h reaction at 100°C over parent niobic acid at different fructose concentrations  | 146 |
| <b>Figure 4.18</b> Conversion of fructose over parent niobic acid and corresponding yields of HMF (white), glucose (black) and other sugars (blue) after 6 h reaction at 100°C as a function of fructose concentration                                   | 147 |
| <b>Figure 4.19</b> Fructose turnover frequency and HMF productivity over parent niobic acid as a function of fructose concentration  | 148 |
| <b>Equation 4.1</b> Rate equation for the calculation of the order of reaction   | 148 |
| <b>Equation 4.2</b> Simplified rate equation   | 149 |
| <b>Figure 4.20</b> Rate of glucose (red) and fructose (blue) conversion as a function of initial reagent concentration over PNA  | 149 |
| <b>Figure 4.21</b> Glucose conversion profile for glucose dehydration after 6 h reaction in DMSO without catalyst at different reaction temperatures   | 150 |
| <b>Figure 4.22</b> Glucose conversion and yield of glucose and HMF profiles for glucose dehydration after 6 h reaction over pre-calcined niobic acid at 75°C in DMSO   | 151 |
| <b>Figure 4.23</b> Conversion of glucose in DMSO after 6 h reaction at 75°C over parent niobic acid and corresponding yield of HMF (white) as a function of pre-calcination temperature  | 152 |

|   |     |
|---|-----|
| <b>Figure 4.24</b> Turnover frequencies for the conversion of associated HMF productivity normalised to total acid loading at 75°C in DMSO over parent niobic acid as a function of pre-calcination temperature   | 153 |
| <b>Figure 4.25</b> Reaction mechanism for the dehydration of fructose to HMF in DMSO[58]  | 153 |
| <b>Figure 4.26</b> Profiles of fructose conversion and yield of HMF, glucose and other sugars for fructose dehydration in DMSO after 6 h reaction without catalyst at different reaction temperatures   | 154 |
| <b>Figure 4.27</b> Profiles of fructose conversion and yield of HMF, glucose and other sugars in DMSO at 75°C after 6 h reaction over pre-calcined niobic acid  | 155 |
| <b>Figure 4.28</b> Conversion of fructose at 75°C in DMSO over parent niobic acid, corresponding yields of HMF (white), glucose (black) and other sugars (blue) (left) and glucose (black), HMF (white) and other sugars (blue) selectivity (right) after 6 h reaction as a function of pre-calcination temperature | 156 |
| <b>Figure 4.29</b> Turnover frequencies for the conversion of fructose and associated HMF productivity normalised to total acid loading at 75°C in DMSO over parent niobic acid as a function of pre-calcination temperature  | 157 |
| <b>Figure 4.30</b> Glucose conversion and yield of HMF and fructose profiles for glucose dehydration after 6 h reaction at 100°C over supported niobic acid   | 159 |
| <b>Figure 4.31</b> Conversion of glucose (red circles) over supported niobic acid and corresponding yield (left) and selectivity (right) of fructose (black) and HMF (white) after 6 h reaction at 100°C as a function of niobium loading   | 160 |
| <b>Figure 4.32</b> Turnover frequencies for the aqueous phase conversion of glucose and associated 5-HMF productivity normalised to total acid loading as a function of niobium loading   | 161 |
| <b>Figure 4.33</b> Profiles of fructose conversion and yield of HMF, glucose and other sugars for fructose dehydration after 6 h reaction at 100°C over supported niobic acid   | 162 |
| <b>Figure 4.34</b> Conversion of fructose over supported niobic acid and corresponding yields of HMF (white), glucose (black) and other sugars (blue) after 6 h reaction at 100°C as a function of niobium loading  | 163 |
| <b>Figure 4.35</b> Turnover frequencies for the aqueous phase conversion of fructose and associated 5-HMF productivity normalised to total acid loading as a function of niobium loading  | 164 |
| <b>Figure 4.36</b> Comparison of fructose turnover frequency (filled symbols) and associated HMF productivity (open symbols) over supported niobic acid (black) and parent niobic acid (red) as a function of niobium loading   | 165 |

**Chapter 5 Bifunctional PO<sub>4</sub><sup>2-</sup>/ZrO<sub>2</sub> catalysts for the transformation of biomass derived sugars to 5-hydroxymethylfurfural**

|   |     |
|---|-----|
| <b>Figure 5.1</b> Crystal structure of monoclinic (left), tetragonal (middle) and cubic (right) zirconia[30]  | 173 |
| <b>Figure 5.2</b> Representative structure of the Lewis and Brønsted acid sites on phosphated zirconia catalysts (adapted from[39])   | 175 |
| <b>Table 5.1</b> Elemental analysis of PZ materials   | 178 |
| <b>Figure 5.3</b> XPS of the Zr 3d (left) and O 1s (right) regions for the PZ materials calcined at different temperatures  | 180 |
| <b>Figure 5.4</b> XPS of the P 2p (left) region for the PZ materials calcined at different temperatures, comparative of bulk and surface P content and P:Zr ratio with P content for the series of catalysts calcined at 550°C (white), 650°C (black) and 750°C (red) | 181 |
| <b>Figure 5.5</b> N <sub>2</sub> porosimetry isotherms (left) and pore size distribution (right) of the series of PZ catalysts calcined at 550°C (top), 650°C (middle) and 750°C (bottom).  | 183 |
| <b>Table 5.2</b> Textural properties of PZ materials  | 184 |
| <b>Figure 5.6</b> Influence of [H <sub>3</sub> PO <sub>4</sub> ] in surface area of PZ materials calcined at 550°C (white) 650°C (black) and 750°C (red)  | 185 |
| <b>Figure 5.7</b> X-Ray Powder diffractograms for phosphated zirconias series calcined at different temperatures  | 187 |
| <b>Figure 5.8</b> – Thermal analysis reported as % mass loss as function of temperature, obtained for each PZ series (left); and differential thermal analysis (right).   | 189 |
| <b>Figure 5.9</b> – Physisorbed water mass loss for PZ materials calcined at different temperatures.  | 190 |
| <b>Figure 5.10</b> Raman spectra of PZ series calcined at different temperatures  | 191 |
| <b>Figure 5.11</b> In-vacuo DRIFT spectra of PZ as a function of bulk P content   | 193 |
| <b>Figure 5.12</b> In-vacuo DRIFT spectra of pyridine treated PZ materials at different calcination temperatures and their Brønsted : Lewis character as a function of acid concentration used during the impregnation procedure                                      | 194 |
| <b>Table 5.3</b> Acid properties of thermally treated PZ materials  | 195 |
| <b>Figure 5.13</b> Propene desorption for the PZ series at different calcination temperatures and variation of acid loading with acid concentration used during impregnation  | 196 |
| <b>Table 5.4</b> Basic sites loadings and densities (in brackets) as a function of P content and calcination temperature  | 197 |
| <b>Figure 5.14</b> Profiles of glucose conversion and yield of HMF, fructose and other sugars for glucose dehydration reactions at 100°C over PZ calcined at 550°C  | 199 |

|   |     |
|---|-----|
| <b>Figure 5.15</b> Conversion of glucose over PZ550 catalysts and corresponding yield (left) and selectivity (right) of fructose (black) and HMF (white) as a function of phosphate loading after 6 h reaction at 100°C   | 200 |
| <b>Figure 5.16</b> Turnover frequencies for the aqueous phase conversion of glucose and associated HMF productivity normalised to total acid loading as a function of bulk phosphorous content  | 202 |
| <b>Figure 5.17</b> Profiles of fructose conversion and yield of HMF, glucose and other sugars for fructose dehydration reactions at 100°C over PZ calcined at 550°C   | 203 |
| <b>Figure 5.18</b> Conversion of fructose over PZ catalysts calcined at 550°C and corresponding yields (left) and selectivity (right) of glucose (black), HMF (white) and other sugars (blue) as a function of phosphorous content after 6 h reaction at 100°C.                                   | 204 |
| <b>Figure 5.19</b> Turnover frequencies for the aqueous phase conversion of fructose and associated HMF productivity normalised to total acid loading as a function of calcination temperature  | 205 |
| <b>Figure 5.20</b> Glucose conversion and yield of HMF and fructose profiles for glucose dehydration reactions at 100°C over PZ catalysts prepared from a 0.5 M solution of phosphoric acid calcined at different temperatures  | 207 |
| <b>Figure 5.21</b> Conversion of glucose over PZ catalysts prepared from a 0.5 M solution of phosphoric acid and corresponding yield (left) and selectivity (right) of fructose (black) and HMF (white) after 6 h reaction at 100°C as a function of calcination temperature                      | 208 |
| <b>Figure 5.22</b> Turnover frequencies for the aqueous phase conversion of glucose normalised to total acid loadings over PZ catalysts prepared from a 0.01M solution of phosphoric acid as a function of calcination temperature  | 209 |
| <b>Figure 5.23</b> Fructose conversion and yield of HMF and glucose profiles for fructose dehydration reactions at 100°C over PZ catalysts prepared from a 0.25M solution of phosphoric acid calcined at different temperatures   | 210 |
| <b>Figure 5.24</b> Conversion of fructose over PZ catalysts prepared from a 0.25M solution of phosphoric acid and corresponding yield (left) and selectivity (right) of glucose (black), HMF (white) and other sugars (blue) after 6 h reaction at 100°C as a function of calcination temperature | 211 |
| <b>Figure 5.25</b> Turnover frequencies for the aqueous phase conversion of fructose and associated HMF productivity normalised to total acid loading as a function of calcination temperature  | 212 |

## ***Chapter 6 Concluding remarks and future work***

|   |     |
|---|-----|
| <b>Figure 6.1</b> Turnover frequencies for the aqueous phase conversion of fructose and associated 5-HMF productivity normalised to total acid loading (left) and to total acid loading and mass of niobium (right) as a function of niobium loading. Red circles refer to bulk PNA and black circles to PNA/SBA-15 | 221 |
|---|-----|

# ***Chapter 1***

## ***Introduction***

## 1.1 Introduction

Fossil fuels are non-renewable resources such as coal, petroleum and natural gas, and are a fundamental factor of the global economy. Crude oil derived from fossil fuels is the primary source of energy worldwide, and is responsible for 35% the global energy consumption. Moreover, due to the fast increase of global population, petroleum demand and world energy consumption are expected to increase by over 28% according to the U.S Energy Information Administration[1]. **Figure 1.1** shows the rapid increase in worldwide energy consumption by region measured in tonne of oil equivalent (Mtoe) since 1990, as reported by Enerdata in the Global Energy Statistical Yearbook 2017[2], proving an striking increase of 58% in consumed energy in the last 26 years.



**Figure 1.1** World energy consumption by region (1990-2016)[2]

Also, most of the essential commodity chemicals are produced from fossil fuels, demonstrating the high dependence of this petrochemical source. However, this feedstock is a finite resource, meaning that the depletion of world reserves is unavoidable if the world continues consuming fossil fuels at the current rate. Although predictions about the reserves lifespan has been subject of debate, they are predicted to be depleted in the next two centuries[3]. Thus, in order to meet the high demand of petroleum derivatives, the development of technologies comprising new energy sources for a long term transition from fossil fuel based energy carriers has become a priority target for researchers and industries around the world.

A great concern associated to the combustion of fossil fuels has been the increase in greenhouse gas (GHG) levels worldwide, leading to environmental pollution and

climate change[4-6]. Therefore, the quest for new energy sources must be sustainable, inexpensive, renewable and environmentally benign. Implementation of renewable energy sources such as solar, wind, hydro and biomass energy has been successfully effectuated by numerous countries around the world in order to limit their dependency of fossil fuels, as well as new sustainable technologies such as biofuels or electric cars. Nonetheless, biomass derived energy, from which biofuels are produced, has been identified by the International Energy Agency as the source with the highest potential to replace fossil fuels, especially for transportation due to the high efficiency of biofuels[7]. It is widely accepted that the use of biomass as a source of energy and biofuels is able to reduce GHG emissions, especially CO<sub>2</sub> which is produced during the combustion of fossil fuels. Considering the discussed aspects, biomass stands out as promising successor due to its higher biodegradability and sustainability compared to its petroleum analogue[8].

## 1.2 Green Chemistry and the role of catalysis

The concept of Green Chemistry emerged in the early 90's due to the increasing concern about climate change and hazardous environmental effects caused by the traditional industrial processes for the production of fuels and chemicals[9]. A well established definition of Green Chemistry was given by Anastas and Warner as the "*design of chemical products and processes to reduce or eliminate the use and generation of hazardous substances*"[10]. More recently Roger Sheldon gave a similar definition of Green Chemistry as "*green chemistry efficiently utilises (preferably renewable) raw materials, eliminates waste and avoids the use of toxic and/or hazardous solvents and reagents in the manufacture and application of chemical products*"[11]. Therefore, the most important aspect of Green Chemistry is the design of environmentally friendly products and processes, that is *benign by design*.

### 1.2.1 Principles of catalysis

In 1998 Anastas and Warner developed the 12 principles of green chemistry to serve as guidance for the development of sustainable and clean processes, products and technologies, involving all stages of the production process, from the raw materials to the final product[10]. These 12 principles are illustrated in **Figure 1.2**, and can be summarized in three main aspects adopting a "better safe than sorry" approach: eluding the use of toxic and/or hazardous substances, the reduction of waste production and the utilization of green renewable raw materials derived from biomass[12].

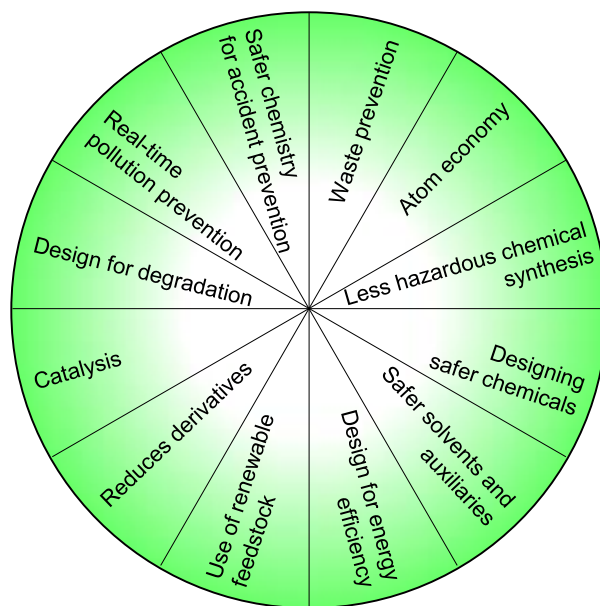


**Figure 1.2** The 12 principles of Green Chemistry

Catalysis plays an important role in Green Chemistry. The application of a catalyst assists to reduce the production of waste linked to the traditional stoichiometric reactions, decrease the energy input required and reduce the generation of by-products increasing the selectivity of the reaction[13]. Thus, a catalyst serves to increase the rate of chemical reaction without itself being consumed. A suitable catalyst can be characterized by four main aspects[14]:

- It should be highly selective towards the desired product and show low predilection for possible by-products.
- It should provide a suitable reaction rate under the given reaction conditions.
- It should possess good stability under such conditions, i.e. the catalytic activity should not decline quickly.
- It should grant reactants and products good accessibility to its active sites.

An ideal catalyst should fulfil these factors, but in practice industrial catalysts usually experience deactivation due to poisoning, leaching of active phase, sintering or degrading, leading to decline in activity and selectivity[14]. Nevertheless, regeneration processes can restore the initial activity of an adequate catalyst. An industrially applied example is the coke oxidation of catalysts used for hydrocarbons cracking after being deactivated by coke deposition[15].

The minimum energy requirement that must be met for a chemical reaction to occur is called the activation energy ( $E_a$ ). Energy profile diagrams as shown in **Figure 1.3** plot the total energy input to a reaction system as it proceeds from reactants to products. The difference between the potential energies of reactants and products is called the enthalpy of reaction ( $\Delta H$ )[16]. In **Figure 1.3**, the potential energy of the reactants is higher than that of the products, therefore energy is released into the environment when the reaction proceeds (exothermic reaction) and  $\Delta H$  has a negative value. Reactions with positive  $\Delta H$  represent products with greater potential energy than the reactants (endothermic reactions). It is worth mentioning that the enthalpy of reaction depends solely on the thermodynamics of the process, not in the kinetics of the reaction. This means that the same reaction can exhibit different activation energies if it can follow alternative pathways[16].

In a chemical reaction, the transition state is defined as the highest-energy state of the system, and should be clearly distinguished from an intermediate, which represents not a maximum but a metastable minimum on the reaction profile. The rate-determining step controls the overall rate of the reaction, as the overall rate cannot proceed any faster than this rate-limiting step. In the potential energy profile, the rate-determining step is the reaction step with the highest energy of transition state. A two-step example is shown in the catalysed pathway in **Figure 1.3** with one intermediate and two transition states. If a catalyst is added to a reaction, the activation energy is lowered because a lower-energy transition state is formed, providing alternate reaction pathways (full line in **Figure 1.3**) with lower activation energies than the original pathway (dash line in **Figure 1.3**). Catalysts increase the reaction rate but do not affect the potential energy of the reactants and products. In **Figure 1.3**, the activation energies of the forward and reverse uncatalysed reactions,  $E_{a1}$  and  $E_{a3}$  respectively, decrease with the presence of a catalyst, giving the activation energies for the forward and reverse catalysed reactions,  $E_{a2}$  and  $E_{a4}$  respectively.

Some common examples of industrial catalytic processes are the manufacture of ammonia by the Haber process using an iron catalyst, nitration of benzene using concentrated sulphuric acid, decomposition of hydrogen peroxide with manganese (IV) oxide or production of sulphuric acid by contact process with vanadium (V) oxide[14].

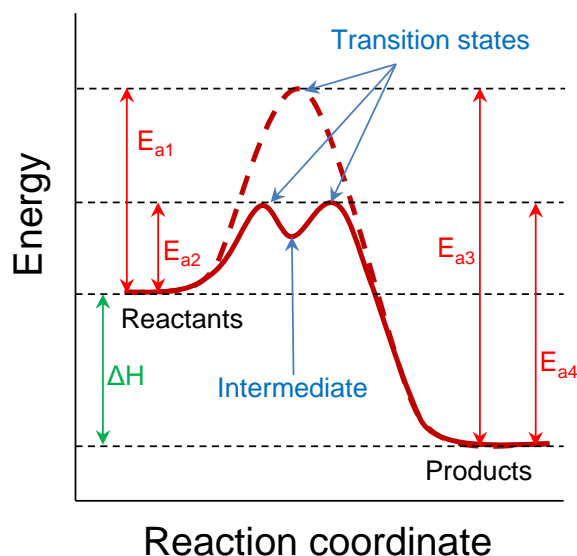


**Figure 1.3** Energy profile diagram for an uncatalysed (dash line) and catalysed (full line) reaction showing the activation energies of the uncatalysed forward reaction ( $E_{a1}$ ), catalysed forward reaction ( $E_{a2}$ ), uncatalysed reverse reaction ( $E_{a3}$ ) and catalysed reverse reaction ( $E_{a4}$ ).

### 1.2.2 Heterogeneous catalysis

Catalysts have been traditionally classified as homogeneous, heterogeneous and enzymatic catalysts. **Figure 1.4** shows the impact of catalysis in industrial applications. Enzymatic catalysis, which is not much implemented in industrial scale uses, is the most complex among the cited types of catalysis, and it comprises the use of biological molecules, typically proteins composed of amino acids and often surrounding a central organometallic structure[17].

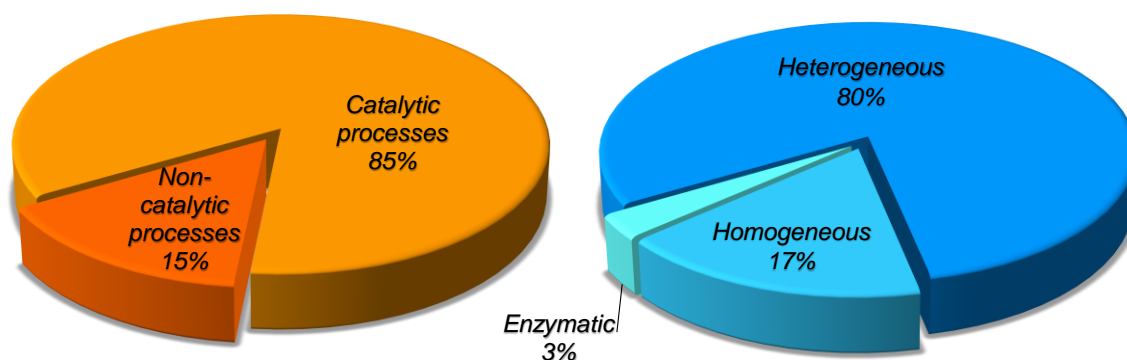


**Figure 1.4** Extent of total catalytic processes (left) and type of catalysis (right) used in industrial applications (adapted from [18])

Enzymatic catalysts were probably the first utilized by mankind since ancient times, since they were and are used for the production of wine, bread, beer or cheese in the form of bacteria or yeast. Homogeneous catalysis refers to catalytic reactions where reactants and catalyst are in the same phase, typically liquid or gas. Homogeneous catalysts tend to give excellent selectivity due to the easier contact between reactants and the active sites of the catalyst. However their major disadvantage is the difficult recovery of the catalyst after reaction. Because the catalyst is dissolved in the reaction solution, the recovery of the catalyst often involves costly separation techniques such as distillation at high temperatures that may destroy the catalyst. Alternatively, heterogeneous catalysts, usually in the solid state, are easier and cheaper to separate and reuse compared to homogeneous catalysts. Moreover, solid heterogeneous catalysts also possess higher thermal stability, making them suitable candidates for high temperature catalytic reactions[19].

Solid acid catalysts, which are the most utilized in an industry scale, can be categorized depending on their morphology and physical properties, with the most used catalysts being zeolites, heteropolyacids, mesoporous molecular sieves and modified metal oxides[20].

- Zeolites are microporous crystalline aluminosilicate materials made from interlinked corner-sharing tetrahedra of alumina ( $\text{AlO}_4$ ) and silica ( $\text{SiO}_4$ ). They are characterized by complex three-dimensional structures with pores and cavities able to accommodate different atoms or molecules, for example water. Brønsted acidity in zeolites arises from the substitution of  $\text{Si}^{4+}$  with  $\text{Al}^{3+}$  (or other trivalent ions). This ion exchange requires a charge compensation, which is usually balanced by protons, providing the Brønsted character to the zeolite. Lewis acid sites form upon dehydroxylation, dealumination or from extra-framework aluminium (not tetrahedrally bound in the framework)[21]. Zeolites possess beneficial properties for catalysis such as high surface area and the ability to tune their pore size or acid properties by carefully modifying the Si:Al ratio. However, they suffer from diffusional limitations of the reactants to and from the pore system due to their low pore size. Zeolites can be classified according to their framework structure and Si:Al ratio and although a high variety of zeolites are known, only a few are applied at industrial scale; some of them are ZSM-5 (silicalite), FAU (faujasite), MOR (mordenite) and BETA (beta).
- Heteropolyacids (HPA), also called polyoxometalates, are formed by the condensation of several oxoanions, typically group 6 atoms (W, Mo) called

addenda atoms, linked together by shared oxygen atoms to form closed 3-dimensional frameworks. This cage-like structure contains a central atom, also called heteroatom, typically Si or P, tetrahedrally coordinated to oxygens and surrounded by 2-18 oxygen atoms depending on the coordination number. Adjusting the number of atoms involved in the 3-dimensional framework, different structures are obtained, with the most common being Keggin ( $\text{XM}_{12}\text{O}_{40}^{n-}$ ), Wells-Dawson ( $\text{X}_2\text{M}_{18}\text{O}_{62}^{n-}$ ) and Lindqvist ( $\text{Mo}_6\text{O}_{19}^{2-}$ ), where X is the heteroatom and M the addenda atoms[20]. HPA possess high Brønsted acidity, reported to be even superior than classic inorganic acids such as HCl or  $\text{H}_2\text{SO}_4$ [22], which can be tuned by varying the type of atoms involved. Among their limitations for the field of catalysis stand the low surface area and water solubility, although the latter can be remedied by the substitution of  $\text{H}^+$  with larger cations such as  $\text{Cs}^+$  or  $\text{Rb}^+$ [20].

- Metal oxides are compounds comprised by transition metals bound to oxygen atoms. They possess Lewis acidity due to the surface metal centres acting as electron acceptors and some of them show Lewis basicity due to the anionic oxygen centres acting as electron donors[23]. Brønsted acidity can arise due to the surface hydroxyl groups. Mixed metal oxides possess more than one cationic species ( $\text{CaTiO}_3$ ,  $\text{TiO}_2\text{-ZrO}_2$ ) or a single cation with different oxidation states (magnetite with  $\text{Fe}^{3+}$  and  $\text{Fe}^{2+}$ ). These materials can adopt a great variety of possible structures and pores sizes. Traditionally, metal oxides have also been modified with phosphate or sulphate groups and calcined at relatively high temperature to create *superacids*, i.e. they have Hammett acidity function ( $H_0$ ) < -12. Some examples of *superacids* are sulfated tin oxide and sulfated zirconia[24].
- Mesoporous molecular sieves (MMS) appeared as an alternative to the small pore size of zeolites, which presented diffusion limitations for the processing of big molecules. MMS have pores in the range of 2-50 nm, and can be of amorphous or crystalline structure, such as the periodically ordered siliceous materials SBA-15 and MCM-41. Although they own little acidity, they can be tuned by impregnation or grafting of acidic moieties to enhance their catalytic properties. Thermal stability can also be tuned by modifying the pore size during the synthesis procedure[20]. They can also serve as a support to increase the surface area of naturally low surface area compounds such as heteropolyacids or metal oxides[25].

### 1.3 Shifting from oil-based products to biomass sources

Currently the fractionation and refinement of crude oil is carried out in oil refineries, where it is transformed into more useful substances such as fuels used for transportation (gasoline, diesel fuel, kerosene...) and specialty chemicals, from which a wide variety of compounds can be prepared (polymers, lubricants, adhesives...). A biorefinery is the analogous concept of a petroleum refinery but using biomass feedstock instead of petroleum for the production of value-added chemicals, heat, power and fuels[26]. The concept of biorefinery is not something new, as proved by the marked increase of biorefinery and biofuels publications in the last decade[27].

#### 1.3.1 Classification of biofuels

Biofuels can be classified into two main categories, primary (unprocessed) and secondary (processed) biofuels[28]. Firewood, pellets and wood chips lie in the category of primary biofuels. They are organic materials that are used as harvested, primarily as a direct source of heat and electricity by means of combustion. Secondary biofuels include processed biomass in the form of solid (charcoal), liquid (biodiesel, ethanol, etc.) or gas (biogas) products, and they can be used as transportation fuels or as an energy source for industrial applications. Liquid biofuels belonging to this secondary group are promising candidates to replace traditional liquid fuels like diesel and petrol, and can at the same time be classified into three main subcategories, namely first, second and third generation, depending on the kind of feedstock used for their processing[28].

##### a) *First-generation biofuels*

The first-generation biofuels are produced from edible feedstocks, such as vegetable oil, animal fats, sugar or starch[29, 30]. The most popular biofuels within this category are biodiesel and bioethanol. Bioethanol is produced from the fermentation of sugar (sugar cane) or starch (mainly corn) carried out by enzymes produced from yeast. These enzymes are able to convert six-carbon compounds (mainly glucose) into two carbon molecules, such as ethanol[31]. Bioethanol can be directly obtained from the fermentation of sugars, while previous hydrolysis to sugar is needed when starches are used as hydrocarbon source. This fermentation process is similar to that used for the production of wine and beer. After fermentation, purification of bioethanol is realized by distillation and dehydration processes. The obtained bioethanol can be used as a fuel in a spark-ignition engine after minor modifications, although when blended with fossil

fuels it reduces the emissions of sulphur oxide and carbon monoxide, while also improving the combustion performance[32]. Biodiesel is obtained via esterification and transesterification reactions of vegetable oils or animal fats with an alcohol (usually methanol) to produce glycerol and fatty acid monoalkyl esters (FAME) which are the main components of biodiesel[29, 30]. Biodiesel can be used in regular diesel vehicles without making any changes to the engine or it can be blended with traditional diesel fuel. Biodiesel has an energy content of 88-95% of petroleum-based diesel but presents several perks in comparison with the latter, like an increased lubricity and less toxic emissions[33].

Although first-generation biofuels are available and commercialized in several countries, their production has been debated as immoral due to the competition with agricultural land for food production[34, 35]. This “food versus fuel” competition was thought to evoke the price rise of food in countries where first-generation biofuels are produced as well as the production cost of these biofuels. These limitations shifted the attention towards non-edible raw materials as a biomass source for the production of biofuels. However, this argument was debunked by the Renewable Fuels Association through a report studying the fluctuations of corn prices and their lack of relation with consumer food prices[36].

#### b) *Second-generation biofuels*

Second-generation biofuels are produced from inedible lignocellulosic feedstocks, which can be waste products from agriculture, forestry or industry, such as wood, grass or crop residues. There are several advantages for the utilization of the aforementioned raw materials; on one side biodiesel produced from lignocellulosic sources could be competitive in a commercial scale due to the low price, greater abundance and high yield of the feedstock[37]. They also show major advantages in terms of environmental sustainability and reduction of GHG emissions[38], but the main advantage would be the limited competition for land with food production presented by the first-generation biofuels[39]. However, the major drawback presented by this lignocellulosic biofuels is the need for more sophisticated equipment and conversion technologies due to the strong structure of lignocellulose, which make it difficult to process[40].

#### c) *Third-generation biofuels*

In order to overcome the disadvantages associated with the production of first and second generation biofuels, fuel versus food competition and land requirement issues, attention has been drawn by the production of renewable fuels derived from microbes

and microalgae[41]. Some examples of microbial species able to synthesised biodiesel are yeast and fungi, due to their ability to store large amounts of lipids in their microbial cells[42]. Microalgae are photosynthetic unicellular or multicellular microorganisms represented by a big variety of species, with around 30.000 of them studied and analysed[43], and are able to reproduce themselves via photosynthesis, converting sunlight into chemical energy[44]. They can also be cultivated in different ways like open ponds, closed-loop systems or photobioreactors, although essentially algae are able to grow anywhere if temperature is warm enough, even in waste water. Other advantages of algae are their rapid growth rate, the nonessential land usage, and their ability to assimilate carbon dioxide because of this they could even be used to purify industrial effluents, reducing the GHG emissions from industrial companies[45]. They can also remove nitrates and phosphates from waste water, since they can use these contaminants as nutrients[46], and they have a higher biofuel production capacity than traditional crops per unit of harvested area, estimated to be between 15 and 300 times more[47]. However, some major drawbacks have kept these processes from industrial implementation. Essentially, algae grow under strictly controlled conditions of light, temperature and large amounts of water and nutrients, making this process more expensive and technologically challenging than the previous two generations of biofuels[48]. Moreover, it is estimated that the generation of fertilizers needed to meet the nutrient demand of microalgae intended for biofuel production would create more CHC emissions than would be saved by using them[49].

#### **1.4 Production of building blocks from lignocellulosic biomass**

Biomass can provide three different sources of feedstock from which biofuels can be produced[50]: starchy feedstocks belonging to the first-generation biofuels source, composed of glucose polysaccharides which can be easily transformed into the constituent monomers by hydrolysis; triglyceride feedstocks, derived from animal fatty acids and vegetable and waste oils, formed by glycerol and lipids; and lignocellulosic feedstocks, the most abundant class of biomass. Starch and lignocellulose are differentiated by their structural composition; while starch is easily degradable to serve as energy supply for plants, lignocellulose is the main construction material of plant cells, providing structural integrity due to its intricate and fibrous architecture, able to resist mechanical and microbial degradation[51]. Lignocellulose is mainly composed of three different fractions, namely cellulose (30-50%), hemicellulose (15-35%) and lignin (10-20%)[52]. As illustrated in **Figure 1.5**, lignocellulose is composed of microfibrils where cellulose is surrounded by hemicellulose and embedded in a matrix of

hemicellulose and lignin. Lignocellulose also contains other components in a lesser extent, such as proteins, fatty acids, terpenic oils, pectins and inorganic compounds mainly based on potassium, phosphorous and nitrogen[53].

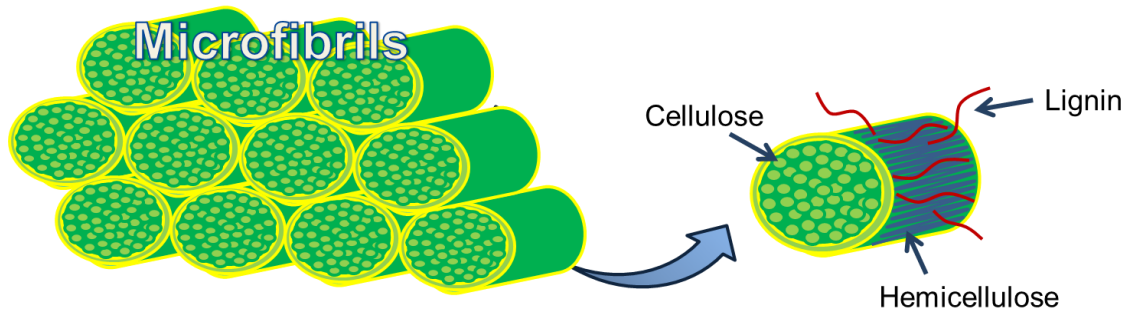


**Figure 1.5** Composition of lignocellulose

Cellulose is the most abundant organic molecule on earth, and 180 billion tons are estimated to be produced annually[54]. It is a linear molecule comprised of long chains of glucose monomers linked by  $\beta$ -1,4-glycosidic bonds, which can be organised in a layer structure due to hydrogen bonding, providing structural strength and crystallinity to the polymeric molecule[55]. The cross-linkage between layers through hydrogen bonding creates microfibrils that grant stability and compactness to the molecule. Cellulose is a hardly accessible part of lignocellulosic biomass, and several pretreatments are necessary to separate their other constituents and enable the isolation of glucose monomers via hydrolysis[56].

Hemicellulose is the second most abundant component of lignocellulose, and is an amorphous branched polymer composed by different C5 and C6 sugars such as glucose, galactose, arabinose, mannose and xylose, being the latter the most abundant, and bound together by xylan  $\beta$ -1,4-linkages[57]. Hemicellulose binds with cellulose by hydrogen bonds to form a fibres entanglement that provides structural strength to the cell wall[58]. Hemicellulose can be extracted from the lignocellulosic conglomerate by either physical (steam explosion, hot water treatment) or chemical methods (acid hydrolysis)[26], and it generally yields high amount of sugars in the form of xylose monomers.

Lignin is the last main component of lignocellulose; it is a tri-dimensional, highly branched, amorphous polymer composed of three phenylpropane compounds, namely coumaryl, coniferyl and sinapyl alcohol[56]. It provides hydrophobicity and compactness to the plant cell wall due to the covalent bonds formed with hemicellulose and cellulose[59]. Lignin can be separated from lignocellulose as a pretreatment step

by depolymerisation/solubilisation in alkaline-alcohol solutions in order to isolate the carbohydrate fraction of biomass[58].

Conversion of lignocellulosic biomass can be accomplished by two different strategies: thermochemical and biochemical routes[30]. In both cases the recalcitrant lignocellulosic cell wall is fractionated into its fundamental constituents, cellulose, hemicellulose and lignin. Thermochemical processes require the treatment of the raw material at high temperatures and pressures (pyrolysis, liquefaction, gasification), followed by catalytic reactions for the formation of value added fuels and chemicals. On the other hand, biochemical processes involve the hydrolysis of the lignocellulose structure to obtain isolated hydrocarbons that can be selectively transformed to value added fuels and chemicals through biological or chemical routes.

#### **1.4.1 Hydrolysis**

Hydrolysis of lignocellulose to produce isolated sugar monomers can be performed by two different processes involving either acidic or enzymatic treatments[60]. In the case of acidic treatments, there are two different methods, dilute acid hydrolysis in which 1-3% volume of acid is used at 200-240°C or concentrated acid hydrolysis, using 10-30% acid concentration at 80-100°C[61]. The dilute method has the advantage of using less amount of acid, although the high temperatures needed to get acceptable biomass conversion induce the formation of undesirable products. On the other hand, the concentrated method has the ability to obtain high selectivity of glucose yield, around 90% due to the mild temperatures used, however the high concentrations of acid can lead to costly maintenance due to the corrosion of the equipment[62]. Enzymatic treatments use a cocktail of enzymes at mild temperature with the advantage of having 100% selectivity towards glucose production[63]. While acidic treatments are able to hydrolyse the lignocellulose to its basic constituents, the enzymatic route presents difficulties for the bulkier enzymes to access the cellulosic substrate, reason why physical and chemical treatments are needed to segregate the structure of the cellulosic raw materials. One of the incentives of this biochemical route is the obtainment of carbohydrates with lower oxygen content, which therefore are compounds with higher energy density[64].

#### **1.4.2 Pyrolysis and liquefaction**

Pyrolysis refers to the thermochemical decomposition of biomass raw materials in the absence of oxygen. Depending on the temperature and the residence time used, pyrolysis can be categorized as slow pyrolysis (~300°C for several hours) to produce

biochar as main product, or fast pyrolysis (~600°C for a few seconds) to yield mainly bio-oil[65]. The biochar produced during the slow pyrolysis due to the depolymerisation of sugars is mainly used as a source of energy by combustion. The high temperatures used during fast pyrolysis lead to the formation of organic vapours, pyrolysis gases and charcoal, which are condensed upon cooling to form a mixture of more than 350 compounds referred to as bio-oil, with a final yield of 60-75 wt% and composed by sugars, acids, alcohols, esters, aromatics, ketones and aldehydes[66]. Aromatic compounds rather than bio-oil can be also produced by catalytic fast pyrolysis, for example aromatics yield of 20-30% has been reported using zeolite HZSM-5 as catalyst[67]. Because pyrolysis does not need a pretreatment step typical in hydrolysis processes, pyrolysis bio-oil is cheaper than the production of sugar-based products. Although this bio-oil can be used for combustion purposes, it is a low-quality fuel due to its low stability, high oxygen content and acidic nature, leading to energy density equivalent to less than half that of petroleum-derived fuels and corrosive properties that can shorten the lifetime of the engine[68]. Therefore, in order to use it as a transportation fuel, further upgrading must be done by means of catalytic cracking, decarbonylation, decarboxylation, hydrocracking, hydrodeoxygenation or hydrogenation[69].

Liquefaction is an alternative method for the production of bio-oil by the catalytic thermal depolymerisation of lignocellulosic biomass. Conditions used for liquefaction are different from those from pyrolysis in terms of medium temperatures (250-450°C), high pressures (5-20 atm), longer residence times (20-60 min) and the addition of water in the presence of a basic catalyst[70]. Although these more demanding conditions can make the process more expensive compared to pyrolysis, liquefaction has the advantages of the capability of using wet raw materials in the process without any pre-drying and lower oxygen content of the final bio-oil compared to pyrolysis bio-oil[71].

### **1.4.3 Gasification**

Gasification is a process by which the lignocellulosic material is heated to high temperatures (>700°C) to produce gases with heating value such as syngas (CO+H<sub>2</sub>) and producer gas (mixture of flammable (CH<sub>4</sub>, CO, H<sub>2</sub>) and non-flammable gases (CO<sub>2</sub>, N<sub>2</sub>))[72]. Combustion is not included in this definition, since the gaseous products produced have no heating value. Fischer-Tropsch processes can be used after syngas purification for the production of liquid fuels such as gasoline and diesel or converted to methanol or dimethyl ether[73, 74]. The advantage of gasification is that a particular

plant feedstock is not necessary, and any kind of lignocellulosic biomass can be suitable for this process. However, the gases impurities and water present in the biomass can be an issue in following Fischer-Tropsch processes where a clean gas feed is required[75].

### 1.5 HMF as a platform chemical

As it has been described above, thermo-chemical processes are able to transform the biomass-based raw materials to smaller organic molecules. Some of these molecules have the potential to be transformed into a broad range of technologically relevant substances, reason why they gained the name of platform chemicals[76]. The conversion of these platform chemicals is attainable only through hydrolysis based methods. The interest in this type of compounds grew in 2004 after the U.S. Department of Energy released a report titled “Top Value Added Chemicals from Biomass”[77] in which it was listed a number of sugar-derived molecules obtained from lignocellulosic biomass with the potential to be converted to a number of high-value chemicals or materials. The 12 bio-based building blocks according to the US DoE are 1,4-diacids (succinic, fumaric and malic), 2,5-furan dicarboxylic acid, 3-hydroxy propionic acid, aspartic acid, glucaric acid, glutamic acid, itaconic acid, levulinic acid, 3-hydroxybutyrolactone, glycerol, sorbitol, and xylitol/arabinitol. In 2010 Bozell and Petersen[78] revised this list and included furan compounds such as furfural and 5-hydroxymethylfurfural (HMF), as well as other molecules as ethanol and isoprene.

5-hydroxymethylfurfural (HMF) is a heterocyclic furanic molecule substituted in 2,5-position with hydroxide and aldehyde functionalities (**Figure 1.6**) which can be obtained by the dehydration of hexoses, essentially glucose and fructose, readily available biomass primary compounds, although it can also be produced from oligo- and polysaccharides which can yield hexoses on hydrolysis, such as inulin or sucrose. However, the transformation of hexoses to HMF is challenging due to the susceptibility of HMF to further react generating undesirable products that lead to low overall selectivities[79].

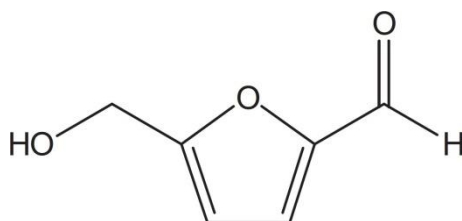


**Figure 1.6** 5-hydroxymethylfurfural (HMF)

The synthesis of HMF was first reported in 1895 by Düll *et al.*[80] when they reported the transformation of inulin with oxalic acid under pressure and thermal treatment. Also in 1895, Kiermayer[81] reported a similar procedure for HMF synthesis, but starting from sugar cane. Haworth and Jones[82] were the first to suggest the mechanism of the dehydration of fructose leading to HMF in 1944. Several important reviews have been published about the synthesis and chemistry of HMF, including one by Kuster[83] focussing on its manufacture, and later on by Lewkowski[84] and Rosatella *et al.*[85] focusing on its synthesis and applications. Due to its remarkable reactivity, HMF can be used to synthesise a wide array of molecules that can be used as a replacement of the current petroleum-based commodity chemicals[12].

### 1.5.1 HMF derivatives

The particular chemical structure of HMF grants it with functional features that make it an ideal molecule for the synthesis of commodity chemicals. To begin with, the substituents in the 2 and 5 positions give HMF the possibility to be used for the synthesis of monomers by either reduction to a diol or oxidation to a dicarboxylic acid. The relatively unsaturated aromatic structure of HMF means that it can also be upgraded to biofuels precursors via hydrogenation. Finally, it can also be transformed into biologically active molecules that can be used with pharmaceutical applications due to its heterocyclic furanic structure[86]. The most important compounds to which HMF can be converted are illustrated in **Figure 1.7**.

HMF can be converted to several compounds that can serve as monomers for polymeric materials. Between them, the most interesting is 2,5-furandicarboxylic acid (FDCA), present in the “Top Value Added Chemicals from Biomass” publication by the US DoE above mentioned[77] and obtained by the oxidation of HMF. The main interest on this molecule comes from its potential to replace petroleum-based terephthalic acid, a widely used component in the production of important polyesters such as polyethylene terephthalate (PET) and polybutyleneterephthalate (PBT)[87]. Selective oxidation of HMF leads to the formation of 2,5-diformylfuran (DFF), another molecule with multiples applications like transformation into valuable polymers, antifungal agents or pharmaceutical grade materials[88, 89]. Selective hydrogenation reaction of HMF can also produce 2,5-bis(hydroxymethyl)furan (BHMF) and 2,5-bis(hydroxymethyl)tetrahydrofuran used for the manufacture of polyurethane foam and polyester preparation respectively, or as intermediates for the synthesis of drugs[90].

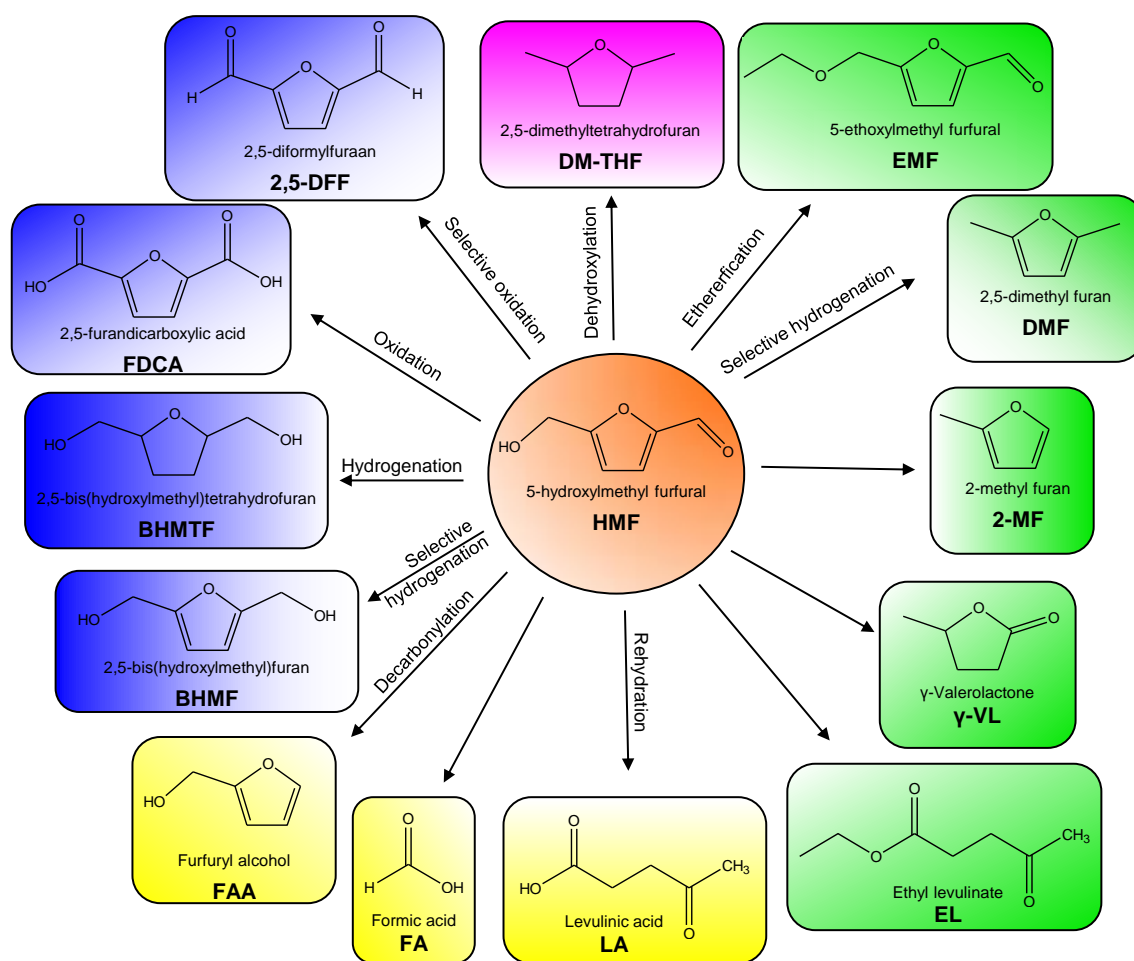


**Figure 1.7** Catalytic conversion of HMF to valuable compounds for the production of biofuels (green), polymers (blue), building blocks (yellow) and solvents (purple)

Numerous liquid transportation biofuels can also be produced from HMF. For example, 2,5-dimethylfuran (DMF) and 2-methylfuran (2-MF) can be synthesised by the hydrogenation of HMF[91], and they are very promising biofuels due to their high energy density similar to that of gasoline and much higher than that of bioethanol[92]. 5-ethoxymethylfurfuryl alcohol (EMF) can be produced by the acid catalysed reaction of HMF with ethanol[93], and it can be used as a potential diesel additive, since it has a similar combustion potential than ethanol but higher miscibility with diesel[94]. Further decomposition and rehydration of EMF can produce ethyl levulinate (EL), although it can also be obtained by esterification of levulinic acid with ethanol[95]. EL is extensively used in fragrances and perfumes, but it can also be used as a diluent for biodiesel fuels with high saturated fatty acid content to improve the properties of biodiesel[96]. Finally,  $\gamma$ -valerolactone (GVL) is produced by hydrogenation of levulinic acid and it has been identified as an interesting molecule for the production of both energy and fine chemicals[97]. GVL can be used as an intermediate for the production of nonane for Diesel fuel or the production of branched alkanes suitable for jet fuel[75].

Levulinic acid (LA) is another of the top molecules listed by the US DoE, since it can be upgraded to several value added compounds, such as the aforementioned GVL and further production of methyltetrahydrofuran (MTHF), which can be blended with gasoline without the need to modify combustion engines. Alkyl esters such as EL can also be produced from LA to be used as fuel additives. The use of LA as a solvent, food flavouring agent, plasticizer, coating material, and antifreeze has also been reported[98]. LA can be easily obtained from the rehydration of HMF in acid catalysed media at relatively high temperature conditions[99]. Apart from LA, the rehydration of HMF can also yield formic acid (FA), which can be purified and sold directly as a commodity chemical, although it is also widely used as an acidulating in the textile industry, as a decalcifier or in the manufacture of insecticides and refrigerants[100]. Moreover, FA can also be used as a reagent together with fructose for the production of the above mentioned potential biofuel 2-Methylfuran[101]. Finally, another important chemical is furfuryl alcohol (FFA) obtained from the decarbonylation of HMF[102]. It is mainly used in the manufacture of fragrances, vitamin C, resins and tetrahydrofurfuryl alcohol. It can also be used for the production of BHMF through hydroxymethylation with formaldehyde[103].

## 1.6 Glucose and fructose dehydration to HMF

### 1.6.1 Mechanism of glucose to HMF formation

HMF formation via triple dehydration of hexoses is quite complex and several reaction routes and mechanisms have been suggested, especially with glucose and fructose as starting materials, although no definite conclusion has been made on the reaction mechanism for hexose dehydration yet. The production of HMF from hexoses tends to be governed by the presence of numerous other side reactions due to isomerisation, dehydration, fragmentation and condensation reactions, which lead mainly to the generation of humins[104] and organic acids like levulinic and formic acid, which can self-catalyse the dehydration of hexoses.

Van Dam *et al.*[105], Kuster[83] and Antal *et al.*[106] proposed that the dehydration of hexoses goes through one of the two possible pathways involving cyclic or acyclic intermediates (**Figure 1.8**). The acyclic mechanism proposes the ring opening of glucose when it is protonated at the pyranose oxygen. Ring opening is followed by either the aldose acyclic mechanism via formation of 1,2-enediol[107] or rearrangement and ring reclosure to fructose through a fructofuranosyl intermediate[108]. In either case the compounds dehydrate further through a series of steps to produce HMF. The

alternate cyclic mechanism involves the direct transformation of the pyranose ring to a five-membered ring intermediate, as proposed by Antal *et al.*[109] and Newth[110]. The most significant evidences found in their studies were: (1) facile conversion of 2,5-anhydro-D-mannose (an intermediate enol in cyclic mechanism) to HMF; (2) facile formation of 5-HMF from d-fructose but difficult from glucose, which could be concluded from the dehydration of sucrose; (3) lack of carbon-deuterium bond formation in 5-HMF due to ketoenol tautomerism in the open-chain mechanism when the reaction was carried out in D<sub>2</sub>O solvent. In another study supporting the cyclic pathway, Amarasekara *et al.*[111] identified the key intermediate (4R,5R)-4-hydroxy-5-hydroxymethyl-4,5-dihydrofuran-2-carbaldehyde by <sup>1</sup>H and <sup>13</sup>C NMR spectra when using dimethylsulfoxide (DMSO) as the solvent.

Glucose is more abundant and therefore cheaper raw material than fructose, making it a preferred option for the production of HMF, however the rate of glucose conversion and selectivity to HMF are both lower than with fructose. The low yield of 5-HMF from glucose is attributed to its stable ring structure, which hinders its ability to form the acyclic enediol intermediate[83]. The cyclic mechanism requires glucose to isomerize to fructose prior to dehydration to HMF. The aldose-ketose isomerization is thought to occur either by proton transfer or by intramolecular hydride transfer. In the presence of a base, the aldose is deprotonated and the isomerization proceeds through a series of enolate intermediates followed by re-protonation[112]. Lewis acid sites catalyse the intramolecular hydride shift that transforms the open form of glucose to the open form of fructose[113].

In conclusion, when starting from glucose a catalyst with Lewis acidity or base character is needed to isomerize glucose to fructose, and Brønsted acidity subsequently performs the conversion of fructose to HMF via triple dehydration.

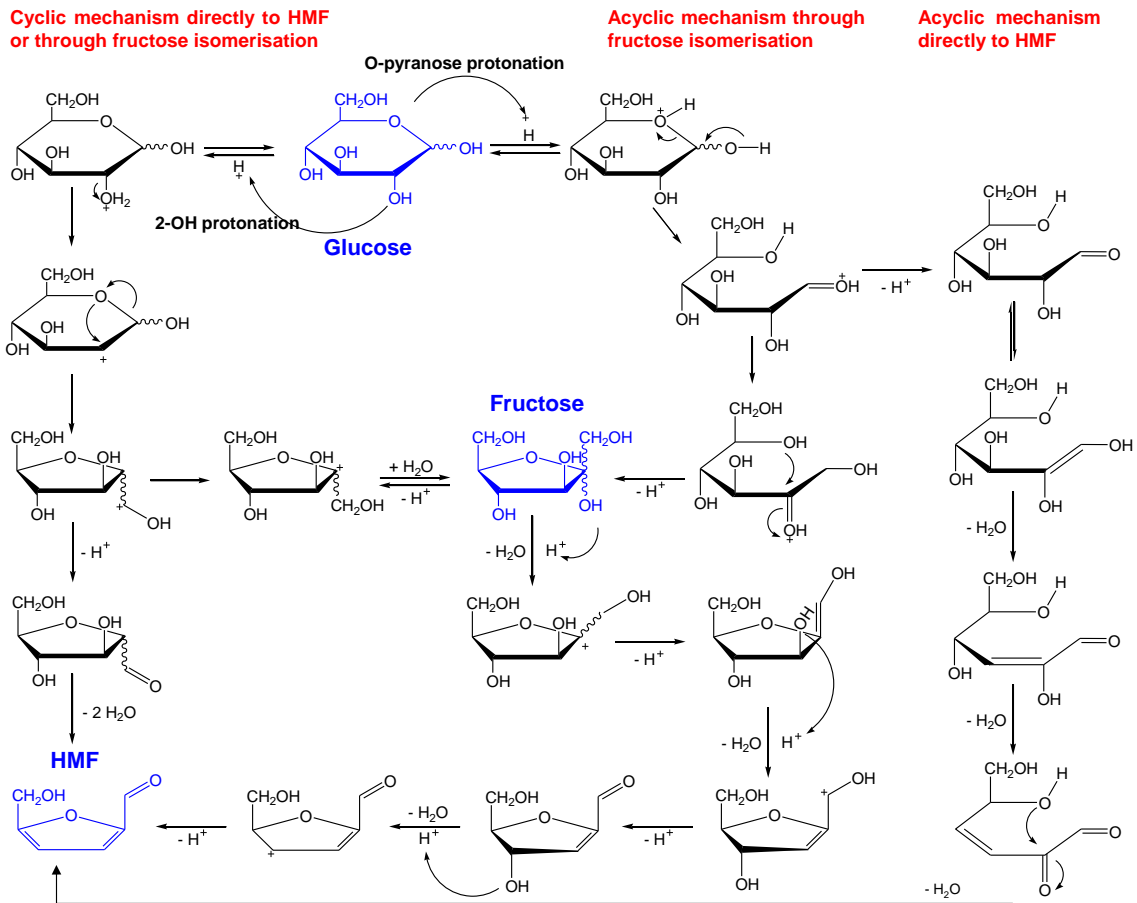


**Figure 1.8** Proposed cyclic (left) and acyclic (right) mechanisms for glucose conversion to HMF (adapted from [114])

## 1.6.2 Production of HMF in different reaction media

### 1.6.2.1 Dehydration reactions in aqueous solutions

#### a) Non-catalytic processes

The glucose and fructose dehydration reactions in water are known to be a complex reactions with parallel, consecutive and equilibrium steps. The conversion of glucose and fructose in the absence of catalyst has been studied in different groups. For example, Lopes de Souza *et al.*[115] studied the glucose conversion in water in the range of temperatures 25-250°C, using 1wt% glucose solution. A maximum HMF yield of 25% was achieved, where 69% of glucose was converted at 220°C. Watanabe *et al.*[116] reported work on glucose reactions in hot compressed water at 200°C with a substrate concentration of 9 wt%, obtaining 6.6% HMF yield at 20% conversion after 10 min. Jing and Lü[117] reported the glucose conversion experiments in water at 180-

220°C and 100 bar obtaining HMF yields as high as 30% at around 70% conversion when 1% glucose solution was heated for 30 min at 220°C. Chareonlimkun[118] reported a 10% HMF yield with a 21% conversion of a 9 wt% glucose solution at 250°C, after only 5 minutes. When fructose was used as a starting reagent, Li et al.[119] reported a conversion of 90% and HMF yield of 50% after approximately 10 min when high temperatures (220°C) and pressures (10 MPa) were used. Kuster and Temmink[120] reported the dehydration of fructose at 175°C and 50 bar, obtaining HMF yield of 56% at 70% conversion after 90 min, and reported a decrease in the pH of the reaction, indicating the formation of acids during the reaction. Hansen et al.[121] carried out the synthesis of HMF from fructose in the absence of catalyst but assisted by microwave radiation. A 30% fructose solution yielded only 1% HMF at 5% conversion after 5 min at 160°C. Increasing the temperature to 190°C led to around 35% HMF yield at ~70% conversion. Summarizing, the use of high temperatures and pressures are necessary in the non-catalytic/autocatalytic conversion of glucose and fructose, making it an inefficient process for HMF production.

#### *b) Homogeneous catalysed processes*

Several methods have been reported in aqueous media using homogeneous acid catalysts such as organic acids and metal halides. In 1977 Kuster *et al.*[122] reported their work in the fructose dehydration catalysed by HCl. The best HMF yields were around 30% and the highest selectivity around 60%. In these experiments, the formation of levulinic acid was observed due to the high HCl concentration (0.25-2 M). More recently Tuercke *et al.*[123] conducted the HCl-catalysed dehydration in a continuous microreactor process, obtaining HMF with 75% selectivity and 71% fructose conversion when the reaction was operated at 185°C and 17 bar. Formic acid has also been studied as an homogeneous catalyst in aqueous media due to its presence as a by-product in the HMF decomposition pathway. Thus, Kuster *et al.*[120] reported work on a 4.5 wt% aqueous fructose solution catalysed by formic acid at 175°C and 50 bar. At a controlled pH of 2.7, 56% conversion was observed after 45 min with 100% selectivity towards HMF. Li *et al.*[119] also reported a kinetic study on the reaction of fructose (11 wt%) to HMF using formic or acetic acid as the catalysts in subcritical water. At 200°C and 100 bar, fructose conversion of 92-96% and HMF yield of 58% was observed within 10 and 20 minutes using formic acid and acetic acid respectively. Asghari and Yoshida[124] published the production of HMF from fructose in subcritical water catalysed by several organic acids (HCl, H<sub>2</sub>SO<sub>4</sub>, H<sub>3</sub>PO<sub>4</sub> or oxalic, maleic and citric acid) at 240°C. Phosphoric acid was the best catalyst used at lower pH and the

best condition was achieved at pH = 2 (HMF yield = 65.3%). Several other mono- and di-saccharides were also tested (sucrose, cellobiose, glucose, galactose, mannose and sorbose), and it was concluded that the ketohexoses give higher yields than aldohexoses.

While homogeneous catalysts exhibit superior activity and selectivity than their heterogeneous counterparts, they necessitate energy intensive separations to isolate the desired product and recover the homogeneous catalyst for recycling, with organic acids suffering comparatively poor thermal stability.

### c) *Heterogeneous catalysed processes*

Watanabe *et al.*[116] examined TiO<sub>2</sub> and ZrO<sub>2</sub> metal oxides in hot compressed water at 200°C, 25 bar argon, and 5 minute reaction time for glucose and fructose dehydration. From fructose, HMF yield was ~20% with TiO<sub>2</sub> and ~15% with ZrO<sub>2</sub>, with conversions being 90-100% for each case. In order to improve the acidic properties of zirconia, phosphated and sulfated materials have also been reported by Asghari *et al.*[124] and Qi *et al.*[125] respectively. In the case of zirconium phosphate, glucose and fructose conversion were investigated in subcritical water at 240°C and 3.35 MPa. 53% glucose conversion with 39% selectivity to HMF and 81% fructose conversion with 61% HMF selectivity was obtained in 3 and 2 minutes of reaction respectively. In the case of sulfated zirconia, a 2 wt% fructose solution was heated by microwave irradiation for 5 min at 200°C, yielding 37% HMF with a conversion of 89%.

Other interesting catalyst is vanadyl phosphate (VOP), studied by Carlini *et al.*[126]. This catalyst showed low HMF selectivity (33%) and moderate conversion (45%) in the high concentrated (30 wt%) fructose dehydration to HMF at 80°C in 30 min. However, the acidity of VOP can be modified by isomorphous substitution of some VO<sup>3+</sup> groups with trivalent metals such as Fe<sup>3+</sup>, Cr<sup>3+</sup>, Ga<sup>3+</sup>, Mn<sup>3+</sup> and Al<sup>3+</sup>, increasing the catalyst activity. FeVOP showed the best performance, achieving 71% fructose conversion and 84% HMF selectivity. Niobic acid (Nb<sub>2</sub>O<sub>5</sub>·nH<sub>2</sub>O) and niobium phosphate (NbOPO<sub>4</sub>) materials have attracted great interest as catalysts for dehydration reactions, due to their strong acid properties which can be preserved in polar liquids like water, presenting them as water-tolerant solid acids. Carlini *et al.*[127] used these catalysts in aqueous reactions at 100°C. HMF selectivity was high (> 90%) at low conversions (< 30%). When the reaction time was increased, fructose conversion increased while the HMF selectivity dramatically decreased. Carniti *et al.*[128] also studied the same catalysts, but in this case experiments were carried out in a continuous flow reactor

under aqueous conditions at temperatures of 90-110°C. The niobium phosphate was found to be more active, obtaining 25% HMF yield at 77% fructose conversion at 110°C. Armaroli *et al.*[129] reported the catalytic activity of commercial niobium phosphates and niobium phosphates prepared by treatment of niobic acid with phosphoric acid, for fructose, sucrose and inulin dehydration reactions. It was observed that the HMF selectivity was very high (98%) at lower reaction times (30 min) for a fructose conversion of 29%. For higher reaction times (2 h), although the sugar conversions increased up to 61%, the HMF selectivity decreased (35%), due to the formation of polymeric by-products. Recently, Edman Tsang's group[130] studied several niobium-based catalysts for the dehydration of sucrose, glucose and fructose, finding that mesoporous niobium oxide gives the overall highest HMF yield (36%) for the conversion of the three saccharides studied, due to the balanced BA and LA of its structure with the most appropriate acid strengths for the conversion of both glucose and fructose components.

Many research groups have tried to synthesize niobium oxide catalysts with higher surface areas employing different supports to improve the dispersion and enhance the number of available active sites. Various oxides such as SiO<sub>2</sub>, Al<sub>2</sub>O<sub>3</sub>, SiO<sub>2</sub>-Al<sub>2</sub>O<sub>3</sub>, TiO<sub>2</sub>, and ZrO<sub>2</sub> have been employed as effective supports for niobium oxide species, mainly studied by Jehng and Wachs[131-134]. Lewis acid sites were found in all of the supported niobium oxide catalysts, but Brønsted acid sites were detected only on SiO<sub>2</sub> and Al<sub>2</sub>O<sub>3</sub> supports[135]. Supported niobium oxide has been studied and proven to be active in several reactions, such as oxidation of cyclohexene[136], hydrolysis of sucrose[137], esterification of acetic acid[138] and propanoic acid[139], methanol oxidation[140] or dehydration of xylose[141]. To the best of our knowledge, only Carniti's group has reported studies for the dehydration of fructose to HMF, but always in a continuous reaction line[142, 143].

Direct synthesis of mesoporous Nb<sub>2</sub>O<sub>5</sub>/SiO<sub>2</sub> has been reported using different techniques. One of them is conventional sol-gel method which generally uses niobium (V) ethoxide in the presence of an organic solvent, such as ethanol[144] or hexane[138]. The second common method of preparing niobium/silica material is co-precipitation, in which niobium (Ammonium niobium oxalate complex[145], niobium (V) chloride[140]) and silicon precursors (TEOS) are precipitated simultaneously in a neutral environment. The last explored method to graft Nb<sub>2</sub>O<sub>5</sub> on silica supports is using incipient wetness impregnation, which generally uses niobium (V) ethoxide[146], niobium oxalate[147] or niobium (V) chloride[139] precursor in an anhydrous organic

solvent (e.g. hexane, oxalic acid or isopropanol) with the concentration of the precursor varied to obtain materials with different niobium loadings. Nowak[136] studied the effect of these different precursors and concluded that the highest activity was observed in the case when niobium chloride was used as a source of niobium.

In this thesis, supported materials are prepared using niobium (V) chloride as a precursor, and its incorporation onto SBA-15, employed as a silica support, is made through the peptisation of a niobic acid sol with H<sub>2</sub>O<sub>2</sub> as will be described in **Chapter 2**.

It is well known that the dehydration of glucose and fructose to HMF in an aqueous environment is accompanied by side reactions leading to formation of insoluble humins and other by-products, evidencing that solvent plays a very important role in this reaction. For this reason, the synthesis of HMF from biomass has been conducted in various reaction media apart from water, such as ionic liquids[148-150], organic solvents[151, 152], or biphasic systems[153, 154].

### **1.6.2.2 Dehydration reactions in organic solvents**

Organic solvents have drawn the attention of many research groups due to their ability to suppress undesirable parallel reactions and the rehydration of HMF. Several research groups have studied the influence of different solvents in the dehydration of glucose and fructose to HMF, such as tetrahydrofuran (THF), ethanol, acetonitrile, dimethylsulfoxide (DMSO), dimethylacetamide (DMAc) or N,N-dimethylformamide (DMF)[155-157]. Compared to other solvents studied, DMSO always stood as the best reaction medium and exhibited superior performance in the dehydration of fructose and glucose. Moreover, non-catalytic reactions proved that DMSO is able to perform the dehydration of fructose in the absence of catalyst. Thus, Brown *et al.*[158] reported 100% conversion with full selectivity to HMF after 16 h at 100°C in the absence of catalyst, although yields were estimated by <sup>1</sup>H NMR analysis only. Yan *et al.*[159] reported HMF yield of 72% in a reaction with 7.6 wt % fructose at 130°C for 4 h in the absence of catalyst. Shimizu *et al.*[160] published an elaborate study on fructose dehydration to HMF in DMSO with a variety of catalysts, including zeolites, ion exchange resins, heteropolyacids, and basic heterogeneous catalysts. The experiments were carried out with 3 wt % fructose and 6 wt % catalyst in DMSO at 120°C for 2 h under continuous water removal by mild evacuation. Without continuous water removal the yields decreased, except in the case of Amberlyst 15 which proved to be the best performer catalyst yielding 100% HMF.

It was concluded that aprotic and polar solvents are more suitable for this reaction system, which can be attributed to their ability to solubilize the raw materials. Moreover, DMSO is also a favourable solvent for the dehydration of glucose and fructose to HMF due to its ability to suppress both the formation of condensation by-products and the HMF rehydration by lowering the overall water concentration[161].

### 1.6.2.3 Dehydration reactions in biphasic systems

*In situ* extraction of HMF from the aqueous reaction media by an organic solvent has been proved as a solution to suppress the rehydration of HMF to levulinic acid, as well as the polymerisation to undesired products known as humins. In 1956 Peniston first patented his biphasic system for HMF extraction from carbohydrates reactions[162]. Three years later, Cope patented a biphasic system for HMF production from glucose, in which water-MIBK system produced 25% HMF yield when glucose solution was reacted at 160°C for 9 h[163].

In 2008 Qi *et al.*[164] studied the dehydration of fructose at different concentrations using a resin as catalyst and assisted by microwave heating (150°C) in acetone-water biphasic system. In a first study in aqueous system and without the microwave assistance, they obtained 83% fructose conversion in 60 min, but selectivity was only 34%. When acetone was implemented as co-solvent 22% conversion and 13% selectivity were obtained in 10 min, while the corresponding value for microwave heating was 91.7% conversion and 70.3% HMF yield, proving the superior performance of microwave irradiation against oil bath heating. When initial fructose concentration increased from 2 wt% to 20 wt%, high fructose conversion was maintained (<98%), but a considerable decrease in HMF selectivity from 70% to 51% was observed. In 1996 Moreau *et al.*[107] studied the fructose dehydration at 165°C for 2 h in a solvent mixture consisting of water and methyl isobutyl ketone (1:5 by volume) in the presence of dealuminated H form mordenites as catalysts. Different Si/Al ratios were tested, finding that 1:1 provided the best fructose conversion (93%) and HMF selectivity (73%). In 2007 Dumesic *et al.*[165] reported the dehydration of different substrates such as fructose, inulin and sucrose on solvent systems containing NMP (1-methyl-2-pyrrolidinone) as additive in the aqueous phase. MIBK (methyl isobutyl ketone) or dichloromethane were used as extraction solvents and an ion exchange resin (DIAION PK216) as catalyst. A 10 wt% fructose solution produced 83% HMF yield at 98% conversion in 4:6 (w/w) water/NMP at 90°C after 18 h with MIBK as extraction solvent. When sucrose was used as reactant at 90°C and 21 h as reaction time, conversion of 58%, with an HMF selectivity of 74% was observed. Under the

same reaction conditions inulin was fully converted with 69% selectivity to HMF. Similar selectivity was obtained even when the reaction was performed in the absence of the resin catalyst, although the reaction temperature had to be increased up to 120°C. The application of  $\text{Ag}_3\text{PW}_{12}\text{O}_{40}$  as catalyst for glucose and fructose dehydration in a water-MIBK system was studied by Fan *et al.*[166] A maximum HMF yield of 78% at 83% fructose conversion at 120°C after 1 h was reported, although it is worth noting that significant conversion (47%) and HMF yield (33%) were produced under the same conditions in the absence of a catalyst. When glucose was tested as reagent at 130°C, 76% HMF yield at 90% conversion after 4 h was reported. Interestingly, lower levulinic acid was observed in the case of glucose compared to the fructose results, indicating that HMF was more stable even under harsher conditions. Nikolla *et al.*[167] published their study in glucose dehydration using tin and titanium  $\beta$ -zeolites in combination with HCl. Using an n-butanol-water system at 160°C over Sn- $\beta$ /HCl, 77% conversion and 26% HMF yield were obtained in 90 min. Under the same conditions, the presence of 26 wt% of NaCl improved the yield up to 55% with a similar conversion. Selectivity was further improved up to 72% at 180°C and 70 min when THF was used as a co-solvent instead of n-butanol. Similar conversion and selectivity was obtained for Ti- $\beta$ /HCl when the reaction time was increased to 105 min. Yang *et al.*[168] reported the impact of niobic acid phosphate for the dehydration of glucose and fructose in 2-butanol-water system. In the fructose reaction, 90% conversion and 89% HMF yield was obtained in 50 min at 160°C, while 72% conversion and 49% HMF yield was observed in 110 min at 160°C in the case of glucose. These results proved themselves surprising due to the lack of HMF rehydration in the presence of a heterogeneous Brønsted acid catalyst.

#### **1.6.2.4 Dehydration reactions in ionic liquids**

Ionic liquids (IL) are defined as a liquid entirely composed of ions that are fluid at relatively low temperature, from ambient temperature to 100°C[169]. They have been subjected to intense study due to characteristics such as high thermal and chemical stability, low volatility and flammability, high ionic conductivity and recyclability and their extremely low vapour pressure compared to conventional solvents make them unique solvents[170]. ILs have been widely used for the conversion of biomass feedstocks due to their ability to effectively modify and/or dissolve biomass and its components. Most of early ionic liquids suffer from sensitivity to air and moisture which significantly limited their applications, but in 1992, Wilkes' group made a breakthrough by reporting the development of a series of air and moisture stable imidazolium type ILs[171]. The most

common ionic liquids are N,N'-dialkylimidazolium, N-alkylpyridinium, alkylammonium and alkylphosphonium based.

ILs have been proved to suitably catalyse the conversion of sugars to HMF in the absence of any other catalyst. Wei *et al.*[172] reported the dehydration of fructose using the IL [BMIm]Cl as only catalyst during 3 h. Conversion and HMF yield were reported at 80°C and 120°C, increasing the conversion from 4% to 100% respectively, with 48% selectivity for the latter. Hu *et al.*[173] reported the fructose dehydration from a 17 mol % fructose solution at 80°C for 1 h using different ionic liquids without additional catalyst. PyHCl and [HMIm]Cl experiments led to similar results of 70% HMF yield at 90–95% conversion. Experiments in choline chloride (ChoCl)/citric acid were reported to yield 75% HMF at 92% fructose conversion. Continuous extraction with ethyl acetate improved the overall HMF yield to 92% at 98% conversion in ChoCl/citric acid. Cao *et al.*[174] published their investigation in the fructose dehydration using imidazolium based ionic liquids, showing contradictory results with the work of Hu and co-workers just mentioned. Thus, they reported no fructose conversion in the presence of [HMIm]Cl and [BMIm]Cl at 100°C for 50 min. Considerable activity was obtained when the reaction temperature was increased, with 93% conversion and 63% HMF yield in the presence of [BMIm]Cl at 120°C for 50 min.

A number of articles have been published in which heterogeneous acid catalysts were applied for fructose and glucose dehydration in ionic liquids. In 2003 Moreau's group popularized the use of IL for the dehydration of carbohydrates. In their publication[150] a solution of 8 wt % fructose in the presence of [BMIm]BF<sub>4</sub>, was catalysed by Amberlyst 15 at 80°C after 3 h yielding 52% HMF. When a mixture of [BMIm]BF<sub>4</sub> and DMSO was used the yields improved to 87% after 32 h. In 2011 Qi *et al.*[175] published a study on fructose dehydration in various imidazolium based ionic liquids catalysed by sulfated zirconia and assisted by microwave heating. Using a reaction temperature of 100°C and 30 min of reaction time, a 5 wt% fructose solution in [BMIm]Cl yielded 88% HMF at 96% conversion. With ZrO<sub>2</sub> in [BMIm]Cl under the same conditions the same selectivity around 90% was obtained, but a decrease in conversion (60%) and HMF yield (55%) was observed. Regarding the dehydration of glucose, Zhang *et al.*[176] studied the effect of GeCl<sub>4</sub> in [BMIm]Cl. Temperatures ranging from 80°C to 120°C were investigated and a considerable increase in the efficiency of the reaction was observed. From a 5 wt % reaction mixture HMF yield of 48% was obtained at 99% conversion after 30 min at 120°C. Chidambaram and Bell[177] published work on glucose dehydration to HMF using different mineral acids,

organic acids, and heteropolyacids in [BMIm]Cl at 120°C for 3 h. The highest HMF yield of 66% at 82% glucose conversion was obtained with 12-tungstophosphoric acid ( $H_3PW_{12}O_{40}$ ). Higher conversion of 93% was observed using  $H_2SO_4$ , but the yield was reduced to 61%. Qi and Watanabe[178] extensively explored the high catalytic performance of  $CrCl_3$  for the dehydration of glucose in [BMIm]Cl system, in the range of temperatures 90-140°C with the assistance of microwave irradiation. The highest yield of around 70% at 95% conversion was obtained at 120°C after 10 min and at 140°C after 30 s. When fructose was used as the substrate, 78% HMF yield was obtained in 1 min at 100°C under the same conditions.

While the 5-HMF yields observed from both glucose and fructose in aqueous systems are far lower than reported in the solvents mentioned above, these also present limitations like the relatively high price of ionic liquids, requiring very efficient recycling strategies, the large amount of solvent required by biphasic systems due to hydro-soluble raw materials and poor partitioning in the organic phase, implying high substrate dilution and consequently reduced productivity. Additional technical difficulties and environmental problems are caused by the removal of organic solvents and purification of HMF comprising energy intensive/complex separation protocols. For this reason, water, although less active as a reaction media, presents some advantages such as being a green solvent, its high solubility for sugars and its generally not impactful disposal in the environment. Moreover, saccharides present in lignocellulosic biomass possess a considerable amount of water when treated in its raw state, which makes aqueous systems a sensible choice of study.

## 1.7 Thesis aims

- To study the environmentally friendly cascade reaction of glucose dehydration to HMF, in aqueous system under mild conditions, employing bifunctional catalysts and identifying the role of Brønsted and Lewis acid sites in the reaction network.
- To design bifunctional heterogeneous catalysts based on hydrated niobium oxide (niobic acid), prepared by a peroxy sol-gel method from a chloride precursor, bulk and supported on SBA-15, to clarify the structure function relationships.
- To design a second bifunctional catalyst based on phosphated zirconia, wet impregnated on the  $\text{ZrO}_2$  hydroxide precursor with phosphoric acid, varying the structural and acid-base properties by controlling the phosphate surface coverage and calcination temperature.

## 1.8 References

- [1] A.E. Outlook, Department of Energy 92010 (2010) 1-15.
- [2] Global energy statistical yearbook, Enerdata, <https://yearbook.enerdata.net/total-energy/world-consumption-statistics.html>, 2017.
- [3] S. Shafiee, E. Topal, Energy policy 37 (2009) 181-189.
- [4] M. Meinshausen, N. Meinshausen, W. Hare, S.C. Raper, K. Frieler, R. Knutti, D.J. Frame, M.R. Allen, Nature 458 (2009) 1158-1162.
- [5] L.R. Lynd, C.E. Wyman, T.U. Gerngross, Biotechnology progress 15 (1999) 777-793.
- [6] M. Huber, R. Knutti, Nature Geosci 5 (2012) 31-36.
- [7] Key world energy statistics, International Energy Agency, <http://www.iea.org/publications/freepublications/publication/KeyWorld2017.pdf>, 2017.
- [8] R.A. Gross, B. Kalra, Science 297 (2002) 803-807.
- [9] P.T. Anastas, T.C. Williamson, ACS Publications, 1996.
- [10] P.T. Anastas, J.C. Warner, Green chemistry: theory and practice, Oxford university press, 2000.
- [11] R.A. Sheldon, I. Arends, U. Hanefeld, Green chemistry and catalysis, John Wiley & Sons, 2007.
- [12] R.A. Sheldon, Green Chemistry 16 (2014) 950-963.
- [13] P. Anastas, N. Eghbali, Chemical Society Reviews 39 (2010) 301-312.
- [14] C.H. Bartholomew, R.J. Farrauto, Fundamentals of industrial catalytic processes, John Wiley & Sons, 2011.
- [15] D. Trimm, Applied Catalysis A: General 212 (2001) 153-160.
- [16] P. Atkins, J. De Paula, Oxford University Press, Oxford (2006).
- [17] S.T. Oyama, G.A. Somorjai, J. Chem. Educ 65 (1988) 765.
- [18] J.M. Thomas, K.D. Harris, Energy & Environmental Science 9 (2016) 687-708.
- [19] J.A. Dumesic, G.W. Huber, M. Boudart, Handbook of Heterogeneous Catalysis (2008).
- [20] A. Corma, Current Opinion in Solid State and Materials Science 2 (1997) 63-75.
- [21] J. Weitkamp, L. Puppe, Catalysis and zeolites: fundamentals and applications, Springer Science & Business Media, 2013.
- [22] M. Timofeeva, Applied Catalysis A: General 256 (2003) 19-35.

- [23] T. Glazneva, N. Kotsarenko, E. Paukshtis, *Kinetics and Catalysis* 49 (2008) 859-867.
- [24] S.D. Jackson, J.S. Hargreaves, *Metal oxide catalysis*, John Wiley & Sons, 2009.
- [25] A. Sayari, *Chemistry of Materials* 8 (1996) 1840-1852.
- [26] F. Carvalheiro, L.C. Duarte, F.M. Gírio, *Journal of Scientific & Industrial Research* (2008) 849-864.
- [27] M. Karimi Alavijeh, S.o. Yaghmaei, *Biochemical production of bioenergy from agricultural crops and residue in Iran*, 2016.
- [28] P.S. Nigam, A. Singh, *Progress in Energy and Combustion Science* 37 (2011) 52-68.
- [29] D. Bajpai, V. Tyagi, *Journal of Oleo Science* 55 (2006) 487-502.
- [30] A. Demirbas, *Energy conversion and management* 50 (2009) 14-34.
- [31] S.H. Mohd Azhar, R. Abdulla, S.A. Jambo, H. Marbawi, J.A. Gansau, A.A. Mohd Faik, K.F. Rodrigues, *Biochemistry and Biophysics Reports* 10 (2017) 52-61.
- [32] W.-D. Hsieh, R.-H. Chen, T.-L. Wu, T.-H. Lin, *Atmospheric Environment* 36 (2002) 403-410.
- [33] A.C. Pinto, L.L. Guarieiro, M.J. Rezende, N.M. Ribeiro, E.A. Torres, W.A. Lopes, P.A.d.P. Pereira, J.B.d. Andrade, *Journal of the Brazilian Chemical Society* 16 (2005) 1313-1330.
- [34] T. Searchinger, R. Heimlich, R.A. Houghton, F. Dong, A. Elobeid, J. Fabiosa, S. Tokgoz, D. Hayes, T.-H. Yu, *Science* 319 (2008) 1238-1240.
- [35] J. Fargione, J. Hill, D. Tilman, S. Polasky, P. Hawthorne, *Science* 319 (2008) 1235-1238.
- [36] *Fueling a nation, feeding the world*, Renewables Fuel Association, <http://www.ethanolrfa.org/wp-content/uploads/2015/09/Fueling-a-Nation-Feeding-the-World-2014.pdf>, 2014.
- [37] J.-P. Lange, *Catalysis for Renewables*, Wiley-VCH Verlag GmbH & Co. KGaA, 2007, pp. 21-51.
- [38] I. Bio-energy, *Second Generation Biofuels—a Review from a Market Barrier Perspective*, IEA Bioenergy Task, 2006.
- [39] J.G. Speight, *The biofuels handbook*, Royal Society of Chemistry, 2011.
- [40] Y. Lin, S. Tanaka, *Applied microbiology and biotechnology* 69 (2006) 627-642.
- [41] L. Brennan, P. Owende, *Renewable and sustainable energy reviews* 14 (2010) 557-577.
- [42] W. Xiong, X. Li, J. Xiang, Q. Wu, *Applied microbiology and biotechnology* 78 (2008) 29-36.

- [43] A. Richmond, Handbook of microalgal culture: biotechnology and applied phycology, John Wiley & Sons, 2008.
- [44] J. Sheehan, T. Dunahay, J. Benemann, P. Roessler, Look back at the US department of energy's aquatic species program: biodiesel from algae; close-out report, National Renewable Energy Lab., Golden, CO.(US), 1998.
- [45] B. Wang, Y. Li, N. Wu, C.Q. Lan, Applied microbiology and biotechnology 79 (2008) 707-718.
- [46] T.M. Mata, A.A. Martins, N.S. Caetano, Renewable and Sustainable Energy Reviews 14 (2010) 217-232.
- [47] G. Dragone, B.D. Fernandes, A.A. Vicente, J.A. Teixeira, Current research, technology and education topics in applied microbiology and microbial biotechnology 2 (2010) 1355-1366.
- [48] F. Alam, S. Mobin, H. Chowdhury, Procedia Engineering 105 (2015) 763-768.
- [49] Third generation biofuels, Biofuel.org.uk, <http://biofuel.org.uk/third-generation-biofuels.html>, 2010.
- [50] G.W. Huber, A. Corma, Angewandte Chemie International Edition 46 (2007) 7184-7201.
- [51] H. Chen, Biotechnology of Lignocellulose: Theory and Practice, Springer Netherlands, Dordrecht, 2014, pp. 25-71.
- [52] R.C. Pettersen, ACS Publications, 1984.
- [53] E. Sjostrom, Wood chemistry: fundamentals and applications, Elsevier, 2013.
- [54] R.A. Festucci-Buselli, W.C. Otoni, C.P. Joshi, Brazilian Journal of Plant Physiology 19 (2007) 1-13.
- [55] A. Ebringerová, Structural diversity and application potential of hemicelluloses, Macromolecular Symposia, Wiley Online Library, 2005, pp. 1-12.
- [56] G.W. Huber, S. Iborra, A. Corma, Chemical reviews 106 (2006) 4044-4098.
- [57] F.M. Gírio, C. Fonseca, F. Carvalheiro, L.C. Duarte, S. Marques, R. Bogel-Lukasik, Bioresource technology 101 (2010) 4775-4800.
- [58] N. Mosier, C. Wyman, B. Dale, R. Elander, Y. Lee, M. Holtzapple, M. Ladisch, Bioresource technology 96 (2005) 673-686.
- [59] J. Ralph, K. Lundquist, G. Brunow, F. Lu, H. Kim, P.F. Schatz, J.M. Marita, R.D. Hatfield, S.A. Ralph, J.H. Christensen, Phytochemistry Reviews 3 (2004) 29-60.
- [60] M. Nazhad, L. Ramos, L. Paszner, J. Saddler, Enzyme and microbial technology 17 (1995) 68-74.
- [61] T.M. Lacerda, M.D. Zambon, E. Frollini, Carbohydrate polymers 93 (2013) 347-356.
- [62] A. Verardi, I. De Bari, E. Ricca, V. Calabrò, Bioethanol, InTech, 2012.

- [63] M.J. Taherzadeh, K. Karimi, *BioResources* 2 (2007) 707-738.
- [64] M.F. Demirbas, *Applied Energy* 86 (2009) S151-S161.
- [65] P. McKendry, *Bioresource technology* 83 (2002) 47-54.
- [66] D. Meier, B. van de Beld, A.V. Bridgwater, D.C. Elliott, A. Oasmaa, F. Preto, *Renewable and Sustainable Energy Reviews* 20 (2013) 619-641.
- [67] T.R. Carlson, G.A. Tompsett, W.C. Conner, G.W. Huber, *Topics in Catalysis* 52 (2009) 241.
- [68] D. Mohan, C.U. Pittman, P.H. Steele, *Energy & fuels* 20 (2006) 848-889.
- [69] P.M. Mortensen, J.-D. Grunwaldt, P.A. Jensen, K. Knudsen, A.D. Jensen, *Applied Catalysis A: General* 407 (2011) 1-19.
- [70] A. Demirbaş, *Energy conversion and management* 41 (2000) 633-646.
- [71] B.t. Chemical, E.B.t.L. Biofuels, G.W. Huber, *Breaking the chemical and engineering barriers to lignocellulosic biofuels: next generation hydrocarbon biorefineries*, National Science Foundation, Chemical, Biogengineering, Environmental and Transport Systems Division Washington, DC, 2008.
- [72] C. Higman, M. Van der Burgt, *Gasification*, Gulf professional publishing, 2011.
- [73] J.-P. Lange, *Catalysis Today* 64 (2001) 3-8.
- [74] J.A. Moulijn, M. Makkee, A.E. Van Diepen, *Chemical process technology*, John Wiley & Sons, 2013.
- [75] D.M. Alonso, J.Q. Bond, J.A. Dumesic, *Green Chemistry* 12 (2010) 1493-1513.
- [76] T.J. Farmer, M. Mascal, *Introduction to Chemicals from Biomass*, John Wiley & Sons, Ltd, 2015, pp. 89-155.
- [77] T. Werpy, G. Petersen, A. Aden, J. Bozell, J. Holladay, J. White, A. Manheim, D. Eliot, L. Lasure, S. Jones, *Top value added chemicals from biomass. Volume 1- Results of screening for potential candidates from sugars and synthesis gas*, DTIC Document, 2004.
- [78] J.J. Bozell, G.R. Petersen, *Green Chemistry* 12 (2010) 539-554.
- [79] S.P. Simeonov, J.A. Coelho, C.A. Afonso, *ChemSusChem* 5 (2012) 1388-1391.
- [80] G. Düll, *Chem. Ztg* 19 (1895) 216-220.
- [81] J. Kiermayer, *Chem. Ztg* 19 (1895) 1003-1006.
- [82] W. Haworth, W. Jones, *Journal of the Chemical Society (Resumed)* (1944) 667-670.
- [83] B. Kuster, *Starch-Stärke* 42 (1990) 314-321.
- [84] J. Lewkowski, (2001).

- [85] A.A. Rosatella, S.P. Simeonov, R.F. Frade, C.A. Afonso, *Green Chemistry* 13 (2011) 754-793.
- [86] T. Wang, M.W. Nolte, B.H. Shanks, *Green Chemistry* 16 (2014) 548-572.
- [87] A. Gandini, *Macromolecules* 41 (2008) 9491-9504.
- [88] A. Corma, S. Iborra, A. Velty, *Chemical reviews* 107 (2007) 2411-2502.
- [89] G.A. Halliday, R.J. Young, V.V. Grushin, *Organic letters* 5 (2003) 2003-2005.
- [90] M. Chatterjee, T. Ishizaka, H. Kawanami, *Green Chemistry* 16 (2014) 4734-4739.
- [91] J. Wang, X. Liu, B. Hu, G. Lu, Y. Wang, *RSC Advances* 4 (2014) 31101-31107.
- [92] Y. Roman-Leshkov, C.J. Barrett, Z.Y. Liu, J.A. Dumesic, *Nature* 447 (2007) 982-985.
- [93] Z. Wang, Q. Chen, *Green Chemistry* 18 (2016) 5884-5889.
- [94] E.J. Ras, S. Maisuls, P. Haesackers, G.J. Gruter, G. Rothenberg, *Advanced Synthesis & Catalysis* 351 (2009) 3175-3185.
- [95] S. Saravanamurugan, O. Nguyen Van Buu, A. Riisager, *ChemSusChem* 4 (2011) 723-726.
- [96] H. Joshi, B.R. Moser, J. Toler, W.F. Smith, T. Walker, *Biomass and bioenergy* 35 (2011) 3262-3266.
- [97] J.Q. Bond, D.M. Alonso, D. Wang, R.M. West, J.A. Dumesic, *Science* 327 (2010) 1110-1114.
- [98] C. Chang, P. Cen, X. Ma, *Bioresource technology* 98 (2007) 1448-1453.
- [99] J. Horvat, B. Klaić, B. Metelko, V. Šunjić, *Tetrahedron Letters* 26 (1985) 2111-2114.
- [100] D.J. Hayes, S. Fitzpatrick, M.H. Hayes, J.R. Ross, *Biorefineries—Industrial Processes and Product 1* (2006) 139-164.
- [101] T. Thananattathanachon, T.B. Rauchfuss, *Angewandte Chemie* 122 (2010) 6766-6768.
- [102] P. Lejemble, A. Gaset, P. Kalck, *Biomass* 4 (1984) 263-274.
- [103] J. Lecomte, A. Finiels, P. Geneste, C. Moreau, *Journal of Molecular Catalysis A: Chemical* 133 (1998) 283-288.
- [104] S.K. Patil, C.R. Lund, *Energy & Fuels* 25 (2011) 4745-4755.
- [105] H. Van Dam, A. Kieboom, H. Van Bekkum, *Starch-Stärke* 38 (1986) 95-101.
- [106] M.J. Antal, W.S. Mok, G.N. Richards, *Carbohydrate research* 199 (1990) 91-109.

- [107] C. Moreau, R. Durand, S. Razigade, J. Duhamet, P. Faugeras, P. Rivalier, P. Ros, G. Avignon, *Applied Catalysis A: General* 145 (1996) 211-224.
- [108] G. Yang, E.A. Pidko, E.J. Hensen, *Journal of Catalysis* 295 (2012) 122-132.
- [109] M.J. Antal, W.S. Mok, G.N. Richards, *Carbohydrate Research* 199 (1990) 111-115.
- [110] F. Newth, *Advances in carbohydrate chemistry* 6 (1951) 83-106.
- [111] A.S. Amarasekara, L.D. Williams, C.C. Ebede, *Carbohydrate research* 343 (2008) 3021-3024.
- [112] P. Daorattanachai, S. Namuangruk, N. Viriya-empikul, N. Laosiripojana, K. Faungnawakij, *Journal of Industrial and Engineering Chemistry* 18 (2012) 1893-1901.
- [113] G. Yang, E.A. Pidko, E.J. Hensen, *ChemSusChem* 6 (2013) 1688-1696.
- [114] H. Rasmussen, H.R. Sørensen, A.S. Meyer, *Carbohydrate Research* 385 (2014) 45-57.
- [115] R.L. de Souza, H. Yu, F. Rataboul, N. Essayem, *Challenges* 3 (2012) 212-232.
- [116] M. Watanabe, Y. Aizawa, T. Iida, T.M. Aida, C. Levy, K. Sue, H. Inomata, *Carbohydrate research* 340 (2005) 1925-1930.
- [117] J. Qi, L. Xiuyang, *Chinese Journal of Chemical Engineering* 16 (2008) 890-894.
- [118] A. Chareonlimkun, V. Champreda, A. Shotipruk, N. Laosiripojana, *Bioresource technology* 101 (2010) 4179-4186.
- [119] Y. Li, X. Lu, L. Yuan, X. Liu, *Biomass and bioenergy* 33 (2009) 1182-1187.
- [120] B.F. Kuster, H.M. Temmink, *Carbohydrate research* 54 (1977) 185-191.
- [121] T.S. Hansen, J.M. Woodley, A. Riisager, *Carbohydrate research* 344 (2009) 2568-2572.
- [122] B.F. Kuster, H.S. van der Baan, *Carbohydrate research* 54 (1977) 165-176.
- [123] T. Tuercke, S. Panic, S. Loebbecke, *Chemical engineering & technology* 32 (2009) 1815-1822.
- [124] F.S. Asghari, H. Yoshida, *Carbohydrate research* 341 (2006) 2379-2387.
- [125] X. Qi, M. Watanabe, T.M. Aida, R.L. Smith, *Catalysis Communications* 10 (2009) 1771-1775.
- [126] C. Carlini, P. Patrono, A.M.R. Galletti, G. Sbrana, *Applied Catalysis A: General* 275 (2004) 111-118.
- [127] C. Carlini, M. Giuttari, A.M.R. Galletti, G. Sbrana, T. Armadori, G. Busca, *Applied Catalysis A: General* 183 (1999) 295-302.
- [128] P. Carniti, A. Gervasini, S. Biella, A. Auroux, *Catalysis today* 118 (2006) 373-378.

- [129] T. Armaroli, G. Busca, C. Carlini, M. Giuttari, A.M. Raspolli Galletti, G. Sbrana, *Journal of Molecular Catalysis A: Chemical* 151 (2000) 233-243.
- [130] H.T. Kreissl, K. Nakagawa, Y.-K. Peng, Y. Koito, J. Zheng, S.C.E. Tsang, *Journal of Catalysis* 338 (2016) 329-339.
- [131] J.-M. Jehng, I.E. Wachs, *Catalysis Today* 8 (1990) 37-55.
- [132] J.M. Jehng, I.E. Wachs, *The Journal of Physical Chemistry* 95 (1991) 7373-7379.
- [133] J.-M. Jehng, I.E. Wachs, *Journal of molecular catalysis* 67 (1991) 369-387.
- [134] J.-M. Jehng, I.E. Wachs, *Catalysis today* 16 (1993) 417-426.
- [135] J. Datka, A. Turek, J. Jehng, I. Wachs, *Journal of Catalysis* 135 (1992) 186-199.
- [136] I. Nowak, *Studies in Surface Science and Catalysis* 154 (2004) 2936-2944.
- [137] S. Sumiya, Y. Oumi, M. Sadakane, T. Sano, *Applied Catalysis A: General* 365 (2009) 261-267.
- [138] M. Shirai, K. Asakura, Y. Iwasawa, *The Journal of Physical Chemistry* 95 (1991) 9999-10004.
- [139] Â. Silva, K. Wilson, A.F. Lee, V.C. dos Santos, A.C.C. Bacilla, K.M. Mantovani, S. Nakagaki, *Applied Catalysis B: Environmental* 205 (2017) 498-504.
- [140] M. Trejda, A. Tuel, J. Kujawa, B. Kilos, M. Ziolk, *Microporous and mesoporous materials* 110 (2008) 271-278.
- [141] C. García-Sancho, I. Agirrezabal-Telleria, M. Güemez, P. Maireles-Torres, *Applied Catalysis B: Environmental* 152 (2014) 1-10.
- [142] P. Carniti, A. Gervasini, M. Marzo, *Catalysis Today* 152 (2010) 42-47.
- [143] M. Marzo, P. Carniti, A. Gervasini, *CHIMICA OGGI-CHEMISTRY TODAY* 30 (2012) 22.-24.
- [144] K.O. Drake, D. Carta, L.J. Skipper, F.E. Sowrey, R.J. Newport, M.E. Smith, *Solid state nuclear magnetic resonance* 27 (2005) 28-36.
- [145] P. Carniti, A. Gervasini, M. Marzo, *The Journal of Physical Chemistry C* 112 (2008) 14064-14074.
- [146] E. Ko, R. Bafra, N. Nuhfer, N. Wagner, *Journal of Catalysis* 95 (1985) 260-270.
- [147] J. He, Q.-J. Li, Y.-N. Fan, *Journal of Solid State Chemistry* 202 (2013) 121-127.
- [148] A. Chinnappan, C. Baskar, H. Kim, *RSC Advances* 6 (2016) 63991-64002.
- [149] C. Moreau, A. Finiels, L. Vanoye, *Journal of Molecular Catalysis A: Chemical* 253 (2006) 165-169.
- [150] C. Lansalot-Matras, C. Moreau, *Catalysis Communications* 4 (2003) 517-520.

- [151] L. Lai, Y. Zhang, *ChemSusChem* 4 (2011) 1745-1748.
- [152] M. Bicker, J. Hirth, H. Vogel, *Green Chemistry* 5 (2003) 280-284.
- [153] B. Saha, M.M. Abu-Omar, *Green Chemistry* 16 (2014) 24-38.
- [154] J.N. Chheda, Y. Román-Leshkov, J.A. Dumesic, *Green Chemistry* 9 (2007) 342-350.
- [155] X. Tong, Y. Li, *ChemSusChem* 3 (2010) 350-355.
- [156] V. Vasudevan, S.H. Mushrif, *RSC Advances* 5 (2015) 20756-20763.
- [157] S.J. Oh, J. Park, J.G. Na, Y.K. Oh, Y.K. Chang, *RSC Advances* 5 (2015) 47983-47989.
- [158] D.W. Brown, A.J. Floyd, R.G. Kinsman, Y. Ali, *Journal of chemical technology and biotechnology* 32 (1982) 920-924.
- [159] H. Yan, Y. Yang, D. Tong, X. Xiang, C. Hu, *Catalysis Communications* 10 (2009) 1558-1563.
- [160] K.-i. Shimizu, R. Uozumi, A. Satsuma, *Catalysis Communications* 10 (2009) 1849-1853.
- [161] S. Despax, C. Maurer, B. Estrine, J. Le Bras, N. Hoffmann, S. Marinkovic, J. Muzart, *Catalysis Communications* 51 (2014) 5-9.
- [162] Q.P. Peniston, *Manufacture of 5-hydroxymethyl 2-furfural*, Google Patents, 1956.
- [163] A.C. Cope, *Production and recovery of furans*, Google Patents, 1959.
- [164] X. Qi, M. Watanabe, T.M. Aida, R.L. Smith Jr, *Green Chemistry* 10 (2008) 799-805.
- [165] J.N. Chheda, J.A. Dumesic, *Catalysis Today* 123 (2007) 59-70.
- [166] C. Fan, H. Guan, H. Zhang, J. Wang, S. Wang, X. Wang, *Biomass and Bioenergy* 35 (2011) 2659-2665.
- [167] E. Nikolla, Y. Román-Leshkov, M. Moliner, M.E. Davis, *Acs Catalysis* 1 (2011) 408-410.
- [168] F. Yang, Q. Liu, X. Bai, Y. Du, *Bioresource technology* 102 (2011) 3424-3429.
- [169] A.S. Amarasekara, *Chemical reviews* 116 (2016) 6133-6183.
- [170] D.R. MacFarlane, N. Tachikawa, M. Forsyth, J.M. Pringle, P.C. Howlett, G.D. Elliott, J.H. Davis, M. Watanabe, P. Simon, C.A. Angell, *Energy & Environmental Science* 7 (2014) 232-250.
- [171] J.S. Wilkes, M.J. Zaworotko, *Journal of the Chemical Society, Chemical Communications* (1992) 965-967.

- [172] Z. Wei, Y. Li, D. Thushara, Y. Liu, Q. Ren, *Journal of the Taiwan Institute of Chemical Engineers* 42 (2011) 363-370.
- [173] S. Hu, Z. Zhang, Y. Zhou, B. Han, H. Fan, W. Li, J. Song, Y. Xie, *Green Chemistry* 10 (2008) 1280-1283.
- [174] Q. Cao, X. Guo, S. Yao, J. Guan, X. Wang, X. Mu, D. Zhang, *Carbohydrate research* 346 (2011) 956-959.
- [175] X. Qi, H. Guo, L. Li, *Industrial & Engineering Chemistry Research* 50 (2011) 7985-7989.
- [176] Z. Zhang, Q. Wang, H. Xie, W. Liu, Z.K. Zhao, *ChemSusChem* 4 (2011) 131-138.
- [177] M. Chidambaram, A.T. Bell, *Green Chemistry* 12 (2010) 1253-1262.
- [178] X. Qi, M. Watanabe, T.M. Aida, R.L. Smith, *ChemSusChem* 3 (2010) 1071-1077.

## ***Chapter 2***

### ***Experimental***

## 2.1 Catalyst preparation

### 2.1.1 Preparation of SBA-15 support

Pure silica SBA-15 was synthesised using the method of Zhao and co-workers [1]. The structure directing agent, Pluronic P123 (10 g) (Sigma Aldrich, number average molecular weight ~ 5800) was dissolved in an aqueous solution of 1.9M HCl (730 cm<sup>3</sup>) (Fisher, 36%) with stirring at 40°C. Tetraethoxysilane (31 cm<sup>3</sup>) (Sigma Aldrich, 98%) was added and left for 20 hours with agitation at 40 °C. The resulting gel was then sealed in a 1L PTFE vessel and aged without agitation at 80°C for 24 hours. The resulting solid was recovered by filtration, washed several times with deionised water (1000 cm<sup>3</sup>) and dried at room temperature overnight. The residing surfactant was removed through calcination at 500°C for 6 hours in static air (ramp rate 1°C·min<sup>-1</sup>). This yielded approximately 12.0 g of white solid which was used as a support for the niobia based catalysts. This synthesis was chosen for its reproducibility and for the resulting material characteristics in terms of high surface area (>800 m<sup>2</sup>/g), ordered structure and chemical/thermal stability. Furthermore the process may be scaled to produce larger batches of material, without compromising the desirable properties of the support.

### 2.1.2 Preparation of bulk precipitated niobic acid (PNA)

Nanoparticulate niobic acid (Nb<sub>2</sub>O<sub>5</sub>·nH<sub>2</sub>O) was prepared following a previously reported precipitation protocol using niobium pentachloride (Sigma Aldrich, ≥99,9%) as the niobium precursor [2]. Due to its high moisture sensitivity, NbCl<sub>5</sub> was handled under inert atmosphere in a Terra Universal Smart Glovebox with a relative humidity control system. For the first stage involving the usage of the glove box, typically the needed materials were introduced in the glove box airlock and nitrogen flow was activated until a value under 10% of relative humidity was achieved. Then 5 g of NbCl<sub>5</sub> powder were weighed in a 50 cm<sup>3</sup> beaker using a Sartorius TE601 battery powered scale, following its dissolution in 10 cm<sup>3</sup> of ethanol (Fisher, 99.5%) giving a clear yellow solution, which can now be withdrawn from the glove box. This solution was slowly added to a 0.3 M aqueous ammonia solution (200 cm<sup>3</sup>, molar ratio NH<sub>3</sub>:NbCl<sub>5</sub> = 3.25:1, ammonia (Fisher, 35% extra pure) under mild stirring, instantly triggering the precipitation of a white compound (Nb<sub>2</sub>O<sub>5</sub>·nH<sub>2</sub>O), which was centrifuged at 10000 rpm for 10 minutes. After centrifugation, the paste-like precipitate was dispersed in deionised water and was again separated by centrifugation in order to eliminate possible chloride groups that may remain attached to the solid. The washing procedure was repeated until a neutral

pH was observed in the supernatant. The obtained precipitate was then dispersed in 20 cm<sup>3</sup> of H<sub>2</sub>O<sub>2</sub> (Sigma Aldrich, 30% aqueous solution) in a 500 cm<sup>3</sup> glass bottle under cooling with ice and mild stirring. The molar ratio of Nb<sup>5+</sup>:H<sub>2</sub>O<sub>2</sub> was 1:10. The resulting peptisation of the niobic acid nanoparticles due to the peroxide treatment generates a clear yellow solution as the white precipitate dissolves. The glass bottle containing this solution was then sealed and ageing process was carried at 80 °C for 24 hours under autogenic pressure. After this thermal treatment, the yellow solution adapts a solidified foam-like structure after expansion of the solid in a close confinement due to the generation of vapours during the thermal treatment. Once the foam-like material is formed, the vessel was opened and the remaining liquid evaporated at 80 °C overnight. The resulting yellow solid was then ground and labelled as precipitated niobic acid (PNA), giving a typical yield in the range of 1.5-2 grams. To evaluate the effect of thermal treatment on the material's physico-chemical properties, part of PNA was calcined at 300°C, 500°C and 700°C (400 mg in each case) in static air for 2 hours (ramp rate 3 °C·min<sup>-1</sup>), and stored at room temperature.

### 2.1.3 Synthesis of supported niobic acid on SBA-15

The primary goal of this preparation method was the synthesis of highly dispersed niobic acid nanoparticles on the surface and in the structural channels of SBA-15, therefore maximising the accessibility of niobic acid's active sites and minimising undesirable cluster formation. The preparation of these catalysts was performed as follows: the necessary amount of NbCl<sub>5</sub> needed for the preparation of each catalyst with a specific Nb wt% loading was obtained according to **Equation 2.1**. The preparation of 1 g of final supported catalyst with 2, 5, 10, 15 and 25 wt% Nb loading requires 0.06, 0.153, 0.323, 0.51 and 0.96 g of NbCl<sub>5</sub> respectively, resulting in a total amount of 2.006 g of NbCl<sub>5</sub>. A glove box under dry nitrogen atmosphere was used to weigh this amount of precursor in a 50 cm<sup>3</sup> beaker, followed by addition of ethanol (40 cm<sup>3</sup>) and the mixture was shaken until the chloride precursor was completely dissolved, whereupon the solution can be withdrawn from the glove box. The volume of solution needed to get the appropriate niobium loading is calculated by **Equation 2.2**, resulting in 1.2 cm<sup>3</sup> for 2 wt%, 3.0 cm<sup>3</sup> for 5 wt%, 6.4 cm<sup>3</sup> for 10 wt%, 10.2 cm<sup>3</sup> for 15 wt% and 19.2 cm<sup>3</sup> for 25 wt%, measured using a pipette with grades up to 10 cm<sup>3</sup> with one decimal. This amount of ethanolic solution was slowly added to a 100 cm<sup>3</sup> beaker containing 1 g SBA-15 dispersed in ethanol (25 cm<sup>3</sup>) under mild stirring for 24 h. Subsequent precipitation and oxidation as described for the PNA were performed, adjusting the volumes of ammonia solution and hydrogen peroxide to amount of Nb.

Therefore, in order to maintain a 3.25:1 ratio of  $\text{NH}_3:\text{NbCl}_5$ , the appropriate amount of 0.3 M aqueous ammonia solution was added to each beaker containing the 2, 5, 10, 15 and 25% niobium solutions, resulting in 4, 8, 14, 22 and 40 cm<sup>3</sup> respectively. Each of these precipitated niobic acid solutions were centrifuged at 10000 rpm for 10 minutes. After centrifugation, the paste-like precipitate was dispersed in deionised water and was again washed by centrifugation until a neutral pH was observed in the supernatant. The obtained precipitate was then dispersed in a 500 cm<sup>3</sup> glass bottle using the corresponding amount of  $\text{H}_2\text{O}_2$  aqueous solution to keep the molar ratio of  $\text{Nb}^{5+}:\text{H}_2\text{O}_2 = 1:10$ , leading to a volume of 0.15, 0.37, 0.77, 1.2 and 2.4 cm<sup>3</sup> for the 2%, 5%, 10%, 15% and 25% solutions respectively. The solutions were stirred at mild speed under cooling with ice. These solutions were dried at 80 °C for 24 hours in the sealed glass bottle in an oven, after which the vessel was opened and the remaining liquid evaporated at 80 °C overnight. These samples were designated X% PNA/SBA-15, they were not subject to further calcination following Nb incorporation and were stored at room temperature.

$$\text{Amount of NbCl}_5 = \frac{\text{mole weight of NbCl}_5}{\text{mole weight of Nb}} \cdot \frac{\text{wt}\%}{(100 - \text{wt}\%)} \cdot \text{g SBA} - 15$$

**Equation 2.1** Calculation of precursor needed

$$\text{Amount of solution} = \frac{40\text{ml ethanol} * \text{amount of NbCl}_5 \text{ needed in g}}{2.006 \text{ g NbCl}_5}$$

**Equation 2.2** Calculation of precursor solution volume

#### 2.1.4 Preparation of phosphated zirconia

A preparation method similar to that reported by Osatiashtiani et al. [3] was followed for the impregnation of different phosphate loadings onto a zirconia catalyst surface. For this purpose, 5 g of zirconium (IV) hydroxide (MEL Chemicals, MELCat x20 1249/01), used as support, was impregnated with 50 cm<sup>3</sup> of the desired molarity (0.01, 0.05, 0.1, 0.25 and 0.5M) of orthophosphoric acid (Fisher, >85%) and stirred for 5 hours at room temperature. Later, it was filtered and dried at 80°C for 24 hours in a static oven. Catalysts with different acid loadings were divided into equal weights (~ 1.5 g) and subjected to different calcination temperatures (550, 650 and 750°C) for 3 hours in

static air (ramp rate  $5^{\circ}\text{C}\cdot\text{min}^{-1}$ ) to follow any structural changes imparted with varying temperature. Finally, the obtained catalysts were stored at room temperature.

## **2.2 Catalyst characterization**

### **2.2.1 Inductively coupled plasma – optical emission spectrometry**

Solid samples required digestion prior to the ICP analysis, which in this project was performed using a CEM Discover SP-D 10/35 and Explorer 48 Sampler Automated Microwave Synthesis System. ICP measurements to determine the phosphorous content, the bulk concentration of atomic niobium present in the silica supported materials and in the bulk niobic acid samples were performed on a Thermo Scientific iCAP 7000 ICP-OES with charge injection device (CID) detector. A Niobium standard solution for ICP (Sigma Aldrich, 1000 ppm in nitric acid) and a phosphorous standard solution for ICP (Sigma Aldrich, 1000 ppm in nitric acid) were used for calibration.

Inductively coupled plasma optical emission spectroscopy (ICP-OES) is a characterization technique used for elemental analysis of materials, offering improved sensitivity to low elemental concentrations in the range of ppb (0.2 ppb in the case of niobium) over conventional atomic absorption methods; exceptionally, ultralow concentrations (ppt) can be detected in the case of elements such as magnesium, iron or calcium[4]. However, ICP-OES also has detection limitations, as is the case of halogens, which require high excitation energy, and elements that either are used to produce the plasma torch (carbon, hydrogen, oxygen) or are present in the atmosphere surrounding the torch (nitrogen)[5]. In this technique, argon plasma (atoms in an ionised state) is employed as an excitation source at temperatures up to  $8000^{\circ}\text{C}$ . The sample to be analysed is injected in a liquid state into the instrument, and nebulised into small droplets which are transferred to the plasma where they are excited or ionised. The atoms in the sample emit monochromatic light of characteristic wavelength which is detected and quantified in an optical emission spectrometer. After amplification and comparison with calibration standards, calculation of elemental concentration is possible [6].

Typically, 20 mg of catalyst were dissolved in an acid mixture comprised of ammonium fluoride (200 mg), nitric acid ( $5\text{ cm}^3$ ), sulphuric acid ( $2\text{ cm}^3$ ) and deionised water ( $4\text{ cm}^3$ )[7], and subjected to digestion in the microwave running at 300W for 20 minutes at  $220^{\circ}\text{C}$  with intense stirring using quartz tubes as the sample vessel with a PTFE liner. After the digestion period is completed,  $1\text{ cm}^3$  of boric acid is added to the solution for neutralisation of formed hydrofluoric acid, and it is stirred in the same vessel for 5

minutes at 150 °C in the microwave. The sample is diluted in a 1:10 ratio using an aqueous solution of 10% nitric acid, which is used also as mobile phase. Results are compared with a calibration curve acquired using the 309.418 nm signal realized prior to the analysis using the Nb standard solution in order to obtain the metal concentration in the samples (**Figure 2.1**).

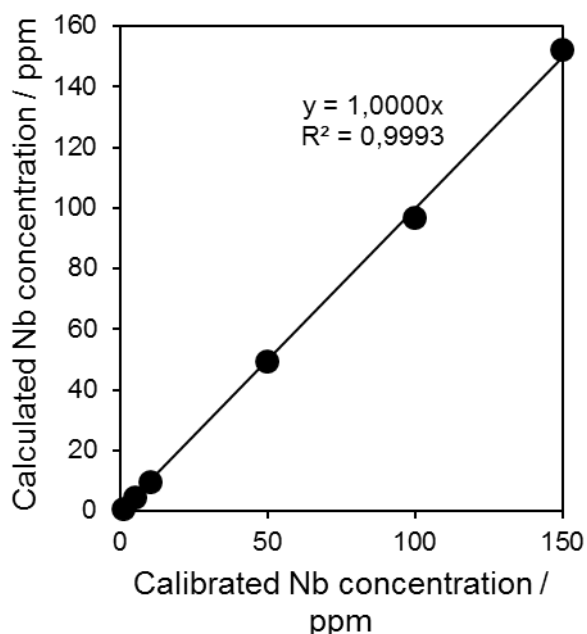


**Figure 2.1** Calibration curve for Nb quantification in ICP-OES

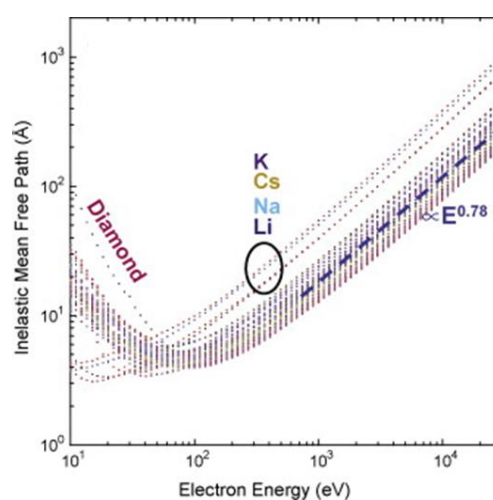
### 2.2.2 X-Ray photoelectron spectroscopy

XPS was performed using a Kratos Axis HSi photoelectron spectrometer equipped with a charge neutraliser, five channeltron detectors and monochromated Al K $\alpha$  ( $h\nu = 1486.6$  eV) X-ray source, using pass energy of 40 eV for high resolution and 160 eV for survey scans were employed. Samples were analysed at an operating pressure below  $10^{-9}$  torr and X-ray emission used was 12 mA and high tension of 13 kV. The software utilized to process the results was CasaXPS Version 2.3.15. Apart from the atoms present in the samples, there is also a strong signal from the carbon 1s state, which is always present due to hydrocarbon contamination of the surface. This peak is used for calibrating the energy scale, which may be shifted due to charging effects; the nominal C 1s binding energy for C-C/C-H is 284.6 eV. A Shirley-type background was used to remove the background from the secondary electrons. **Table 2.1** displays a list of the sought elements using XPS and the parameters fixed for the analysis. For the line shape GL (30) refers to a Gaussian-Lorentz 70% Gaussian and 30% Lorentzian, whilst DS indicates a Doniach-Sunjic modified Gaussian-Lorentz line shape, where 0.01 is the asymmetry parameter and 400 the convolution width.

**Table 2.1** List of scanned elements in XPS

| Element | Orbital | Start (eV) | End (eV) | Dwell (ms) | Scans | Line shape                |
|---------|---------|------------|----------|------------|-------|---------------------------|
| O       | 1s      | 540        | 520      | 332        | 10    | GL (30)                   |
| C       | 1s      | 300        | 220      | 260        | 10    | GL (30)                   |
| Nb      | 3d      | 212        | 195      | 458        | 30    | DS (0.01, 400)<br>GL (30) |
| Cl      | 2p      | 212        | 195      | 458        | 30    | GL (30)                   |
| Si      | 2p      | 110        | 90       | 397        | 10    | GL (30)                   |
| Zr      | 3d      | 190        | 175      | 458        | 10    | GL (30)                   |
| P       | 2p      | 138        | 130      | 458        | 30    | GL (30)                   |

X-ray photoelectron spectroscopy (XPS) is a surface-sensitive analytical technique that relies on the photoelectric effect, and provides quantitative elemental and chemical information regarding the relative number of atoms of each type present on the surface. The kinetic energy of photo-emitted electrons is also sensitive to the oxidation state and chemical environment of element under investigation. Elements can be identified from the unique binding energy of electrons in each element's orbitals, which act as a 'fingerprint'. The reason why only electrons from surface atoms contribute to the photoelectron peak is because those emitted from the bulk are inelastically scattered. Low energy photoelectrons emitted have a short value of inelastic mean free path (IMFP), which is an index of how far an electron on average travels through a solid before losing energy, in the electron kinetic energy range of 10-1300 eV[8]. The IMFP is generally described by the Universal Escape Depth curve, which has a broad minimum at a kinetic energy of around 70-100 eV (**Figure 2.2**)[9].

**Figure 2.2** Calculated IMFPs for a range of elements spanning Li-Bi as a function of electron KE

When the sample being analysed is irradiated with monochromatic soft X-rays, i.e. with energies 100 eV - 5 keV (10 - 0.1 nm wavelength), excitation of photoelectrons from the specimen with a kinetic energy characteristic of their initial atomic energy level and element leaves a core hole, which creates an excited ionic state (**Figure 2.3**)[10, 11]. The kinetic energy of ejected photoelectrons is related to the electron binding energy by **Equation 2.3**, and it can be measured by XPS to identify the elements present in the sample of study.

The core hole resulting from the photoemission process generally causes a rearrangement of the electronic levels, so that this vacancy can be filled by an electron from a higher energy level, which can lead to two possible final states having different binding energies, known as the spin orbit coupling effect which is manifested in form of a doublet (**Equation 2.4**)[12]. For example, analysis of the Nb 3d state will result in doublet peaks corresponding to 3d<sub>5/2</sub> and 3d<sub>3/2</sub> states.

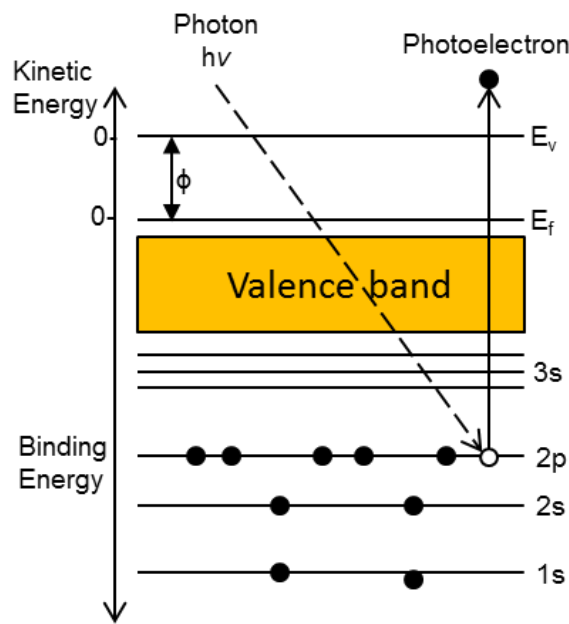


**Figure 2.3** Schematic representation of the photoemission process

$$E_k = h\nu - E_B - \phi$$

**Equation 2.3** Photoelectron kinetic energy

Where  $E_k$  is the photoelectron kinetic energy,  $h\nu$  is the photon energy,  $E_B$  is the electron binding energy and  $\phi$  is the spectrometer work function.

$$j = l + s$$

**Equation 2.4** Spin orbit coupling effect

Where  $j$  is the total angular momentum number,  $l$  is the orbit angular momentum number ( $l = 0, 1, 2, 3$ , corresponding to s, p, d, f orbitals) and  $s$  is the spin angular momentum number ( $s = \pm 1/2$ ).

Interactions with other electrons can lead to additional energy losses, arising peaks at high binding energies in the spectrum due to shake-up (electrons promoted to an unoccupied state) and shake-off (electrons that scape from the atom)[13]. For low binding energies the continuous background, made up of photoelectrons with little energy loss prior to emission, is not intense and a model function can easily be found[6].

### **2.2.3 Powder X-Ray diffraction**

X-ray diffraction (XRD) patterns were recorded on a Bruker D8 Advance diffractometer fitted with a 192 channel LynxEye high-speed strip detector and a Cu K $\alpha$  source (1.54 Å, 8.04 keV) with a nickel filter and divergent beam, calibrated against a corundum standard with a primary slit size of 0.3 mm and a secondary slit size of 2.4 mm. K $\alpha_2$  contributions were removed post analysis using an algorithm within the Bruker diffrac.EVA software. The patterns were obtained by measuring the diffracted X-ray beam intensity as a function of angle. Low angle patterns were collected over a range of  $2\theta = 0.45-8^\circ$  (step size  $0.01^\circ$ , time per step 0.6 s) and wide angle patterns over a range of  $2\theta = 10- 80^\circ$  (step size  $0.02^\circ$ , time per step 1 s). In situ measurements were performed under air following heating to the desired temperature (ramp rate  $10^\circ\text{C min}^{-1}$ ) for 60 min at each temperature. In-situ measurements were performed using an Anton-Paar XRK-900 cell fitted with Beryllium windows and gas flow was controlled using Bronkhorst EL-flow select mass flow controllers with an error of  $\pm 0.1 \text{ cm}^3/\text{min}$  and a Eurotherm 2604 advanced controller tcu. The X-ray source was aligned using the parallel beam geometry for in-situ measurements, using a Göbel mirror and 0.2 mm slit, resulting in a spot size of 0.3 mm.

X-ray powder diffraction (XRD) is a non-destructive analytical technique that provides structural information about the internal lattice of crystalline materials. It is commonly used for phase identification of a crystalline material and can provide information on unit cell dimensions, crystallite size, lattice strain, surface and interface roughness, chemical composition, and crystal orientation.[14] The phenomenon of X-ray diffraction is based on the interference of a monochromatic X-ray beam with the lattice planes in an ordered material. These X-rays are generated by a cathode ray tube working under vacuum, which produce and concentrate monochromatic radiation and direct it toward

the sample[15]. The three-dimensional structure of crystalline materials is formed by atoms arranged in a periodic array that form a crystal lattice. When a focused X-ray beam interacts with these planes of atoms, part of the beam is transmitted, part is absorbed by the sample, part is refracted and scattered, and part is diffracted. Diffraction occurs due to constructive/destructive interference between X-rays reflected from the planes in a crystal lattice. The intensity of the diffracted X-ray beam can be detected as a function of incident angle, and because of the random orientation of the powdered material, only a fraction of any crystallites will be oriented with crystal planes at the correct angle for constructive interference for any specific angle of incidence, producing a diffractogram.

Distances between the planes of the atoms that constitute the sample structure of lattice parameter (a) can be calculated from the relationship between Bragg's Law (**Equation 2.5**) and Miller indices (**Equation 2.6**) characteristic of hexagonal and orthorhombic systems, giving rise to a full form for calculating lattice parameters (**Equation 2.7**)[16].

$$n\lambda = 2d \sin \theta$$

**Equation 2.5** Bragg's Law

$$\frac{1}{d^2} = \frac{4}{3} \left( \frac{h^2 + hk + k^2}{a^2} \right) + \frac{l^2}{c^2} \qquad \frac{1}{d^2} = \frac{h^2}{a^2} + \frac{k^2}{b^2} + \frac{l^2}{c^2}$$

**Equation 2.6** Distance between planes in hexagonal (left) and orthorhombic (right) systems

$$a = \sqrt{\frac{4}{3} \frac{(h^2 + hk + k^2)}{\left(\frac{\lambda}{2\sin\theta}\right)^2} + \frac{l^2}{c^2}} \qquad a = \sqrt{\frac{h^2}{\left(\frac{\lambda}{2\sin\theta}\right)^2} + \frac{k^2}{b^2} + \frac{l^2}{c^2}}$$

**Equation 2.7** Lattice parameter calculation in hexagonal (left) and orthorhombic (right) systems

Where  $\lambda$  is the wavelength of electromagnetic radiation (in nm),  $\theta$  is the diffraction angle,  $d$  is the lattice spacing in a crystalline sample, h, k, l are the Miller indices and a is the lattice parameter. A simple schematic of the experimental setup for powder XRD is shown in **Figure 2.4**.



**Figure 2.4** Schematic representation of the X-Ray Diffraction instrument[17]

Crystallite size is defined as “the dimensions of a coherently diffracting domain in the direction perpendicular to the diffracting plane”[18]. The evaluation of the samples’ crystallite size was performed using the Scherrer equation (**Equation 2.8**) in which an average of the Full Width at Half Maximum (FWHM) of the largest peak in the diffraction pattern was employed. Moreover, the shape of the diffraction peaks contains additional information, like the evidence that the width of the peaks increases as the crystallite size decreases. However, this method is only valid down to crystallite sizes of about 3nm using a copper source, hence probing particulate sizes below this threshold requires an X-ray source of higher energy (e.g. Mo or Ag).

$$L = \frac{k \cdot \lambda}{\sqrt{(FWHM)^2 - S^2} \cdot \cos\theta}$$

**Equation 2.8** Scherrer equation

Where  $L$  is the average crystallite size,  $k=0.9$  is a constant,  $\lambda$  is the wavelength of electromagnetic radiation,  $FWHM$  is the full width half maximum of the peak,  $S=0.15$  is the systematic broadening caused by the diffractometer, and  $\theta$  is the diffraction angle.

#### **2.2.4 Nitrogen porosimetry**

Data acquisition was accomplished using Quantasorb Nova 4000e and 4200e porosimeters. Before starting the experiment, solid surfaces must be purged from physisorbed water and other impurities by heating the sample under vacuum

(degassing). For these experiments, degassing of approximately 50 mg catalyst sample weighed in a glass 9 mm large bulb sample cell was carried out at 120°C using a heating mantle during 18h. After this pre-treatment, the sample cell is transferred to a liquid nitrogen bath in order to keep a constant temperature of -196 °C. BET surface areas were calculated over the relative pressure range 0.05-0.3 where a linear relationship was observed, pore diameters and volumes were calculated applying the BJH method to the desorption branch using relative pressure >0.35. The software used for the data analysis was Quantachrome Novawin 11.0.

Nitrogen physisorption, also known as nitrogen porosimetry, is a procedure employed to determine the textural properties of porous materials, such as specific surface area, pore size distributions, pore shape or pore volume. The measurement of these parameters is based upon the determination of nitrogen volume necessary to cover the surface of the catalyst with a monolayer of the gas at different relative pressures.

During the analysis, the sample is exposed to an adsorbate gas (nitrogen) at a constant temperature of -196 °C (nitrogen boiling point), and the partial pressure of nitrogen is increased stepwise. This temperature is necessary because due to the weak enthalpy of adsorption (low in magnitude), of nitrogen physisorption, it only occurs at temperatures below the adsorbate boiling point. Nitrogen adsorption arises from London forces which are due to the formation of temporarily induced dipoles, via the variation of electron density within the adsorbate molecule[19]. At dynamic equilibrium (rate of adsorption = rate of desorption), experimental isotherms of adsorbed gas volumes versus partial pressures ( $P/P_0$ ) are then constructed. As the equilibrium adsorbate pressures approach saturation, the pores become completely filled with adsorbate, which allows an estimation of the volume occupied and the total pore volume of the sample. The close proximity between the adsorbate and the pore walls in the mesoporous materials provoke an increase in the attractive interactions, leading to a new form of adsorption called capillary condensation. Subsequently, desorption isotherms can be generated by reversing the adsorption process. In this case, the evaporation of the liquid adsorbate is hindered by its surface tension, as consequence of the liquid's meniscus shape. This evaporation effect causes a desorption step at lower pressure than for adsorption, resulting in a characteristic isotherm shapes, with the presence of a hysteresis loop, which can be related to particular pore architectures. In 1985, IUPAC proposed six classifications of isotherm, depicted in **Figure 2.5 (left)**[20]. Type I isotherms are given by microporous adsorbents (pore size < 2 nm) with strong interactions between adsorbate and adsorbent; type II

isotherms appear in most non-porous or macroporous adsorbents (pore size > 50 nm); type III isotherms are characteristic of relatively weak interactions between adsorbent–adsorbate, leading to an agglomeration of around the most favourable sites; type IV isotherms are characteristic of materials with mesopores (2 nm < pore size < 50 nm), in this case, the monolayer–multilayer adsorption on the mesopore walls is followed by capillary condensation; type V isotherm shape is similar to that of type III and can be attributed to relatively weak adsorbent–adsorbate interactions; type VI indicates consecutive adsorbate layer-by-layer formation due to uniform surface.

Hysteresis loops correspond to mesoporous systems (isotherms IV and V), and is formed due to adsorption and desorption differences of the adsorbate in the mesopores. This phenomenon is classified in four types, depicted in **Figure 2.5 (right)**. The H1 loop is indicative of narrow pore size distributions due to strongly interlinked particles (agglomerates) of solids; the more common H2 loop corresponds to mesoporous materials with variable ink bottle pore shape and size, and effects as pore blockage play an important role; slit shape pores formed by aggregates lead to H3 loops (non uniform size pores) and H4 loops (uniform size pores).

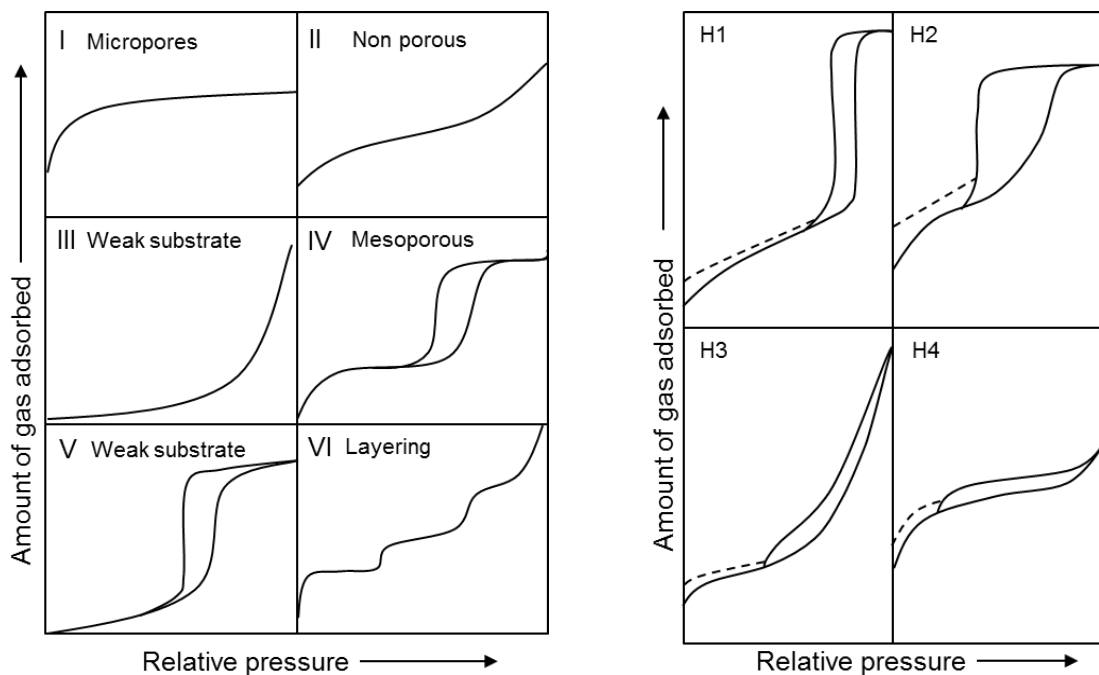


**Figure 2.5** Classification of adsorption isotherms (left) and type of hysteresis loop (right)

Specific surface area may be obtained by implementation of various mathematical models; the most commonly reported being the Brunauer, Emmett and Teller (BET) model[21]. In BET theory a multilayer modification is applied to Langmuir’s theory of

monolayer adsorption, extending the concept to include an infinite or a finite number of adsorbed layers. According to the BET model, the adsorbate molecules used to create a monolayer, act as adsorption sites for the next layer. After the first layer, the adsorption energy is equivalent to the heat of condensation, making the interaction with the solid negligible. Since this is a reversible phenomenon, there is a permanent equilibrium between the number of molecules adsorbed and desorbed. The linear form of the BET equation (**Equation 2.9**)[22] was used to calculate surface areas.

$$\frac{1}{V[P_0 - P]} = \frac{1}{V_m \cdot C} + \frac{C - 1}{V_m \cdot C} \cdot \left(\frac{P}{P_0}\right)$$

**Equation 2.9** Linear BET equation

Where P and P<sub>0</sub> are the partial and saturated pressure of adsorbate gas in equilibrium (in Pa), V is volume of gas adsorbed (in cm<sup>3</sup>), V<sub>m</sub> is the volume of gas adsorbed in a monolayer (in cm<sup>3</sup>), and C is the BET constant exponentially related to the heat of adsorption through the next simplified **Equation 2.10**:

$$C \approx \exp\left(\frac{E_1 - E_L}{RT}\right)$$

**Equation 2.10** Definition of constant C

Through this equation it is possible to calculate the amount of adsorbate gas necessary to form a monolayer (V<sub>m</sub>) in the relative pressure area 0.05-0.3. The obtained V<sub>m</sub> value is used to calculate the total surface area by means of the **Equation 2.11**[23, 24]:

$$S_{total} = \frac{(V_m \cdot N_A \cdot S)}{V}$$

**Equation 2.11** BET surface area calculation

Where N<sub>A</sub> is the Avogadro's number and S is adsorption cross section. Evaluation of the pore size distribution and mesopore volumes were calculated by means of the Barrett-Joyner-Halenda (BJH) method, which is based on a modification of the Kelvin equation (**Equation 2.12**), applied to the desorption branch of the isotherm[25]. The model is used to describe condensation of gases within a pore, here it has been used to relate the amount of adsorbate removed from the pores of the material, as the relative pressure (P/P<sub>0</sub>) is decreased from a high to low value, with the size of the pores. Cylindrically shaped pores are assumed in this method and the radius of the capillary is estimated as equal to the sum of the Kelvin radius and the thickness of the

adsorbate film on the pore walls. The statistical thickness of the adsorbed layer during multilayer adsorption is determined by means of a t-plot, which may also be utilised for the estimation of micropore (< 2nm), surface area and volumes[26]. This method should be carefully interpreted in the micropore region since the Kelvin equation (basis of BJH) is reliable only for pores >2 nm.

$$\ln \frac{P}{P_0} = \frac{-2 \cdot \gamma \cdot V_m}{r_k \cdot R \cdot T} \cdot \cos\theta$$

**Equation 2.12** Kelvin equation

Where  $r_k$  is the Kelvin radius which represents the radius of curvature of a hemispherical meniscus,  $\gamma$  is surface tension of condensed phase, R is the universal gas constant, T is the temperature, and  $\theta$  is contact angle of liquid with the pore wall.

The method used for micropore analysis was the t-plot method, developed by Lippens and de Boer[27]. In this method, the amount of adsorbate was plotted against the multilayer thickness using the surface area calculated from the BET equation. The external surface area is calculated from the linear part of the t-plot, which takes place before the capillary condensation occurs. Since micropores do not experience multilayer adsorption, the micropore volume can be calculated from subtracting the external surface area from the total surface area obtained from the BET method[25].

**2.2.5 Transmission electron microscopy**

High resolution TEM images were recorded on a JEOL 2100F FEG STEM operating at 200 keV and equipped with a spherical aberration probe corrector (CEOS GmbH) and a Bruker XFlash 5030 EDX, with analysis carried out at the University of Birmingham. The sample was prepared by supporting a dispersion of the catalyst in ethanol onto a carbon Cu grid coated with a holey carbon support film (Agar Scientific Ltd) and images were analysed using the software ImageJ 1.41.

Transmission electron microscopy (TEM) is an analytical tool allowing high resolution images of specimens in the nanoscale realm. A TEM image is formed when a beam of electrons passes through the material object of study. The beam, of very short wavelength, is emitted from a tungsten filament at the top of a cylindrical column of about 2 m high, being able to achieve a resolution of 0.2 nm and magnifications up to 2.000.000x.

The electron beam produced at the top of the microscope travels through vacuum in the column of the microscope. Along the column, at specific intervals magnetic coils are placed in order to focus the electron beam like glass lenses do in a light microscope. The magnetic coils placed at specific intervals in the column acts as an electromagnetic condenser lens system[28]. **Figure 2.6** depicts a schematic view of a TEM showing the different lenses and the pathway of the electrons.

The resultant beam contains some of the original free electrons that have not been changed in velocity or direction and some that have been changed either way or both. Depending on the density of the material present, some of the electrons are scattered and disappear from the beam. Since the electron image cannot be viewed directly by the eye, the image is projected onto a fluorescent screen at the bottom of the microscope, and then transmitted to a photographic plate or film, giving rise to a "shadow image" of the specimen, with its different parts displayed in varied darkness according to their density[29].



**Figure 2.6** Schematic view of a TEM [30]

### **2.2.6 Thermogravimetric analysis**

Thermogravimetric analysis (TGA) experiments were performed using a Mettler Toledo TGA/DSC1 Star System with a temperature range from ambient to 1100 °C, autosampler and a thermostatted balance with fast cooling. Samples (5-7 mg) were

placed into an alumina crucible (70  $\mu$ l) and placed in the autosampler positions. Nitrogen was used as a purge gas at a flow rate of 60 cm<sup>3</sup>/min. TGA is performed with a linear rate of 10°C/min, ranging from 40°C to 800°C. This temperature is chosen so that all chemical reactions are completed (i.e., all of the carbon is burnt off leaving behind metal oxides). The sample's mass was recorded as function of temperature, and analysed after subtraction of the corresponding mass variation of an empty crucible. Data was process using STARe Evaluation Software. TGA-MS analyses were performed in conjunction with a ThermoStar TM GSD 301 T3 mass spectrometer.

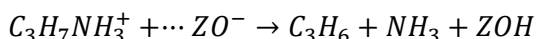
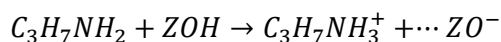
TGA is an analytical technique used to determine a material's thermal stability and its fraction of volatile components by monitoring the weight change that occurs as a function of temperature. It consists of a sample pan that is supported by a precision microbalance in a furnace that is heated during the experiment, monitoring its mass. In this thesis, the analysis is normally carried out in a nitrogen atmosphere or in a 20% oxygen in nitrogen atmosphere to simulate air conditions, although it can be performed under many gaseous environments, ideally 'non-corrosive', such as argon or helium. TGA in combination with differential scanning calorimetry (DSC) can be used to monitor the energy exchanged between the sample and the a reference holder, providing information regarding thermodynamics of sample decomposition and phase changes[31]. Thermal gravimetric analysis can also be interfaced with a mass spectrometer to measure the vapours generated, thus identifying the volatile components released.

### **2.2.7 Propylamine chemisorption and temperature programmed desorption**

Propylamine chemisorption and TPD analyses were performed in the previously mentioned Mettler Toledo used for TGA analysis in conjunction with a ThermoStar TM GSD 301 T3 mass spectrometer. Prior to analysis, the samples (5-7 mg) were impregnated with neat propylamine (Sigma Aldrich,  $\geq 99\%$ ) (enough to soak the catalyst) and excess physisorbed propylamine removed in vacuo at 70°C for 18 h. During the thermogravimetric analysis of propylamine impregnated samples, the temperature was increased up to 800°C at a rate of 10°C/min under nitrogen flow, and propene desorption was monitored by mass spectrometry ( $m/z = 41$ ). Moreover, mass channels of  $m/z = 17, 30, 35, 70, 79$  and  $95$  were also controlled to inspect the presence of ammonia, unreacted propylamine, chloride, chlorine, phosphoryl and phosphate respectively. Since the niobium precursor was a chloride compound, chlorine species were investigated to track possible traces remaining from the

synthesis process, which could misleadingly enhance the activity of the catalysts. The loss of phosphate groups was monitored by following the desorption of  $\text{PO}_3^{2-}$  and  $\text{PO}_4^{2-}$ . Acid sites densities were obtained after quantification of the propene signal obtained by the mass spectrometer.

Propylamine chemisorption and temperature programmed desorption was used to determine the number and strength of acid sites present in the samples. The method is based on the fact that Brønsted acids sites protonate the propylamine molecule forming propylammonium ion, which is decomposed to ammonia and propene by a reaction similar to the Hofmann-elimination (**Equation 2.13**)[32]. An unreactive carrier gas (nitrogen in this case) carries the reactively formed propene from the sample to the detector of the mass spectrometer as the temperature increases.



**Equation 2.13** Adsorption and reaction of propylamine with the catalyst

### 2.2.8 Diffuse reflection infrared Fourier transform spectroscopy and *in situ* pyridine chemisorption

DRIFTS spectra were obtained using a Thermo Scientific Nicolet iS50 FT-IR spectrometer equipped with a praying mantis environmental cell, a tungsten-halogen white light source, able to perform both in-situ and ex-situ analyses and mercury cadmium telluride (MCT-A) photon detector at  $-196^\circ\text{C}$ , cooled by liquid nitrogen. Samples were diluted homogeneously to 5 wt% by grinding in KBr, a reference compound which doesn't absorb infrared radiation. Diluting the sample in this matrix increases the proportion of diffuse reflectance in the reflected light[33]. For ex situ pyridine adsorption, diluted samples were impregnated with neat pyridine, and excess physisorbed pyridine removed in vacuo at  $70^\circ\text{C}$  for 18 h. Analysis was conducted *in vacuo* at room temperature, 64 scans were realized for each sample in the wavenumber range of 4000 and  $650\text{ cm}^{-1}$  at a resolution of  $4\text{ cm}^{-1}$ . Data analysis was carried out with Omnic software and spectra plotted using the Kubelka-Munk approximation (**Equation 2.14**) as function of wavenumber[34].

$$f(R_{\infty}) = \frac{(1 - R_{\infty})^2}{2R_{\infty}} = \frac{k}{s}$$

**Equation 2.14** Kubelka-Munk equation

Where R is absolute reflectance, s is scattering coefficient and k is molar adsorption coefficient.

Infrared spectroscopy is used to characterize the vibrational properties of bonds in molecules and identify the strength and type of bonds that are present. It can be used to identify the components of an unknown compound (functional groups) from fingerprint vibrational modes, quantify the presence of known compounds or to measure the strength of bonds from shifts in vibrational frequency. The analysis is performed by recording the variation of the transmission with frequency. The frequency domain is obtained converting the information acquired in the time domain by means of a Fourier transformation, from whose interferogram, the final spectrum is extracted[35]. DRIFTS analysis is conducted by focusing infrared light onto the sample, where it can be reflected, scattered or transmitted. The absorption of infrared radiation excites the vibrational modes of bonding moieties in molecular species and the scattered radiation is collected and relayed to the IR detector, where the sample functionalities can be identified (**Figure 2.7**).



**Figure 2.7** General mechanism of DRIFTS[36]

Pyridine has been widely used as a basic probe molecule to study the surface acidity of solid catalysts since it can function as either a Lewis or Brønsted base[37]. It is chosen as a probe molecule over ammonia because it is classified as weaker base than

ammonia, it is more easily protonated, and the pyridinium ion is thermally more stable than the ammonium ion[38]. The pyridine molecule can form the pyridinium ion through protonation on acidic OH groups as a manner of identification of Brønsted acid sites, it can undergo H-bonding with less acidic OH groups and can experience coordination to aprotic sites, hence determining the presence of Lewis acid sites[14] (**Figure 2.8**). A clear difference can be observed between the infrared spectra of these surface species, making their distinction reasonably simple. The relationships of these vibrational modes to the identities of the adsorption sites are as follows: protonation by surface Brønsted site: 1535-1550, 1640  $\text{cm}^{-1}$ ; hydrogen bonding: 1440-1447, 1580-1600  $\text{cm}^{-1}$  and coordination bonding to a surface Lewis acid site: 1440-1464, 1600-1634  $\text{cm}^{-1}$ [39].

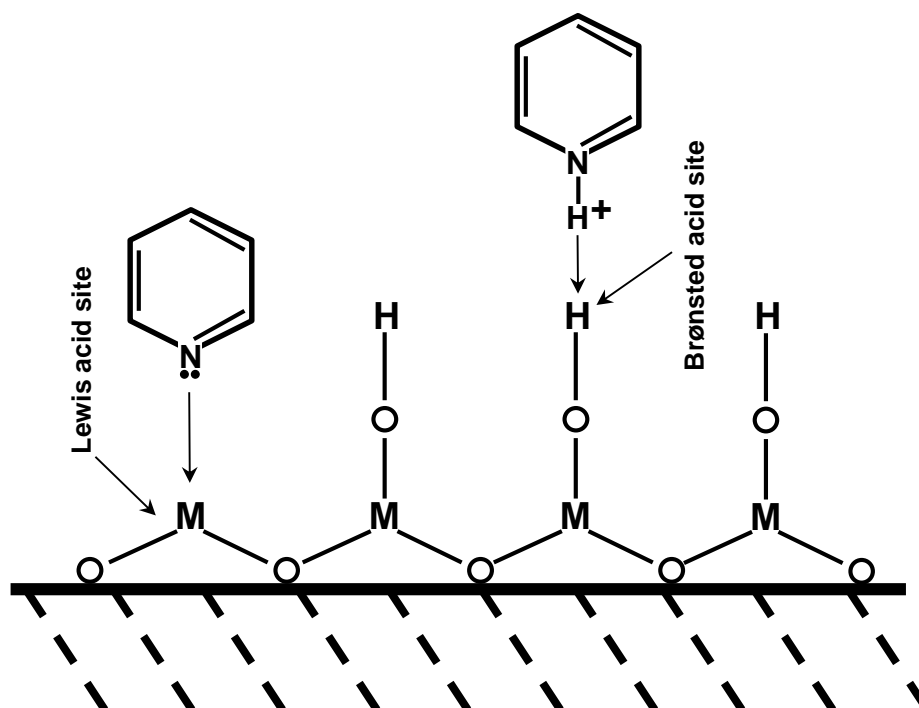


**Figure 2.8** Pyridine adsorption mechanism

### 2.2.9 Carbon dioxide chemisorption

Surface basicity was studied via  $\text{CO}_2$  chemisorption using a Quantachrome ChemBET3000 system equipped with a thermal conductivity detector (TCD). Samples (60 mg) were placed in a quartz U-shaped chemisorption cell and outgassed at  $300^\circ\text{C}$  under flowing He ( $150 \text{ cm}^3 \text{ min}^{-1}$ ) for 1 h prior to titration. Manual injections ( $0.10 \text{ cm}^3$ ) of 10 vol%  $\text{CO}_2$  in He were carried out at  $44^\circ\text{C}$ , and the  $\text{CO}_2$  TCD signal monitored in real-time. Titration of basic sites was carried out until complete saturation by

consecutive injections was achieved. Thus, the number of basic centres, expressed in mmol and normalised per g of sample, was calculated assuming a stoichiometry 1:1 between the basic site and CO<sub>2</sub>.

CO<sub>2</sub> chemisorption is a very useful technique to investigate on the basic properties of heterogeneous solid catalysts. Adsorption of carbon dioxide over solid materials occurs via either physical or chemical adsorption, with the latter possibly leading to dissociation of the probe molecule, depending on the components and analysis conditions. CO<sub>2</sub> chemisorption on metal oxides typically results with the formation of carbonate species displaying different theoretical configurations, as reported in **Figure 2.9**, where O is oxygen surface site and M is related to metal surface site. The widely accepted carbonate geometry is the bidentate oxygen oriented system located on the same or different adsorption sites. The carbon-down[40] and the side-on[41] geometries are further proposed carbonates configurations, where in the latter both carbon and oxygen are oriented on different adsorption sites.

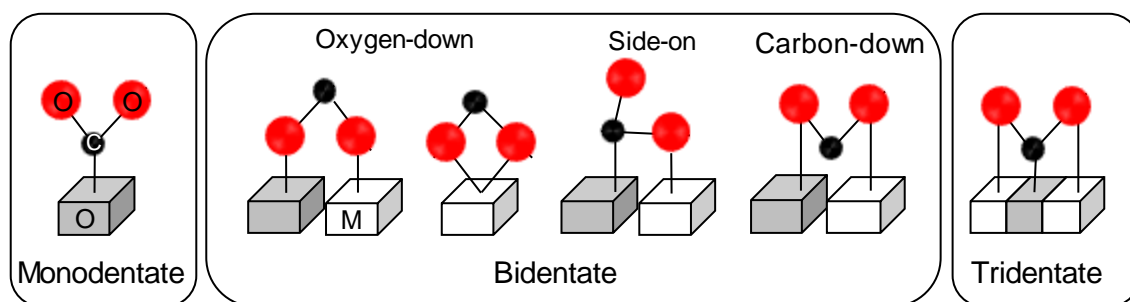


**Figure 2.9** Adsorption configuration of carbonates (adapted from[42])

### 2.2.10 Raman spectroscopy

Raman spectra were obtained on an InVia Raman Microscope Renishaw fitted with a 532 and 633 nm lasers, and Wire 3.4 software. Data were collected ranging between 100–1200 cm<sup>-1</sup>, employing 532 nm source and x20 lens magnification; samples were exposed for 10 seconds to the beam source, recoding 10 accumulations at 50 % laser power for bulk samples and 10 accumulations at 100 % laser power for SBA-15 supported samples and phosphated zirconia materials.

In Raman spectroscopy the sample is irradiated with a monochromatic beam in the visible region of the spectrum, which induces the transition of the photon to a virtual energy state, which then fall down to a real lower state, emitting the detected photon in the process. Most of the photons are scattered elastically (with no change of frequency,

also known as Rayleigh scattering), but a small proportion of the radiation is scattered inelastically, meaning that these photons give up part of their energy to excite vibrations, corresponding the energy loss to the vibrational modes of the molecule[43]. Combining DRIFTS and Raman can offer more detailed chemical information, because although both techniques measure the vibrational energies of molecules, they are dependent on different selection rules, i.e., an adsorption of electromagnetic radiation for the former and an inelastic scattering of electromagnetic radiation for the latter. An advantage of Raman spectroscopy is that silica support, as the one used in this thesis, is weak Raman scatterer, meaning that adsorbed species can be measured at wavenumbers as low as  $50\text{ cm}^{-1}$ .

## 2.3 Catalytic tests

### 2.3.1 Glucose and fructose conversion to HMF

Catalytic studies of glucose and fructose were conducted at different temperatures in a Radleys StarFish Multi-Experiment Work Station equipped with a PT1000 temperature sensor under stirred batch conditions. Reactions were performed using 0.1 g glucose or fructose (Sigma Aldrich, 99.5%), 0.1 g catalyst,  $20\text{ cm}^3$  deionised water and  $0.1\text{ cm}^3$  dimethyl sulfoxide as an internal standard, together in a  $50\text{ cm}^3$  round bottom flask at  $100\text{ }^\circ\text{C}$  and ambient pressure, although a reaction temperature study was carried out at temperatures ranging between  $80\text{ }^\circ\text{C}$  and  $110\text{ }^\circ\text{C}$ , and a pressure flask was used for temperatures above  $100\text{ }^\circ\text{C}$ . Aliquots ( $0.3\text{ cm}^3$ ) were periodically sampled, filtered using a 25 mm PTFE syringe filter (pore size  $0.22\text{ }\mu\text{m}$ ) and analysed without diluting by HPLC injecting  $5\text{ }\mu\text{l}$  of the sample in an Agilent 1260 Infinity Quaternary HPLC equipped with both diode array and refractive index detectors, an Agilent Hi-Plex H column  $7.7 \times 300\text{ mm}$ ,  $8\text{ }\mu\text{m}$  with a PL Hi-Plex H guard column  $50 \times 7.7\text{ mm}$ , employing a 5 mM aqueous solution of sulphuric acid as isocratic mobile phase, with a flow rate of  $0.6\text{ cm}^3\cdot\text{min}^{-1}$  and column temperature held at  $65^\circ\text{C}$ . A vacuum degasser is integrated into the pump module to avoid bubble formation in the mobile phase. The column temperature was maintained at  $65^\circ\text{C}$  for the analysis for a set run time of 60 min. Response factors calculated from multi-point calibration curves were used to assess the yield of possible products present in the hexoses dehydration reactions. **Table 2.2** displays the list of compounds that were calibrated in HPLC. Also, their calibration curves are shown on **Figure 2.10**, and a typical chromatogram from HPLC for the dehydration of glucose and fructose is given in **Figure 2.11**.

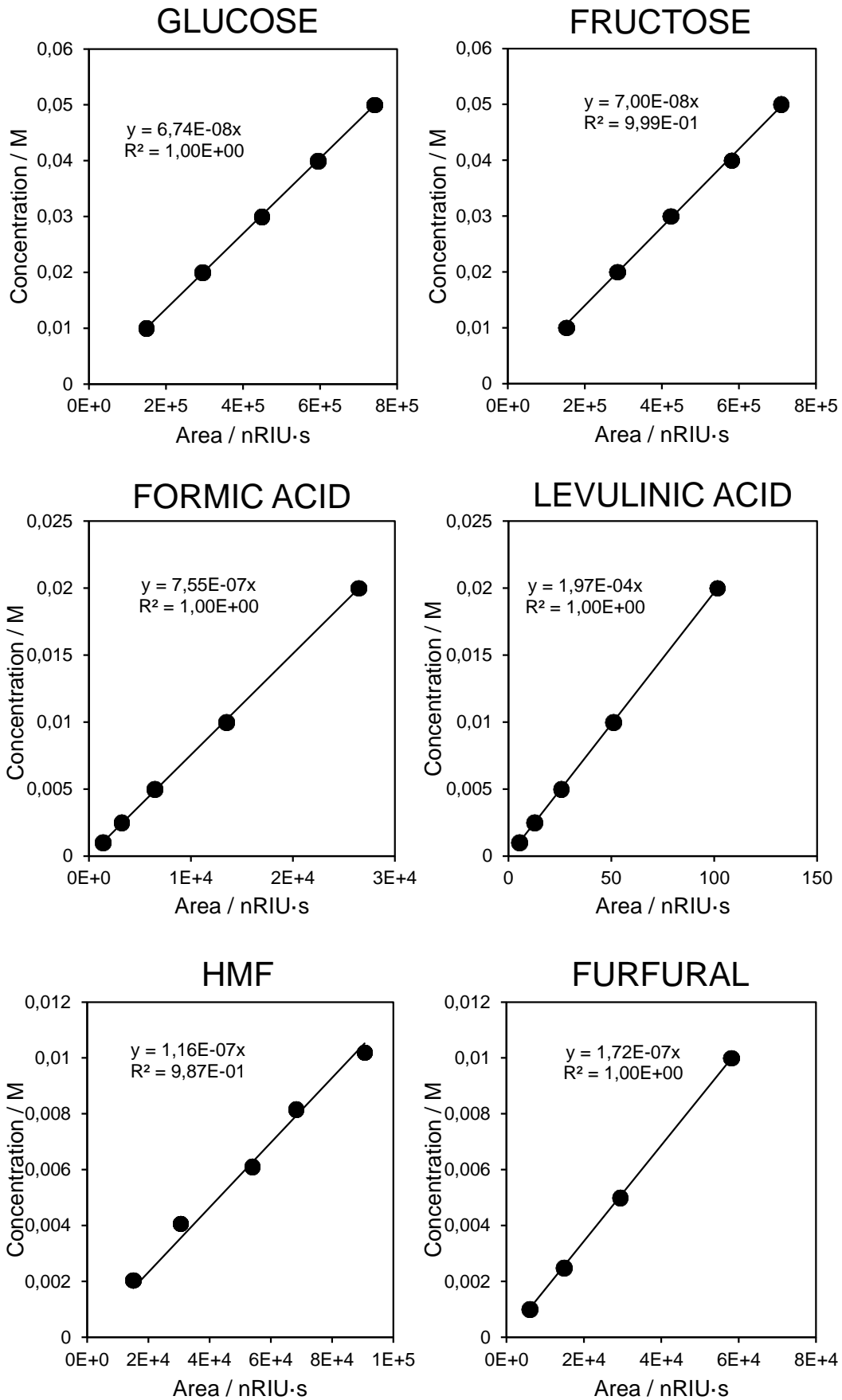


**Figure 2.10** Calibration of reactants and potential products in HPLC

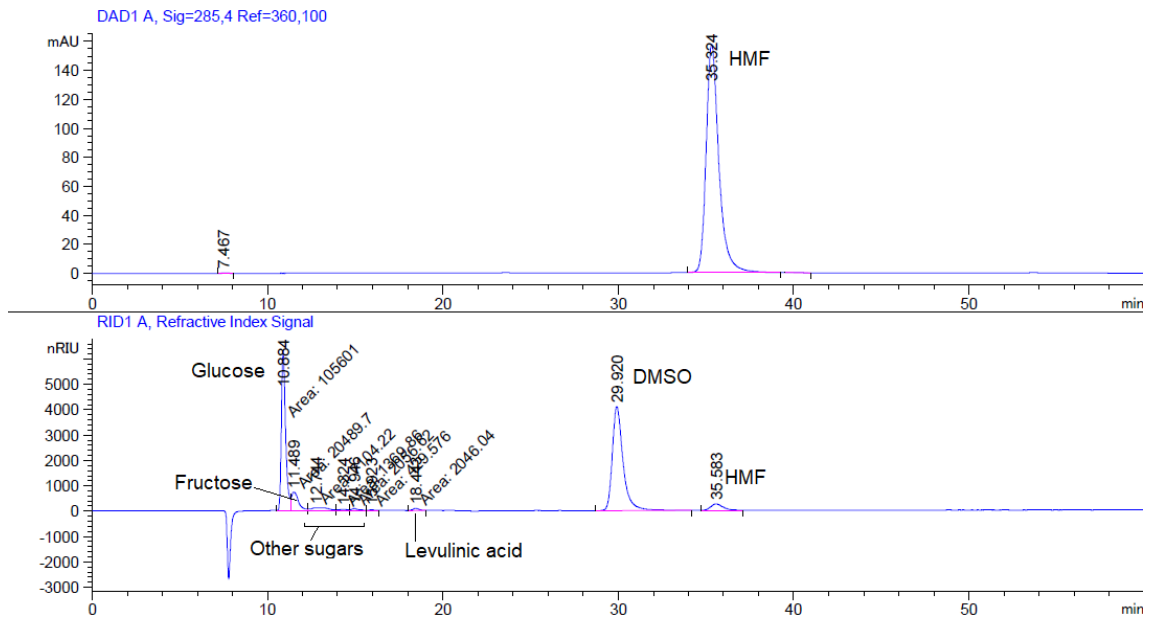


**Figure 2.11** An example of typical HPLC chromatograms for glucose dehydration in water from DA detector (top) and RI detector (bottom)

Several small signals are detected at retention times between 12 and 16 minutes, corresponding to unidentified products which will be labelled as “other sugars”, since they fall in the region of sugar degradation products. Identification of these products is not included in this thesis, and can be subject of study in future work.

**Table 2.2** List of compounds calibrated in HPLC

| Compound       | Detector | Retention time / min | Response factor / M(nRIU-s) |
|----------------|----------|----------------------|-----------------------------|
| Glucose        | RI       | 10.9                 | 6.74E-08                    |
| Fructose       | RI       | 11.6                 | 7.00E-08                    |
| Formic acid    | RI       | 15.9                 | 7.55E-07                    |
| DMSO           | RI       | 30.0                 | -                           |
| Levulinic acid | DA       | 18.1                 | 1.97E-04                    |
| HMF            | DA       | 34.9                 | 1.16E-08                    |
| Furfural       | DA       | 52.9                 | 1.72E-07                    |

Glucose conversion ( $X_G$ ), 5-HMF yield ( $Y_{HMF}$ ), selectivity to HMF ( $S_{HMF}$ ), fructose yield ( $Y_F$ ) and selectivity to fructose ( $S_F$ ) were calculated according to:

$$a) X_G = \frac{n_{G_0} - n_G}{n_{G_0}}$$

$$b) Y_{HMF} = \frac{n_{HMF}}{n_{G_0}} * 100$$

$$c) S_{HMF} = \frac{Y_{HMF}}{X_G} * 100$$

$$d) Y_F = \frac{n_F}{n_{G_0}} * 100$$

$$e) S_F = \frac{Y_F}{X_G} * 100$$

**Equation 2.15** Calculation of a) Glucose conversion, b) 5-HMF yield, c) selectivity to HMF, d) fructose yield and e) selectivity to fructose

Where  $n_{G_0}$  is the initial moles of glucose,  $n_G$ ,  $n_F$  and  $n_{HMF}$  are the moles of glucose, fructose and 5-HMF respectively at a specific reaction time. Initial rate of reactions were determined from the initial linear part of the conversion profile ( $t < 1$  h). Turnover frequency (TOF) was obtained by normalizing the rate of reaction with the mass of catalyst as well as the acid site concentration determined from propylamine adsorption.

## 2.4 References

- [1] D. Zhao, Q. Huo, J. Feng, B.F. Chmelka, G.D. Stucky, *Journal of the American Chemical Society* 120 (1998) 6024-6036.
- [2] N. Uekawa, T. Kudo, F. Mori, Y.J. Wu, K. Takegawa, *Journal of Colloid and Interface science* 264 (2003) 378-384.
- [3] A. Osatiashtiani, A.F. Lee, D.R. Brown, J.A. Melero, G. Morales, K. Wilson, *Catalysis Science & Technology* 4 (2014) 333-342.
- [4] T.J. Bruno, P.D. Svoronos, *CRC handbook of basic tables for chemical analysis*, CRC press, 2003.
- [5] M. Brennan, *A practical approach to quantitative metal analysis of organic matrices*, John Wiley & Sons, 2008.
- [6] J. Lynch, *Physico-chemical analysis of industrial catalysts: a practical guide to characterisation*, in: E. Technip (Ed.), 2003.
- [7] M. Nete, W. Purcell, E. Snyders, J.T. Nel, *South African Journal of Chemistry* 63 (2010) 130-134.
- [8] I. Chorkendorff, J.W. Niemantsverdriet, *Concepts of modern catalysis and kinetics*, John Wiley & Sons, 2006.
- [9] C.S. Fadley, *Journal of Electron Spectroscopy and Related Phenomena* 178–179 (2010) 2-32.

- [10] C.D. Wagner, G. Muilenberg, Handbook of X-ray photoelectron spectroscopy, Perkin-Elmer, 1979.
- [11] J.I. Gersten, F.W. Smith, The physics and chemistry of materials, Wiley New York, 2001.
- [12] D. Briggs, Surface Analysis by Auger and X-ray Photoelectron Spectroscopy, Cromwell Press, Trowbridge (2003) 37-38.
- [13] J.W. Niemantsverdriet, Spectroscopy in catalysis, John Wiley & Sons, 2007.
- [14] G. Ertl, H. Knözinger, F. Schüth, J. Weitkamp, Handbook of Heterogeneous Catalysis, Wiley-VCH, 2008.
- [15] A.A. Bunaciu, E.g. Udriștioiu, H.Y. Aboul-Enein, Critical Reviews in Analytical Chemistry 45 (2015) 289-299.
- [16] P. Atkins, J. De Paula, Oxford University Press, Oxford (2006).
- [17] M. Birkholz, Thin Film Analysis by X-Ray Scattering, Wiley-VCH Verlag GmbH & Co. KGaA, 2006, pp. 1-40.
- [18] W.T. JIANG, D. Peacor, P. Arkai, M. Tóth, J. Kim, Journal of Metamorphic Geology 15 (1997) 267-281.
- [19] R.P.H. Gasser, G. Ehrlich, An introduction to chemisorption and catalysis by metals, AIP, 1987.
- [20] R. Pierotti, J. Rouquerol, Pure Appl. Chem 57 (1985) 603-619.
- [21] K.F. Purcell, J.C. Kotz, Inorganic Chemistry, Saunders, 1977.
- [22] S. Brunauer, P.H. Emmett, E. Teller, Journal of the American Chemical Society 60 (1938) 309-319.
- [23] J.L. Figueiredo, M.M. Pereira, J. Faria, Catalysis from Theory to Application, Imprensa da Univ. de Coimbra, 2008.
- [24] F. Rouquerol, J. Rouquerol, K. Sing, Adsorption by Powders and Porous Solids, Academic Press, London, 1999, pp. 165-189.
- [25] P. Webb, C. Orr, Analytical methods in fine particle technology, Micromeritics Instrument Corporation., 1997.
- [26] K.K. Aligizaki, Pore structure of cement-based materials: testing, interpretation and requirements, CRC Press, 2005.
- [27] B.C. Lippens, J.H. de Boer, Journal of Catalysis 4 (1965) 319-323.
- [28] S.L. Flegler, J.W. Heckman Jr, K.L. Klomparens, Oxford University Press(UK), 1993 (1993) 225.
- [29] E. Rochow, An introduction to microscopy by means of light, electrons, x-rays, or ultrasound, Springer Science & Business Media, 2012.
- [30] Ternopil State Medical University, Microscopic equipment.

- [31] M. Kaurav, Engineering chemistry with laboratory experiments, PHI Learning Pvt. Ltd., 2011.
- [32] O. Kresnawahjuesa, R.J. Gorte, D. De Oliveira, L. Lau, Catalysis letters 82 (2002) 155-160.
- [33] Z.M. Khoshhesab, Infrared Spectroscopy - Materials Science, Engineering and Technology, InTech, 2012.
- [34] M.P. Fuller, P.R. Griffiths, Analytical Chemistry 50 (1978) 1906-1910.
- [35] D.F. Shriver, Shriver & Atkins' Inorganic Chemistry, Oxford University Press, 2006.
- [36] M.M. Herron, S. Herron, A. CHARSKY, R. Akkurt, Diffuse reflectance infrared fourier transform spectroscopy for characterization of earth materials, Google Patents, 2013.
- [37] R.L. Richardson, S.W. Benson, The Journal of Physical Chemistry 61 (1957) 405-411.
- [38] E.P. Parry, Journal of Catalysis 2 (1963) 371-379.
- [39] D.L. Perry, Applications of analytical techniques to the characterization of materials, Springer, 1991.
- [40] X. Ding, L. De Rogatis, E. Vesselli, A. Baraldi, G. Comelli, R. Rosei, L. Savio, L. Vattuone, M. Rocca, P. Fornasiero, Physical Review B 76 (2007) 195425.
- [41] R. Davis, J. Walsh, C. Murn, G. Thornton, V. Dhanak, K. Prince, Surface science 298 (1993) L196-L202.
- [42] U. Burghaus, Progress in Surface Science 89 (2014) 161-217.
- [43] G. Gauglitz, T. Vo-Dinh, Handbook of spectroscopy, John Wiley & Sons, 2006.

## ***Chapter 3***

### ***Characterization of niobic acid nanoparticle catalysts***

### 3.1 Introduction

Niobium pentoxide has been developed as a widely used material in the production of capacitors[1] and optical glass[2] due to its electrical and dielectric properties[3]. Due to its thermal stability, most studies involving niobium oxide focus on using it as a support for other materials which would act as the active phase for catalysed reactions[4] and as surface modifiers[5], using it together with other components. Hydrated niobium oxide ( $\text{Nb}_2\text{O}_5 \cdot n\text{H}_2\text{O}$ ), also known as niobic acid, has attracted attention from a catalysis point of view due to its high surface acidity and the ability to maintain it in the presence of water[6], classifying it as a water-tolerant solid acid[7] suitable for any sort of reactions involving, but not exclusively, the presence of water, such as hydrolysis, dehydration of alcohols, hydration, esterification, condensation, etc., and some reviews on these applications have been published[8, 9]. However, thermal treatments play an important role in the physicochemical properties of niobium oxide as a solid acid catalyst, inducing the loss of its strong acid character following heat treatment over  $500^\circ\text{C}$  and decreasing its reactivity substantially[10].

#### 3.1.1 Crystallinity

The polymorphous transformations of niobium pentoxide subjected to thermal treatment are difficult to assess, as it is proven by the contradictory results reported by different authors[11], with an array of up to 20 different modifications of niobium pentoxide. The most commonly observed forms of niobium pentoxide were named by Schäfer *et al.*[12], and are defined as an initial amorphous form which crystallises to a low temperature form at around  $300\text{-}500^\circ\text{C}$  denoted as pseudo-hexagonal (TT- $\text{Nb}_2\text{O}_5$ ), a medium temperature form at  $700\text{-}800^\circ\text{C}$  corresponding to orthorhombic niobium oxide (T- $\text{Nb}_2\text{O}_5$ ) and a high temperature form at  $1000^\circ\text{C}$  related to monoclinic niobium oxide (H- $\text{Nb}_2\text{O}_5$ ). The named phase change temperatures are only indicative, since they can vary depending on starting material, level of impurity or heating procedure[13]. Although niobic acid composition is uncertain because of its inconsistent water content, Sen *et al.* estimated the empirical composition of the material dried at  $150^\circ\text{C}$  to be  $3\text{Nb}_2\text{O}_5 \cdot 4\text{H}_2\text{O}$ , which may be written as  $\text{H}_8\text{Nb}_6\text{O}_{19}$ . The acid  $\text{H}_8\text{Nb}_6\text{O}_{19}$  is extensively hydrated due to the uptake of water molecules held by H-bonding through the oxygen atoms. These water molecules are not strongly held and on drying at  $150^\circ\text{C}$  they are lost to produce  $\text{Nb}_2\text{O}_5$ . [14]

**Figure 3.1** shows the basic structure of amorphous niobic acid (A) reported by Sen *et al.*[14] formed by a central oxygen atom octahedrally surrounded by six niobium atoms,

each niobium being coordinated to six oxygen atoms. This structure can be depicted by the presence of the eight protons above eight triangular faces of the octahedron formed by six niobium atoms. These hydrogens, which provide the Brønsted acidity to the niobic acid, are embedded in the electron cloud produced by three bridging oxygen, three terminal oxygens and the central oxygen atom, making them difficult to remove at low temperatures. Water molecules are also shown attached to the peripheral oxygen atoms of  $H_8Nb_6O_{19}$  through hydrogen bonding. **Figure 3.1** also shows the unit cells for the pseudo-hexagonal (TT) and orthorhombic (T) structures of niobium oxide, modified from [15]. The TT phase contains half of the formula equivalent, with a constitutional defect of an oxygen atom per unit cell. Each Nb atom is at the centre of four, five or six oxygen atoms on the ab-plane and Nb-O-Nb-O chain structure is along the c-axis. Thus, the oxygen deficiency leads to the distortion of these polyhedra. In the T phase each Nb atom is surrounded by six or seven oxygen atoms, making distorted octahedra or pentagonal bipyramids. These polyhedra are connected by edge- or corner-sharing in the ab-plane and by corner-sharing along the c-axis[15].

Niobic acid possesses highly distorted  $NbO_6$  octahedra and slightly distorted  $NbO_6$ ,  $NbO_7$ , and  $NbO_8$  as structural units. The pseudohexagonal phase possesses a constitutional defect of an oxygen atom per unit cell, and forms tetragonal and pentagonal bipyramids with six or seven oxygen atoms coordinated to the Nb atom. The orthorhombic phase forms distorted tetragonal or pentagonal bipyramids with six or seven oxygen atoms coordinated to the Nb atom. These polyhedra are joined by corner or edge sharing in the ab plane and by corner sharing along the c axis[16].

Moreover, niobia species have been studied on different oxide supports, such as  $Al_2O_3$ ,  $TiO_2$ ,  $ZrO_2$ , and  $SiO_2$ , revealing different species depending on the niobia coverage. Therefore, 4-fold coordinated surface  $NbO_4$  species appear at very low surface coverages, 5-fold coordinated surface  $NbO_5$  species present at intermediate surface coverages, and 6-fold coordinated surface  $NbO_6$  found at high surface coverages. On silica, only  $NbO_4$  is present because high surface coverages cannot be achieved on this support due to the low number and reactivity of the silica surface hydroxyls.[8]



Aston University

Illustration removed for copyright restrictions



Aston University

Illustration removed for copyright restrictions



Aston University

Illustration removed for copyright restrictions

**Figure 3.1** Basic unit cell of niobic acid in amorphous (A), hexagonal (T) and orthorhombic (TT) form[14]

Direct synthesis of mesoporous Nb<sub>2</sub>O<sub>5</sub>/SiO<sub>2</sub> has been reported using different techniques. One of them is conventional sol–gel method which generally uses niobium (V) ethoxide in the presence of an organic solvent, such as ethanol[17] or hexane[18]. The second common method of preparing niobium/silica material is co-precipitation, in which niobium (Ammonium niobium oxalate complex[19], niobium (V) chloride[20] or niobium tartrate[21]) and silicon precursors (TEOS) are precipitated simultaneously in a neutral environment. The last explored method to graft Nb<sub>2</sub>O<sub>5</sub> on silica supports is using incipient wetness impregnation, which generally uses niobium (V) ethoxide[22], niobium oxalate[23] or niobium (V) chloride[24] precursor in an anhydrous organic solvent (e.g. hexane, oxalic acid or isopropanol) with the concentration of the precursor varied to obtain materials with different niobium loadings. Nowak[25] studied the effect of these different precursors and concluded that the highest activity was observed in the case when niobium chloride was used as a source of niobium.

In this thesis, supported materials are prepared using niobium (V) chloride as a precursor, and its incorporation onto SBA-15, employed as a silica support, is made through the peptization of a niobic acid sol with H<sub>2</sub>O<sub>2</sub> as described in **Chapter 2**. This preparation method combining the peptization procedure with the impregnation on a support has not been reported, and it allows the incorporation of small niobia nanoparticles onto the silica support.

### 3.1.2 Acidity

Amorphous niobic acid shows strong Brønsted acidity due to the proton generation from water molecule on exposed Nb<sup>5+</sup>[26]. It exhibits a high acid strength (H<sub>0</sub> = -5.6), equal to ca. 70% H<sub>2</sub>SO<sub>4</sub>[27]. Nb-O bonds belonging to the distorted polyhedrons of the niobic acid structure are highly polarized, so that a part of the surface OH groups function as Brønsted acid sites[28], while the highly distorted NbO<sub>6</sub> octahedra function as Lewis acid sites[29]. However, this high acid strength has been reported to decrease intensely when niobic acid is subjected to thermal treatment. Several groups have reported the evolution of acid strength with calcination temperature, and established a relationship between the loss of acidity and the worsening of the catalytic performance of the materials. This acidity decrease is associated with a subsequent decrease in surface area, the dehydration of the niobic acid surface and the transformation of the amorphous phase of niobic acid to crystalline niobium oxide [30-32]. Instead, variable surface Lewis acidities due to the exposed cations in proximity of oxygen vacant sites on the powder surface become more important at elevated temperature[33].

Numerous catalysts possessing Lewis acid sites such as zeolites and other metal oxides have been regarded as inactive sites for reactions in water, due to the formation of Lewis acid-base adducts by the coordination of water to the Lewis acid sites. However, niobic acid has been categorised as a water-tolerant solid acid, meaning that it is able to retain its acidity in aqueous solutions and catalyse reactions involving Lewis acidity such as the isomerization of glucose and the allylation of benzaldehyde [34]. Thus, due to the remarkable acidity present in amorphous niobic acid and its categorization as water-tolerant solid acid, this material can be used as effective catalyst in aqueous media for esterification, olefin hydration and alcohol dehydration reactions.

The effects on acidity of niobia on different supports were studied by Datka *et al.*[35] Lewis acidity was found in all of the supported niobium oxide systems, while Brønsted acid sites were only detected in niobium supported on alumina and silica. The addition of niobia to alumina was found to increase the acidity of the alumina support[36]. The formation of Si-O-Nb bonds via reaction of the NbCl<sub>5</sub> precursor with the surface hydroxyls of a high surface area mesoporous SBA-15 support should give rise to a highly dispersed form of NbO<sub>4</sub> as observed on MCM-41[37]. Moreover, silica has been reported to play an important role in stabilizing dispersed niobium against particle sintering, even after aggressive calcination treatments, which leads to an improved preservation of active sites with thermal treatment[24].

This chapter demonstrates that the peroxy niobic acid catalysts prepared by newly reported peptization method produce materials with high surface area and remarkable Lewis and Brønsted acid character. Herein, the structural and acidic changes induced by thermal treatment in the bulk materials are exposed. Moreover, the precipitated niobic acid can be dispersed onto a mesoporous silica support with the goal to enhance its textural properties and therefore its catalytic behaviour.

## **3.2 Results and discussion**

### **3.2.1 Characterization of bulk niobic acid catalysts**

#### **3.2.1.1 Surface and bulk compositional analysis**

ICP and XPS analyses were employed to determine the bulk and surface niobium content respectively present in the bulk niobia catalysts pre-calcined at temperatures in the range 80-700°C. **Figure 3.2** shows the spectra of Nb 3d (left) and O 1s (right) of the precipitated niobic acid (PNA) catalysts pre-calcined at different temperatures,

where the presence of a doublet is observed at binding energy values of 207.05 and 209.8 eV, corresponding to Nb 3d<sub>5/2</sub> and Nb 3d<sub>3/2</sub> respectively, according to the values reported in the NIST database[38], which are associated with an oxidation state of Nb<sup>5+</sup> i.e., stoichiometric Nb<sub>2</sub>O<sub>5</sub> [39]. The Nb 3d<sub>3/2</sub> peak for each species is constrained to be at a fixed value of 2.75 eV above the Nb 3d<sub>5/2</sub> peak, corresponding to the spin-orbit splitting, while the intensity ratio of the Nb 3d<sub>5/2</sub> and Nb 3d<sub>3/2</sub> peaks is fixed to 3 : 2.

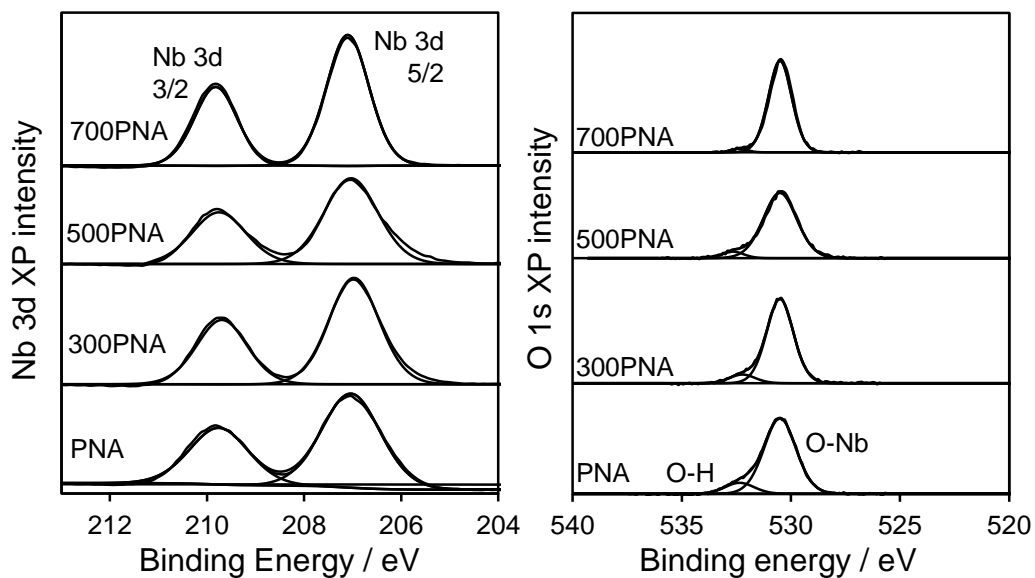


**Figure 3.2** XPS of the Nb 3d (left) and O 1s (right) regions for the PNA materials calcined at different temperatures

The O 1s spectrum exhibits a double peak at 530.5 eV and 532.4 eV. The most intensive peak at 530.5 eV is due to the oxygen species O<sup>2-</sup> in niobium oxide, while the smaller peak at 532.4 eV falls in the hydroxylated region, thus belonging to Nb-O bonds characteristic of Brønsted acidity[40]. The intensity of the smaller peak at higher binding energy decreases with increasing calcination temperature, consistent with the loss of surface hydroxyls which contribute to the Brønsted acidity of the materials. No binding energy shifts were found for either the niobium or the oxygen signals, indicating that there are no changes in the oxidation state of the materials or the local chemical and physical environment of the investigated elements. Niobium (V) chloride was used as a precursor for the synthesis of catalysts and since chlorine can act as a catalyst poison, its presence was investigated by XPS and no traces of chlorine ions were found.

**Table 3.1** displays the values for the bulk niobium content from ICP and surface niobium content from XPS. Nb content obtained from ICP reveals a constant Nb content around 61 wt% along the PNA series, similar to the Nb content found by Carlini

et al.[41] in a commercial niobic acid sample. **Figure 3.3** exhibits the O:Nb atomic ratio, which was found to be an average of 2.1 up to calcination temperatures of 500°C. For the 700PNA sample, the ratio decreased to 1.7 due to oxygen atoms lost from the structure creating defective voids in the niobium oxide matrix[15, 42].

**Table 3.1** Surface and bulk compositional analysis of as-prepared niobic acid

| Catalyst | Bulk Nb content <sup>a</sup> / wt% | Surface content <sup>b</sup> / wt% |       | Surface content <sup>b</sup> / at% |       |
|----------|------------------------------------|------------------------------------|-------|------------------------------------|-------|
|          |                                    | Nb±0.5                             | O±0.2 | Nb±0.2                             | O±0.5 |
| PNA      | 61±0.2                             | 74                                 | 26    | 32                                 | 68    |
| 300PNA   | 60±0.2                             | 74                                 | 26    | 33                                 | 67    |
| 500PNA   | 61±0.2                             | 73                                 | 27    | 32                                 | 68    |
| 700PNA   | 61±0.2                             | 78                                 | 22    | 37                                 | 63    |

From <sup>a</sup>ICP; <sup>b</sup>XPS

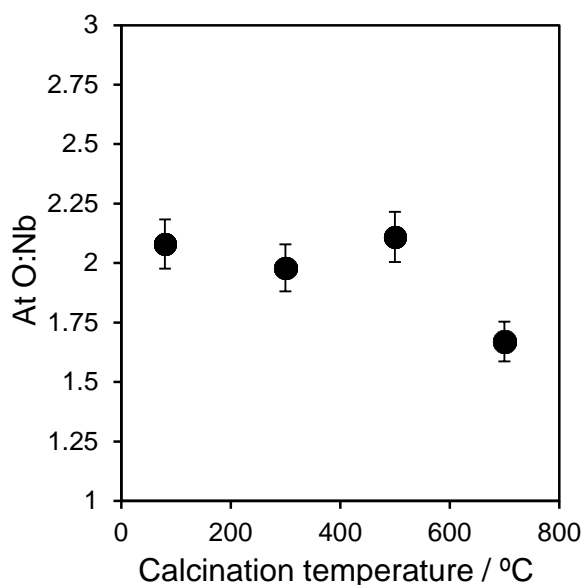


**Figure 3.3** Oxygen-niobium atomic ratio measured by XPS

### 3.2.1.2 Textural properties

Niobic acid is an amorphous material with BET surface area around 150 to 200 m<sup>2</sup>·g<sup>-1</sup> and average pore volume of 0.15 cm<sup>3</sup>·g<sup>-1</sup>[43]. **Figure 3.4** displays the porosimetry results of bulk niobic acid samples calcined at different temperatures regarding their adsorption-desorption isotherms and the pore size distribution. The plots are presented without offset, so that the different position of the isotherms represents the actual nitrogen adsorbed by the catalysts. Textural properties of bulk PNA materials are

summarised in **Table 3.2**. A decrease in the adsorbed volume of N<sub>2</sub> indicates a progressive decrease of the surface area of the materials as the synthesis calcination temperature increases. All prepared catalysts exhibited type IV hysteresis loops associated with mesoporous materials. However, the PNA samples were not expected to possess well-defined, ordered mesopores since they were prepared without a structure directing agent, hence their mesoporosity is attributed to the presence of interparticle voids formed during niobia precipitation. Amorphous samples (PNA and 300PNA) show almost identical pore size distribution, indicating similar structural arrangement of the niobic acid. An increase in pore size distribution from 3.4nm to 6.6nm is observed for 500PNA, coincident with crystallization and sintering of the niobia particles as it is proved by XRD later on. The crystallite size increase provoked by the crystallization of the catalyst leads to larger particles and therefore to larger interparticle voids represented by that increase in pore size distribution.

**Table 3.2** Textural properties of PNA materials

| Catalyst | Surface area <sup>a</sup><br>/ m <sup>2</sup> ·g <sup>-1</sup> | Pore diameter <sup>b</sup><br>/ nm | Pore volume <sup>c</sup><br>/ cm <sup>3</sup> ·g <sup>-1</sup> |
|----------|--|------------------------------------|--|
| PNA      | 348  | 3.4                                | 0.33   |
| 300PNA   | 273  | 3.4                                | 0.27   |
| 500PNA   | 112  | 6.6                                | 0.20   |
| 700PNA   | 35   | N/A                                | N/A  |

<sup>a</sup>N<sub>2</sub> BET; <sup>b</sup>BJH desorption branch of isotherm; <sup>c</sup>recorded at P/P<sub>0</sub>=0.98

A linear decrease is observed in surface area and interparticle pore volume (**Figure 3.5**) due to niobia crystallization during calcination, dropping from 348 m<sup>2</sup>·g<sup>-1</sup> and 0.33 cm<sup>3</sup>·g<sup>-1</sup> for the fresh catalyst down to 35 m<sup>2</sup>·g<sup>-1</sup> and 0.11 cm<sup>3</sup>·g<sup>-1</sup> for the PNA calcined at 700°C. This surface area decrease with increasing calcination temperature has been previously observed in different studies. When commercial niobic acid was used in these studies [16, 31, 44], the reported surface area was considerably lower (around 200°C) than the values here reported, which are in the same range than those reported by Uekawa *et al.* [45] using the same preparation method, exposing the superior textural properties provided by the peroxo sol-gel synthesis method. No microporosity was observed in either of the samples.

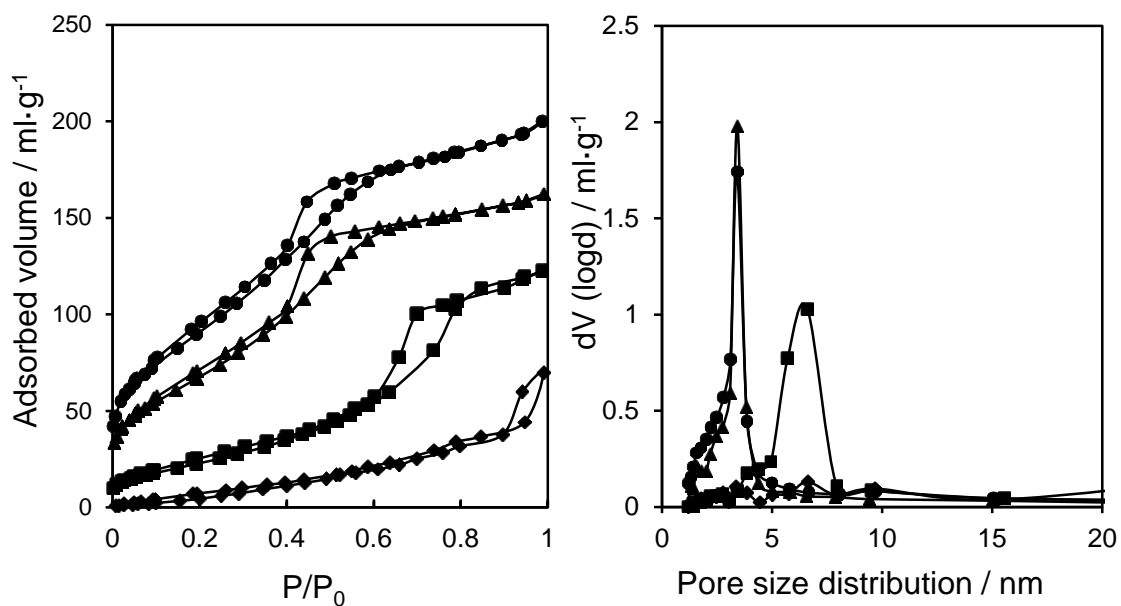


**Figure 3.4** N<sub>2</sub> porosimetry isotherms (left) and pore size distribution (right) of: PNA (●), 300PNA (▲), 500PNA (■) and 700PNA (◆)

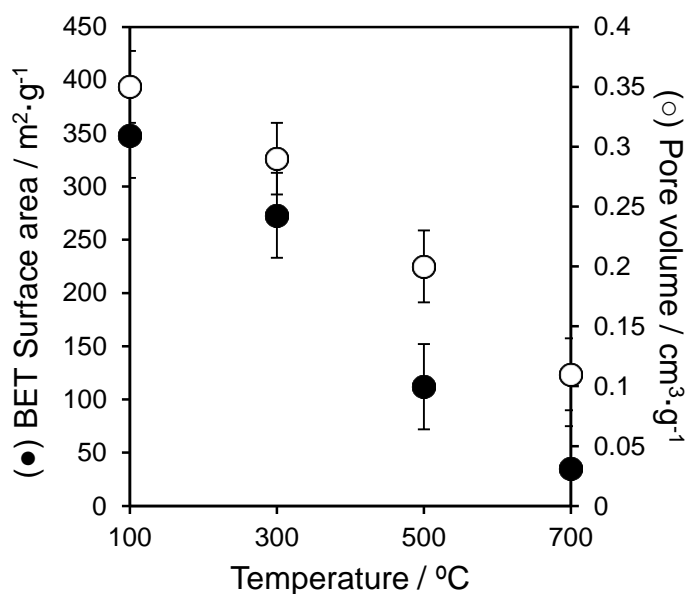


**Figure 3.5** Influence of calcination temperature in surface area (●) and pore volume (○)

### 3.2.1.3 Structure and morphology

Powder X-Ray diffraction and STEM were performed in order to assess the crystallinity and morphology of the bulk materials subjected to thermal treatment. TGA and DTA were performed to assess the mass loss, water content and structural change of the catalysts. Raman spectroscopy was performed to confirm the niobium oxide structure of the catalysts.

### 3.2.1.3.1 Powder X-Ray diffraction

The transformation of the amorphous niobic acid to a crystalline structure has been widely investigated and reported in several studies [13, 30, 46]. Herein, it was explored using *in situ* powder XRD between 100°C and 700°C (**Figure 3.6**). The absence of reflection signals below 400°C is indicative of amorphous niobium species. At temperatures above 500°C a crystalline hexagonal niobia phase emerged, proved by the appearance a set of reflection peaks, whose  $2\theta$  positions are tabulated on **Table 3.3** together with their respective Miller indexes and the interplanar distance ( $d$ ) calculated from Bragg's Law as shown in **Chapter 2**. These reflexions are characteristic of the space group  $P6/mmm$  of the hexagonal phase of  $Nb_2O_5$  structure [47].

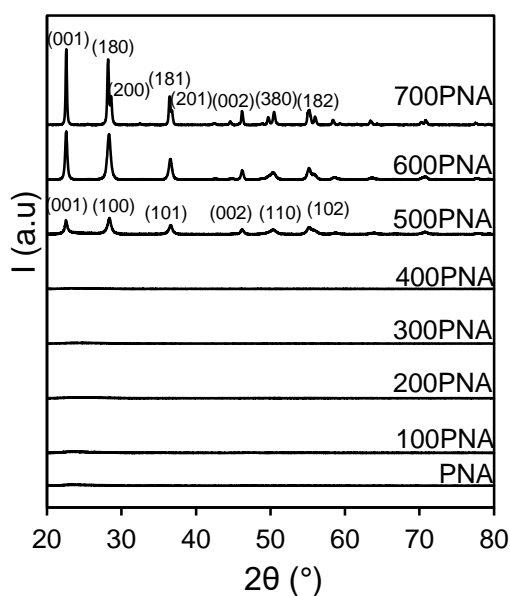


**Figure 3.6** *In situ* XRD patterns of PNA as a function of calcination temperature

**Table 3.3** XRD reflection positions, Miller index and interplanar distance of the hexagonal structure of PNA obtained from in-situ PNA analysis

| $2\theta / ^\circ$ | Miller index | $d / \text{Å} \pm 0.1$ |
|--------------------|--------------|------------------------|
| 22.6               | (0 0 1)      | 3.9                    |
| 28.3               | (1 0 0)      | 3.1                    |
| 37.0               | (1 0 1)      | 2.4                    |
| 46.2               | (0 0 2)      | 2.0                    |
| 50.4               | (1 1 0)      | 1.8                    |
| 64.0               | (1 0 2)      | 1.4                    |

When the niobium oxide starts the crystallization process the peaks are broad and the signal-to-noise ratio is low, which is indicative of small crystal size and/or poor crystallinity. Intensity of the reflexions increased at higher temperature, consistent with crystallite sintering. The hexagonal phase of niobium oxide is frequently reported in literature, and is believed to appear when the structure of amorphous niobic acid is stabilized by vacancies or impurities, such as OH<sup>-</sup> or Cl<sup>-</sup>, more specifically, it is reported that it can be obtained by heating niobic acid prepared from sulphate or chloride precursors to temperatures around 500°C, as is the case in the preparation route followed in this thesis[48]. A peak splitting at 700°C is observed due to the transition to orthorhombic niobia phase. This splitting is explained due to the occupancy of niobium atoms in separate but closely-spaced equivalent sites in the orthorhombic form, giving rise to the split peaks observed from certain reflections, and the ability of Nb to occupy either of these sites in the hexagonal form[13]. The 2θ positions of the orthorhombic reflexions are tabulated on **Table 3.4**, together with their Miller indexes and the interplanar distance (d) calculated from Bragg's Law as shown in **Chapter 2**. These reflexions belong to the space group *Pbam* of the orthorhombic phase of Nb<sub>2</sub>O<sub>5</sub> structure.

**Table 3.4** XRD reflection positions, Miller index and interplanar distance of the orthorhombic structure of PNA obtained from in-situ PNA analysis

| 2θ / ° | Miller index | d / Å ±0.1 |
|--------|--------------|------------|
| 22.6   | (0 0 1)      | 3.9        |
| 28.2   | (1 8 0)      | 3.2        |
| 28.6   | (2 0 0)      | 3.1        |
| 36.5   | (1 8 1)      | 2.5        |
| 36.8   | (2 0 1)      | 2.4        |
| 46.2   | (0 0 2)      | 2.0        |
| 50.5   | (3 8 0)      | 1.8        |
| 55.2   | (1 8 2)      | 1.7        |

The sintering of niobia particles and subsequent increase in crystallite size was probed by applying the Scherrer equation (See **Chapter 2**) on the (001), (100) and (101) diffraction peaks for the hexagonal phase and on the (001), (180), (200), (181) and (201) diffraction peaks for the orthorhombic phase. The average crystallite sizes of the samples were found to be 18, 20 and 42 nm for 500PNA, 600PNA and 700PNA respectively, which is in good agreement with the reported values of crystallite size observed in niobium oxides catalysts prepared with a chloride precursor in ammonia environment[49, 50]. The lattice parameters for the hexagonal and orthorhombic

structures were calculated according to the combination of the lattice distance and Bragg's Law equations displayed in **Chapter 2**. Thus, the hexagonal phase showed lattice parameters of  $a = 3.63 \text{ \AA}$  and  $c = 3.93 \text{ \AA}$  calculated from the reflexions (100) and (001) respectively, almost identical values to those found by Frevel and Rinn for their hexagonal phase of niobium oxide[51]. For the orthorhombic phase,  $a$ ,  $b$  and  $c$  parameters were calculated based on the reflexions (200), (180) and (001) respectively, and they were found to be  $a = 6.23 \text{ \AA}$ ,  $b = 25.29 \text{ \AA}$  and  $c = 3.93 \text{ \AA}$ , which are very similar values to those reported by K. Kato and S. Tamura[52] (COD no. 2106534) with unit-cell dimensions  $a = 6.17 \text{ \AA}$ ,  $b = 29.17 \text{ \AA}$  and  $c = 3.93 \text{ \AA}$ , whose structure is shown in **Figure 3.7**.



**Figure 3.7** Orthorhombic structure of  $\text{Nb}_2\text{O}_5$  [52]

### 3.2.1.3.2 Scanning transmission electron microscopy

STEM analysis was utilised to further control the crystalline structural change of niobic acid subjected to thermal treatment. The bright field images presented in **Figure 3.8** and **Figure 3.9** show the amorphous arrangement of niobic acid nanoparticles present on the PNA and 300PNA catalysts, in agreement with the XRD results, presenting a rough surface which contributes to the substantial surface area of these materials observed from the porosimetry results. Particle size distributions for both amorphous materials are very similar, with an average particle size of  $4.2 \pm 1.4 \text{ nm}$  and  $4.7 \pm 1.2 \text{ nm}$  for PNA and 300PNA respectively. However, niobia nanoparticles for these amorphous materials are not clearly visible in the obtained TEM pictures, so size measurements should be supported by other characterization techniques.

The image of 500PNA shows that better defined crystalline nanoparticles can be found after thermal treatment at  $500^\circ\text{C}$ , as it was discovered on XRD analysis, with particle

size averaging  $14.7 \pm 2.7$  nm, close to the 18 nm found using the Scherrer equation on different reflexions from XRD. At greater magnifications there is evidence of an interplanar spacing of  $2.4 \text{ \AA}$ , which coincides with the  $d$  value observed for the (101) reflexion for hexagonal phase from XRD. Further thermal treatment up to  $700^\circ\text{C}$  led to particles with higher degree of crystallization, which present visible interplanar spacing in two different directions. The measurement of the major one resulted in a value of  $25.5 \pm 2.7 \text{ \AA}$ , in agreement with the lattice parameter  $b$  obtained by XRD. The pattern with closer interplanar spaces resulted in a distance of  $3.1 \pm 0.2 \text{ \AA}$ , which correlates with the value of  $d$  obtained from the reflexion (180) from the orthorhombic XRD diffractogram. The size measurement of the crystallites observed in several TEM images led to a broad particle size distribution ranging between 40 and 110 nm, with an average of  $73 \pm 22 \text{ \AA}$ . This value almost doubles that obtained from XRD, which can be explained by the different analysis method of these two techniques. On one side, XRD calculates an average of total number of particles detectable by the instrument, while TEM calculations are based in a more reduced number of particles (50-70 particles in these measurements) that may not faithfully represent the real morphology of the sample. Also, particles measured from TEM could be formed by conjoined particles, giving an overestimation of the crystallite size.

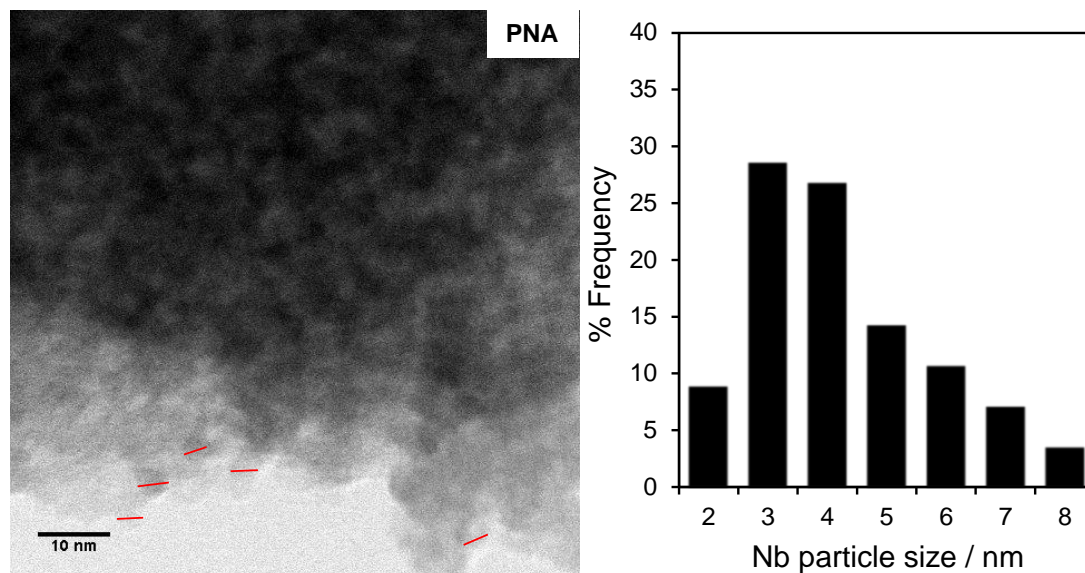


**Figure 3.8** STEM pictures of amorphous PNA and its particle size distribution at the right calculated from 60 particles

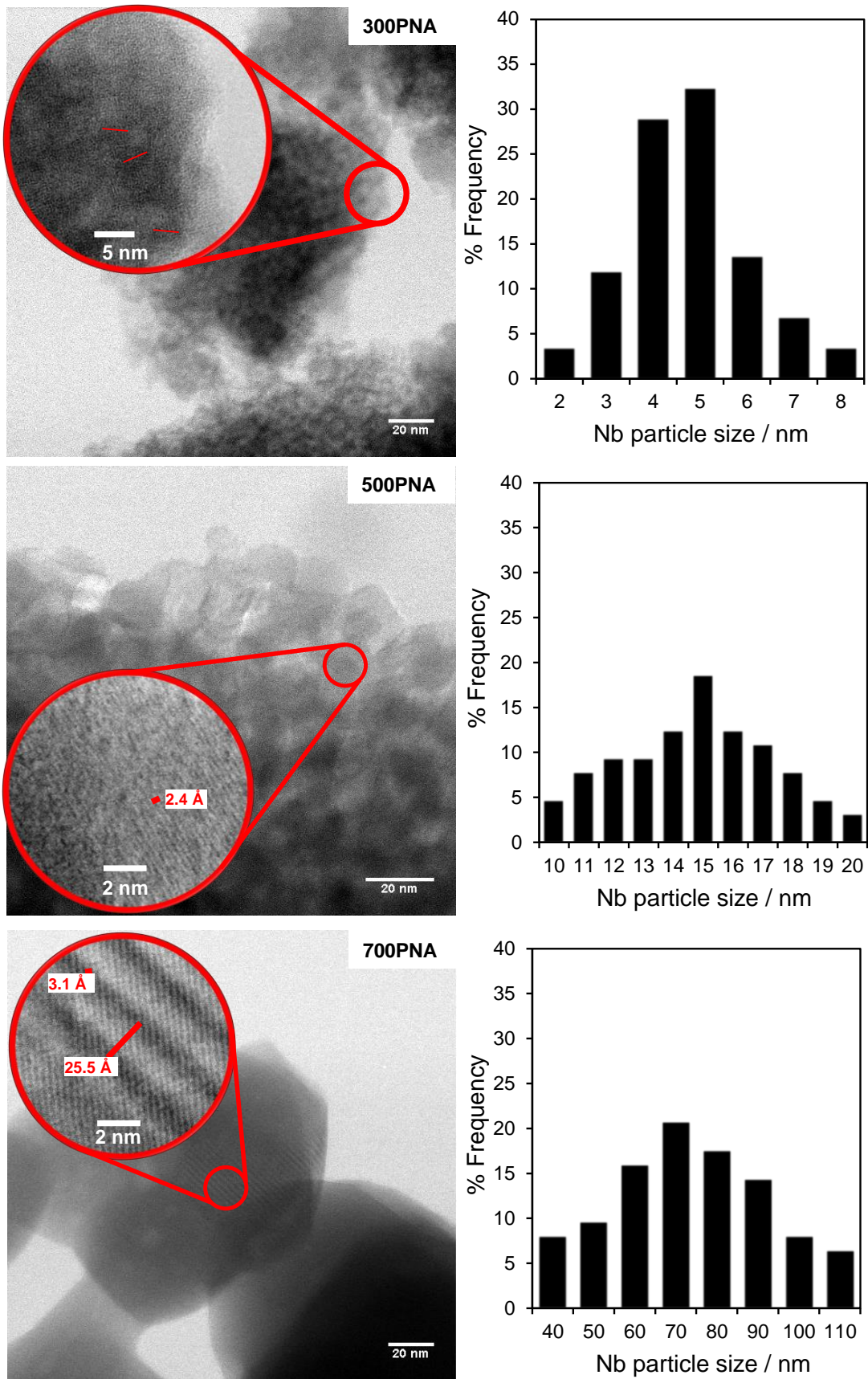


**Figure 3.9** STEM picture of 300PNA, 500PNA and 700PNA with their particle size distribution at the right calculated from 60-70 particles

### 3.2.1.3.3 Thermogravimetric analysis and differential thermal analysis

**Figure 3.10** exhibits the differential mass loss of the catalysts, where PNA shows two clear peaks at 70°C and 130°C related to desorption of physisorbed and structural water respectively which continues up to ~300°C. The rest of the catalysts show only one peak related to physisorbed water, suggesting that structural water was removed during calcination. PNA experiences a mass loss of 16.2% from which a 5.75% is attributed to physically adsorbed water and 10.25% to structural water. Mass loss observed in the rest of the series is 8.9%, 4.1% and 0.1% for 300PNA, 500PNA and 700PNA respectively. These weigh modifications related to the water loss of the catalysts correspond to the followings compositions:  $\text{Nb}_2\text{O}_5 \cdot 2.8\text{H}_2\text{O}$ ,  $\text{Nb}_2\text{O}_5 \cdot 1.5\text{H}_2\text{O}$ ,  $\text{Nb}_2\text{O}_5 \cdot 0.7\text{H}_2\text{O}$  and  $\text{Nb}_2\text{O}_5$  for PNA, 300PNA, 500PNA and 700PNA respectively. In the literature, the attempts to isolate hydrated niobium of constant compositions were unfruitful, demonstrating that the water content of hydrated niobium oxide has a non-adjustable nature, yielding different compositions in its thermal transformations[11].

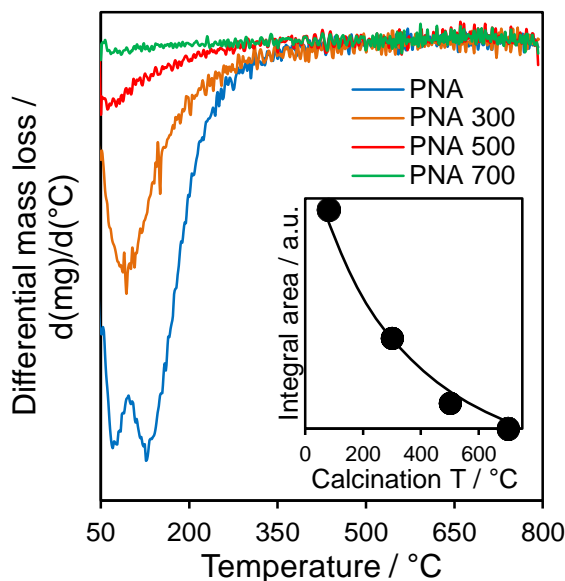


**Figure 3.10** Differential mass loss of PNA calcined at different temperatures under nitrogen flow; (inset) structural water integration area as function of calcination temperature

Nevertheless, the water content observed is within the same range that those values reported by several authors. Lebarbier *et al.*[31] observed 12% mass loss between 50-300°C for a commercial niobic acid. Xu *et al.*[53] synthesised niobic acid by a similar preparation method, and observed two weight loss stages accompanied by two endothermic peaks at ~98 and ~175°C in sequence, attributed to the loss of physically adsorbed water and a portion of the crystal lattice water respectively with a total weight

loss of 11% between 50-350°C. Ouqour *et al.*[54] reported lower values for catalysts prepared from NbCl<sub>5</sub> in aqueous solution with NH<sub>4</sub>OH, with 5.7% and 1.8% for samples calcined at 100°C and 300°C respectively. The higher value found in the literature was reported by Marin *et al.*[55] who reported 20% mass loss in the range 50-300°C in an as-prepared niobic acid obtained in a similar way than the mentioned above for Ouqour *et al.*

DTA curves (**Figure 3.11**) show an endothermic weight loss as niobic acid loses water up to 300°C. This was followed by a sharp exothermic peak at ~560°C, indicating that crystallization of amorphous niobic acid to an hexagonal structure has occurred[32]. This crystallization effect is observed in the amorphous catalysts (PNA, 300PNA) but not in 500PNA and 700PNA, since crystallization has already occurred, in accordance with XRD results.

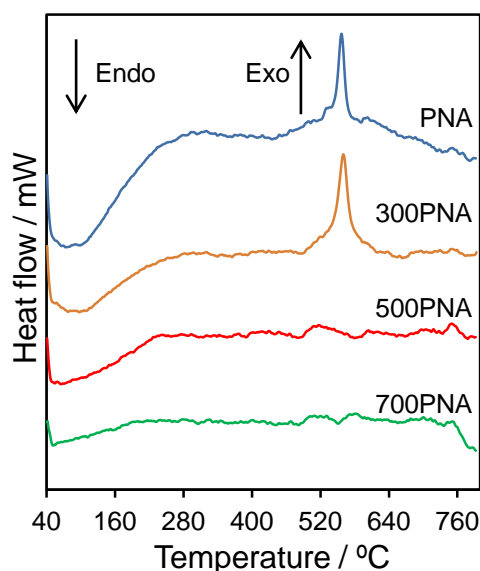


**Figure 3.11** DTA of PNA calcined at different temperatures

#### 3.2.1.3.4 Raman spectroscopy

Raman spectroscopy was performed to confirm the niobium oxide structure of the catalysts. Its importance lies in the fact that this technique is very sensitive to the structure and binding order of metal oxides, especially in the region corresponding to the metal-oxygen stretching modes[16]. **Figure 3.12** displays the Raman spectra of the PNA series. Samples calcined below 500 °C exhibit a broad band with a maximum at ~660 cm<sup>-1</sup>, characteristic of amorphous niobic acid and attributed to the symmetric stretching modes of slightly distorted NbO<sub>6</sub> octahedral, as well as NbO<sub>7</sub> and NbO<sub>8</sub>.

They also possess two weak shoulders around  $890\text{ cm}^{-1}$  and  $960\text{ cm}^{-1}$  which are assigned to the symmetric stretching mode of surface Nb=O present in highly distorted NbO<sub>6</sub> octahedral[30, 56] and NbO<sub>4</sub> tetrahedral respectively. For temperatures over 500 °C the broad band sharpens and its maximum shifts to  $\sim 690\text{ cm}^{-1}$  as a result of the transformation of amorphous niobic acid to crystalline hexagonal niobium oxide[57]. In parallel, two bands at  $\sim 230$  and  $\sim 310\text{ cm}^{-1}$  attributed to the bending modes of the Nb-O-Nb bond were detected[16, 58]. It has been reported that NbO<sub>4</sub> tetrahedral and highly distorted NbO<sub>6</sub> octahedral sites possess Nb=O bonds which correspond to the Lewis acid sites, whereas slightly distorted octahedral as well as NbO<sub>7</sub> and NbO<sub>8</sub> sites only possess Nb-O bonds and are associated to Brønsted acid sites[59].

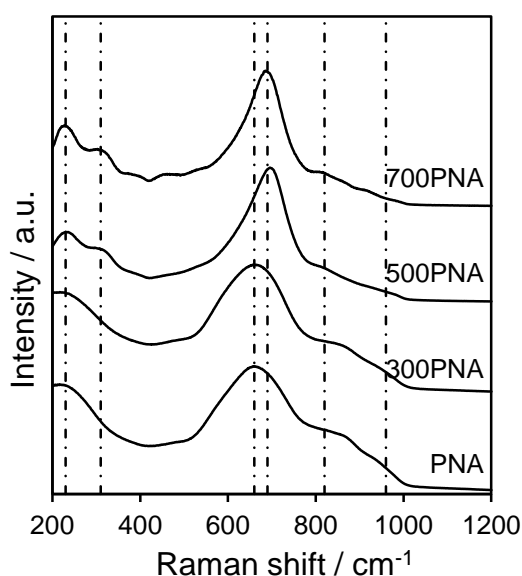


**Figure 3.12** Raman spectra of thermally treated PNA

#### 3.2.1.4 Acidity measurement

Surface acidity was probed by both pyridine and propylamine adsorption. The nature of acid sites in the supported materials was first examined through DRIFTS following pyridine treatment, and propylamine adsorption was used for the intrinsic acid site measurement of these catalysts.

##### 3.2.1.4.1 Diffuse reflection infrared Fourier transform spectroscopy (DRIFTS) and in situ pyridine chemisorption

Niobic acid is known to exhibit a high surface acidity, presenting both Lewis and Brønsted acid sites [57, 60]. Brønsted acidity arises from the distorted NbO<sub>6</sub> octahedral

comprising its structure, so that a part of the surface OH groups function as Brønsted acid sites, while NbO<sub>4</sub> tetrahedral provide the Lewis acidity [34, 55] as shown in **Figure 3.13**.

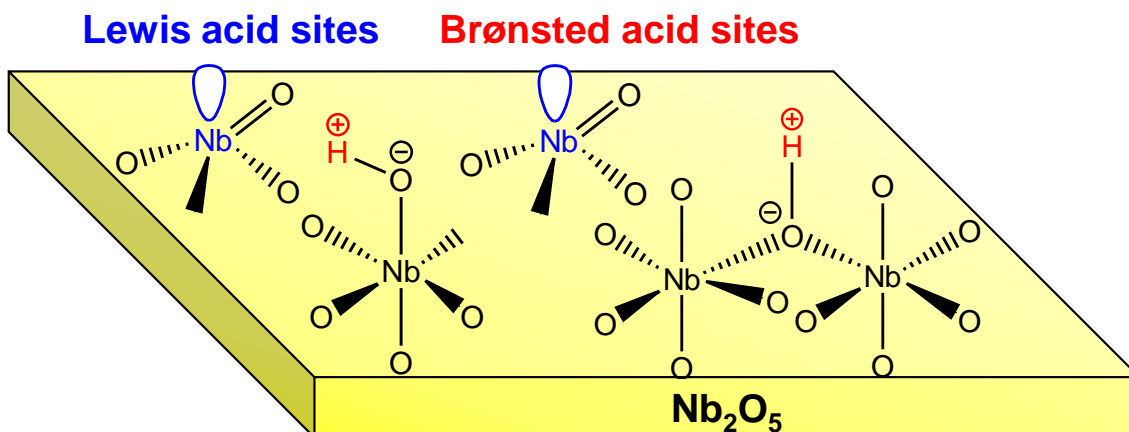


**Figure 3.13** Representative structure of the Lewis and Brønsted acid sites on niobic acid catalysts

The nature of acid sites in the PNA materials was examined through DRIFTS following pyridine treatment (**Figure 3.14** left). Vibrational bands attributable to Lewis acid sites were observed at 1444 and 1607 cm<sup>-1</sup>, together with a 1540 cm<sup>-1</sup> band characteristic of a pyridinium ion coordinated to Brønsted sites and a band at 1487 cm<sup>-1</sup> which is common to both Lewis and Brønsted acid sites[61, 62]. The intensity of the bands at 1444 cm<sup>-1</sup> and 1540 cm<sup>-1</sup> related to Lewis and Brønsted acid sites respectively, decreases with increasing calcination temperature due to the loss of superficial water and the crystallization of amorphous niobic acid into niobium oxide, which is in good agreement with the results previously reported by Moraes[44] and Lebarbier[31]. **Figure 3.14** (right) shows the relative B/L acid character (determined from the 1444 cm<sup>-1</sup> and 1540 cm<sup>-1</sup> peak areas). A monotonic decrease in Brønsted acidity with calcination temperature is observed, which can be attributed to transformations of protonic sites to Lewis sites with elimination of water[63], explaining the decreasing trend from B/L ratio.

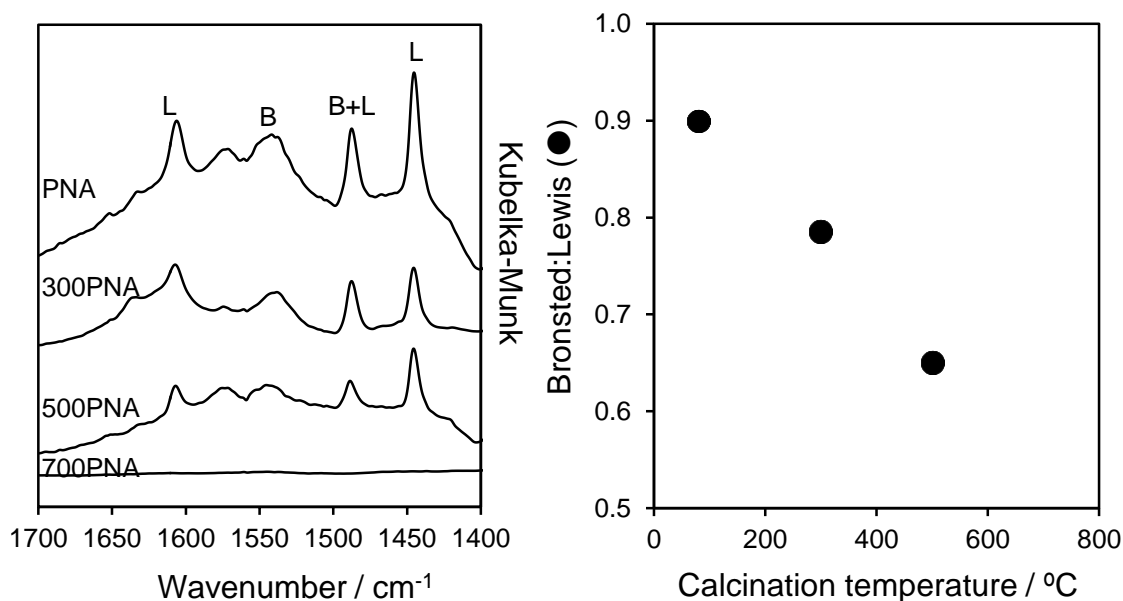


**Figure 3.14** In-vacuo DRIFT spectra of pyridine treated PNA (left) and Brønsted : Lewis character of PNA (right) as a function of calcination temperature

### 3.2.1.4.2 Propylamine chemisorption and temperature programmed desorption

Acid site densities were evaluated by propylamine chemisorption and subsequent thermal analysis using thermogravimetric analysis. As explained in **Chapter 2**, propene reactively formed in the presence of acid sites was monitored by MS and used for the quantification of acid site density[64]. Determination of Brønsted acid sites (BAS) and Lewis acid sites (LAS) was carried out by means of the number of total acid sites in conjunction with the B:L ratio obtained from pyridine chemisorption, which is in agreement with that previously reported by Moraes et al.[44]. **Table 3.5** shows strong temperature dependence, falling from  $\sim 1 \text{ mmol g}^{-1}$  in the as-precipitated pure material, to essentially zero by 700°C. A substantial decrease in Lewis and Brønsted acidity was observed with increasing calcination temperature in agreement with previous reported studies[27, 32, 63]. The acid loadings found on these catalysts are comparable to values reported for niobic acid calcined at similar temperatures. For example, Tanabe reported  $\sim 1 \text{ mmol g}^{-1}$  and  $\sim 0.6 \text{ mmol g}^{-1}$  for uncalcined and 300°C calcined niobic acid respectively using n-butylamine titration together with Hammet indicators[27], and Guo *et al.*[65] recently reported  $0.27 \text{ mmol g}^{-1}$  for mesoporous niobium oxide prepared from  $\text{NbCl}_5$  and calcined at 450°C, using trimethylphosphine as a probe molecule for the acidity sites measurement. This thermally induced loss in acidity can be understood largely in terms of the coincident sintering of PNA crystallites and the attendant loss of

external surface area; the preferential disappearance of Brønsted acidity follows that previously reported by Foo and co-workers[66] wherein 700°C calcination of a commercial HY-340 niobic acid (of unknown preparative method) eliminated all Brønsted character, due to the loss of water of hydration, but left a small number of Lewis acid sites. Thus, the decrease in acid loading cannot be attributed entirely to the decrease in surface area, since the calculation of acid densities after normalization with surface area showed a similar decreasing trend that the one found for the calculated acid loadings. Therefore, other variables must be taken into account for the acidity loss, such as crystallization and phase change, which can induce the disappearance of acid sites as mentioned before. **Figure 3.15** depicts the propene desorption measured by MS, where a peak with maximum at 400 °C is found and remains constant for the entire series, indicative of constant acid strength. The uncalcined material shows an additional peak with maximum at 220 °C which can be attributed to structural water acting as strong Brønsted centres. As shown in the TGA results, structural water is completely removed at 300 °C, reason why the calcined catalysts do not possess this peak. The PNA signal is comprised of a broad peak which seems to have different contributions from different temperatures. The acidity of niobic acid has been studied in the literature, for example, do Prado *et al.*[67] found different types of acid strength (weak, moderate and strong) after performing NH<sub>3</sub>-TPD on a commercial sample of niobic acid. These contributions seem to disappear after thermal treatment is conducted on the parent PNA, since the peak observed for the catalyst calcined at 300°C shows a sharp peak at 400°C for the reactively formed propene.

**Table 3.5** Acid properties of thermally treated PNA materials

| Catalyst | Acid loading /<br>mmol·g <sup>-1</sup> | B/L ratio | BAS /<br>mmol·g <sup>-1</sup> | LAS /<br>mmol·g <sup>-1</sup> |
|----------|--|-----------|-------------------------------|-------------------------------|
| PNA      | 0.99                                   | 0.90      | 0.47                          | 0.52                          |
| 300PNA   | 0.64                                   | 0.79      | 0.28                          | 0.36                          |
| 500PNA   | 0.19                                   | 0.65      | 0.07                          | 0.12                          |
| 700PNA   | 0.01                                   | N/A       | N/A                           | 0.01                          |

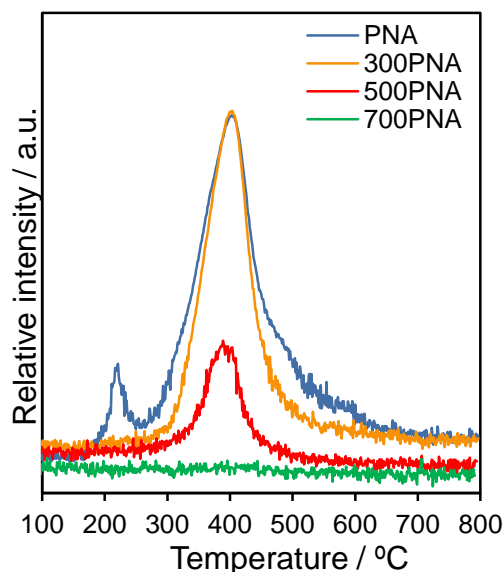


**Figure 3.15** Propene desorption for the PNA series

### 3.2.2 Characterization of x%PNA/SBA-15

Niobic acid was supported on SBA-15 with the aim of achieving high nanoparticulate dispersion in a high surface area support to enhance the activity of these materials in the dehydration reactions performed in this thesis. Nominal loadings of 2 wt%, 5 wt%, 10wt% 15wt% and 25wt% of niobium were synthesised as described in **Chapter 2**.

#### 3.2.2.1 Surface and bulk compositional analysis

Elemental analysis was performed to determine the niobium content present in the supported niobic acid. ICP-OES was used to assess the presence and quantification of bulk niobium in the SBA-15 supported catalysts. Complementary, XPS was carried out to determine the niobium surface content as well as its oxidation state. XPS results shown in **Figure 3.16** (left) revealed a double spin-orbit split doublet whose intensity increases with increasing niobium content. At low niobium loadings, a main doublet dominates the spectra with Nb  $3d_{5/2}$  and Nb  $3d_{3/2}$  binding energy at 207.7 and 210.5 eV respectively characteristic of Nb<sup>5+</sup> chemical environment. At higher niobium coverage another doublet rises for the  $3d_{5/2}$  and  $3d_{3/2}$  states at 205.7 and 208.5 eV, characteristic of a Nb<sup>4+</sup> chemical environment due to the formation of NbO<sub>2</sub>, which has been previously reported during oxidation at room temperature and low pressure due to difficult oxygen diffusion[68]. For loadings below 9 wt%, Nb 3d peaks appear shifted by ~0.7 eV to higher binding energy with respect to the signal obtained from the

unsupported materials, which has been previously observed and attributed to atomic dispersion of niobium on the support and to the change in the Nb coordination by formation of Nb-O-Si linkages[69]. This effect has also been reported for conformal alumina[70] and zirconia[71] films grown over SBA-15 architectures. **Figure 3.16** (right) shows the O 1s XPS peak region, where a main peak at 532.0 eV related to O-Si can be observed. Another peak at 529.9 eV emerges with increasing the niobium loading and is assigned to O-Nb[19]. A detailed summary of the atomic compositions analysed by XPS along with the bulk niobium compositions obtained by ICP-OES is displayed in **Table 3.6**. A constant increase in the surface and bulk niobium composition is detected by XPS and ICP respectively, together with an increase on the Nb/Si atomic ratio, result of the good incorporation of the niobia nanoparticles onto the surface of the mesoporous silica support.

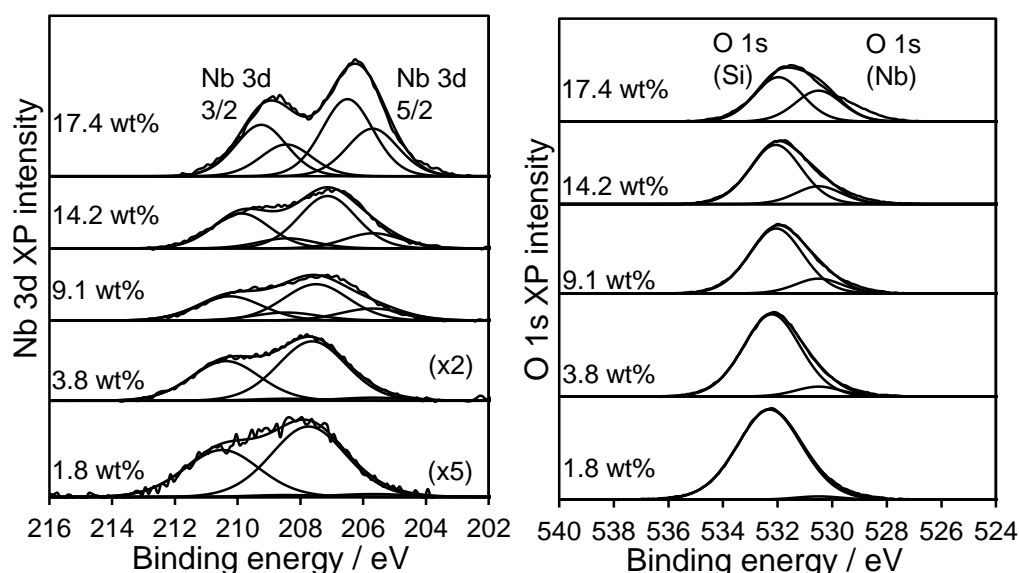


**Figure 3.16** XPS of the Nb 3d (left) and O 1s (right) regions for the PNA/SBA-15 series

**Table 3.6** Surface and bulk composition of PNA/SBA-15 as a function of niobia loading

| Catalyst      | Bulk Nb content <sup>a</sup> / wt% | Surface content <sup>b</sup> / wt% |      |      | Atomic ratio <sup>b</sup> |
|---------------|------------------------------------|------------------------------------|------|------|---------------------------|
|               |                                    | Nb                                 | O    | Si   | Nb/Si                     |
| 2%PNA/SBA-15  | 1.8                                | 2.0                                | 59.7 | 38.3 | 0.01                      |
| 5%PNA/SBA-15  | 3.8                                | 4.3                                | 56.0 | 39.7 | 0.03                      |
| 10%PNA/SBA-15 | 9.1                                | 7.5                                | 55.2 | 37.3 | 0.06                      |
| 15%PNA/SBA-15 | 14.2                               | 9.8                                | 54.1 | 36.1 | 0.08                      |
| 25%PNA/SBA-15 | 17.4                               | 16.7                               | 52.7 | 30.6 | 0.16                      |

From <sup>a</sup>ICP; <sup>b</sup>XPS

Although co-precipitation of niobia species in the silica support is a well established method widely reported in the literature [19-21], not many studies have been published about impregnation of niobium species on a mesoporous silica. García-Sancho *et al.* have reported several publications using an impregnation method with an aqueous solution of niobium oxalate in oxalic acid to incorporate niobic acid on SBA-15[72] and MCM-41[73, 74]. However, the surface Nb/Si atomic ratio calculated by XPS is lower than that reported in **Table 3.6**, with values below 0.03 for the materials reported by Garcia-Sancho, indicating higher amount of niobia species on the surface of the silica support for the materials herein synthesised. Likewise, materials prepared by co-precipitation method tend to yield a lower Nb/Si ratio due to the incorporation of niobium species into the silica framework, and hence fewer species present on the surface[19]. These findings suggest that the peroxy niobic acid sol-gel impregnation method used for the preparation of the catalysts in this thesis is able to provide a higher surface amount of impregnated niobia species compared with the results reported in the literature. **Figure 3.17** displays the relation between bulk and superficial niobium, representing a linear trend indicative of uniform niobium dispersion across the series. Error bars represent the little to none variation in niobium loading calculated from two different batches of prepared supported catalysts.

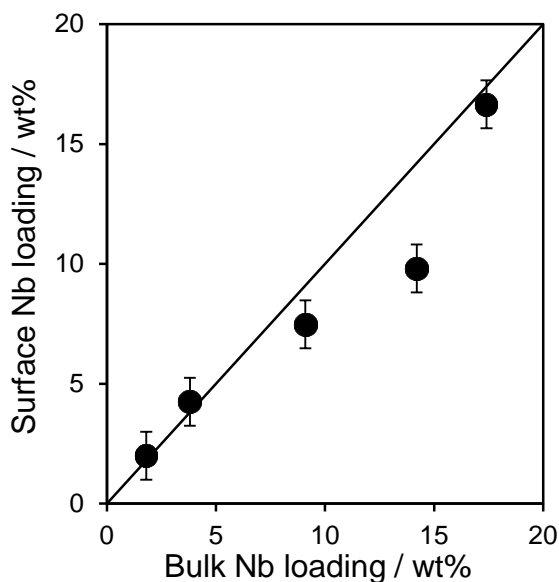


**Figure 3.17** Surface versus bulk niobium concentration

### 3.2.2.2 Textural properties

Porosimetry results for the parent SBA-15 used for the impregnation of the supported materials revealed type IV hysteresis loops associated with mesoporous materials (**Figure 3.18**). The PNA/SBA materials present a similar type IV hysteresis loop, indicating the preservation of support hierarchical structure after niobium impregnation. The hysteresis loop for the niobium containing materials was narrower than that observed in SBA-15, indicating the absence of plugs in ordered channels of the samples[20]. Pore size distributions show a slight increase from the 4.8 nm observed on the SBA-15 sample up to 6.2 nm for the higher niobium loading samples. This widening of the mesopore structure can be explained due to the hermetic hydrothermal treatment in which the materials were prepared. During this synthesis step, detailed in **Chapter 2**, the expansion of the formed niobic acid in a foam-like structure inside the mesopores of the support can provoke the augmentation of the mesopore size. Niobium addition to the parent SBA-15 progressively lowered the surface area and mesopore volume of the silica support (**Figure 3.19**), consistent with uniform dispersion throughout the pore network. The initial pore volume increase through the series is consistent with the widening of pore diameter observed, and start decreasing as the niobic acid is deposited onto the inner wall of the pores. **Table 3.7** summarizes the textural properties of the supported materials, where it is noteworthy the complete blockage of microporosity during the precipitation procedure for all the prepared catalysts.

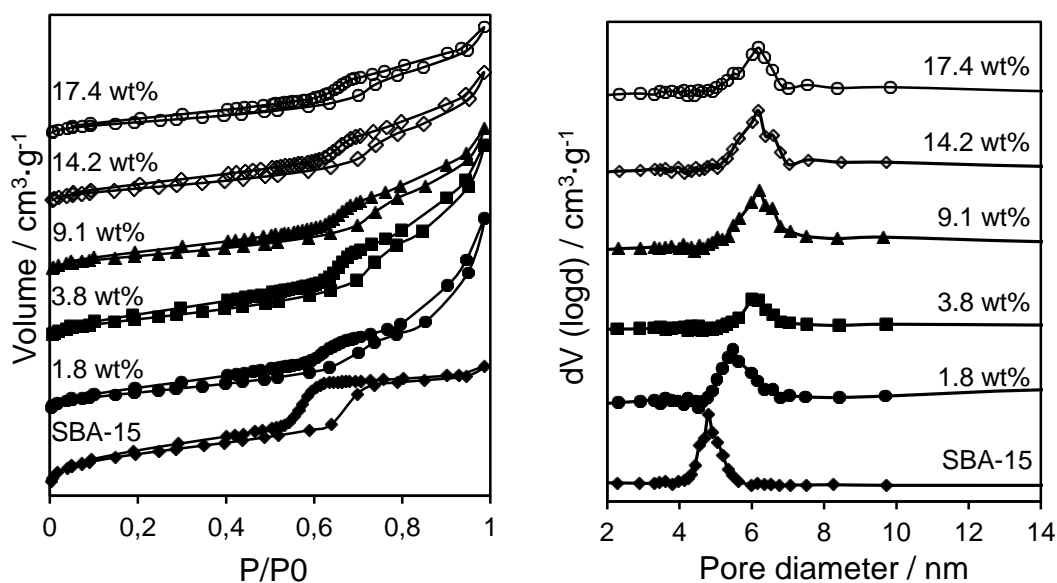


**Figure 3.18** Nitrogen adsorption-desorption isotherms (left) and BJH pore size distribution of supported niobium materials (right)

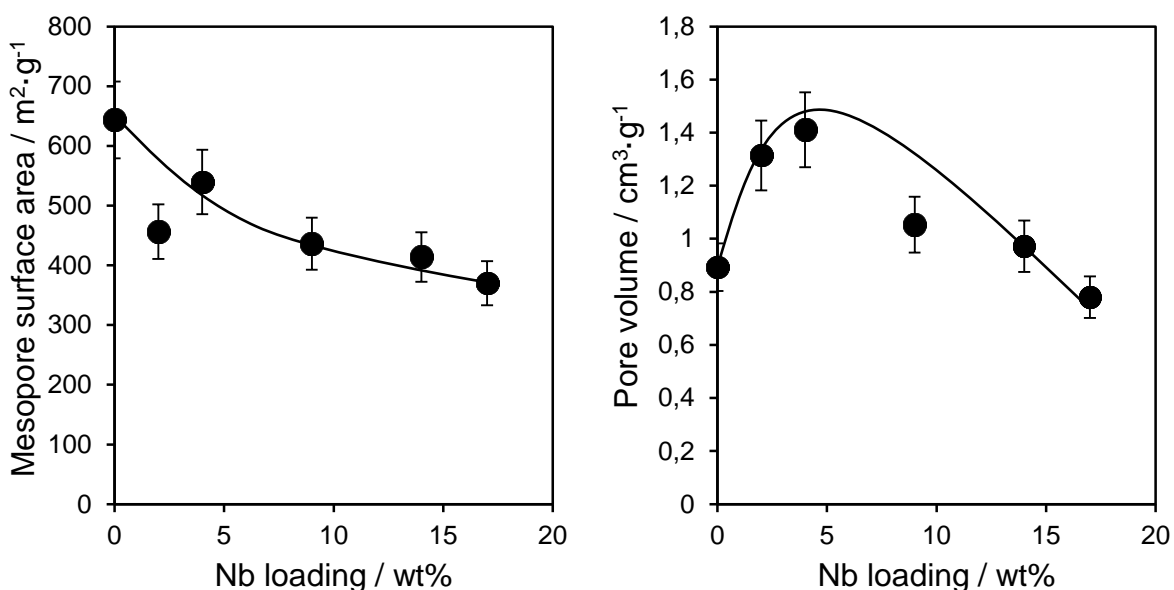


**Figure 3.19** Correlation between niobium mesopore surface area (left) and mesopore pore volume (right) of supported niobium materials

**Table 3.7** Textural properties of niobic acid supported materials

| Catalyst<br>PNA/SBA-15<br>/ wt% | Total surface<br>area <sup>a</sup><br>/ m <sup>2</sup> ·g <sup>-1</sup> | Micropore<br>surface area <sup>a</sup><br>/ m <sup>2</sup> ·g <sup>-1</sup> | Pore<br>diameter <sup>b</sup><br>/ nm | Micropore pore<br>volume <sup>b</sup><br>/ cm <sup>3</sup> ·g <sup>-1</sup> | Total pore<br>volume <sup>b</sup><br>/ cm <sup>3</sup> ·g <sup>-1</sup> |
|---------------------------------|---|---|---------------------------------------|---|---|
| SBA-15                          | 942   | 299   | 4.8                                   | 0.13  | 1.02  |
| 1.8                             | 456   | 0   | 5.5                                   | 0   | 1.31  |
| 3.8                             | 540   | 0   | 6.0                                   | 0   | 1.41  |
| 9.1                             | 436   | 0   | 6.2                                   | 0   | 1.05  |
| 12.2                            | 414   | 0   | 6.2                                   | 0   | 0.97  |
| 17.4                            | 370   | 0   | 6.2                                   | 0   | 0.78  |

Similar surface areas in the range of 300-600 m<sup>2</sup>·g<sup>-1</sup> have been reported by García-Sancho *et al.* for impregnated niobic acid onto SBA-15 support [72, 75].

### 3.2.2.3 Structure and morphology

Powder X-Ray diffraction and STEM analyses were performed in order to confirm the preservation of the mesoporous structure of the support and confirm the sought uniform dispersion on niobic acid onto the silica support. Besides, Raman spectroscopy technique was utilised to verify the presence of interaction between the niobia nanoparticles and the support by means of identifying the chemical bond formed during the synthesis of the materials.

### 3.2.2.3.1 Powder X-Ray diffraction

**Figure 3.20** shows the low angle XRD patterns for the x%PNA/SBA-15 materials. XRD patterns exhibit reflections at  $2\theta = 0.96, 1.55$  and  $1.8^\circ$  characteristic of the (100), (110) and (200) planes of the  $p6mm$  SBA-15 support architecture[76], as it was observed by the presence of the hysteresis loop in the  $N_2$  adsorption-desorption measurements, together with the sharp pore size distribution. Therefore, it can be confirmed that the support has retained its well-ordered meso-structure after precipitation of niobic acid onto it. **Table 3.8** shows d spacing, wall thickness and lattice parameter calculated from the (100) reflexion as reported in **Chapter 2**. D spacing and lattice parameter “a” of the hexagonal structure of SBA-15 can be considered to remain constant with increasing niobium content. Thus, the pore size increase experienced during the aging process impacts just on the wall thickness of the materials.

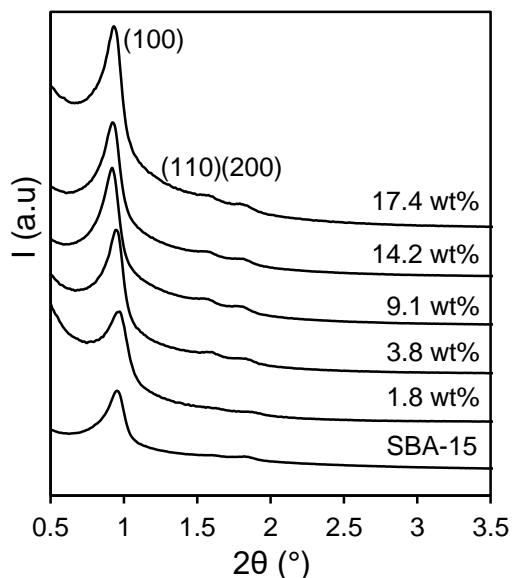


**Figure 3.20** Low angle (left) and wide angle (right) X-Ray powder diffraction patterns of the x%PNA/SBA-15 materials

**Table 3.8** Unit cell sizes and pore wall thickness calculated from XRD and N<sub>2</sub> adsorption-desorption analyses

| Catalyst<br>PNA/SBA-15/ wt% | $2\theta / ^\circ$ | d / nm | a / nm | Pore diameter<br>/ nm | Wall thickness<br>/ nm |
|-----------------------------|--------------------|--------|--------|-----------------------|------------------------|
| SBA-15                      | 0.95               | 9.3    | 10.7   | 4.8                   | 5.9                    |
| 1.8                         | 0.95               | 9.3    | 10.7   | 5.5                   | 5.2                    |
| 3.8                         | 0.95               | 9.3    | 10.7   | 6.0                   | 4.7                    |
| 9.1                         | 0.92               | 9.5    | 11.1   | 6.2                   | 4.9                    |
| 12.2                        | 0.92               | 9.5    | 11.1   | 6.2                   | 4.9                    |
| 17.4                        | 0.93               | 9.5    | 11.1   | 6.2                   | 4.9                    |

### 3.2.2.3.2 Scanning transmission electron microscopy

**Figure 3.21** shows a representative STEM image of 9.1%PNA/SBA-15. **Figure 3.21a** reveals the presence of ~1 nm particles decorating the walls and mesopore channels of the silica support, showing highly dispersed Nb-containing nanoparticles decorating hexagonal close-packed silica mesopore channels. The size of the SBA-15 mesopores can also be determined from **Figure 3.21b**, and after the measurement of 20 different pores, and average of  $6.2 \pm 0.3$  nm was found, which is in good agreement with the pore size detected in the porosimetry analysis. Both images confirm the preservation of the hexagonal structure of SBA-15, while the pore walls morphology is retained upon incorporation of niobic acid, with no evidence for large crystallite deposition. EDX mapping of 1.8% PNA/SBA-15 as a representative sample can be found in **Figure 3.22**. Images revealed a homogeneous distribution of niobium, represented by purple dots in image c, onto the silica support (green dots in image b), indicating that niobia species are impregnated throughout the SBA-15 surface, proving the effectiveness of the catalyst preparation method.

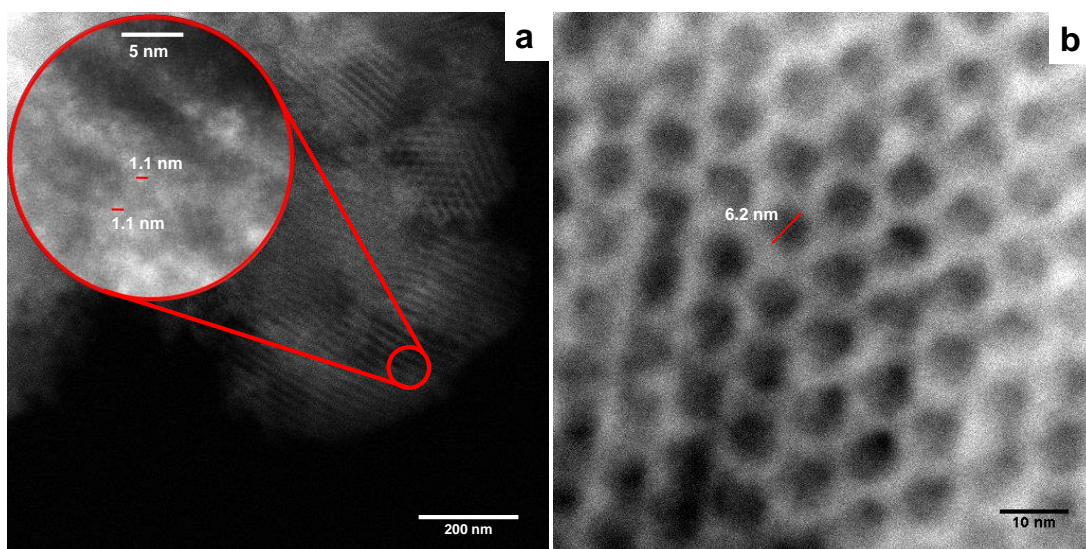


**Figure 3.21** STEM of 9.1%PNA/SBA-15 showing a) presence of niobia nanoparticles in/on the silica channels and b) hexagonal honeycomb mesopore channels

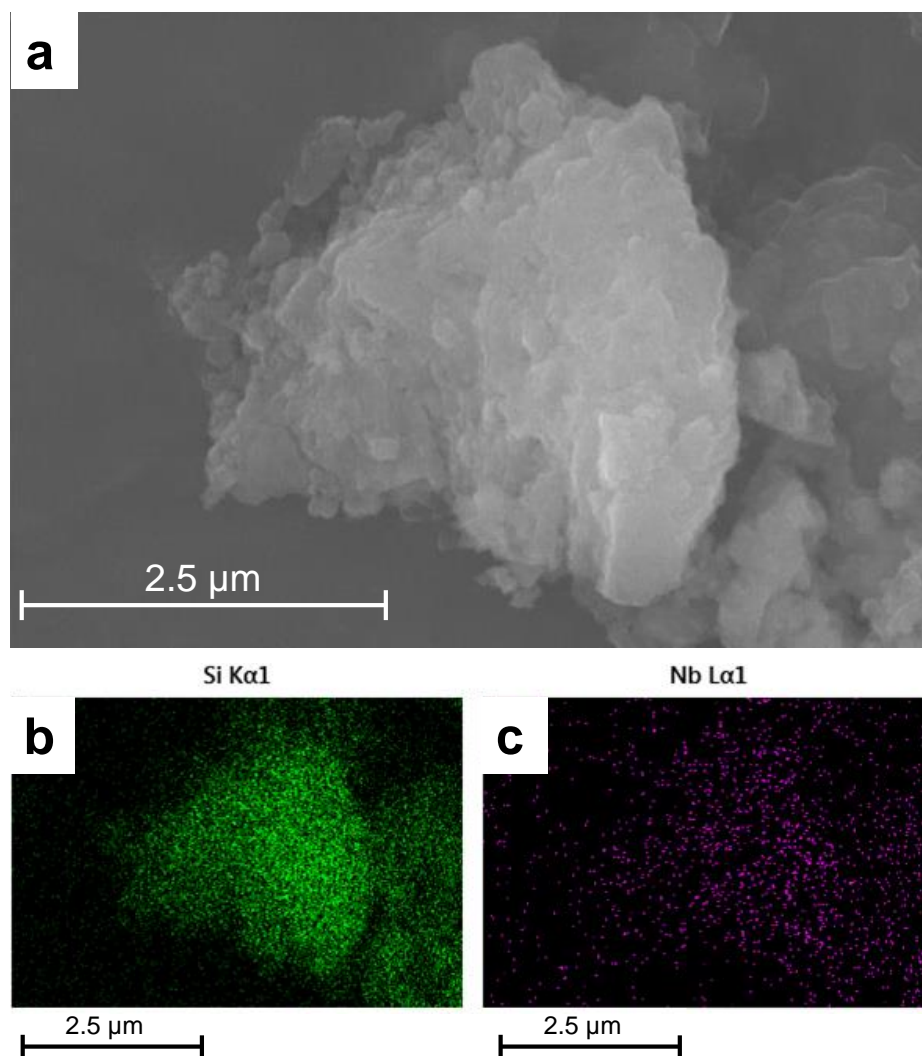


**Figure 3.22** a) STEM, b) EDX Si mapping (green) and c) EDX Nb mapping (purple) of 1.8% PNA/SBA-15

### 3.2.2.3.3 Raman spectroscopy

**Figure 3.23** shows the raman spectra of the x%PNA/SBA-15 samples. Raman signals present in the SBA-15 analysis have been previously observed and assigned to:  $1050\text{ cm}^{-1}$  (the asymmetric mode of Si-O-Si linkages),  $979\text{ cm}^{-1}$  (surface silanol groups),  $605\text{ cm}^{-1}$  and  $485\text{ cm}^{-1}$  (three- and four-fold siloxane rings), and  $800\text{ cm}^{-1}$  (Si-O-Si symmetric stretching vibration)[77]. The band near  $900\text{ cm}^{-1}$  showed an increase in the band intensity after the introduction of niobium. This vibration has been assigned to the superimposition of the stretching vibrations of Si-O and Si-O-Nb bonds[78], indicating that niobium was successfully incorporated into the silica framework. The band at  $972\text{ cm}^{-1}$  is the characteristic band of terminal Nb=O in  $\text{NbO}_6$  octahedral unit of amorphous  $\text{Nb}_2\text{O}_5$ [23], which overlaps with the surface silanol groups (Raman band at  $979\text{ cm}^{-1}$ )[79]. For the higher loading of PNA/SBA-15, another new band appears at  $660\text{ cm}^{-1}$  that is characteristic of the stretching mode of Nb-O-Nb polymerised bonds[80], forming a six-fold coordinated surface NbO species. This band is similar to that observed for the bulk niobic acid, therefore, this Raman band could reveal the presence of small  $\text{Nb}_2\text{O}_5$  particles, not detected by XRD, on the surface of this catalyst[73]. After this analysis we can define two sorts of dispersion methods of niobic acid on SBA-15 as presented in **Figure 3.24**. At low loading, isolated niobia species comprised of a  $\text{NbO}_6$  unit are dispersed through the support forming Si-O-Nb bonds. As the concentration of niobic species increases, isolated species interact with their analogues in the vicinity to generate polymerised niobia species by forming Nb-O-Nb bridge bonds[23].

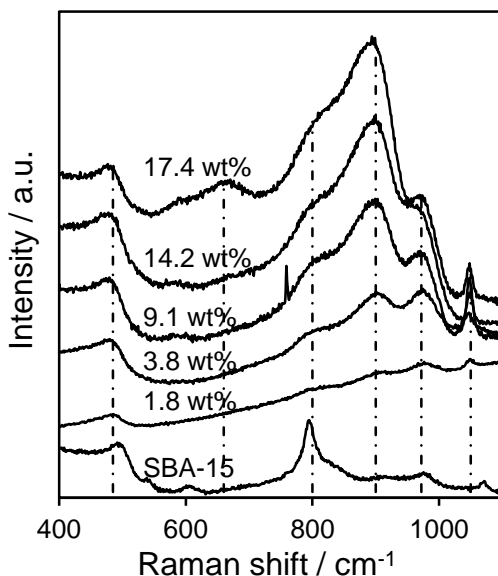


**Figure 3.23** Raman spectra of x%PNA/SBA-15 samples



support previous indications (Raman, N<sub>2</sub> adsorption-desorption) of the efficiency of incorporation of niobium species into the SBA-15 support. The B/L ratio is determined from the 1448 cm<sup>-1</sup> and 1542 cm<sup>-1</sup> peak areas, and is tabulated in **Table 3.9** later in this chapter after measurement of acid sites loading, in order to have a complete understanding of the acidic properties of the materials.

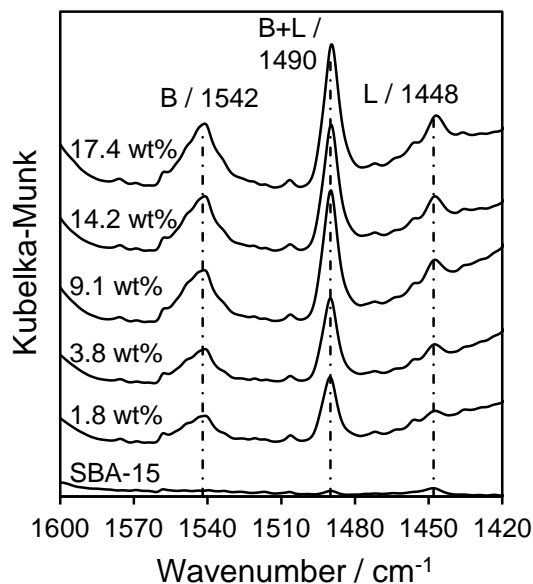


**Figure 3.25** In-vacuo DRIFT spectra of pyridine treated x%PNA/SBA-15 as a function of Nb loading

#### 3.2.2.4.2 Propylamine chemisorption and temperature programmed desorption

Acid site densities (total, Brønsted (BAS) and Lewis (LAS)) were evaluated as explained for the bulk materials (3.2.1.4.2) and are displayed in **Table 3.9**. Total acid densities for the PNA/SBA-15 materials increased rapidly for the low loading samples, reaching a linear dependency with increasing niobium content for the higher loadings, consistent with the evolution of a conformal niobic acid adlayer (**Figure 3.26**). B/L ratio was calculated by integration of the signals obtained by DRIFTS - pyridine adsorption using CasaXPS. Areas at 1448 and 1542 cm<sup>-1</sup> were used for the calculation of Lewis and Brønsted acidity respectively. **Figure 3.27** exhibits the propene desorption measured by MS, where a peak with maximum at 396 °C is found for all the catalysts except for the lowest loading, whose peak is at 365 °C. This difference in acid strength could be due to the different arrangement of niobia species in the surface of the support, with more predominant isolated species in the low loading, and polymerised

niobia species appearing for higher loadings, providing acidic properties more similar to the bulk species. Another peak appears at lower temperature, which with exception of the lowest loading, shifts from 292 °C down to 235 °C as the niobium content increases. This peak was also found for uncalcined bulk PNA, and was attributed to crystalline water.

**Table 3.9** Acid properties of niobic acid supported on SBA-15 materials

| Catalyst        | Acid density / mmol·g <sup>-1</sup> | BAS / mmol·g <sup>-1</sup> | LAS / mmol·g <sup>-1</sup> | B/L ratio |
|-----------------|-------------------------------------|----------------------------|----------------------------|-----------|
| 1.8%PNA/SBA-15  | 0.21                                | 0.19                       | 0.02                       | 8.87      |
| 3.8%PNA/SBA-15  | 0.44                                | 0.38                       | 0.06                       | 6.85      |
| 9.1%PNA/SBA-15  | 0.56                                | 0.49                       | 0.07                       | 6.77      |
| 14.2%PNA/SBA-15 | 0.61                                | 0.53                       | 0.08                       | 6.57      |
| 17.4%PNA/SBA-15 | 0.67                                | 0.58                       | 0.09                       | 6.15      |

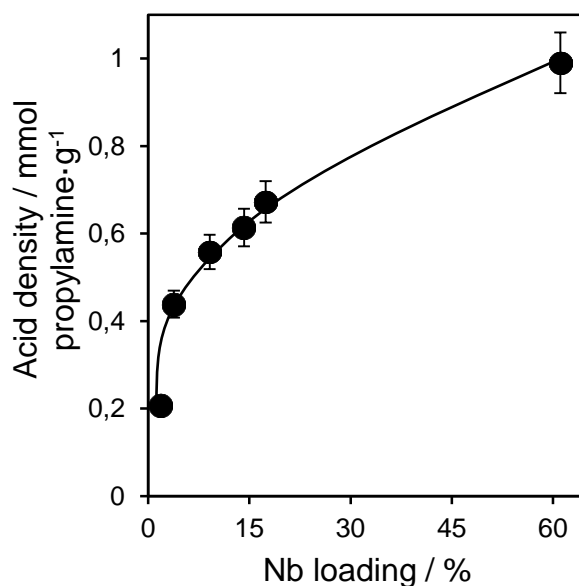


**Figure 3.26** Total acid site density of PNA/SBA-15 as a function of Nb loading

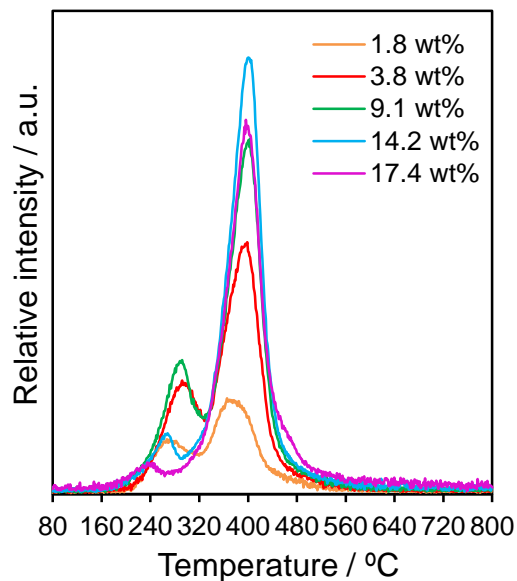


**Figure 3.27** Propene desorption for the x%PNA/SBA-15 series obtained by TGA-MS

### 3.3 Conclusions

Series of bulk niobic acid nanoparticles and niobic acid functionalised SBA-15 were successfully synthesised by soft chemical route employing a peptized niobic acid sols prepared from ethanolic  $\text{NbCl}_5$  at low temperature. The impact of thermal treatment upon the physico-chemical properties of the bulk niobic acid series was investigated, revealing drastic changes induced mainly by nanoparticle sintering. Calcination at temperatures over  $500^\circ\text{C}$  provokes the crystallization of the parent niobic acid to hexagonal phase followed by the transformation to orthorhombic phase. This phase change is coincident with a steep decrease in surface area and crystallite growth. Calcination of parent niobic acid also promotes the dehydroxylation of the catalyst surface, leading to a decrease in the Brønsted-Lewis ratio. The total acidity of the catalysts is progressively reduced until complete loss at calcination temperatures over  $700^\circ\text{C}$ , as a result of the reduced surface area and elimination of superficial Brønsted acidity.

Analyses performed on the uncalcined  $\text{Nb}_2\text{O}_5/\text{SBA-15}$  series exhibited the preservation of the support hierarchical structure after niobium impregnation, and the presence of niobia nanoparticles decorating the walls of the silica structure. As a result of the increase in niobia loading, an increase in the acidity of the catalysts was proved by propylamine and pyridine acidity measurements. While bulk materials present marked Lewis acidity, only high loadings of supported niobia materials display this type of

acidity, therefore producing higher Brønsted-Lewis ratio than those observed for the bulk materials. Moreover, the adequate dispersion of niobia nanoparticles was demonstrated, although only the lowest loading was found to possess isolated niobia species, while the rest of the series show polymerised niobia species, presenting some agglomeration of nanoparticles for the higher loadings.

### 3.4 References

- [1] K. Kukli, M. Ritala, M. Leskelä, *Journal of the Electrochemical Society* 148 (2001) F35-F41.
- [2] G.V. Prakash, D.N. Rao, A. Bhatnagar, *Solid State Communications* 119 (2001) 39-44.
- [3] I. Abuetwirat, T. Palai-Dany, Dielectric properties of niobium oxide film and tantalum oxide film at electrolytic niobium and tantalum capacitors, *ELEKTRO*, 2012, IEEE, 2012, pp. 484-487.
- [4] K. Sasaki, L. Zhang, R. Adzic, *Physical Chemistry Chemical Physics* 10 (2008) 159-167.
- [5] K. Asakura, Y. Iwasawa, *Chemistry Letters* 17 (1988) 633-636.
- [6] T. Ushikubo, K. Wada, *Applied catalysis* 67 (1990) 25-38.
- [7] T. Okuhara, *Chemical Reviews* 102 (2002) 3641-3666.
- [8] I. Nowak, M. Ziolk, *Chemical Reviews* 99 (1999) 3603-3624.
- [9] C. Guo, Z. Qian, *Catalysis Today* 16 (1993) 379-385.
- [10] J. Weissman, E.I. Ko, P. Wynblatt, J. Howe, *Chemistry of Materials* 1 (1989) 187-193.
- [11] E. Nikishina, E. Lebedeva, D. Drobot, *Inorganic Materials* 48 (2012) 1243-1260.
- [12] H. Schäfer, R. Gruehn, F. Schulte, *Angewandte Chemie International Edition in English* 5 (1966) 40-52.
- [13] E. Ko, J. Weissman, *Catalysis Today* 8 (1990) 27-36.
- [14] B. Sen, A. Saha, N. Chatterjee, *Materials Research Bulletin* 16 (1981) 923-932.
- [15] T. Ikeya, M. Senna, *Journal of non-crystalline solids* 105 (1988) 243-250.
- [16] J.M. Jehng, I.E. Wachs, *Chemistry of Materials* 3 (1991) 100-107.
- [17] K.O. Drake, D. Carta, L.J. Skipper, F.E. Sowrey, R.J. Newport, M.E. Smith, *Solid state nuclear magnetic resonance* 27 (2005) 28-36.
- [18] M. Shirai, K. Asakura, Y. Iwasawa, *The Journal of Physical Chemistry* 95 (1991) 9999-10004.

- [19] P. Carniti, A. Gervasini, M. Marzo, *The Journal of Physical Chemistry C* 112 (2008) 14064-14074.
- [20] M. Trejda, A. Tuel, J. Kujawa, B. Kilos, M. Ziolk, *Microporous and mesoporous materials* 110 (2008) 271-278.
- [21] K. Peng, X. Li, X. Liu, Y. Wang, *Molecular Catalysis* 441 (2017) 72-80.
- [22] E. Ko, R. Bafra, N. Nuhfer, N. Wagner, *Journal of Catalysis* 95 (1985) 260-270.
- [23] J. He, Q.-J. Li, Y.-N. Fan, *Journal of Solid State Chemistry* 202 (2013) 121-127.
- [24] Â. Silva, K. Wilson, A.F. Lee, V.C. dos Santos, A.C.C. Bacilla, K.M. Mantovani, S. Nakagaki, *Applied Catalysis B: Environmental* 205 (2017) 498-504.
- [25] I. Nowak, *Studies in Surface Science and Catalysis* 154 (2004) 2936-2944.
- [26] T. Shishido, T. Kitano, K. Teramura, T. Tanaka, *Catalysis letters* 129 (2009) 383-386.
- [27] K. Tanabe, *Materials chemistry and physics* 17 (1987) 217-225.
- [28] J.M. Jehng, I.E. Wachs, *The Journal of Physical Chemistry* 95 (1991) 7373-7379.
- [29] S. Maurer, E. Ko, *Journal of Catalysis* 135 (1992) 125-134.
- [30] R. Brayner, F. Bozon-Verduraz, *Physical Chemistry Chemical Physics* 5 (2003) 1457-1466.
- [31] V. Lebarbier, M. Houalla, T. Onfroy, *Catalysis today* 192 (2012) 123-129.
- [32] T. Iizuka, K. Ogasawara, K. Tanabe, *Bulletin of the Chemical Society of Japan* 56 (1983) 2927-2931.
- [33] Y. Zhao, X. Zhou, L. Ye, S. Chi Edman Tsang, *Nano Reviews* 3 (2012) 17631.
- [34] K. Nakajima, Y. Baba, R. Noma, M. Kitano, J. N. Kondo, S. Hayashi, M. Hara, *Journal of the American Chemical Society* 133 (2011) 4224-4227.
- [35] J. Datka, A. Turek, J. Jehng, I. Wachs, *Journal of Catalysis* 135 (1992) 186-199.
- [36] J.G. Weissman, *Catalysis today* 28 (1996) 159-166.
- [37] X. Gao, I.E. Wachs, M.S. Wong, J.Y. Ying, *Journal of Catalysis* 203 (2001) 18-24.
- [38] NIST Standard Reference Database 20, Version 3.4 (web version).
- [39] J. Chastain, R.C. King, J. Moulder, *Handbook of X-ray photoelectron spectroscopy: a reference book of standard spectra for identification and interpretation of XPS data*, Physical Electronics Eden Prairie, MN, 1995.
- [40] A. Mozalev, R.M. Vázquez, C. Bittencourt, D. Cossement, F. Gispert-Guirado, E. Llobet, H. Habazaki, *Journal of Materials Chemistry C* 2 (2014) 4847-4860.

- [41] C. Carlini, M. Giuttari, A.M.R. Galletti, G. Sbrana, T. Armaroli, G. Busca, *Applied Catalysis A: General* 183 (1999) 295-302.
- [42] B.K. Sen, A.V. Saha, *Materials Research Bulletin* 17 (1982) 161-169.
- [43] K. Eguchi, M. Machida, I. Yamanaka, *Science and Technology in Catalysis 2006: Proceedings of the Fifth Tokyo Conference on Advanced Catalytic Science and Technology*, Tokyo, July 23-28, 2006, Elsevier, 2007.
- [44] M. Moraes, W.d.S. Pinto, W. Gonzalez, L. Carmo, N. Pastura, E. Lachter, *Applied Catalysis A: General* 138 (1996) L7-L12.
- [45] N. Uekawa, T. Kudo, F. Mori, Y.J. Wu, K. Takegawa, *Journal of Colloid and Interface science* 264 (2003) 378-384.
- [46] M. Paulis, M. Martín, D. Soria, A. Díaz, J. Odriozola, M. Montes, *Applied Catalysis A: General* 180 (1999) 411-420.
- [47] S. Li, Q. Xu, E. Uchaker, X. Cao, G. Cao, *CrystEngComm* 18 (2016) 2532-2540.
- [48] C. Nico, T. Monteiro, M. Graça, *Progress in Materials Science* 80 (2016) 1-37.
- [49] A.M. Raba, J. Bautista-Ruiz, M.R. Joya, *Materials Research* 19 (2016) 1381-1387.
- [50] M. Ristić, S. Popović, S. Musić, *Materials Letters* 58 (2004) 2658-2663.
- [51] L. Frevel, H. Rinn, *Analytical Chemistry* 27 (1955) 1329-1330.
- [52] K. Kato, S. Tamura, *Acta Crystallographica Section B: Structural Crystallography and Crystal Chemistry* 31 (1975) 673-677.
- [53] X. Xu, F. Liu, X. Han, Y. Wu, W. Liu, R. Zhang, N. Zhang, X. Wang, *Catalysis Science & Technology* 6 (2016) 5280-5291.
- [54] A. Ouqour, G. Coudurier, J.C. Vedrine, *Journal of the Chemical Society, Faraday Transactions* 89 (1993) 3151-3155.
- [55] M. Luisa Marin, G.L. Hallett-Tapley, S. Impellizzeri, C. Fasciani, S. Simoncelli, J.C. Netto-Ferreira, J.C. Scaiano, *Catalysis Science & Technology* 4 (2014) 3044-3052.
- [56] F.D. Hardcastle, I.E. Wachs, *Solid State Ionics* 45 (1991) 201-213.
- [57] J.-M. Jehng, A.M. Turek, I.E. Wachs, *Applied Catalysis A: General* 83 (1992) 179-200.
- [58] T. Murayama, J. Chen, J. Hirata, K. Matsumoto, W. Ueda, *Catalysis Science & Technology* 4 (2014) 4250-4257.
- [59] J.-M. Jehng, I.E. Wachs, *Catalysis Today* 8 (1990) 37-55.
- [60] K. Tanabe, S. Okazaki, *Applied Catalysis A: General* 133 (1995) 191-218.
- [61] G. Busca, *Catalysis today* 41 (1998) 191-206.

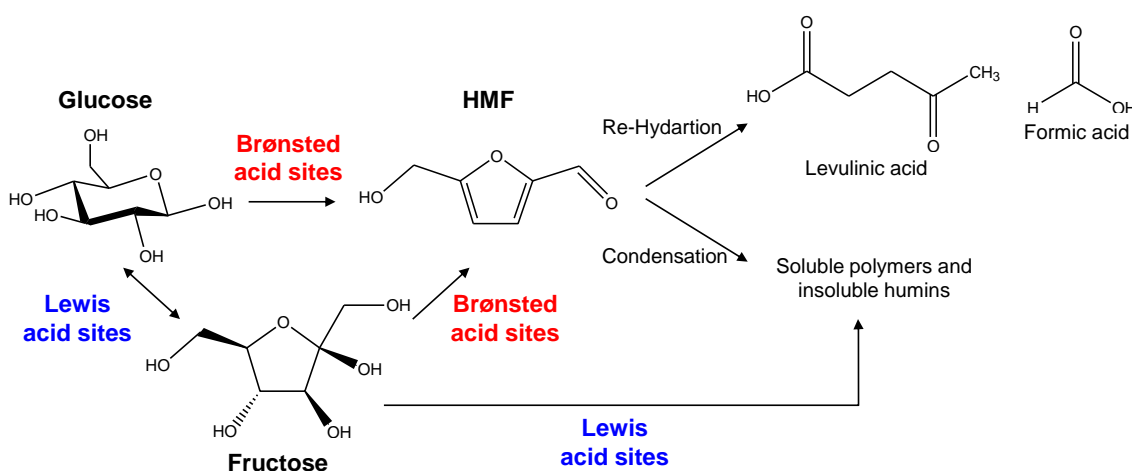
- [62] E.P. Parry, *Journal of Catalysis* 2 (1963) 371-379.
- [63] A. Florentino, P. Cartraud, P. Magnoux, M. Guisnet, *Applied Catalysis A: General* 89 (1992) 143-153.
- [64] O. Kresnawahjuesa, R.J. Gorte, D. De Oliveira, L. Lau, *Catalysis letters* 82 (2002) 155-160.
- [65] B. Guo, L. Ye, G. Tang, L. Zhang, B. Yue, S.C.E. Tsang, H. He, *Chinese Journal of Chemistry* (2017) 1-11.
- [66] G.S. Foo, D. Wei, D.S. Sholl, C. Sievers, *ACS Catalysis* 4 (2014) 3180-3192.
- [67] N.T. do Prado, T.E. Souza, A.R.T. Machado, P.P. Souza, R.S. Monteiro, L.C. Oliveira, *Journal of Molecular Catalysis A: Chemical* 422 (2016) 23-34.
- [68] B. An, S. Fukuyama, K. Yokogawa, M. Yoshimura, *Physical Review B* 68 (2003) 115423.
- [69] S. Damyanova, L. Dimitrov, L. Petrov, P. Grange, *Applied surface science* 214 (2003) 68-74.
- [70] J.J. Creasey, C.M. Parlett, J.C. Manayil, M.A. Isaacs, K. Wilson, A.F. Lee, *Green Chemistry* 17 (2015) 2398-2405.
- [71] A. Osatiashtiani, A.F. Lee, M. Granollers, D.R. Brown, L. Olivi, G. Morales, J.A. Melero, K. Wilson, *ACS Catalysis* 5 (2015) 4345-4352.
- [72] C. García-Sancho, R. Saboya, J. Cecilia, A. Sales, F. Luna, E. Rodríguez-Castellón, C. Cavalcante, *Molecular Catalysis* 436 (2017) 267-275.
- [73] C. García-Sancho, R. Moreno-Tost, J.M. Mérida-Robles, J. Santamaría-González, A. Jiménez-López, P. Maireles-Torres, *Applied Catalysis B: Environmental* 108 (2011) 161-167.
- [74] C. García-Sancho, I. Sádaba, R. Moreno-Tost, J. Mérida-Robles, J. Santamaría-González, M. López-Granados, P. Maireles-Torres, *ChemSusChem* 6 (2013) 635-642.
- [75] C. García-Sancho, I. Agirrezabal-Telleria, M. Güemez, P. Maireles-Torres, *Applied Catalysis B: Environmental* 152 (2014) 1-10.
- [76] D. Zhao, J. Feng, Q. Huo, N. Melosh, G.H. Fredrickson, B.F. Chmelka, G.D. Stucky, *science* 279 (1998) 548-552.
- [77] J.-M. Jehng, I.E. Wachs, *Catalysis letters* 13 (1992) 9-19.
- [78] A. Feliczak, I. Nowak, *Studies in Surface Science and Catalysis* 170 (2007) 519-524.
- [79] J.-M. Jehng, H. Hu, X. Gao, I.E. Wachs, *Catalysis Today* 28 (1996) 335-350.
- [80] L.J. Burcham, J. Datka, I.E. Wachs, *The Journal of Physical Chemistry B* 103 (1999) 6015-6024.

## ***Chapter 4***

***Niobic acid nanoparticle catalysts  
for the transformation of biomass  
derived sugars to 5-  
hydroxymethylfurfural***

## 4.1 Introduction

HMF formation via triple dehydration of hexoses is quite complex and several reaction routes and mechanisms have been suggested, especially with glucose and fructose as starting materials, although no definite conclusion has been made on the reaction mechanism for hexose dehydration yet. The production of HMF from hexoses tends to be governed by the presence of numerous other side reactions due to isomerisation, dehydration, fragmentation and condensation reactions, which lead mainly to the generation of humins[1] and organic acids like levulinic and formic acid, which can self-catalyse the dehydration of hexose. A simplified reaction mechanism is shown in **Scheme 4.1**.



**Scheme 4.1** Simplified pathways for the conversion of glucose to fructose and generation of undesirable side reactions

The classification of niobic acid ( $\text{Nb}_2\text{O}_5 \cdot n\text{H}_2\text{O}$ ) as a water tolerant solid acid together with the presence of both Lewis and Brønsted acidity, makes it a suitable candidate for the dehydration of glucose and fructose to HMF. In addition to its good catalytic properties, niobic acid has also been reported as a good support material for bimetallic catalysts, like the recent publications of Guo *et al.*[2] and Yue *et al.*[3] in which a combination of niobium and tungsten materials were tested for the conversion of glucose to HMF, or the investigation of different structures and morphologies of niobium oxide published by Edman Tsang's group[4], in which mesoporous niobic acid was found to show the best catalytic performance. To further improve the activity of the catalysts, the utilization of phosphate niobium catalysts have been widely reported[5-8]. Phosphation treatment adds more acidic groups (increases total number of acid sites) and reduces the natural high acid strength of niobic acid.

Niobic acid and niobium phosphate ( $\text{NbOPO}_4$ ) materials have attracted great interest as catalysts for dehydration reactions, due to their strong acid properties which can be preserved in polar liquids like water, presenting them as water-tolerant solid acids. Carlini *et al.*[9] used these catalysts in aqueous reactions at  $100^\circ\text{C}$ . HMF selectivity was high ( $> 90\%$ ) at low conversions ( $< 30\%$ ). When the reaction time was increased, fructose conversion increased while the HMF selectivity dramatically decreased. Carniti *et al.*[5] also studied the same catalysts, but in this case experiments were carried out in a continuous flow reactor under aqueous conditions at temperatures of  $90\text{--}110^\circ\text{C}$ . The niobium phosphate was found to be more active, obtaining 25% HMF yield at 77% fructose conversion at  $110^\circ\text{C}$ . Armaroli *et al.*[8] reported the catalytic activity of commercial niobium phosphates and niobium phosphates prepared by treatment of niobic acid with phosphoric acid, for fructose, sucrose and inulin dehydration reactions. It was observed that the HMF selectivity was very high (98%) at lower reaction times (30 min) for a fructose conversion of 29%. For higher reaction times (2 h), although the sugar conversions increased up to 61%, the HMF selectivity decreased (35%), due to the formation of polymeric by-products. Recently, Edman Tsang's group[4] studied several niobium-based catalysts for the dehydration of sucrose, glucose and fructose, finding that mesoporous niobium oxide gives the overall highest HMF yield (36%) for the conversion of the three saccharides studied, due to the balanced BA and LA of its structure with the most appropriate acid strengths for the conversion of both glucose and fructose components.

Many research groups have tried to synthesize niobium oxide catalysts with higher surface areas employing different supports to improve the dispersion and enhance the number of available active sites. Various oxides such as  $\text{SiO}_2$ ,  $\text{Al}_2\text{O}_3$ ,  $\text{SiO}_2\text{--Al}_2\text{O}_3$ ,  $\text{TiO}_2$ , and  $\text{ZrO}_2$  have been employed as effective supports for niobium oxide species, mainly studied by Jehng and Wachs[10-13]. Lewis acid sites were found in all of the supported niobium oxide catalysts, but Brønsted acid sites were detected only on  $\text{SiO}_2$  and  $\text{Al}_2\text{O}_3$  supports[14]. Supported niobium oxide has been studied and proven to be active in several reactions, such as oxidation of cyclohexene[15], hydrolysis of sucrose[16], esterification of acetic acid[17] and propanoic acid[18], methanol oxidation[19] or dehydration of xylose[20]. To the best of our knowledge, only Carniti's group has reported studies for the dehydration of fructose to HMF using silica supported  $\text{Nb}_2\text{O}_5$ , but always using a non-ordered silica support due to the absence of structure directing agent, providing surface areas between  $90\text{--}450\text{ m}^2/\text{g}$  and working in a continuous reaction line[21, 22].

This chapter reports on the catalytic performance of niobia-based materials in reactions requiring Lewis/Brønsted acidity such as the aqueous phase transformation of glucose and fructose to HMF. When starting from glucose, a catalyst with Lewis acidity or base character is needed to isomerize glucose to fructose, and Brønsted acidity subsequently performs the conversion of fructose to HMF via triple dehydration. Good Brønsted and Lewis acidic characteristics were found on the prepared bulk and supported niobic acid materials in **Chapter 3**, which make them ideal candidates for the aforementioned reactions.

## **4.2 Results and discussion**

### **4.2.1 Glucose and fructose conversion to HMF over bulk PNA catalysts**

Glucose and fructose dehydration reactions were subsequently conducted over thermally treated niobic acid catalysts to investigate their performance. Full reaction conditions are described in **Chapter 2**. Both Brønsted and Lewis acid sites have been identified on the studied niobia catalysts in **Chapter 3**, with acid sites density dependent on structural modifications occurring after thermal treatment. As previously mentioned, glucose transformation to HMF takes place via isomerization of glucose to fructose over Lewis acid sites, followed by dehydration of fructose to HMF over Brønsted acid sites. Here we investigate the different reaction conditions to optimize the aqueous conversion of glucose and fructose to HMF catalysed by bulk niobia catalysts.

#### **4.2.1.1 Effect of catalyst calcination temperature**

The impact of PNA pre-calcination temperature on reactivity was subsequently explored for the aqueous dehydration of glucose and fructose at 100°C, conditions under which good glucose and fructose conversions and modest 5-HMF yields were obtained over the parent amorphous PNA.

##### **4.2.1.1.1 Glucose conversion**

**Figure 4.1** shows glucose dehydration reactions profiles over the series of PNA catalysts. The main products of glucose dehydration in water were fructose, HMF and other unidentified compounds labelled as “other sugars”, since their retention time lies on the area where different saccharides should appear. Moreover, small amounts of levulinic acid and formic acid due to rehydration of HMF were detected, together with other unidentified soluble products[23]. HMF yield experiences a linear increase up to

values of ~8% for amorphous PNA and 300PNA, while orthorhombic 700PNA with no observed Brønsted acidity yielded a mere 0.1% of HMF. Fructose yield stabilizes at 10-14% after 2 h of reaction, and then presumably additional fructose formation is converted to HMF over the Brønsted acid sites present in the niobia catalysts. Additionally, the formation of other sugars is evident by the presence of small peaks in the HPLC chromatogram as shown in **Chapter 2**, and after 2 h of reaction it accounts for a considerable portion of the glucose conversion.

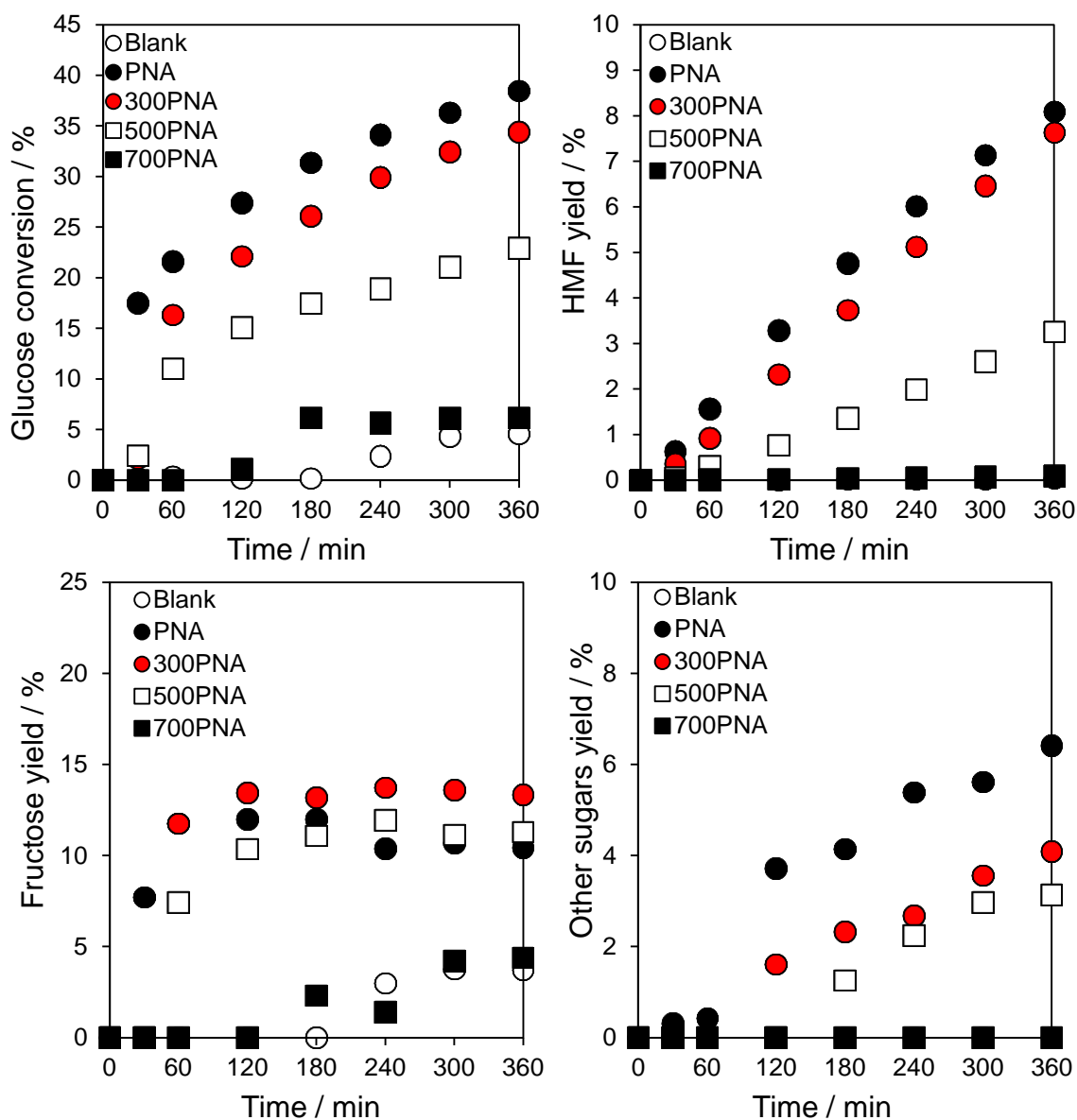


**Figure 4.1** Profiles of glucose conversion and yield of HMF, fructose profiles and other sugars for glucose dehydration after 6 h reaction at 100°C over calcined niobic acid

**Figure 4.2** shows the resulting variations in glucose conversions and the yield and selectivity of main products of glucose dehydration reaction, fructose and HMF, after 6 h as a function of pre-calcination temperature. PNA calcined above 300°C experienced

a noteworthy decrease in glucose conversion, coincident with the modifications in acidity and structural properties arising due to the crystallisation of hexagonal niobia and concomitant drop in surface area, diminishing from a glucose conversion of 38% for the parent material down to 6% conversion over 700PNA, comparable with the stoichiometric reaction. The isomerisation of glucose to fructose proceeded invariable with yield between 10-14% for calcination temperatures between 300–500°C, which can be explained due to the retention of significant Lewis acidity after calcination up to 500°C, whereas the preferential loss of Brønsted acidity over this temperature range systematically suppressed the dehydration of reactively-formed fructose to 5-HMF, decreasing from the 8% obtained with PNA down to 0.1% over 700PNA.

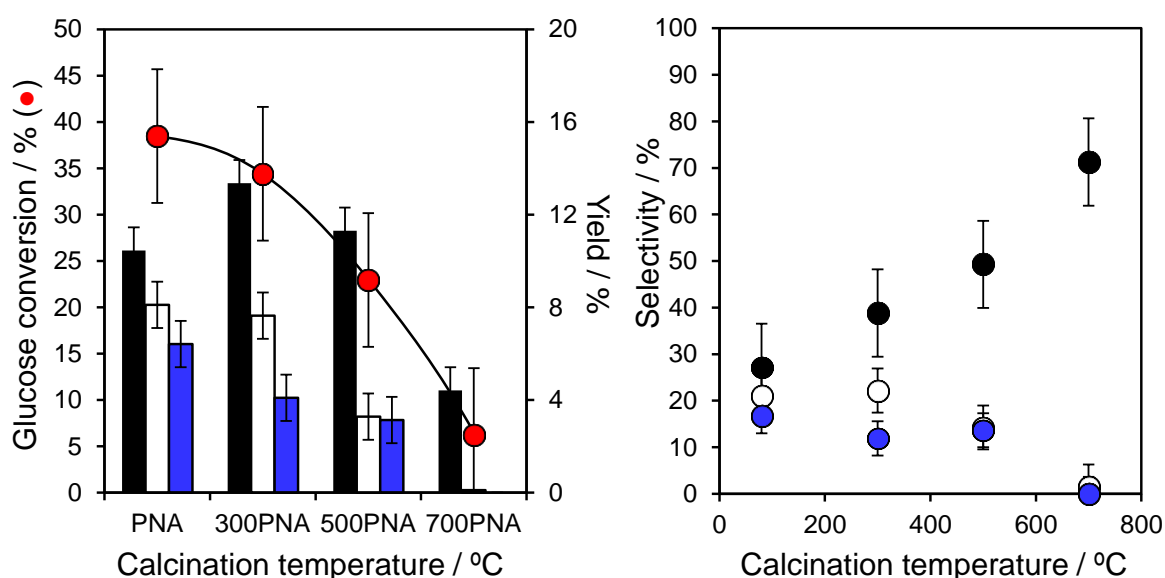


**Figure 4.2** Conversion of glucose over parent niobic acid and corresponding yield (left) and selectivity (right) of HMF (white), fructose (black) and other sugars (blue) as a function of pre-calcination temperature after 6 h reaction at 100°C

The selectivity to HMF decreased in a similar trend to that observed for glucose conversion, falling from a value of 21% for the parent PNA down to 1.6% for 700PNA, a value comparable to the reaction performed in the absence of catalyst. On the other hand, increase in pre-calcination temperature induces a progressive increase in fructose selectivity, changing from 27% to 71% when the parent catalyst is calcined at 700°C. This inverse correlation between HMF and fructose selectivity can be explained by the decrease in B/L ratio experienced by the bulk niobia catalysts when subjected to thermal treatment shown in **Chapter 3**. The decrease in the B/L ratio occurs due to the transformations of protonic sites to Lewis sites with the elimination of water, favouring the isomerization reaction over the dehydration to HMF[24]. However, the products here taken into account stand for 65-75% of the glucose converted, corresponding the

remaining 25-35% to the formation of humins, which were not separated and analysed in this study. Guo *et al.* [2] recently studied the dehydration of glucose to HMF over mesoporous niobia and Nb-W oxides at 140°C in butanol/water system, and found an unsatisfactory mass balance, attributing 50-60% of glucose conversion to humins formation. Yue *et al.* [3] studied the dehydration of glucose to HMF over Nb<sub>x</sub>-WO<sub>3</sub> catalysts in water at 100°C, finding that glucose conversion to HMF was less than 10% and the fructose yield was below 1% using a much higher catalyst-sugar ratio than in the present study. They stated that the strength of acid sites influences over the selectivity towards HMF, thus, strong Brønsted acid sites are responsible for several side reactions, including oligomerization to humins. Ordonsky *et al.* [25] also postulated that rehydration of HMF to levulinic acid and formic acid over Brønsted acid sites and condensation to soluble polymers and humins over Lewis acid sites. Therefore, the modest selectivity towards HMF and substantial rate of humins formation observed in the performed experiments can be explained by the high acid strength characteristic of niobic acid, which remained unperturbed after calcination temperature according to the performed propylamine studies (see **Chapter 3**).

The conversion obtained by the uncalcined material is considerably higher than the best value reported by Osatiashtiani *et al.* (23%) over sulfated zirconia using the same reaction conditions, although similar selectivity to HMF ~20% was obtained. The higher performance of PNA could be due to its higher acidic properties as reported in **Chapter 3**. Similar or lower selectivity (15-20%) has also been found in other studies conducted at higher reaction temperatures, for example Zeng *et al.*[26] used Al-Zr mixed oxides in hot compressed water at 180°C, and although conversion of glucose was almost complete after 2 h, selectivity to HMF could not surpass 15%. Also Nakajima *et al.*[27] obtained the same selectivity with full glucose conversion using niobic acid prepared from a chloride precursor after 3 h reaction at 120°C. However, in both cases reaction conditions are quite different, with a much higher catalyst loading, 75 wt% and 10 wt% respectively, compared with the 0.5 wt% used in the present studies.

From the reaction profiles, the rates of glucose conversion and HMF formation and consequently glucose turnover frequency and HMF productivity were calculated. **Figure 4.3** shows glucose turnover frequency and HMF productivity normalized to the total number of acid sites, and after the subtraction of the background contribution observed in the stoichiometric reaction. As seen in this figure, glucose TOF systematically increase from a value of 0.7 h<sup>-1</sup> for the amorphous PNA and 300PNA up to 2.5 h<sup>-1</sup> for the orthogonal 700PNA, in spite of the fall in glucose conversion upon

calcination. This trend reflects the steep fall in acid loading following calcination, i.e. presence of fewer, but more active catalytic sites, for both isomerisation and dehydration steps. On the other hand, HMF productivity displays a value of  $0.06 \text{ h}^{-1}$  for the parent PNA catalysts and stabilizes around  $0.04 \text{ h}^{-1}$  for the calcined catalysts. When subjected to thermogravimetric analysis, the parent PNA presented desorption of structural and physisorbed water, while the rest of calcined catalysts showed only desorption of the latter. The presence of water in niobic acid gives rise to the Brønsted acidity of the catalyst, thus the structural water present only in the parent PNA could explain the slightly higher HMF productivity of this catalyst. Although the calcined catalysts suffer the progressive loss of surface water, it has been suggested that the presence of niobic acid in aqueous media can rehydrate the surface of the catalyst, regenerating the Brønsted acidity of the materials and thus promoting the fructose dehydration to HMF[28]. This rehydration of the calcined catalysts explains the stable productivity of HMF for the pre-calcined materials.

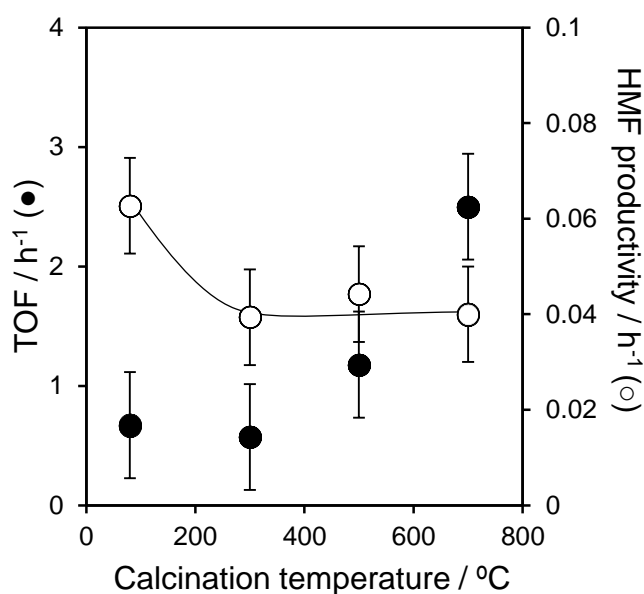


**Figure 4.3** Turnover frequencies for the aqueous phase conversion of glucose and associated HMF productivity normalised to total acid loading as a function of pre-calcination temperature

#### 4.2.1.1.2 Fructose conversion

In order to verify the idea of dehydration of glucose to HMF via previous isomerization to fructose, experiments using fructose as starting material were conducted over the pre-calcined niobia catalysts under the same catalytic conditions.

**Figure 4.4** shows fructose conversion and yield of main products reactions profiles over the series of PNA catalysts. The main products of fructose dehydration in water were HMF, glucose, and other unidentified sugars; however small amounts of levulinic acid and formic acid due to rehydration of HMF were detected, together with other unidentified insoluble products (humins). The low amount of levulinic and formic acid, together with the always increasing HMF yield with the conversion of fructose, suggest that HMF was a final product, in agreement with the studies carried out by Marzo *et al.* for the aqueous fructose dehydration in a flow reactor with fixed catalytic bed at constant temperature of 100°C[29]. Contrarily, glucose and other sugars are formed rapidly during the first 2 h of reaction and stabilize for the rest of the reaction.

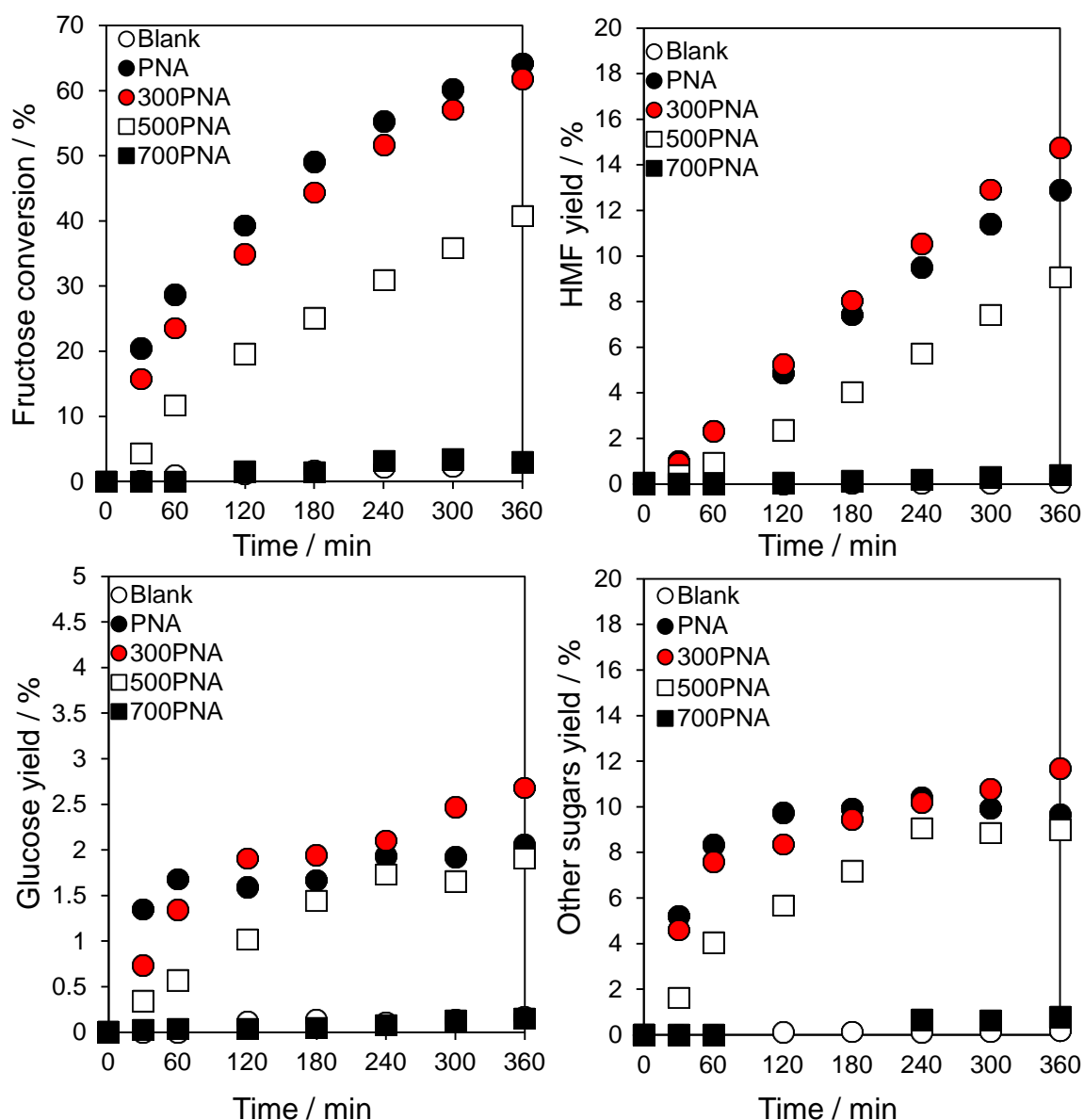


**Figure 4.4** Profiles of fructose conversion and yield of HMF, glucose and other sugars for fructose dehydration after 6 h reaction over calcined niobic acid at 100°C

**Figure 4.5** shows the results for conversions and the yield and selectivity of main products of fructose dehydration reaction, HMF, glucose and other sugars, after 6 h of reaction as a function of pre-calcination temperature. It is noteworthy that a higher activity was achieved when fructose was used as starting reagent compared to that observed for glucose. PNA and 300PNA as amorphous materials able to retain their textural and acidic properties showed conversions ~63%, representing a 60% increase with regard to the 38% attained during glucose dehydration over the same catalyst. Although the overall conversions obtained for the dehydration of fructose are considerably higher than the ones obtained from glucose, the same declining trend with calcination temperature is observed. The same gradual decrease in conversion was observed by Wang *et al.* [30] in their study of niobic acid calcined at different temperatures for the catalytic dehydration of fructose to HMF, which was also attributed to the transformation of niobic acid to pseudo-hexagonal phase and further to the orthorhombic phase, resulting in the decrease of surface area, acid strength, and acid sites loading. However, even at 90°C and 2 h reaction time, their conversion and selectivity were much higher compared to those presented here due to the choice of an organic solvent as reaction media, which inhibits the further transformation of HMF to rehydration products as well as the production of humins.

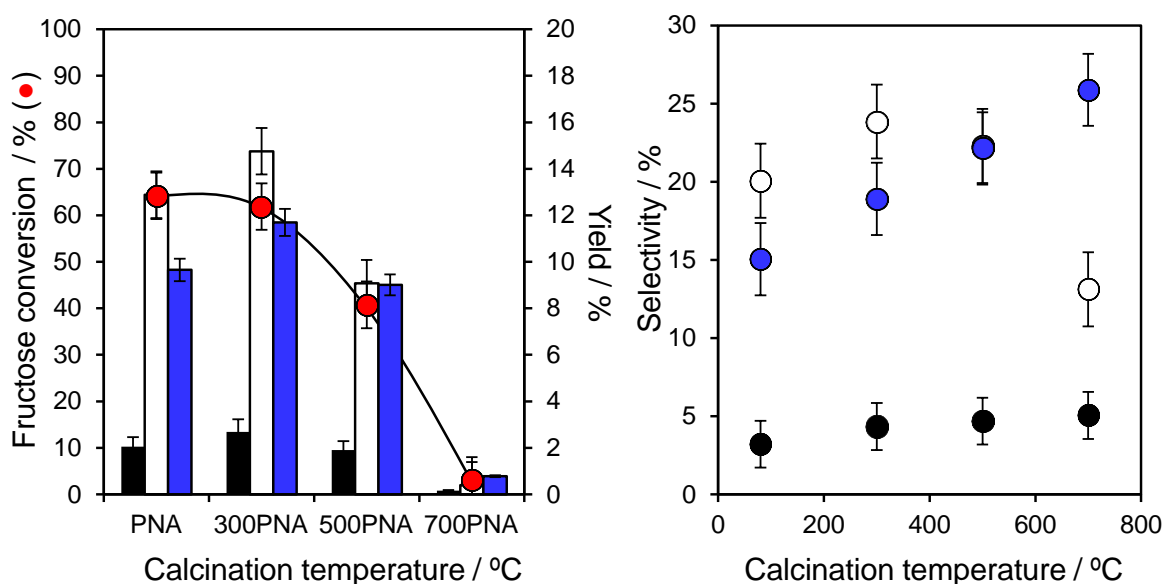


**Figure 4.5** Conversion of fructose over parent niobic acid and corresponding yields (left) and selectivity (right) of HMF (white), glucose (black) and other sugars (blue) as a function of pre-calcination temperature after 6 h reaction at 100°C

A minor amount of glucose is observed for all the catalysts studied, although never surpassing a yield value of 3%. An almost two-fold increase in HMF yield was also observed for fructose dehydration in comparison with glucose, reaching up to 15%

HMF yield, which rapidly decrease with the crystallization of the catalysts. However, selectivity values were comparable to those found for glucose dehydration, with values between 20-25% for catalysts calcined under 500°C and a slight decrease for the highest calcined material due to the loss of Brønsted acidity, although the low conversion and yields achieved by this catalyst, make difficult the quantification of products. Moreover, the overall selectivity to accountable products is between 40-50%, resulting in a striking 50% production of humins, as evident from the reaction mixtures acquiring a brown coloration intensified with reaction time. Similar selectivity (20-30%) to HMF was reported by Osatiashtiani *et al.*[31] under the same reaction conditions using a bifunctional sulfated zirconia catalyst with different sulphate loadings, although the maximum fructose conversion achieved by those catalysts was 25%, proving the greater performance of niobic acid solid acids.

In their study of glucose dehydration to HMF over phosphate catalysts, Ordonsky *et al.* [6] found evidence that while Brønsted acid sites account for the dehydration of fructose to HMF, Lewis acid sites transform fructose mainly to glucose and humins. Antonetti *et al.* [32] recently studied the dehydration of fructose and inulin to HMF catalysed by niobium and zirconium phosphate catalysts under microwaves assistance, and hypothesised that while strong Brønsted acid sites are responsible for the fructose conversion, selectivity to HMF is driven by medium strength Brønsted acid sites. In the light of the presented results, we can theorize that the relatively high conversion considering the mild experimental conditions can be attributed to the high acid strength of the niobic acid, simultaneously causing the modest HMF selectivity in favour of humins formation.

From the reaction profiles, the rates of fructose conversion and HMF formation and consequently fructose turnover frequency and HMF productivity were calculated. **Figure 4.6** shows fructose turnover frequency and HMF productivity normalized to the number of total acid sites, and after the subtraction of the background contribution observed in the stoichiometric reaction. In this figure we can observe a similar TOF trend than the obtained for glucose experiments, with a systematic increase from a value of 0.9 h<sup>-1</sup> for the amorphous PNA and 300PNA up to 1.6 h<sup>-1</sup> for the pseudohexagonal 500PNA, and dropping for the orthogonal 700PNA, in spite of the fall in fructose conversion upon calcination, highlighting the presence of fewer, but more active catalytic sites, also when fructose is used as reactant. On the other hand, HMF productivity displays a value of 0.07 h<sup>-1</sup> for the parent PNA catalysts and increases up to 0.18 h<sup>-1</sup> for the calcined catalysts.

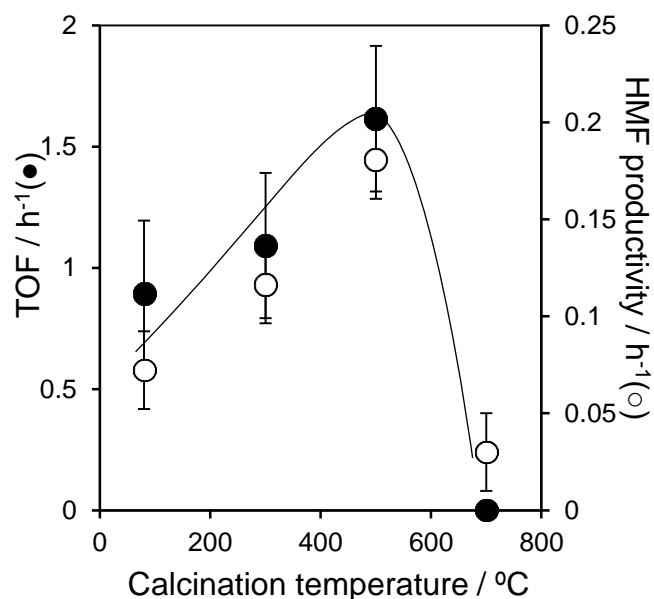


**Figure 4.6** Turnover frequencies for the aqueous phase conversion of fructose and associated HMF productivity normalised to total acid loading as a function of pre-calcination temperature

In conclusion, fructose dehydration to HMF can be realized over Brønsted acid sites more easily than glucose because the reactivity of fructose (ketose) is higher than that of glucose (aldose) in aqueous solution. In both cases, the direct dehydration of glucose and fructose leads to low selectivity of HMF due to side reactions like unselective condensation, but especially due to the formation of humins due to the high acid strength of the catalysts. Since parent PNA was the most active catalyst in the glucose and fructose reactions, it was used for the subsequent tests.

#### 4.2.1.2 Effect of reaction temperature

Reaction temperature is a crucial parameter for HMF formation, thus the influence of reaction temperature for the dehydration of glucose and fructose to HMF was studied between 80-110°C over parent niobic acid. Extensive studies have been performed in a wide range of temperatures and using different catalysts for the sugar dehydration reaction to HMF. Do Prado *et al.* [33] observed a fructose conversion increase from 6 to 71% by increasing the temperature from 70°C to 130°C, with no formation of HMF at temperatures below 70°C in aqueous system over thermally treated niobium oxide. Zhang *et al.* [7] studied the aqueous dehydration of fructose to HMF over mesoporous niobium phosphate between 110-130°C, and concluded that fructose conversion and HMF yield are positively related to reaction temperature below 130°C although the selectivity to HMF decreased with increasing temperature. For reaction temperatures over 130°C, the yield decreased from 45.0 to 29.4% due to decomposition of HMF to

humins when the reaction is subjected to high temperature. Thus, the effect of glucose and fructose reaction temperature has been investigated ranging from 80°C to 110°C using PNA as catalyst.

#### 4.2.1.2.1 Glucose conversion

Figure 4.7 shows glucose dehydration reactions profiles over parent PNA at different reaction temperatures. The main products observed were HMF, fructose and other sugars, while also smaller amounts of levulinic acid and formic acid due to rehydration of HMF were detected, together with other unidentified insoluble products referred to as humins.

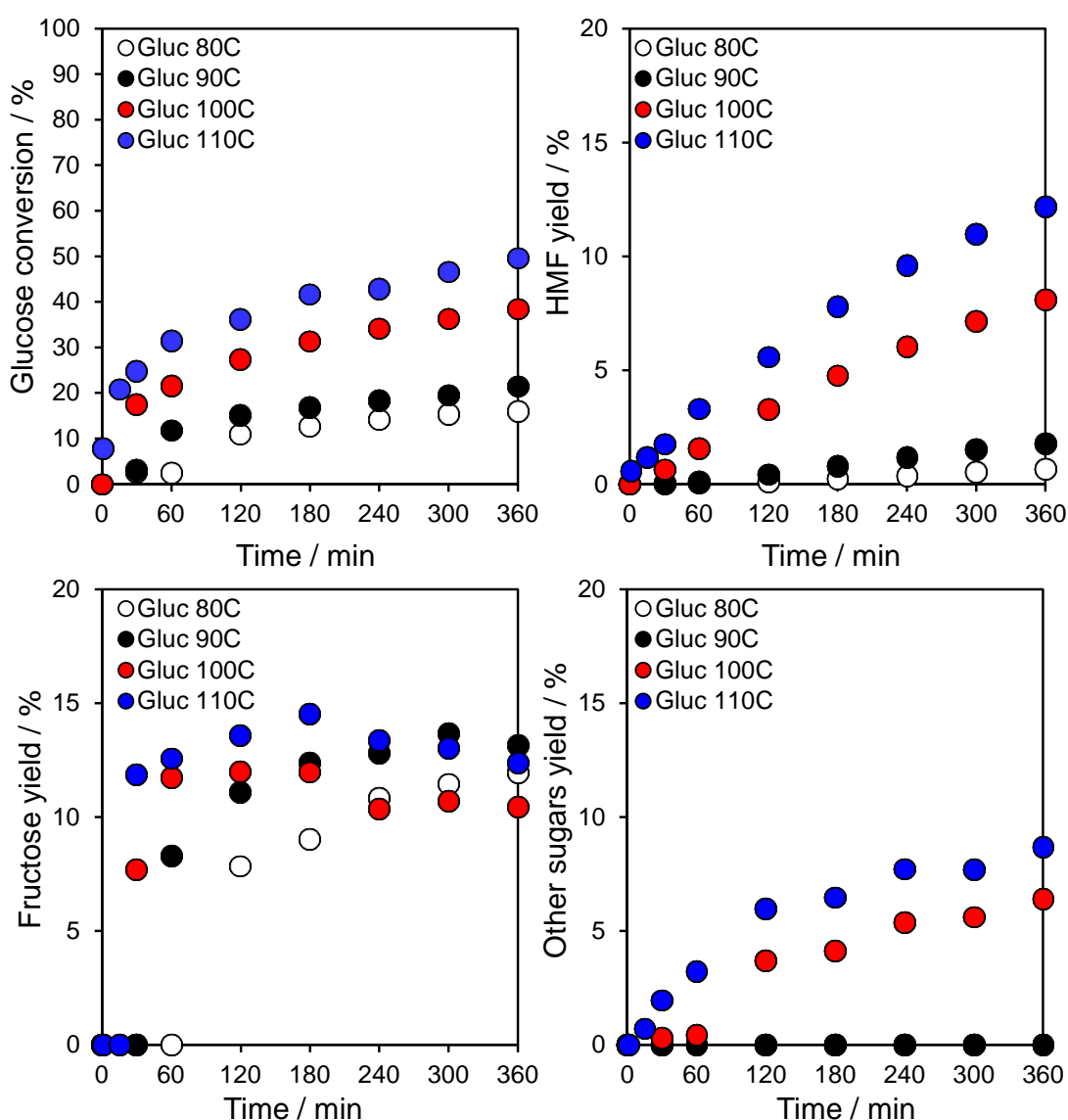
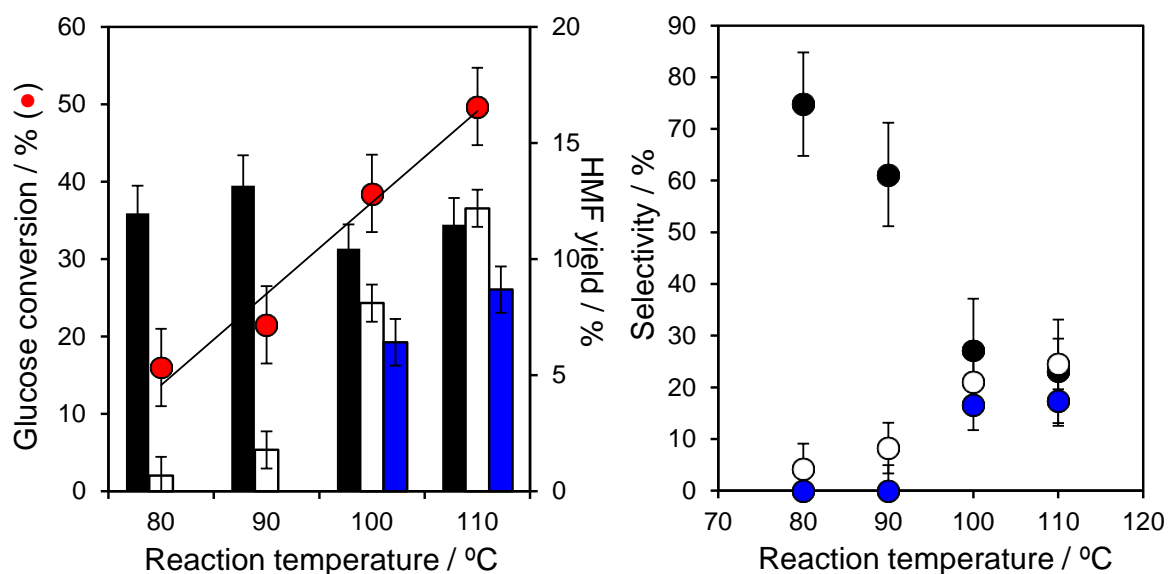


Figure 4.7 Profiles of glucose conversion and yield of HMF, fructose and other sugars for glucose dehydration after 6 h reaction over parent niobic acid at different reaction temperatures

**Figure 4.8** shows the resulting variations in glucose conversions and the yield and selectivity of main products of glucose dehydration reaction, HMF, fructose and other sugars, after 6 h as a function of reaction temperature. The linear increase of glucose conversion from 16 to 50% after temperature in increased from 80°C to 110°C evidences the remarkable temperature sensitivity of the reaction. These conversions are comparable or superior to literature values for glucose over sulphated zirconia[31] or sulfated mesoporous niobia[34] at similar fructose/glucose concentrations, but at lower temperature and in the absence of any co-solvents. HMF yield is unsurprisingly small, it experiences an almost linear increase with reaction temperature, reaching 12% at 110°C (comparable to the performance of TiO<sub>2</sub> and ZrO<sub>2</sub> at 200°C[35]). An HPLC chromatogram free of alternate peaks other than glucose, fructose, HMF and internal standard is observed at reaction temperatures below 100°C, but after this temperature is reached, other by-products in the form of unidentified saccharides are produced in a considerable manner, getting yields of up to ~9% for the highest reaction temperature studied, while the production of glucose is quite stable at 10-14% at any temperature studied.



**Figure 4.8** Conversion of glucose over parent niobic acid and corresponding yields (left) and selectivity (right) of HMF (white), fructose (black) and other sugars (blue) as a function of reaction temperature after 6 h reaction

Reaction temperature also shows a noticeable effect in the selectivity of the observed products. Thus, fructose selectivity linearly decreases from a striking 75% down to 24% and HMF selectivity experiences a linear increase from 4% to 25% between 80°C and 110°C, meaning that the increase of temperature induces the transformation of HMF through the dehydration of the fructose formed by isomerization of glucose. However,

the total selectivity of main products decreases from 79% to 65%, meaning that there is a relative increase of unidentified products (mainly humins) because of the promotion of side reactions with the increase of reaction temperature. The inhibition of these side reactions can be observed in the study of Guo *et al.* [2], who investigated the conversion of glucose into HMF over Nb<sub>2</sub>O<sub>5</sub> in the 2-butanol/H<sub>2</sub>O biphasic system at 140°C. Under this solvent, over 55% of glucose was converted but only with a 2% HMF yield, which nonetheless was increase up to 35% with 95% of glucose conversion when reaction temperature was increased up to 120°C. HMF selectivity experienced a constant increase from 80°C up to 140°C. However, at reaction temperature over 140°C, the side reactions such as HMF rehydration and condensation resulted in the decrease of HMF yield and selectivity. Also Zhang *et al.* [28] detected 140°C as limit temperature when glucose conversion increased from 19.9% to 71.0% and yield of HMF increased from 14% to 31% over niobium phosphate in aqueous system. Beyond that temperature no increase of HMF was detected due to the favoured side reactions.

From the reaction profiles, the rates of glucose conversion and HMF formation and consequently glucose turnover frequency and HMF productivity were calculated. **Figure 4.9** shows glucose turnover frequency and HMF productivity normalized to the number of total acid sites, and after the subtraction of the background contribution observed in the stoichiometric reaction. Glucose TOF and HMF productivity increase from 0.14 h<sup>-1</sup> to 0.78 h<sup>-1</sup> and from 0.001 h<sup>-1</sup> to 0.082 h<sup>-1</sup> respectively when the reaction temperature is increased from 80°C to 110°C, evidencing the clear temperature sensitivity of the reaction.

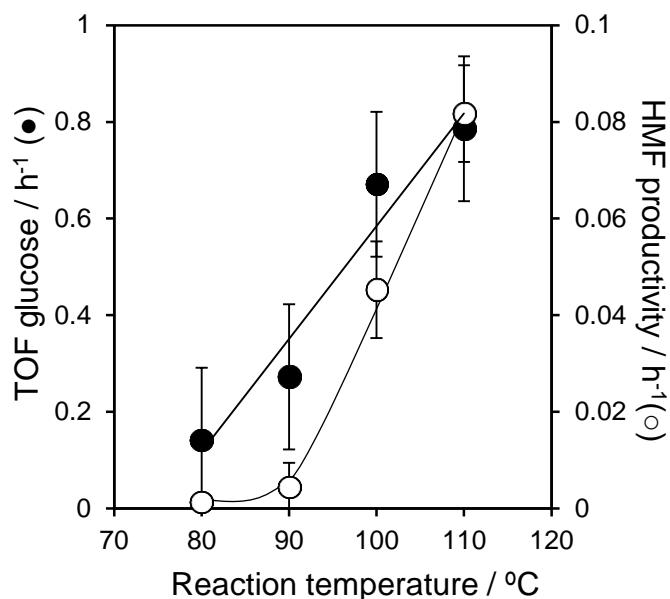


**Figure 4.9** Turnover frequencies for the aqueous phase conversion of glucose and associated HMF productivity normalised to total acid loading as a function of reaction temperature

#### 4.2.1.2.2 Fructose conversion

**Figure 4.10** shows fructose dehydration reactions profiles over parent PNA at different reaction temperatures. As expected, the fructose conversion and HMF yield regularly increase with contact time as well as with temperature, while glucose was never produced over 3% yield at any reaction time or temperature. Linear increase in fructose formation and HMF yield is observed for reaction temperatures below 100°C, while the reaction performed at 110°C shows the start of a plateau for these parameters after 4 h of reaction time. As in the case of glucose, the formation of other sugars reach a degree of stability at a certain time of the reaction, with the exception of the reaction performed at 110°C, in which a maximum production of unidentified saccharides is observed at 3 h, to decrease after this point, likely due to the transformation of these sugars to condensation products as deduced from the brown coloration of the reaction media.

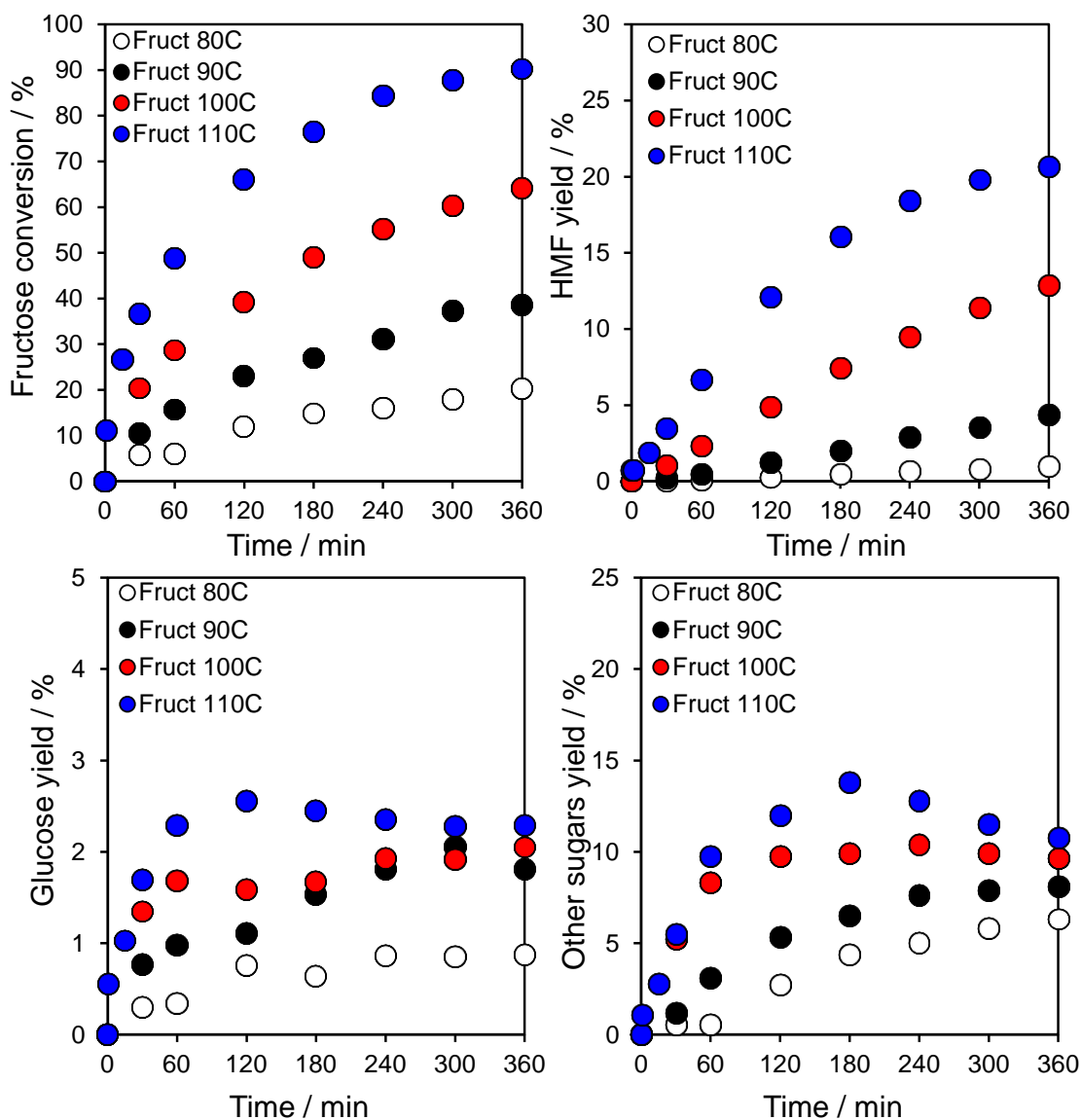


**Figure 4.10** Profiles for fructose conversion and yield of HMF, glucose and other sugars for fructose dehydration after 6 h reaction over parent niobic acid at different reaction temperatures

**Figure 4.11** shows a similar linear increasing trend with increasing reaction temperature for fructose conversion and HMF yield than those found for the glucose dehydration reactions. Nonetheless, these values are much higher than those obtained for glucose dehydration, with fructose conversion increasing from 20% to 90% increasing the reaction temperature from 80°C to 110°C. These conversions are comparable or superior to literature values for fructose over tungstated zirconia[31], 25%CeO<sub>2</sub>/75%Nb<sub>2</sub>O<sub>5</sub>[36] and Ag<sub>3</sub>PW<sub>12</sub>O<sub>40</sub>[37], at similar fructose/glucose concentrations, but at lower temperature and in the absence of any co-solvents. An exponential increase in HMF formation was observed with temperature dependence, producing up to 21% for the higher investigated reaction temperature, which means a

two-fold yield increase when compared with that obtained by the stepwise isomerisation and subsequent dehydration of glucose. Although glucose selectivity slightly increases with reaction temperature, it never surpasses a value of 5%, while HMF experiences a steep increase in selectivity in the considered range of reaction temperature. The decrease in selectivity of “other sugars” in favour of HMF selectivity with increasing temperature indicates that the preference for HMF formation is enhanced at higher temperatures in the range of reaction temperatures studied and in the presence of the highly active niobic acid catalyst. The higher reactivity of fructose (to predominantly 5-HMF) is in accordance with previous reports that its solid acid catalysed dehydration is more facile than glucose isomerisation [35, 37]. Thus, in light of the above results, we can conclude that glucose isomerisation to fructose is clearly the rate-determining step in 5-HMF production over PNA.

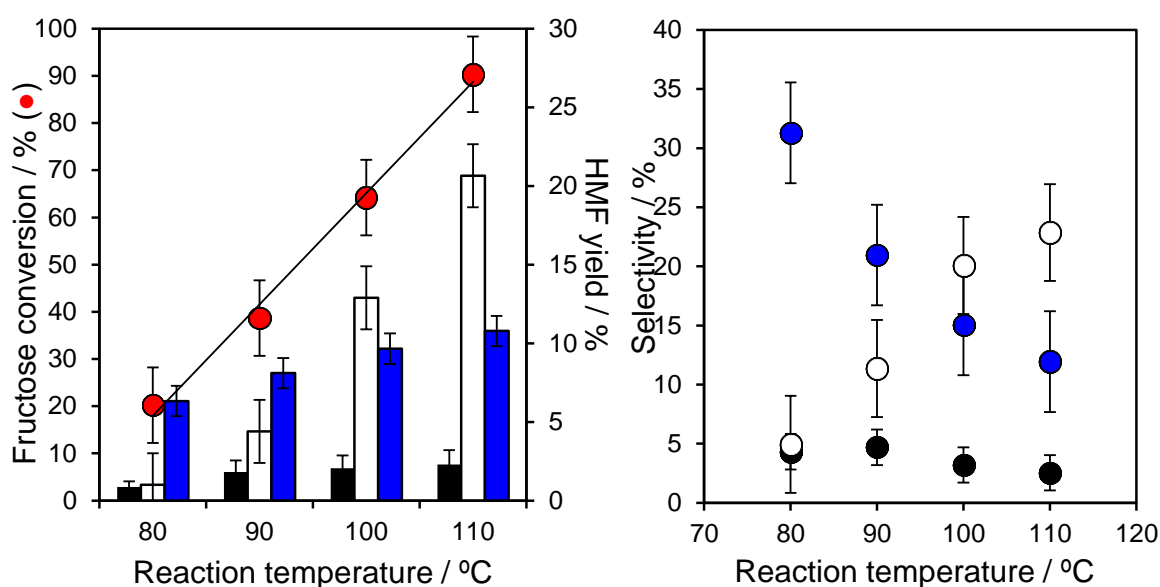


**Figure 4.11** Conversion of fructose over parent niobic acid and corresponding yields (left) and selectivity (right) of glucose (black), HMF (white) and other sugars (blue) as a function of reaction temperature after 6 h reaction

From the reaction profiles, the rates of fructose conversion and HMF formation and consequently glucose turnover frequency and HMF productivity were calculated. **Figure 4.12** shows glucose turnover frequency and HMF productivity normalized to the total number of acid sites, and after the subtraction of the background contribution observed in the stoichiometric reaction for each reaction temperature. Fructose TOF and HMF productivity increase from  $0.14 \text{ h}^{-1}$  to  $1.1 \text{ h}^{-1}$  and from  $0.003 \text{ h}^{-1}$  to  $0.19 \text{ h}^{-1}$  respectively when the reaction temperature is increased from  $80^\circ\text{C}$  to  $110^\circ\text{C}$ , evidencing the clear temperature sensitivity of the reaction. A relative increase of 29% and 57% was observed for TOF and productivity respectively when the reagent was

fructose instead of glucose, proving the simpler transformation to HMF when the isomerization step is not involved in the reaction.

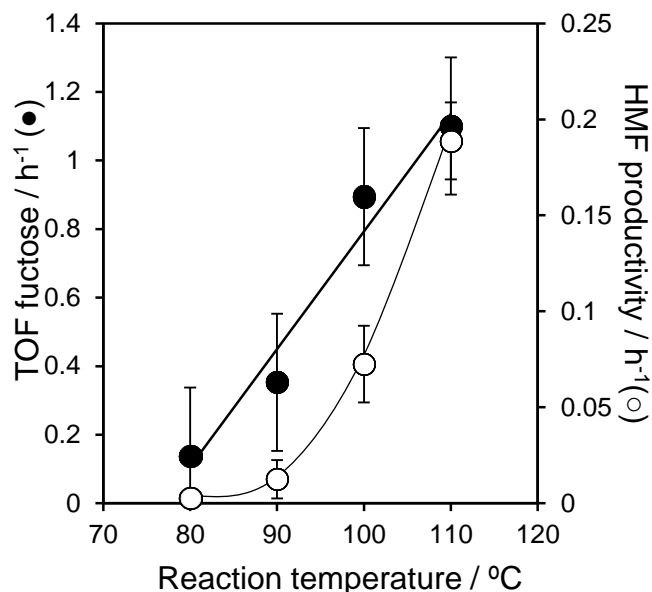


**Figure 4.12** Turnover frequencies for the aqueous phase conversion of fructose over parent niobic acid normalised to Brønsted acid loadings and associated HMF productivity normalised to total acid loading as a function of reaction temperature

#### 4.2.1.2.3 Calculation of activation energy

The Arrhenius plot for glucose and fructose conversion and HMF production from glucose and fructose as reactants is depicted **Figure 4.13**. The estimated apparent activation energy for glucose and fructose conversion was found to be 79.3 kJ/mol and 87.4 kJ/mol respectively, while HMF production from glucose and fructose over PNA possesses apparent activation energy of 188.6 kJ/mol and 174.7 kJ/mol respectively. Therefore, it can be concluded the much higher activation energy for HMF production compared to the one from conversion of glucose and fructose, thus the side reactions have a lower activation barrier, explaining low selectivity to HMF and why the reactants tend to be converted to other compounds rather than to HMF.

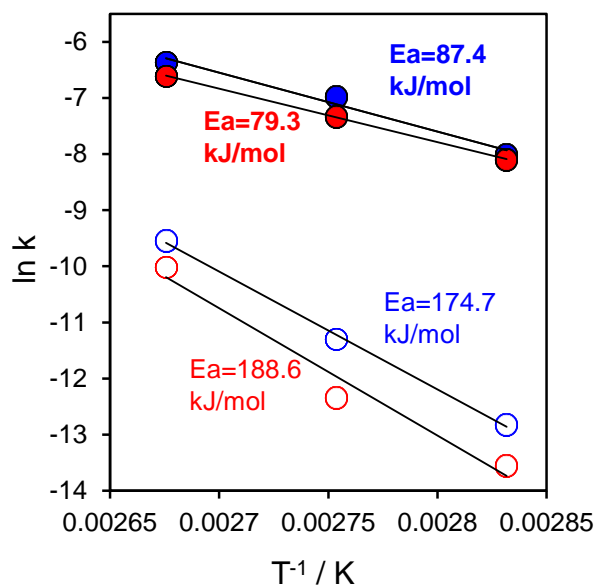


**Figure 4.13** Determination of the activation energy from Arrhenius equation for the conversion of glucose (red) fructose (blue) (filled symbols), and for the HMF formation (open symbols) from glucose (red) and fructose (blue)

In 2013 Van Putten *et al.* [38] published a study reviewing the kinetic studies on HMF formation from glucose, fructose and other biomass-based compounds reported up to that date. Due to the different range of catalysts and/or solvents reviewed, it was difficult to draw general conclusions, but some interesting results for aqueous systems were gathered. The activation energy for the hydrothermal decomposition of fructose in water was determined in two separate studies [39, 40] and reported to be about 120 kJ/mol. In aqueous systems, activation energies for fructose conversion ranged from 66 kJ/mol for the dehydration of fructose using niobium phosphate at relatively low temperatures (90–120°C) [5] and 160 kJ/mol for the conversion of fructose at high temperatures (210–270°C) using HCl as the catalyst at a fixed pH of 1.8 [41]. In this last study, also the activation energy for the side reaction to humins was reported, which with a value of 102 kJ/mol explains the preferred conversion of fructose to humins instead of to HMF due to its lower activation energy. The lowest activation energy for a non-aqueous system was 60.4 kJ/mol, reported for fructose conversion in acetone/DMSO (70:30) using an ion-exchange resin as the catalyst[42].

When glucose was used as a reactant, reported activation energy for the dehydration to HMF spans a range of 55–152 kJ/mol when it was studied over 1–3 wt % sulfuric acid as the catalyst at 170–190°C for the former[43] and varying sulfuric acid concentration (0.05–1M) and temperature (140–200°C) for the latter[44], underlining the sensitivity of the HMF production on temperature. Other interesting results that fall between these values for glucose conversion, and approximate those obtained in this

thesis, were reported by Guo *et al.* [45] over Nb<sub>4</sub>W<sub>4</sub> at 100-120°C in aqueous system (90.2 kJ/mol) and Rajabbeigi *et al.* [46] over Sn-beta at 70-130°C in aqueous system for the isomerization of glucose to fructose (95 kJ/mol).

After this literature analysis it is possible to conclude that the precipitated niobic acid presents a good activation energy taking into account the milder conditions compared with the reported in the literature. Also, activation energy for the humins formation, when reported, is lower than that of HMF production, justifying the preferred formation of these undesired products.

#### **4.2.1.3 Effect of reactant concentration**

Generally, the substrate concentration has a significant influence on the HMF yield and selectivity for heterogeneous catalytic reactions. In order to achieve a more economical and sustainable process, the reaction mixtures should be able to be performed at a high feedstock concentration to evaluate their potential use in practical applications. However, the main drawback for the use of high concentration solutions is the resulting low selectivity towards the desired products. The rate of cross-polymerization and humin formation has been reported to increase with an increase in starting saccharides concentrations, and thereby lower the desired HMF yield. The formation of humins can be as high as 35% for 18 wt% fructose solution and 20% for 4.5 wt% fructose solution in water[23]. Therefore, a significant loss of HMF yield has been reported in aqueous medium. Thus, the effect of glucose and fructose initial concentration has been investigated for concentration values of 1, 5 and 10 g/L, corresponding to 0.1, 0.5 and 1 wt% using PNA as catalyst at 100°C.

##### **4.2.1.3.1 Glucose conversion**

**Figure 4.14** shows glucose dehydration reactions profiles as mmol of glucose converted and mmol of product (HMF, fructose and other sugars) formed over parent PNA at different initial glucose concentrations. A fast increase in glucose conversion is observed in the first hour of reaction, after which a slow rate of conversion is observed for glucose concentrations of 1 and 5 g/L, almost plateauing after the second hour of the reaction, suggesting that the catalyst activity is limited by the high dilution of glucose. In these systems the combination of mass transport limitation and competitive adsorption of water and sugar on the surface of the catalyst hinders its potential activity. Higher concentrations enable an enhanced contact of the reagent with the active sites of the catalyst, leading to a higher molar conversion of reagent in the range of reaction time studied.

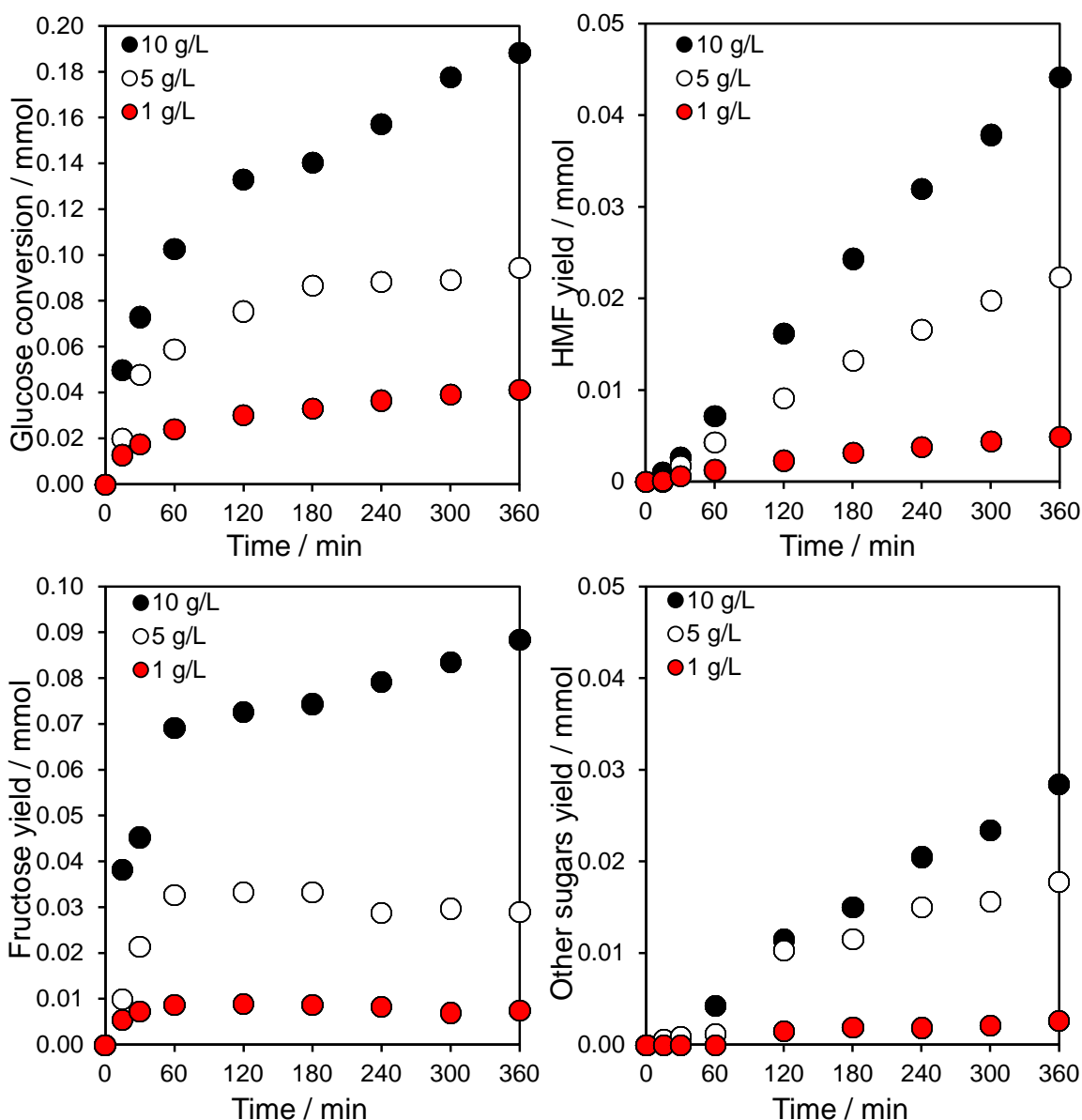


**Figure 4.14** Profiles of glucose conversion and yield of HMF, fructose and other sugars for glucose dehydration after 6 h reaction at 100°C over parent niobic acid at different glucose concentrations

The effect of glucose initial concentration on the efficiency of the dehydration reaction after 6 h is presented in **Figure 4.15**. A linear increase in glucose conversion in terms of mmol produced is observed with increasing initial reagent concentration. Likewise, similar increasing trend is observed for the main reaction products studied, HMF, fructose and other sugars. This can be explained by the influence of transport limitation phenomena as explained above. When extremely diluted solutions are used, the contact of the catalyst active sites with the reagent is not optimum, being influenced by a competition with water molecules on the surface of the catalyst. As sugar concentration is increased, the adsorption of sugar on the catalyst surface is favoured,

leading to an improved product formation, including HMF. Also natural concentration effects will favour nucleation and reaction.

It has been widely reported in the literature that an increase in feedstock concentration causes a drop in HMF formation due to the thriving of side reactions. Guo *et al.* [2] studied the variation in initial glucose concentration in the range of 1-10 wt% over Nb<sub>2</sub>O<sub>5</sub> in the 2-butanol/H<sub>2</sub>O biphasic system at 140°C, and although high conversion was maintained for the higher concentration (92%), a decrease in conversion, HMF selectivity and HMF yield was observed due to excessive unreacted glucose and formed HMF, leading to side reactions such as condensation and rehydration. Zhang *et al.* [28] reported a decrease in HMF yield from 38% to 25% when glucose dosage increased from 1 wt% to 7 wt% over niobium phosphate in aqueous system at 140°C. Atanda *et al.* [47] contemplated a HMF yield decrease from 81% to 45% when initial glucose concentration was increased from 2 to 10 wt% in the n-butanol/H<sub>2</sub>O biphasic system at 170°C over phosphate TiO<sub>2</sub> catalysts. Wang *et al.* [48] also developed a literature review gathering studies for the glucose and fructose dehydration in monophasic, biphasic and ionic liquid systems performed at different reactant concentrations (1-10 wt%) and catalyst loadings (10-100 wt%).

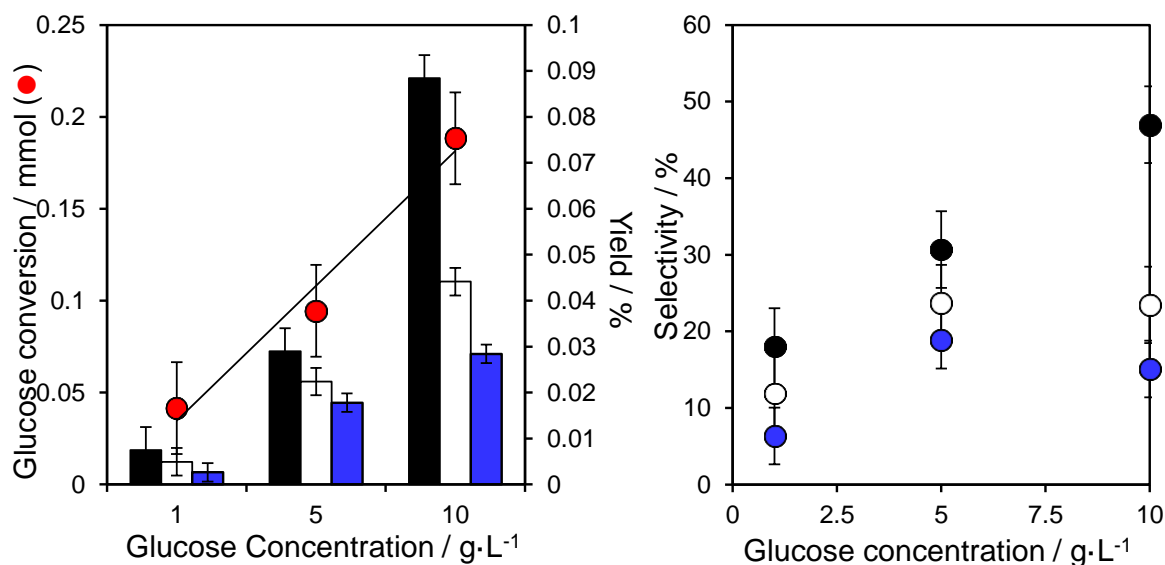


**Figure 4.15** Conversion of glucose over parent niobic acid and corresponding yields of fructose (black), HMF (white) and other sugars (blue) after 6 h reaction at 100°C as a function of glucose concentration

Regarding the selectivity to main products, an increase from 12% to 24% is observed when initial glucose concentration was varied from 1 to 5 g/L, and remained at 24% for the highest concentration studied. Fructose was the preferential product obtained at any of the glucose concentrations studied, and its selectivity increased even when

glucose concentration of 10 g/L was used, reaching a value of 47%. It is noteworthy that the adopted conditions for this study are much milder compared to those usually reported in the literature. The higher production of humins with increasing feedstock concentration found in the literature could be also affected by the other promoting effects such as higher reaction temperatures, usually over 140°C and higher glucose concentration studied (up to 10 wt% compared with the maximum 1 wt% here reported), since usually when 1 wt% is used in the literature, it tends to be the best studied value.

From the reaction profiles, the rates of glucose conversion and HMF formation and consequently glucose turnover frequency and HMF productivity were calculated. **Figure 4.16** shows glucose turnover frequency and HMF productivity normalized to the number of acid sites of PNA, and after the subtraction of the background contribution observed in the stoichiometric reaction. Glucose TOF and HMF productivity increase from 0.3 h<sup>-1</sup> to 1.2 h<sup>-1</sup> and from 0.01 h<sup>-1</sup> to 0.08 h<sup>-1</sup> respectively when the glucose concentration is increased from 1 g/L to 10 g/L. The increasing values of TOF and productivity are explained by the aforementioned enhancement of reagent-catalyst contact with increasing reagent concentration.

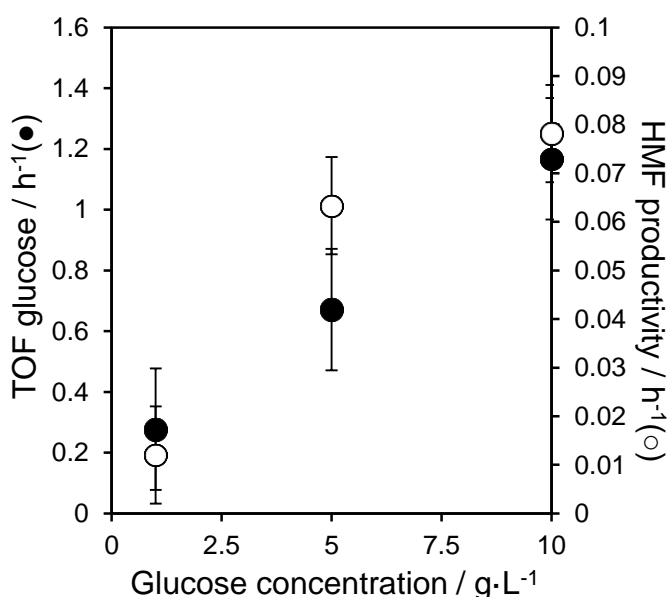


**Figure 4.16** Glucose turnover frequency and HMF productivity over parent niobic acid as a function of glucose concentration

#### 4.2.1.3.2 Fructose conversion

Figure 4.17 shows fructose dehydration reactions profiles over parent PNA at different initial fructose concentrations. As observed in the case of glucose conversion, a fast increase in fructose conversion and production of glucose and other sugars is attained in the first hour of reaction, and the yield of these products stabilizes after the second hour of reaction. Contrarily, HMF generation is determined by a linear increase in the period of time studied for these reactions.

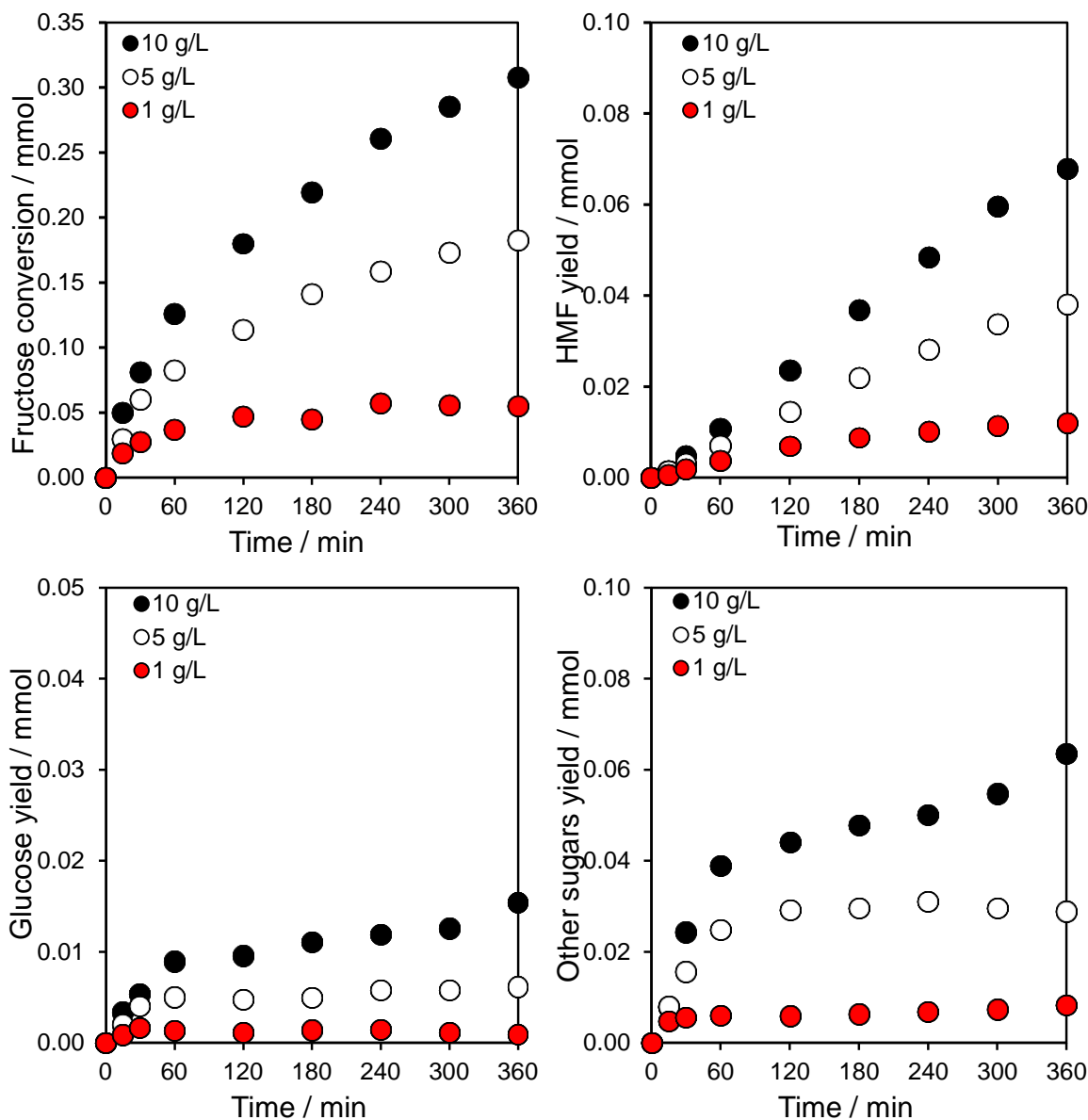
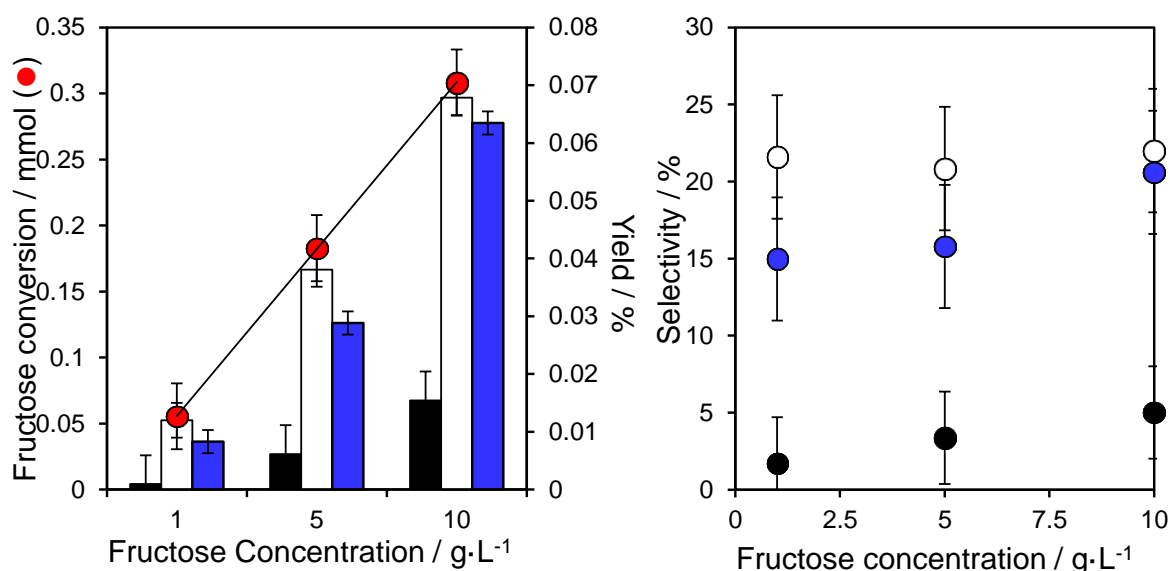


Figure 4.17 Profiles of fructose conversion and yield of HMF, glucose and other sugars for fructose dehydration after 6 h reaction at 100°C over parent niobic acid at different fructose concentrations

The effect of fructose concentration on the efficiency of the dehydration reaction is presented in **Figure 4.18**. An increasing conversion trend similar to that from glucose dehydration reactions is observed here for both fructose conversion and products formation. However, the reaction pathway is not modified by the concentration variation, as it is suggested by the stable product selectivity of HMF (~21%), glucose (~3%), and other sugars (~16%).

Carlini *et al.* [9] observed a decrease of fructose conversion from 75% to 45% over commercial niobic acid calcined at 255°C when initial concentration was modified from 6 wt% to 10 wt% respectively. Performing extraction with washing of the reaction media with an organic solvent, only a slight decrease in products selectivity from 98% to 90% after 1 h in aqueous system at 100°C was reported.



**Figure 4.18** Conversion of fructose over parent niobic acid and corresponding yields of HMF (white), glucose (black) and other sugars (blue) after 6 h reaction at 100°C as a function of fructose concentration

From the reaction profiles, the rates of fructose conversion and HMF formation and consequently fructose turnover frequency and HMF productivity were calculated. **Figure 4.19** shows fructose turnover frequency and HMF productivity normalized to the number of acid sites of PNA, and after the subtraction of the background contribution observed in the stoichiometric reaction. Fructose TOF and HMF productivity increase from 0.4 h<sup>-1</sup> to 1.3 h<sup>-1</sup> and from 0.04 h<sup>-1</sup> to 0.2 h<sup>-1</sup> respectively when the fructose concentration is increased from 1 g/L to 10 g/L. As explained above, this improvement of the catalytic system is due to the better reagent-catalyst contact generated with increasing reagent concentration.

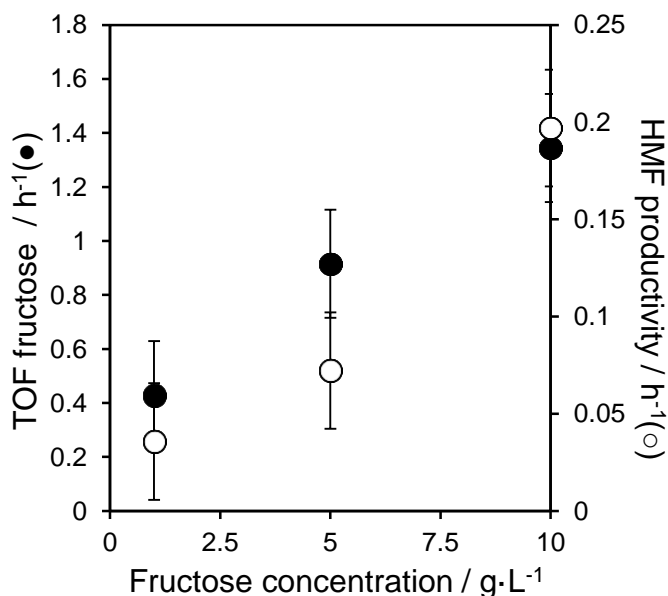


**Figure 4.19** Fructose turnover frequency and HMF productivity over parent niobic acid as a function of fructose concentration

#### 4.2.1.3.3 Calculation of the order of reaction

In order to study the impact of the initial reagent concentration on its reactivity and also to measure the order of the glucose and fructose dehydration reaction with respect to their initial concentrations, PNA was chosen to carry out the reactivity and kinetic studies at 100°C. In all cases, the amount of catalyst and water were kept constant at 0.1 g and 20 ml respectively.

The rates of glucose and fructose conversion calculated for the first hour of reaction are plotted against the initial concentration of glucose and fructose. According to the definition, rate of reagent conversion is explained by the following equation:

$$r = k [\text{reagent}]^a [\text{catalyst}]^b$$

**Equation 4.1** Rate equation for the calculation of the order of reaction

Where  $r$  is the rate of glucose or fructose conversion,  $k$  is the rate constant,  $[\text{reagent}]$  is the initial concentration of glucose or fructose,  $a$  is the order of reaction with regard to glucose or fructose,  $[\text{catalyst}]$  is the concentration of catalyst and  $b$  is the order of reaction in respect to catalyst. Since the same amount of catalyst was used in all reactions, **Equation 4.1** can be simplified as:

$$r = k'[\text{reagent}]^a \equiv \log[r] = a \cdot \log[\text{reagent}] + \log(k')$$

**Equation 4.2** Simplified rate equation

Where  $k' = k [\text{catalyst}]^b$ . Thus, the order of reaction (a) can be calculated by plotting the logarithms of initial rate and sugar concentration as shown in **Figure 4.20**. The order of reaction for glucose and fructose dehydration was found to be 0.610 and 0.485 respectively. The conclusion that can be drawn from this fractional order coefficient is that there are multiple steps involved in the reaction creating a complex mechanism, and the order of reaction below 1 represent a “slowing down” of the reaction, i.e. the rate of reaction increases in a minor way at higher reagent concentrations.[49]

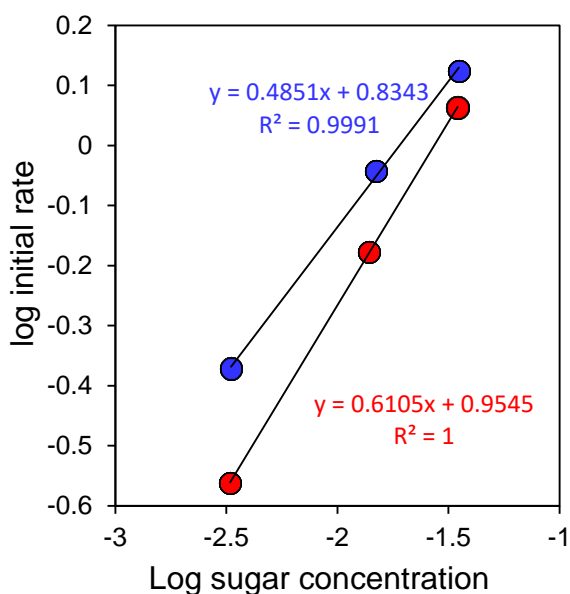


**Figure 4.20** Rate of glucose (red) and fructose (blue) conversion as a function of initial reagent concentration over PNA

#### 4.2.1.4 Effect of solvent (DMSO)

The main drawback of using DMSO in HMF production is the difficulty of the separation of the chemicals by conventional processes such as distillation due to the high boiling point of HMF and its sensitivity to high temperatures. However, HMF can be isolated by phase extraction method with various organic solvents, specially methyl isobutyl ketone and ethyl acetate, according to a recent publication by Gajula *et al.* [50].

#### 4.2.1.4.1 Glucose conversion

Morales *et al.* [51] reported 87% glucose conversion in DMSO at 140°C after 24h, with HMF production of 8%. Due to the high catalytic performance of this solvent, the glucose dehydration reaction was studied in the absence of a catalyst at different temperatures. Reaction at 100°C shows a background glucose conversion of 14% (**Figure 4.21**), although negligible HMF and levulinic acid formation was observed, therefore this conversion is attributed to unidentified products. Different temperatures were studied in order to have the least contribution due to thermal effects, and 75°C was chosen as reaction temperature in DMSO.

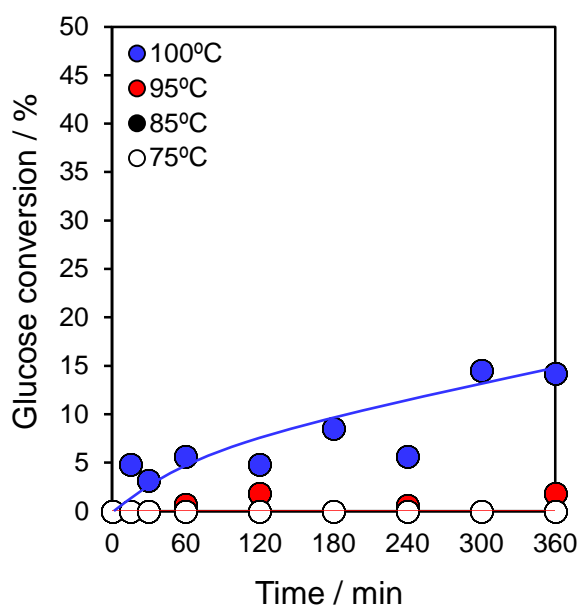


**Figure 4.21** Glucose conversion profile for glucose dehydration after 6 h reaction in DMSO without catalyst at different reaction temperatures

**Figure 4.22** shows glucose dehydration reactions profiles over pre-calcined PNA. Catalysts calcined below 500°C show similar behaviour, with initial glucose conversion and stabilisation after the first hour of reaction. These results are indicative of the inability of the catalysts to carry out the isomerization of glucose at this temperature in the given system, but it is difficult to relate with literature results since to the best of our knowledge this reaction has not been reported at such low temperature in DMSO. Only the parent niobic acid shows a modest conversion of HMF, with a linear trend with increasing reaction time. No fructose or any other products were observed in any case during the glucose dehydration reactions in DMSO at 75°C. Due to the absence of internal standard (in aqueous system DMSO is used as IS), the reaction profiles can appear erratic, and determination of initial rate can be difficult.

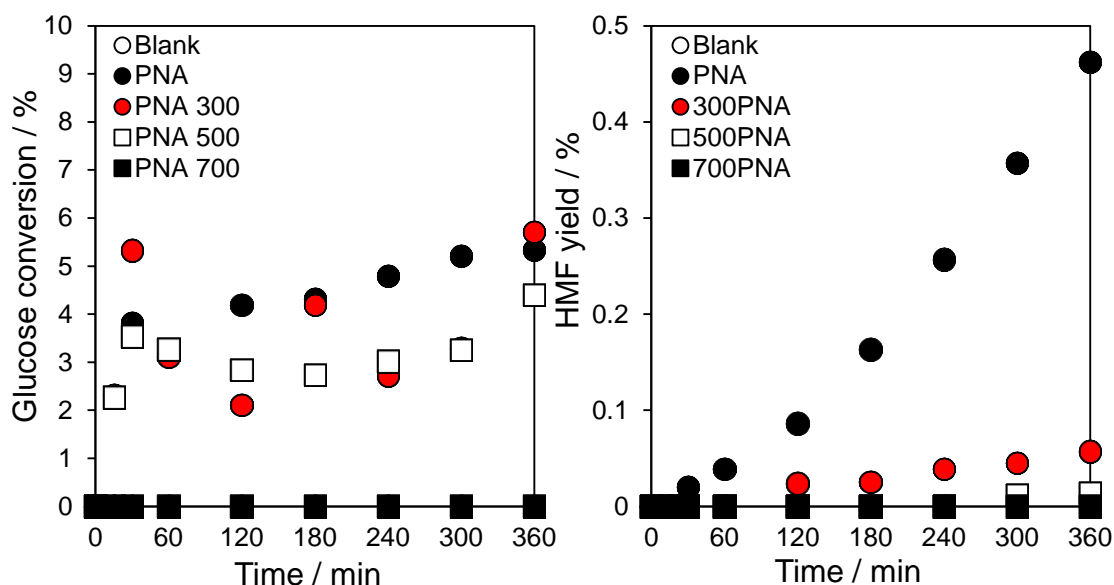


**Figure 4.22** Glucose conversion and yield of glucose and HMF profiles for glucose dehydration after 6 h reaction over pre-calcined niobic acid at 75°C in DMSO

**Figure 4.23** shows the conversion and yield of the catalysed dehydration of glucose in DMSO at 75°C over pre-calcined niobic acid. Modest glucose conversions are obtained for all the catalysts studied: 5.5% for amorphous niobic acid, 4.5% for pseudo-hexagonal and null for orthorhombic material. In all cases, HMF yield is negligible, never surpassing 0.3%, giving a maximum of 5% selectivity (not shown). These results suggest a poorer performance for the dehydration of glucose than that obtained with water as a solvent, when 38% glucose conversion was attained at 100°C. The lower activity for glucose isomerization in DMSO can be attributed to Lewis base properties of DMSO, which might reduce the Lewis acid concentration on the catalyst surface[20]. Several groups have observed the weak performance of glucose conversion in DMSO, for example Wang *et al.*[52] studied the glucose and fructose dehydration reaction over SnO<sub>2</sub>-ZrO<sub>2</sub> and sulfated SnO<sub>2</sub>-ZrO<sub>2</sub> in DMSO at 120°C, and found that the same catalyst was able to convert up to 76% of HMF when fructose was the reactant but only 9% starting from glucose, proving the conversion of ketose is superior to the conversion of aldose to HMF. Elmously *et al.* [53] also reported a study in the dehydration of glucose and fructose in DMSO over metal catalysts. In their temperature study they found that at 110°C only a 4% HMF yield is obtained when a large amount of catalyst is used and temperatures over 140°C are necessary to get 23% yield within the first hour of the reaction. Jia *et al.* [54] reported the glucose and fructose conversion to HMF at 110°C in binary water/DMSO system over CrCl<sub>3</sub>·6H<sub>2</sub>O. They reported 23% glucose conversion for all the studied concentrations of water in DMSO, with the pure DMSO system providing a higher HMF yield (9%) than the aqueous system, whose main product was fructose. Anhydrous DMSO is a strong dehydration

medium, which facilitates HMF formation from the in situ formed fructose, for this reason a strong Lewis acid catalyst like  $\text{CrCl}_3 \cdot 6\text{H}_2\text{O}$  is necessary to perform the isomerisation of glucose (the rate limiting step) to subsequently dehydrate the fructose with the DMSO assistance.

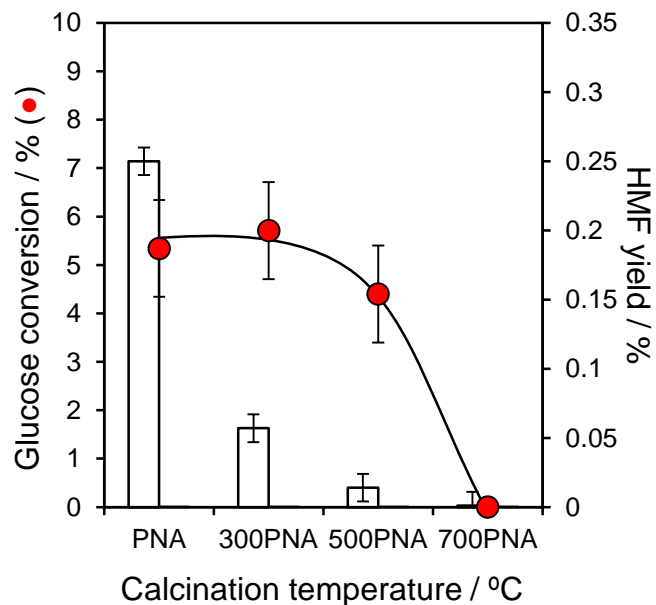


**Figure 4.23** Conversion of glucose in DMSO after 6 h reaction at 75°C over parent niobic acid and corresponding yield of HMF (white) as a function of pre-calcination temperature

From the reaction profiles, the rates of glucose conversion and HMF formation and consequently glucose turnover frequency and HMF productivity were calculated. As mentioned before, the erratic profiles of glucose conversion make difficult the determination of initial rate. For this purpose, only the amount of glucose converted after one hour was considered for the determination of initial rate of reaction. **Figure 4.24** shows a stable glucose TOF of  $\sim 0.3 \text{ h}^{-1}$  for catalysts calcined below 500°C, due to their similar inefficiency to isomerize glucose at this temperature. HMF productivity can be considered stable lower values of  $0.002 \text{ h}^{-1}$  but due to the low amount produced, quantification of rate of formation is also difficult in this system, leading to greater error compared to the reactions performed in aqueous system.

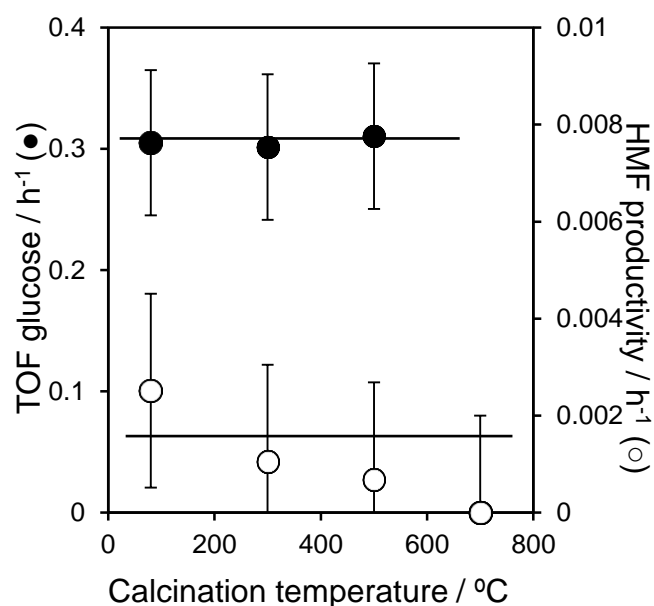


**Figure 4.24** Turnover frequencies for the conversion of associated HMF productivity normalised to total acid loading at 75°C in DMSO over parent niobic acid as a function of pre-calcination temperature

#### 4.2.1.4.2 Fructose conversion

As in the case of glucose, a non-catalysed reaction was performed at different temperatures, since the promoting effect of DMSO in the dehydration of fructose to HMF has been reported by different groups between 100-150°C[51, 55, 56]. Recently, Ren *et al.*[57] published their study on the performance of DMSO for the fructose conversion to HMF in the presence and absence of Brønsted acid catalysts. They proposed that the catalytic performance of DMSO arises from the valence unsaturation of both S and O atoms and the unsaturated double bond of S=O, supporting the role of the S acting as a Lewis acid and O acting as a Brønsted base in this reaction. The proposed reaction mechanism displayed in **Figure 4.25** has also been endorsed by NMR studies performed by Amaseraka *et al.*[58] and Kimura *et al.*[59].

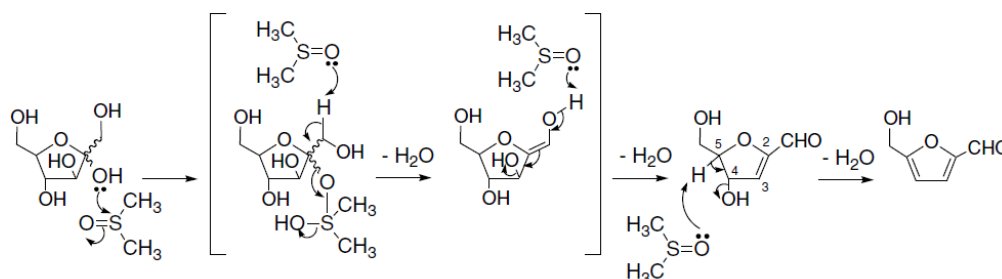


**Figure 4.25** Reaction mechanism for the dehydration of fructose to HMF in DMSO[58]

**Figure 4.26** shows the reaction profiles of fructose conversion and glucose and HMF yield at different temperatures in the absence of catalyst. The promoting effect of DMSO in the dehydration reaction is clearly observed, since fructose is fully converted at 100°C after 4h.

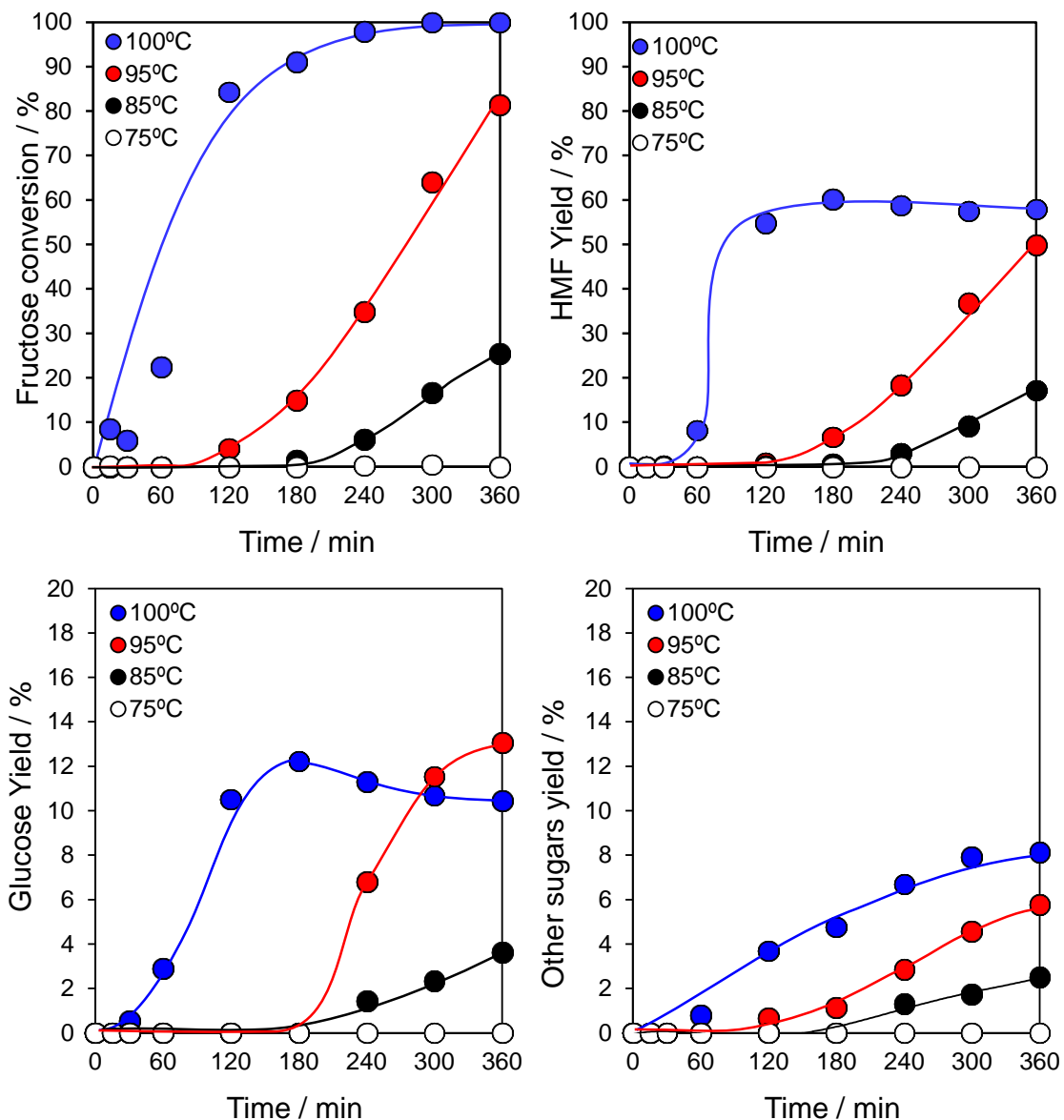


**Figure 4.26** Profiles of fructose conversion and yield of HMF, glucose and other sugars for fructose dehydration in DMSO after 6 h reaction without catalyst at different reaction temperatures

Transformation of fructose occurs rapidly within the first two hours achieving 84% fructose conversion, yields of main products of ~60% HMF and ~11% glucose which remain constant during the rest of the reaction, and a progressive increase of other products up to 8% after 6 h of reaction. HMF is produced with selectivity of 50-60% for those reaction temperatures studied which showed some HMF production, a value

much higher than those achieved in the catalytic aqueous media studied in this thesis due to the inhibiting effect of DMSO for the production of side reactions. In order to avoid the solvent contribution in the dehydration reaction, the temperature must be lowered down to 75°C, temperature at which no fructose conversion was observed. These results are in agreement with those reported by Wang et al. [30], who observed 76% fructose conversion and 65% HMF yield in DMSO over niobium oxide catalyst calcined at 700°C (with no acid sites) when the reaction was carried out for 2h at 90°C. **Figure 4.27** shows the reaction profiles for the fructose conversion and yields of HMF, glucose and other sugars for the fructose dehydration reaction in DMSO at 75°C.

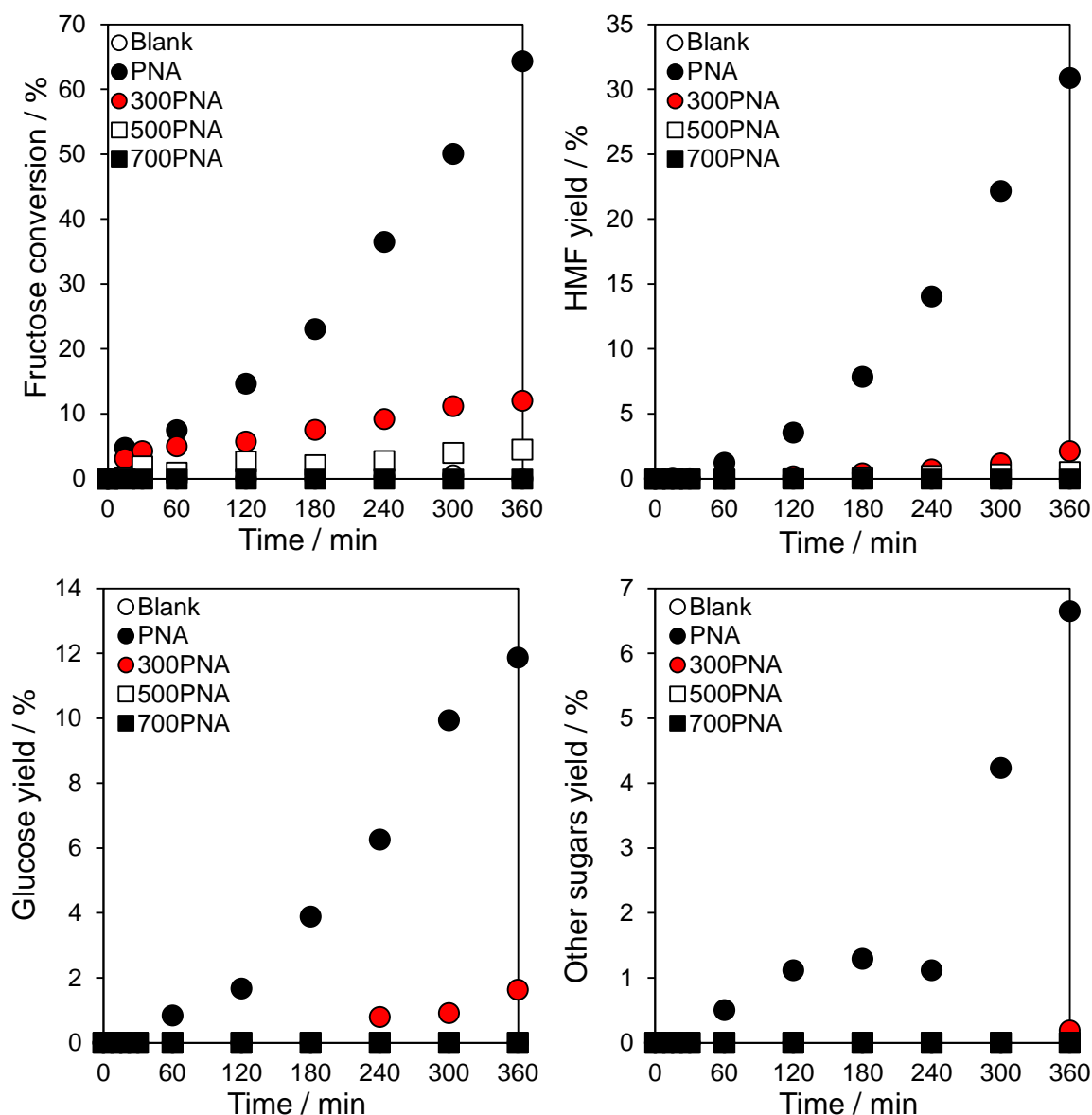


**Figure 4.27** Profiles of fructose conversion and yield of HMF, glucose and other sugars in DMSO at 75°C after 6 h reaction over pre-calcined niobic acid

It is noteworthy that although the aqueous reaction at 100°C and the DMSO reaction at 75°C reach the same fructose conversion at 6 h (~60%), the latter is slower, achieving only 14% conversion after 2h compared to the 39% reached in aqueous media. Thus, reaction temperature is a crucial factor in order to overcome the initial energy barrier for the dehydration of fructose in DMSO. **Figure 4.28** shows the fructose conversion, and yields of HMF, glucose and other sugars for the dehydration of fructose at 75°C in DMSO over pre-calcined niobic acid. Fructose conversion is 64% when the reaction is catalysed by parent PNA, the same than the one obtained in aqueous system at 100°C, but in this case the HMF yield experiences a two-fold increase compared to the aqueous system, attaining 31% yield. These results prove that besides promoting the dehydration of fructose, DMSO improves the stability of HMF by interacting strongly with it through solvation and restricts the contact of HMF with intermediates, thereby preventing undesired side reactions as the formation of humins.

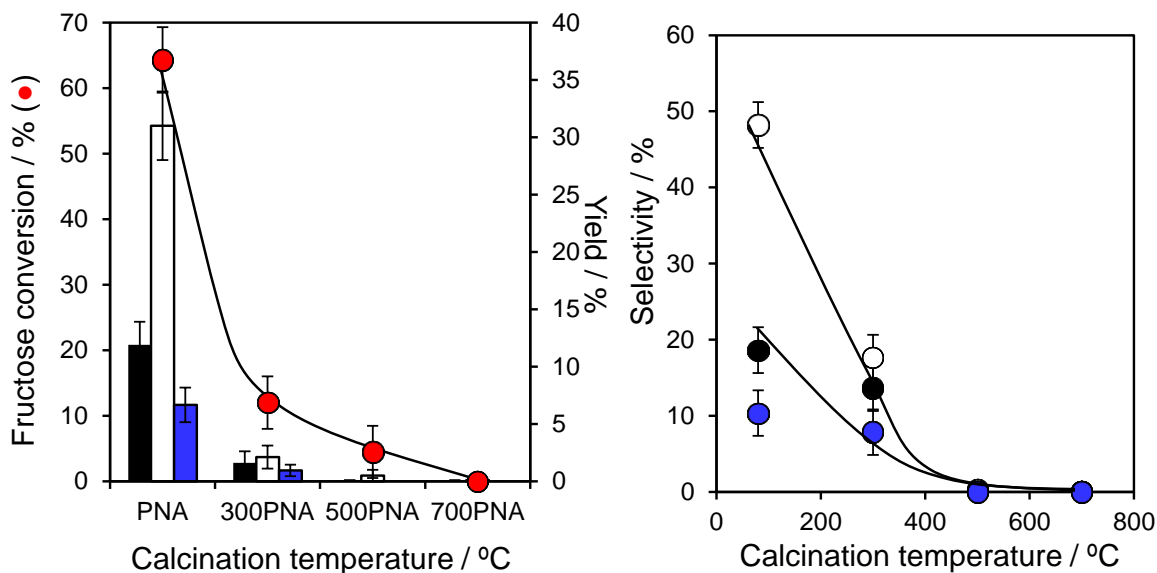


**Figure 4.28** Conversion of fructose at 75°C in DMSO over parent niobic acid, corresponding yields of HMF (white), glucose (black) and other sugars (blue) (left) and glucose (black), HMF (white) and other sugars (blue) selectivity (right) after 6 h reaction as a function of pre-calcination temperature

For the bulk calcined catalysts a considerable decrease in conversion and selectivity was observed. While in aqueous system the performance of PNA and 300PNA was similar, the activity of the latter is remarkably decreased in the presence of DMSO. This can be explained by the presence of structural water acting as Brønsted acid sites in the case of PNA. After calcination at 300°C this structural water is eliminated, leaving just the Brønsted acidity provided by physisorbed water, which is maintained in aqueous system. However, when DMSO is used as solvent, DMSO competes with the physisorbed water to be in the first solvation shell of fructose and coordinate with the

hydrogen atom of the hydroxyl groups in order to perform the dehydration of fructose. This effect was reported by Mushrif *et al.* in their computational studies about solvent effects on the hexoses conversion to HMF[60, 61]. The deep drop in HMF selectivity can be then attributed to the loss of Brønsted acidity after calcination over 300°C. These results indicate that only uncalcined PNA presents demonstrable activity for the dehydration of fructose in DMSO, and that thermal treatment of niobic acid has a more detrimental impact on activity in DMSO compared to aqueous reaction.

From the reaction profiles, the rates of fructose conversion and HMF formation and consequently fructose turnover frequency and HMF productivity were calculated (Figure 4.29).

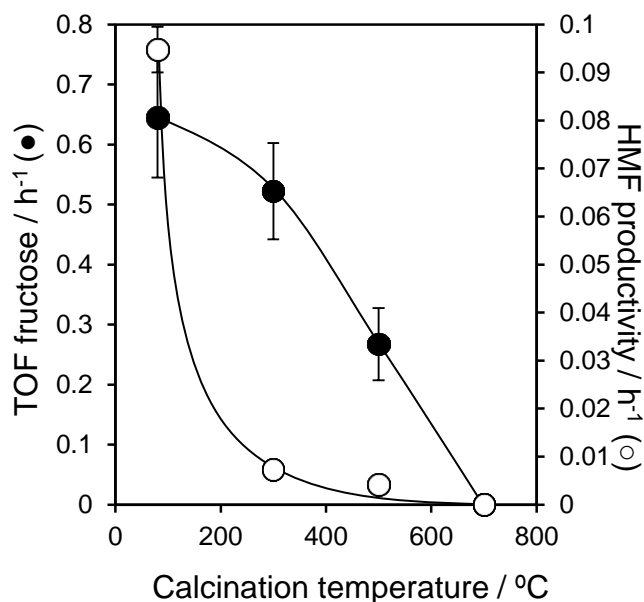


**Figure 4.29** Turnover frequencies for the conversion of fructose and associated HMF productivity normalised to total acid loading at 75°C in DMSO over parent niobic acid as a function of pre-calcination temperature

Glucose TOF of  $\sim 0.6 \text{ h}^{-1}$  measured after the first hour of reaction, much lower than that observed for the aqueous reaction at higher temperature ( $1.7 \text{ h}^{-1}$ ), followed by an almost linear decrease for the pre-calcined catalysts. However, this TOF calculated from the initial rate of fructose conversion in the first hour doesn't display the superior performance of uncalcined PNA after the first hour of reaction. Slightly superior HMF productivity is achieved with PNA in DMSO ( $0.095 \text{ h}^{-1}$ ) compared to that obtained by the same catalyst in water ( $0.07 \text{ h}^{-1}$ ), proving the capacity to dehydrate fructose even at such low temperature due to promoting effect of DMSO. However, a striking decrease in HMF productivity is observed for the pre-calcined catalysts due to the loss of structural Brønsted acidity. In other words, when calcined PNA is in contact with the

aqueous media is able to recover some Brønsted acidity due to the adsorption of hydroxyls on the surface of the catalyst, while in DMSO this phenomenon does not occur, leading to the significant drop in HMF productivity.

#### **4.2.2 Glucose and fructose conversion to HMF over x%PNA/SBA-15 catalysts**

The main objective of this investigation was to prepare high surface area PNA/SBA-15 catalysts with good textural and high accessibility of Nb<sub>2</sub>O<sub>5</sub> species in order to improve the performance of the most active as-precipitated amorphous niobic acid. Therefore, glucose and fructose dehydration reactions were subsequently conducted over PNA/SBA-15 catalysts, with Nb loadings from 2 to 25 wt%, to investigate their performance under the chosen conditions investigated for the bulk materials.

##### **4.2.2.1 Glucose conversion**

**Figure 4.30** shows the reaction profiles of glucose conversion and yields of HMF and fructose. Very erratic conversion profiles are observed due to due to the difficulty of manual integration for low conversions, but in every case the conversion achieved by the blank reaction is not exceeded. Contrarily, a clear steady increase is observed for the HMF formation, which modestly increases with increasing niobium content. On the other hand, some fructose is formed within the first hour of the reaction and remains stable for the remaining reaction time. No other peaks are observed in the chromatogram for any of the supported materials, including any of the so-called other sugars. Increasing the amount of niobia, the formation of both fructose and HMF increase, which is explained due to the formation of more Lewis acidic sites which are responsible for the isomerization of glucose to fructose, and subsequently because there are more fructose molecules available in the reaction media, the yield of HMF gets increased as well.

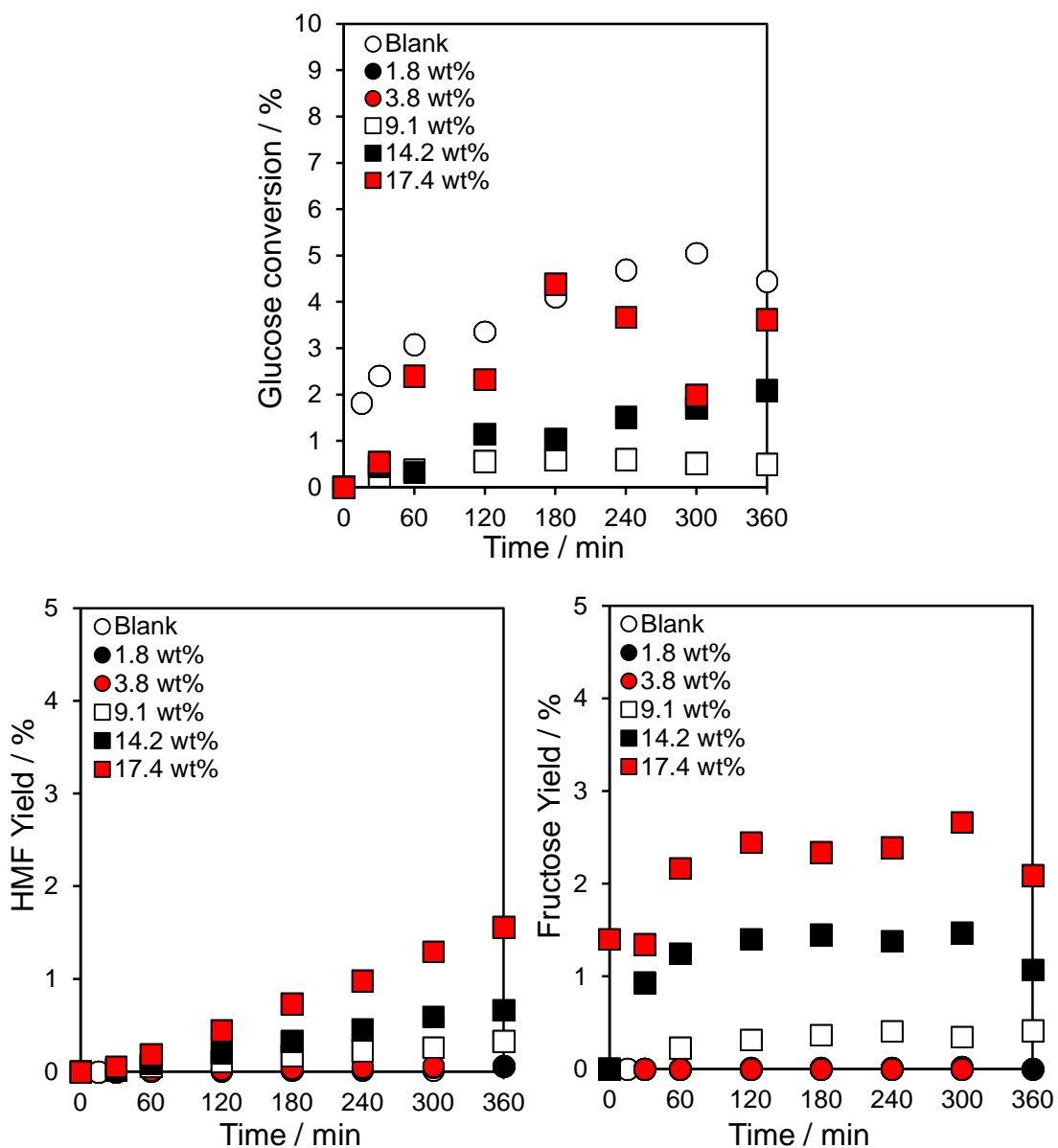


**Figure 4.30** Glucose conversion and yield of HMF and fructose profiles for glucose dehydration after 6 h reaction at 100°C over supported niobic acid

**Figure 4.31** depicts the glucose conversion and yields of fructose and HMF over the silica supported catalysts. Due to the very low amount of surface niobium concentration, initial conversion was much lower than on bulk PNA as expected, because of the silica dilution effect. However, the yield of major products (fructose and HMF) progressively increases over the time, except for the lower loading catalysts, with which little or no glucose conversion was observed. Probably the very low concentration of niobium species at low loading, and therefore small amount of Lewis acid sites, is not enough to carry out the isomerization of glucose. Selectivity to main products obtained by catalysts with niobium content over 9% is found to be stable, showing values of 50-60% and 30-45% for fructose and HMF respectively. These

selectivity values double those obtained by bulk PNA materials, probably due to the higher dispersion of niobia nanoparticles, making more accessible the active centres for the isomerization to fructose and subsequent dehydration to HMF.

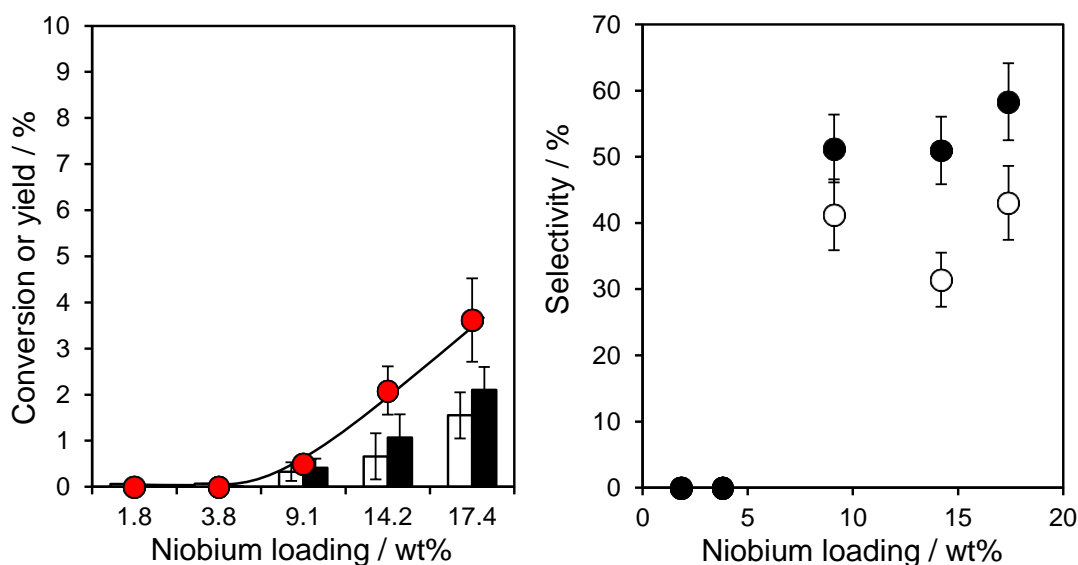


**Figure 4.31** Conversion of glucose (red circles) over supported niobic acid and corresponding yield (left) and selectivity (right) of fructose (black) and HMF (white) after 6 h reaction at 100°C as a function of niobium loading

**Figure 4.32** shows the glucose TOF and productivity of HMF calculated by the amount of glucose converted and HMF produced normalised to the amount of total acid sites. Precise calculation of TOF and productivity at this low conversion can be misleading due to the low accuracy to calculate the initial rate based on the reaction profile, even though both glucose TOF and HMF productivity experience a linear increase at higher loadings of niobia due to aggregation of the surface niobia species. The catalytic activity of the bridge hydroxyl group Nb-OH-Nb, which provides Brønsted acidity and formed when isolated niobia species aggregate, is more active compared to Nb-OH-Si present on isolated species[62]. This change in nature of the acid sites on the surface of the catalysts modifies the catalytic performance of the materials, hence the change in TOF and productivity.

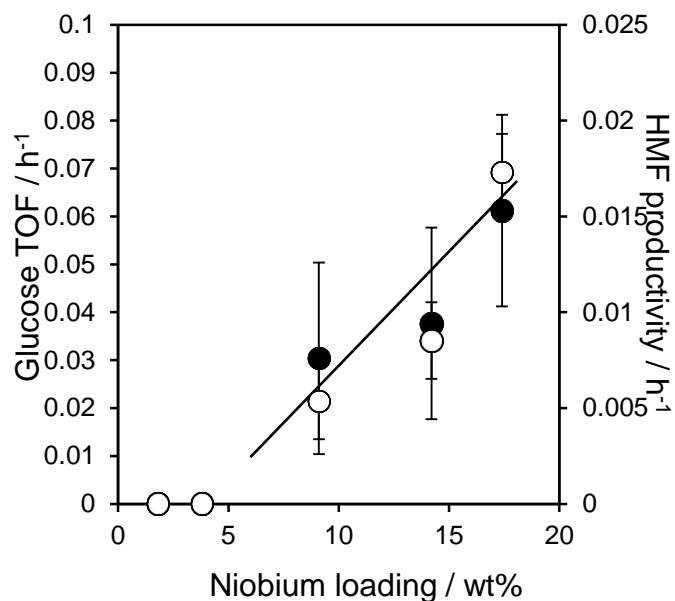


**Figure 4.32** Turnover frequencies for the aqueous phase conversion of glucose and associated 5-HMF productivity normalised to total acid loading as a function of niobium loading

#### 4.2.2.2 Fructose conversion

**Figure 4.33** shows fructose dehydration reactions profiles over the series of PNA/SBA-15 catalysts. The main products of fructose dehydration in water were HMF, glucose and other sugars.

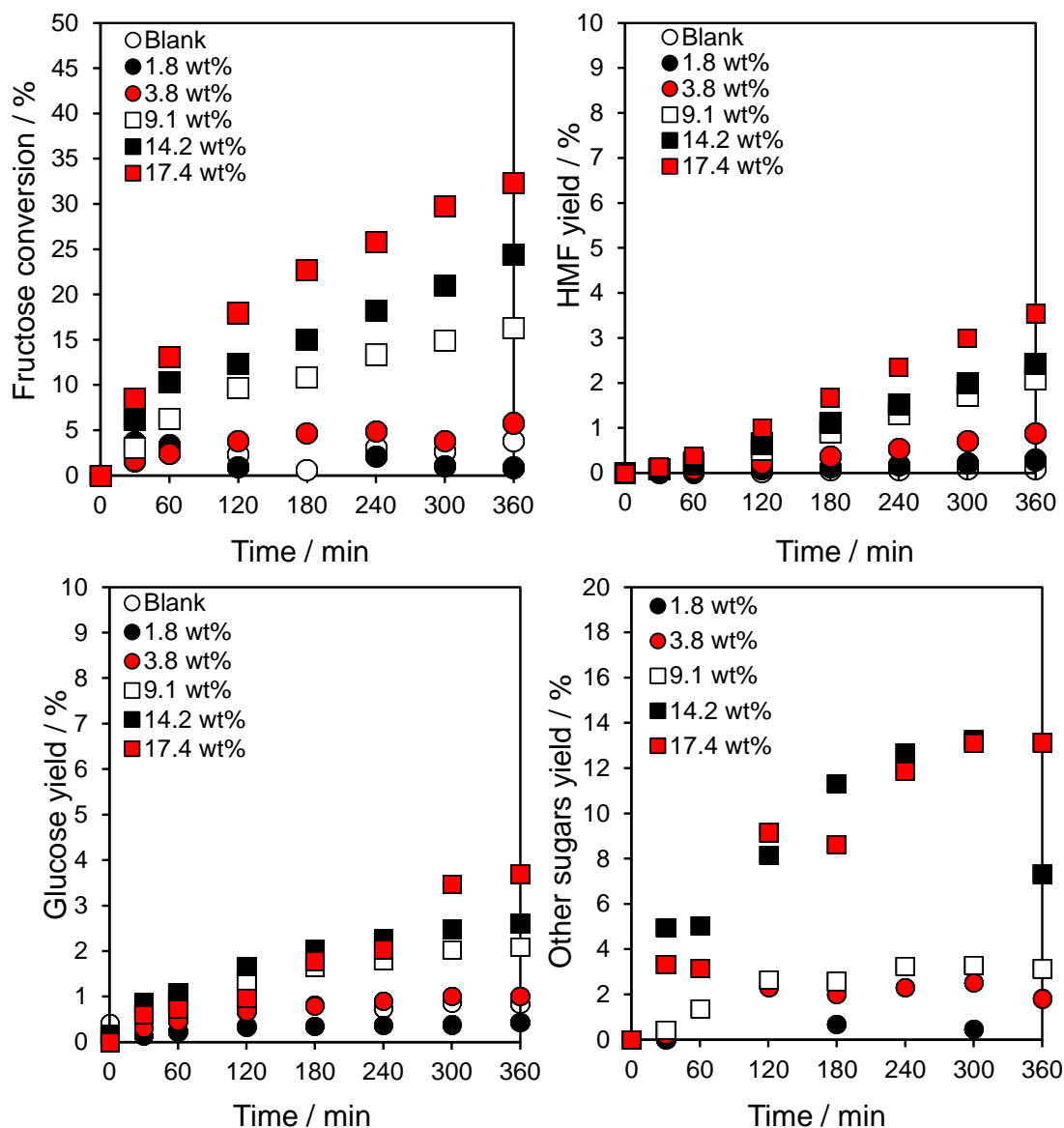


**Figure 4.33** Profiles of fructose conversion and yield of HMF, glucose and other sugars for fructose dehydration after 6 h reaction at 100°C over supported niobic acid

**Figure 4.34** shows the fructose conversion and yields of HMF, glucose and other sugars over the silica supported catalysts. Fructose conversion increased almost linearly with Nb loading from 1% (1.8%PNA/SBA-15) to 32% (17.4%PNA/SBA-15), consistent with the formation of a two-dimensional niobic acid overlayer and linear increase in the acid loading as seen in **Chapter 3**. Yields of HMF mirrored the fructose conversion, increasing from 0.5% to ~7% while the reverse isomerization to glucose follows the same trend except for the highest niobia loading, which experiences a decrease due to the splitting of the glucose peak in the chromatogram, appearing an unidentified compound included in the other sugars set. Low loadings of supported niobium comprise mainly isolated tetrahedra which provide Lewis acidity, thus the high selectivity towards glucose reverse isomerization. Glucose selectivity attained with bulk

PNA materials was ~5%, while in the case of supported PNA, a notable selectivity increase is observed (20-45%), probably due to the higher dispersion of niobia centres, making more accessible the uncoordinated niobium centres which provide Lewis acid sites for the isomerization reaction to glucose. For the highest loading, the materials are reverting to the properties of bulk PNA, indicated by the analogue glucose selectivity attained by 17.4%PNA/SBA-15. Glucose selectivity decreases with increasing niobium loading, while the formation of other sugars is subsequently promoted due to the changes in acidity induced on the catalysts surface after aggregation of niobia nanoparticles. Surprisingly, HMF selectivity remained constant at around 20-25%.

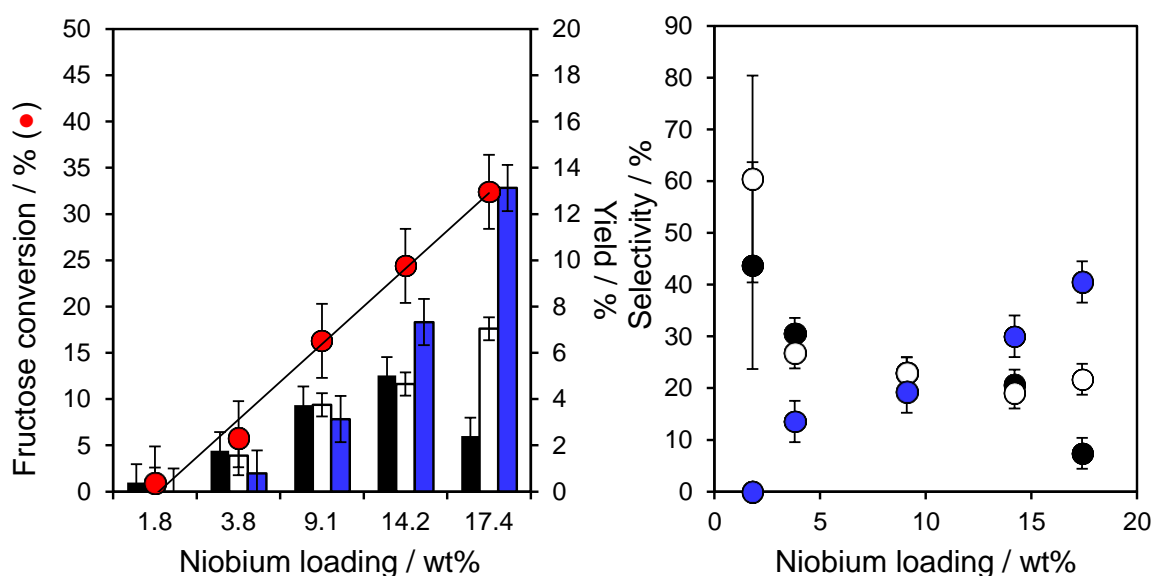


**Figure 4.34** Conversion of fructose over supported niobic acid and corresponding yields of HMF (white), glucose (black) and other sugars (blue) after 6 h reaction at 100°C as a function of niobium loading

From the reaction profiles, the rates of fructose conversion and HMF formation and consequently fructose turnover frequency and HMF productivity were calculated. **Figure 4.35** shows fructose turnover frequency and HMF productivity normalized to the number of total acid sites. As seen in the case of glucose conversion, a linear increase in TOF with increasing niobium content is observed, explained by the appearance of more active acid sites after isolated species start aggregating in two dimensional polymerised species, which induce the formation of bridged hydroxyl groups (Nb-OH-Nb) able to generate additional Brønsted acidity.

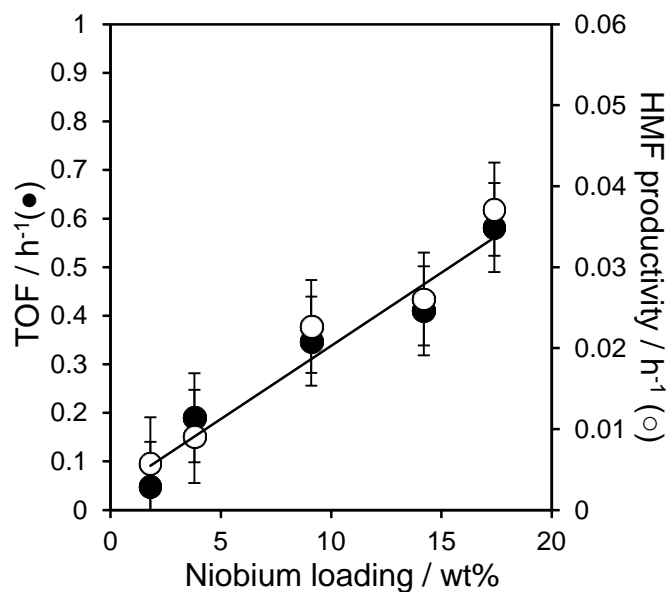


**Figure 4.35** Turnover frequencies for the aqueous phase conversion of fructose and associated 5-HMF productivity normalised to total acid loading as a function of niobium loading

### 4.2.3 Comparison between bulk PNA and SBA-15 supported PNA

This chapter exposed the catalytic performance in glucose and fructose dehydration into HMF of as-prepared niobic acid and supported materials prepared by its impregnation on a high surface area meso-structured SBA-15 support. This section will provide a comparison between these two sets of catalysts in glucose transformation into HMF.

In order to have a fair comparison between the activities of the two series of catalysts, turnover frequency is normalized to Nb content in the bulk of each catalyst. Associated TOFs for fructose conversion and HMF productivity over parent PNA and PNA/SBA-15 catalysts are compared in **Figure 4.36**, which reveals an inverse correlation between Nb loading and reactivity, evidencing the superior performance of highly dispersed niobic acid (per acid site/mass of niobium), presumably due to the latter's superior dispersion and hence enhanced activity of Brønsted acid sites.

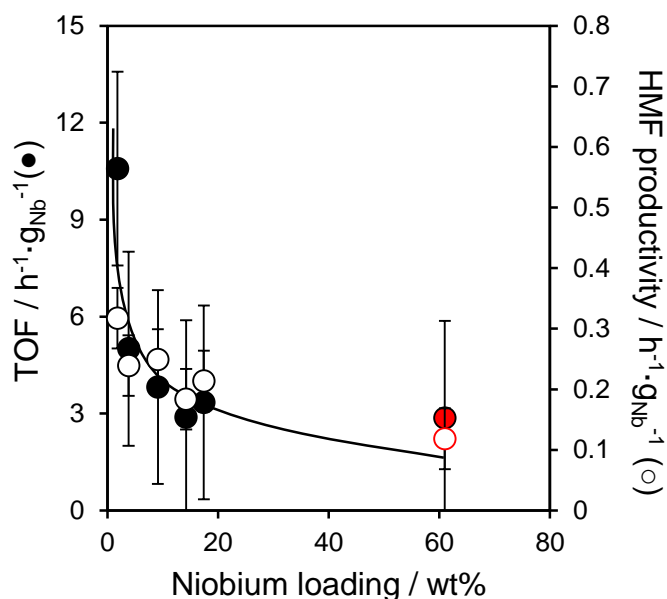


**Figure 4.36** Comparison of fructose turnover frequency (filled symbols) and associated HMF productivity (open symbols) over supported niobic acid (black) and parent niobic acid (red) as a function of niobium loading

### 4.3 Conclusion

Nanoparticulate niobic acid with different Brønsted-Lewis ratio due to pre-calcination at different temperatures was tested for the aqueous phase isomerisation of glucose to fructose, and subsequent fructose dehydration to 5-HMF under mild reaction conditions. A series of reaction variables have been studied in order to examine their influence on the reaction system. The physicochemical changes induced by the crystallization of niobia after thermal treatment studied in **Chapter 3**, such as decrease of surface area, crystallite growth associated to phase change and decreased acid loading, notably lowers activity, for both glucose and fructose dehydration reactions. The impact of reaction temperature was found to be a crucial parameter for the activity of the reaction system and also shed light on the preferential reaction pathway via determination of activation energy. The much higher activation energy for HMF formation compared to the activation energy for reagent conversion explains the relatively low HMF selectivity attained on the studied catalytic tests and the formation of by-products such as unidentified saccharides and insoluble compounds. The influence of reactant concentration proved that the extremely dilute systems here studied hamper the activity of the catalysts due to a combination of mass transport limitation and competitive adsorption of water and sugar on the surface of the catalyst. When higher reactant concentrations are used, the adsorption of sugars on the surface of the

catalyst is enhanced, leading to an improvement in catalytic activity. This study also helped to determine the order of reaction, which resulted in a value less than one, demonstrating that the reaction rate for glucose and fructose dehydration reactions stops increasing with the increase of reactant concentration at a determined value not determined here. In order to study the development of this reaction in a non-aqueous system, DMSO was used as reaction media and an important background contribution was observed at 100°C, especially when fructose was used as the reagent, reaching full conversion in the autocatalytic reaction after 4 h, reason why DMSO reaction were performed at 75°C. Isomerization of glucose could not be performed effectively, probably due to deactivation of Lewis acid sites by the Lewis base properties of DMSO. However, dehydration of fructose was found to be very efficient, even at such low temperature, attaining the same conversion of fructose than in aqueous system at 100°C, but with a two-fold increase in HMF selectivity due to the ability of this organic solvent to prevent rehydration of HMF and the formation of humin species.

Niobic acid nanoparticles dispersed over SBA-15 were unable to properly isomerise glucose due to scarce amount of Lewis acid sites. However, the high dispersion of the few Lewis acid sites led to a higher fructose selectivity observed from the little glucose conversion attained. On the other hand, a constant increase in the activity of fructose dehydration was observed with increasing niobium loading due to the aggregation of isolated species in two dimensional polymerised species, which induce the promotion of Brønsted acidity. In this case, the highly dispersed supported niobia nanoparticles also provided a superior selectivity for the retro aldol reaction to glucose due to the greater accessibility of Lewis acid sites, while the selectivity to HMF remained the same compared to the bulk materials. The turnover frequency for fructose dehydration to 5-HMF determined for both bulk and supported materials showed enhanced TOF for the highly dispersed niobic acid (per acid site/mass of niobium), indicating that lower amount of niobium is able to transform more substrate per gram of niobium compared to higher loadings. Niobic acid nanoparticles are promising solid acids for the aqueous phase conversion of waste-derived sugars to platform chemicals.

#### 4.4 References

- [1] S.K. Patil, C.R. Lund, *Energy & Fuels* 25 (2011) 4745-4755.
- [2] B. Guo, L. Ye, G. Tang, L. Zhang, B. Yue, S.C.E. Tsang, H. He, *Chinese Journal of Chemistry* (2017) 1-11.
- [3] C. Yue, G. Li, E.A. Pidko, J.J. Wiesfeld, M. Rigutto, E.J. Hensen, *ChemSusChem* 9 (2016) 2421-2429.
- [4] H.T. Kreissl, K. Nakagawa, Y.-K. Peng, Y. Koito, J. Zheng, S.C.E. Tsang, *Journal of Catalysis* 338 (2016) 329-339.
- [5] P. Carniti, A. Gervasini, S. Biella, A. Auroux, *Catalysis today* 118 (2006) 373-378.
- [6] V. Ordonsky, V. Sushkevich, J. Schouten, J. van der Schaaf, T. Nijhuis, *Journal of Catalysis* 300 (2013) 37-46.
- [7] Y. Zhang, J. Wang, J. Ren, X. Liu, X. Li, Y. Xia, G. Lu, Y. Wang, *Catalysis Science & Technology* 2 (2012) 2485-2491.
- [8] T. Armaroli, G. Busca, C. Carlini, M. Giuttari, A.M. Raspolli Galletti, G. Sbrana, *Journal of Molecular Catalysis A: Chemical* 151 (2000) 233-243.
- [9] C. Carlini, M. Giuttari, A.M.R. Galletti, G. Sbrana, T. Armaroli, G. Busca, *Applied Catalysis A: General* 183 (1999) 295-302.
- [10] J.-M. Jehng, I.E. Wachs, *Catalysis Today* 8 (1990) 37-55.
- [11] J.M. Jehng, I.E. Wachs, *The Journal of Physical Chemistry* 95 (1991) 7373-7379.
- [12] J.-M. Jehng, I.E. Wachs, *Journal of molecular catalysis* 67 (1991) 369-387.
- [13] J.-M. Jehng, I.E. Wachs, *Catalysis today* 16 (1993) 417-426.
- [14] J. Datka, A. Turek, J. Jehng, I. Wachs, *Journal of Catalysis* 135 (1992) 186-199.
- [15] I. Nowak, *Studies in Surface Science and Catalysis* 154 (2004) 2936-2944.
- [16] S. Sumiya, Y. Oumi, M. Sadakane, T. Sano, *Applied Catalysis A: General* 365 (2009) 261-267.
- [17] M. Shirai, K. Asakura, Y. Iwasawa, *The Journal of Physical Chemistry* 95 (1991) 9999-10004.
- [18] Â. Silva, K. Wilson, A.F. Lee, V.C. dos Santos, A.C.C. Bacilla, K.M. Mantovani, S. Nakagaki, *Applied Catalysis B: Environmental* 205 (2017) 498-504.
- [19] M. Trejda, A. Tuel, J. Kujawa, B. Kilos, M. Ziolek, *Microporous and mesoporous materials* 110 (2008) 271-278.
- [20] C. García-Sancho, I. Agirrezabal-Telleria, M. Güemez, P. Maireles-Torres, *Applied Catalysis B: Environmental* 152 (2014) 1-10.

- [21] P. Carniti, A. Gervasini, M. Marzo, *Catalysis Today* 152 (2010) 42-47.
- [22] M. Marzo, P. Carniti, A. Gervasini, *CHIMICA OGGI-CHEMISTRY TODAY* 30 (2012) 22.-24.
- [23] B. Kuster, *Starch-Stärke* 42 (1990) 314-321.
- [24] A. Florentino, P. Cartraud, P. Magnoux, M. Guisnet, *Applied Catalysis A: General* 89 (1992) 143-153.
- [25] V.V. Ordonsky, J. van der Schaaf, J.C. Schouten, T.A. Nijhuis, *ChemSusChem* 5 (2012) 1812-1819.
- [26] W. Zeng, D.-g. Cheng, F. Chen, X. Zhan, *Catalysis letters* 133 (2009) 221.
- [27] K. Nakajima, Y. Baba, R. Noma, M. Kitano, J. N. Kondo, S. Hayashi, M. Hara, *Journal of the American Chemical Society* 133 (2011) 4224-4227.
- [28] Y. Zhang, J. Wang, X. Li, X. Liu, Y. Xia, B. Hu, G. Lu, Y. Wang, *Fuel* 139 (2015) 301-307.
- [29] M. Marzo, A. Gervasini, P. Carniti, *Catalysis today* 192 (2012) 89-95.
- [30] F. Wang, H.-Z. Wu, C.-L. Liu, R.-Z. Yang, W.-S. Dong, *Carbohydrate research* 368 (2013) 78-83.
- [31] A. Osatiashtiani, A.F. Lee, D.R. Brown, J.A. Melero, G. Morales, K. Wilson, *Catalysis Science & Technology* 4 (2014) 333-342.
- [32] C. Antonetti, M. Melloni, D. Licursi, S. Fulignati, E. Ribechini, S. Rivas, J.C. Parajó, F. Cavani, A.M.R. Galletti, *Applied Catalysis B: Environmental* 206 (2017) 364-377.
- [33] N.T. do Prado, T.E. Souza, A.R.T. Machado, P.P. Souza, R.S. Monteiro, L.C. Oliveira, *Journal of Molecular Catalysis A: Chemical* 422 (2016) 23-34.
- [34] E.L.S. Ngee, Y. Gao, X. Chen, T.M. Lee, Z. Hu, D. Zhao, N. Yan, *Industrial & Engineering Chemistry Research* 53 (2014) 14225-14233.
- [35] X. Qi, M. Watanabe, T.M. Aida, R.L. Smith, *Catalysis Communications* 9 (2008) 2244-2249.
- [36] D. Stošić, S. Bennici, V. Rakić, A. Auroux, *Catalysis Today* 192 (2012) 160.
- [37] C. Fan, H. Guan, H. Zhang, J. Wang, S. Wang, X. Wang, *Biomass and Bioenergy* 35 (2011) 2659-2665.
- [38] R.-J. van Putten, J.C. van der Waal, E. de Jong, C.B. Rasrendra, H.J. Heeres, J.G. de Vries, *Chemical Reviews* 113 (2013) 1499-1597.
- [39] S.H. Khajavi, Y. Kimura, T. Oomori, R. Matsuno, S. Adachi, *Journal of Food Engineering* 68 (2005) 309-313.
- [40] Y. Li, X. Lu, L. Yuan, X. Liu, *Biomass and bioenergy* 33 (2009) 1182-1187.

- [41] F.S. Asghari, H. Yoshida, *Industrial & Engineering Chemistry Research* 46 (2007) 7703-7710.
- [42] X. Qi, M. Watanabe, T.M. Aida, R.L. Smith Jr, *Industrial & Engineering Chemistry Research* 47 (2008) 9234-9239.
- [43] C. Chang, M. Xiaojian, C. Peilin, *Chinese Journal of Chemical Engineering* 14 (2006) 708-712.
- [44] B. Girisuta, L. Janssen, H. Heeres, *Green chemistry* 8 (2006) 701-709.
- [45] J. Guo, S. Zhu, Y. Cen, Z. Qin, J. Wang, W. Fan, *Applied Catalysis B: Environmental* 200 (2017) 611-619.
- [46] N. Rajabbeigi, A.I. Torres, C.M. Lew, B. Elyassi, L. Ren, Z. Wang, H.J. Cho, W. Fan, P. Daoutidis, M. Tsapatsis, *Chemical Engineering Science* 116 (2014) 235-242.
- [47] L. Atanda, S. Mukundan, A. Shrotri, Q. Ma, J. Beltramini, *ChemCatChem* 7 (2015) 781-790.
- [48] T. Wang, M.W. Nolte, B.H. Shanks, *Green Chemistry* 16 (2014) 548-572.
- [49] C.G. Hill, *An introduction to chemical engineering kinetics & reactor design*, Рипол Классик, 1977.
- [50] S. Gajula, K. Inthumathi, S.R. Arumugam, K. Srinivasan, *ACS Sustainable Chemistry & Engineering* 5 (2017) 5373-5381.
- [51] G. Morales, J.A. Melero, M. Paniagua, J. Iglesias, B. Hernández, M. Sanz, *Chinese Journal of Catalysis* 35 (2014) 644-655.
- [52] Y. Wang, X. Tong, Y. Yan, S. Xue, Y. Zhang, *Catalysis Communications* 50 (2014) 38-43.
- [53] M.A. Elmously, A. Emara, O. S. M. Abu-Elyazeed, *Conversion of Glucose Into 5-Hydroxymethylfurfural in DMSO as Single Organic Solvent*, ASME International Mechanical Engineering Congress and Exposition, Montreal, Quebec, Canada, 2014.
- [54] S. Jia, Z. Xu, Z.C. Zhang, *Chemical Engineering Journal* 254 (2014) 333-339.
- [55] R.M. Musau, R.M. Munavu, *Biomass* 13 (1987) 67-74.
- [56] C. Rasrendra, J. Soetedjo, I. Makertihartha, S. Adisasmito, H. Heeres, *Topics in Catalysis* 55 (2012) 543-549.
- [57] L.-K. Ren, L.-F. Zhu, T. Qi, J.-Q. Tang, H.-Q. Yang, C.-W. Hu, *ACS Catalysis* 7 (2017) 2199-2212.
- [58] A.S. Amarasekara, L.D. Williams, C.C. Ebede, *Carbohydrate research* 343 (2008) 3021-3024.
- [59] H. Kimura, M. Nakahara, N. Matubayasi, *The Journal of Physical Chemistry A* 117 (2013) 2102-2113.
- [60] V. Vasudevan, S.H. Mushrif, *RSC Advances* 5 (2015) 20756-20763.

[61] S.H. Mushrif, S. Caratzoulas, D.G. Vlachos, *Physical Chemistry Chemical Physics* 14 (2012) 2637-2644.

[62] J. He, Q.-J. Li, Y.-N. Fan, *Journal of Solid State Chemistry* 202 (2013) 121-127.

## ***Chapter 5***

***Bifunctional  $PO_4^{2-}/ZrO_2$  catalysts  
for the transformation of biomass  
derived sugars to 5-  
hydroxymethylfurfural***

## 5.1 Introduction

Zirconium oxide,  $ZrO_2$ , is a very attractive material for catalysis because of its thermal and hydrothermal stability and excellent chemical and mechanical properties. Moreover, zirconium oxide is claimed to be the only material which possesses acidic, basic, oxidizing and/or reducing surface properties[1]. In the mid-eighties Clearfield and Stynes[2] synthesised for the first time a crystalline phase of zirconium phosphate. It has been widely studied that the modification of the zirconia surface with small amounts of phosphorus compounds remarkably enhances the acidic properties and activity of this material[3], regardless of the type of phosphate compound used, e.g.  $(NH_4)_2HPO_4$ [4-7],  $(NH_4)H_2PO_4$ [8],  $C_{12}H_{27}O_4P$ [9] or  $H_3PO_4$  [10-13].

Different precursors have been used for the preparation of phosphated zirconia (PZ), but it is established that crystalline  $ZrO_2$  is obtained by either calcination of the hydroxide precursor ( $Zr(OH)_4$ ) or by refluxing the precursor in phosphoric acid solution[14-16]. Moreover,  $Zr(OH)_4$  can be directly acquired[4-6, 17], or synthesised from different materials before its crystallization, such as sol-gel method from zirconium propoxide[9, 11, 13] or via anion-cation promoting zirconia method reacting the nitrate[10, 18] or chloride[12, 19, 20] zirconium salt with ammonium-based compound like ammonia. Cutrufello *et al.*[21] reported that zirconia prepared by direct decomposition of zirconium nitrate had the highest concentration and strength of basic sites, while the poorly basic sample obtained from zirconyl chloride showed a high concentration of acid sites. Additionally, Ali and Zaki[22] studied the effect of phosphate impregnation on the hydroxide precursor and already crystalline material, concluding that only the materials prepared from  $Zr(OH)_4$  showed Brønsted acidity. For this reason, the materials herein presented were synthesised from the hydroxide precursor as discussed in **Chapter 2**.

The physicochemical properties of PZ make them compatible materials for aqueous reactions and also those reactions where water is generated. Phosphated zirconia solid acids have been primarily used as ion exchangers[23]. However, these materials have received attention in last few years for their use as solid acid catalysts in various reactions, such as 1-butene isomerization[14, 24], 2-propanol dehydration[24], n-hexane isomerization[13], isomerization of isobutene[11], Friedel-Crafts benzylation and benzoylation of toluene[10], esterification of acetic acid with ethanol[25] acetylation of salicylic acid[18], cumene cracking dehydrogenation and conversion of 2-propanol[26], transfer hydrogenation of butyl levulinate to  $\gamma$ -valerolactone[8] and dehydration of xylose to furfural[27].

Different aspects make phosphated zirconia an interesting catalytic material, such as its ability to withstand high temperatures due to its strong inorganic structure or the tunability of its textural properties and surface acidity by the appropriate modification of the synthesis method[28].

### 5.1.1 Crystallinity

It has been established that  $ZrO_2$  adopts three different polymorphic structures, which are shown in **Figure 5.1**. The monoclinic phase is stable in the range of temperatures 500–1200°C, after which it will be transformed to the tetragonal phase, which transforms to cubic phase at 2370°C and remains in this phase until the melting point is reached at 2680°C[20]. In 1926 Kathleen Yardley reported the first X-ray study of monoclinic zirconia[29]. The space group was found to be  $P2_1/c$  with 4  $ZrO_2$  in the unit cell, but a definite structure was not proposed.



**Figure 5.1** Crystal structure of monoclinic (left), tetragonal (middle) and cubic (right) zirconia[30]

It appears that the crystalline form of zirconia possesses catalytic activity, more specifically the tetragonal phase, while the amorphous form is inactive. The reason for this could be that the tetragonal phase has a higher content of non-bridging surface hydroxyl groups than the monoclinic phase and this seems to be a crucial factor for producing active materials[31]. For example, Tanabe[1] found that the most active form of zirconia for the hydrogenation of 1,3-butadiene was the material prepared from  $Zr(OH)_4$  and calcined at 600°C, whereas the catalyst pre-treated at 800°C gave maximum activities for the isomerization of 1-butene. In the case of PZ the activity of the catalysts has been found to be directly related to the amount of acid sites together with the high surface area provided by the phosphate treatment, independently of the crystalline structure of the materials. For example, Antonetti *et al.*[32] reported high conversion for the microwave-assisted dehydration of fructose and inulin to HMF

catalysed by amorphous forms of niobium and zirconium phosphate catalysts. Also Asghari and Yoshida found high conversion of fructose to HMF over amorphous zirconium phosphate catalysts.

It has been reported that the presence of moderate amounts of phosphate ions in  $Zr(OH)_4$  stabilizes the tetragonal structure at low temperatures (at 500–700°C)[19, 33], while higher concentrations of phosphate species stabilizes the amorphous zirconia phase[34]. This phenomenon seems to be attributed to the higher resistance to crystallite sintering obtained by phosphate doping, which retards the phase transition and increases considerably the surface area of the materials[10].

### 5.1.2 Acidity

Zirconium phosphate has remarkable acidic properties as a solid acid catalyst since it is able to catalyse reactions in aqueous media. A number of different studies attempted to determine the nature of acid sites in the catalyst. Hattori *et al.*[19] conducted a study on the source of the active sites on crystalline zirconium phosphate, and concluded that the catalyst possesses weak and strong acid sites attributed to P(OH) groups. Clearfield and Thakur[35, 36] associated the active sites of PZ to surface hydroxyl groups but also assigned some of the activity to Lewis acid sites after performing a poisoning study with quinoline or following proton exchange with  $Cs^+$  on the catalyst surface and observing a decrease in the activity of zirconium phosphate. On the other hand, La Ginestra *et al.*[24] attributed the catalytic activity of zirconium phosphate only to Brønsted acid sites on the surface of the catalyst after employing a similar surface poisoning technique. Spielbauer *et al.*[5] attributed the presence of Lewis acid sites to the  $Zr^{4+}$  on the coordinately unsaturated zirconium centre present on the surface of the catalyst. Sinhamahapatra *et al.*[37] also reported both Brønsted and Lewis acid sites in their study on mesoporous zirconium phosphate and theorized that Brønsted acid sites possibly arise from geminal P(OH) groups. The high acid character of PZ is produced following phosphate adsorption onto amorphous zirconia, and subsequent calcination in air. It has been reported that the maximum Brønsted acidity present on catalysts prepared from different precursors was obtained after calcination at 350-700°C[5, 19].

**Figure 5.2** shows the different types of bonds that phosphate ion can form with zirconium. First, the uncoordinated zirconium centres ( $Zr^{4+}$ ) can act as Lewis acid sites (A). When zirconia is subjected to phosphate treatment, the phosphate ions can bind either on isolated zirconium centres (B) or across two zirconium atoms in a cross-linked manner (C). When higher concentrations of phosphate precursor are used, the

phosphate species condense with neighbouring phosphate groups or free phosphate ions to form a superficial network of phosphate species (D)[37, 38]. When the monolayer regime is exceeded, higher concentrations of phosphate ions start forming agglomerates in a multilayer arrangement (E). It has also been postulated that the Lewis acid strength can be increased upon phosphate treatment due to the electron withdrawing nature of the surface phosphate group, which makes the metal centre more electron deficient[10].

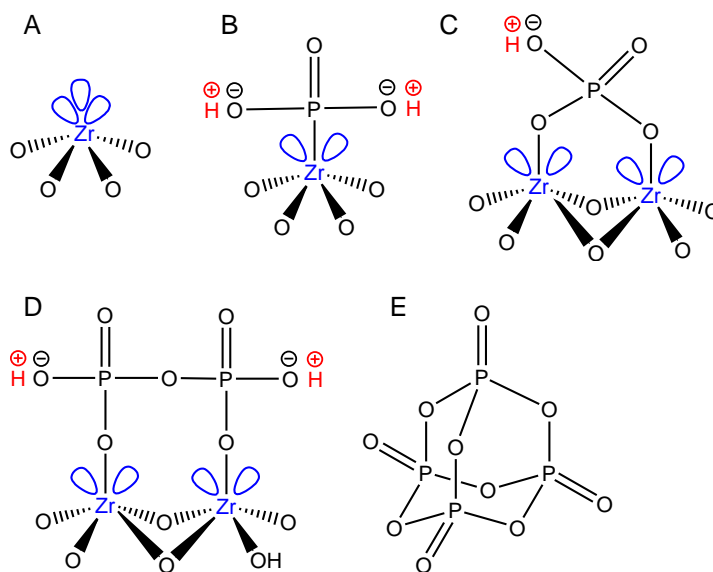


**Figure 5.2** Representative structure of the Lewis and Brønsted acid sites on phosphated zirconia catalysts (adapted from[39])

Comparing the acidic and catalytic properties of PZ with other phosphate catalysts, Antonetti *et al.*[32] recently reported a study on niobium and zirconium phosphate catalysts, and concluded that phosphated zirconia shows a greater concentration of Lewis acid sites than phosphated niobium, but the latter's somehow are of a stronger nature. On the other hand, although both catalysts exhibit similar concentration and strength of Brønsted acid sites, under hydrous conditions phosphated niobium is able to generate strong Brønsted acid sites, while phosphated zirconia shows a comparatively lower strength of Brønsted acidity. Weingarten *et al.*[40] synthesised and characterized series of solid acid zirconium and tin phosphates, and in their acid study they found a higher overall concentration of acid sites for the zirconium phosphates, while the tin phosphate catalysts showed the highest Lewis acidity, which lead to a higher selectivity towards fructose in the aqueous phase conversion of glucose to levulinic acid but lower dehydration performance than their zirconia counterpart. In 1986, Clearfield and Thakur published a review describing the physicochemical and

catalytic properties of zirconium and titanium phosphates, proving themselves as active catalysts for a wide range of reactions due to their moderately strong acid nature[36].

Several studies have also been reported comparing the acidic features of PZ with sulfated zirconia[7, 11, 13], which has been considered as a “superacid” material[41]. Comparing these two modified zirconia catalysts, it appears that phosphate modification induces lower protonic acidity on the surface of zirconia, thus attaining a slightly greater Lewis acid strength and lower Brønsted acid strength than the sulfated analogue[5, 42]. This milder acid strength provided by the phosphate treatment can be beneficial for the formation of HMF from hexoses, since it has been theorized that medium Brønsted acid strength grants a superior HMF selectivity, whereas strong acidity can promote undesirable side reactions as the formation of humins[32].

### **5.1.3 The application of phosphated zirconia in the production of HMF**

The dual acidity feature of  $ZrO_2$  due to the presence of both Lewis and Brønsted acid sites makes it a suitable catalyst for the dehydration of glucose and fructose to HMF as discussed in the previous chapter of this thesis. Indeed Qi and Watanabe reported the activity of  $ZrO_2$  as a catalyst for the isomerisation of glucose to fructose at 200°C[17, 43]. Jimenez Morales *et al.*[44] also reported the glucose dehydration to HMF on zirconium containing mesoporous MCM-41 silica catalysts in a water-MIBK biphasic reactor, observing a maximum glucose conversion of 82% and 23% HMF at 175°C and after 2.5 h of reaction time.

Zirconia also stands as a remarkable candidate for this reaction due to the potential for tuning not only the acid strength by the impregnation of phosphate functionalities, but also the Brønsted : Lewis ratio by carefully selecting the amount of phosphates incorporated. The application of PZ as solid acid catalysts for saccharides reactions is limited to a few available academic and patent reports. In 1980, Nakamura[45] published a patent for the production of HMF from hexoses in DMSO with PZ catalysts, obtaining a maximum HMF yield of 81% after 3 h of reaction at 140°C. In 2000, Benvenuti *et al.*[46] studied the effect of different zirconium and titanium phase modifications treated with phosphate salts in the dehydration of fructose and inulin to HMF in aqueous media at 100°C. They obtained conversions of fructose and inulin over 70% and almost complete selectivity to HMF performing subsequent extractions of reaction products with MIBK. In 2006, Asghari and Yoshida[16] reported the dehydration of fructose to HMF in sub-critical water over zirconium phosphate catalysts, and they observed about 80% of fructose conversion at 240°C after only 2

minutes, with 61% selectivity to HMF. Under the same experimental conditions, using glucose as reactant, 39% of selectivity to HMF was obtained. More recently, in 2013, Ordonsky *et al.*[12] published a study where they measured the physicochemical properties of several metal phosphates, and phosphated zirconium outperformed aluminium and titanium phosphates in the glucose dehydration to HMF. Higher glucose conversion was observed for catalysts with higher acid strength, while the selectivity to HMF increased with the increase in the ratio of Brønsted to Lewis acid sites. In 2015, Xu *et al.*[47] reported their results for the dehydration of fructose to HMF by high stable ordered mesoporous zirconium phosphate in DMSO at 120°C for 90 min, with 90% conversion and 70% HMF yield. The same year Jain *et al.*[48] reported the conversion of fructose, glucose and sucrose to HMF over mesoporous zirconium phosphate catalyst in water-diglyme biphasic system, and observed the highest HMF yield of 80% after 60 min reaction at 150°C. Finally, in 2017 Antonetti *et al.*[32] published the microwave-assisted dehydration of fructose and inulin to HMF catalysed by phosphated zirconium and niobium. HMF yield of 39% was observed at 190°C and short times (8 min) using PZ.

The tunability of acid-base properties of zirconia with addition of sulphate species has been investigated and proven successful for the dehydration of sugars to HMF[49]. However, to the best of our knowledge, the detailed impact of phosphate coverage on the acid-base properties of ZrO<sub>2</sub> for the dehydration of glucose and fructose to HMF has not yet been reported. Sulfated zirconia has been considered as a superacid, and high acid strength may lead to the formation of side reactions. So the main objective of this investigation is to study whether phosphated species are able to tune the acid-base properties of zirconia, providing milder acid strength than the sulfated counterpart, and whether these catalysts are active for the dehydration of glucose and fructose to HMF.

## 5.2 Results and discussion

### 5.2.1 Characterization of phosphated zirconia catalysts

#### 5.2.1.1 Surface and bulk compositional analysis

The impact of zirconium hydroxide impregnation by 0.01-0.5 M H<sub>3</sub>PO<sub>4</sub> followed by calcination at 550, 650 and 750°C was probed by XPS and ICP to determine the atomic composition as well as the phosphorous content achieved after impregnation in the prepared phosphated materials. **Table 5.1** displays the values for the bulk and surface phosphorous content obtained from ICP and XPS respectively. ICP analysis

shows a constant increase in P content with increasing the concentration of the phosphoric solution used during the impregnation process, consistent with satisfactory incorporation of the phosphate species onto the zirconia structure. The P wt% measured by ICP was found to be very similar for the same solution concentration upon calcination at different temperatures, proving the thermal stability of the phosphate groups in the range of temperatures studied. With increasing the phosphate amount, the oxygen content also increases systematically, which accounts for the  $\text{PO}_4^{3-}$  species loaded onto the zirconia matrix, which leads to a progressive decrease in the relative zirconium content. With increasing calcination temperature, the oxygen content decreases for a same phosphate loading due to the condensation of some hydroxyl groups present in form of Zr-OH[44].

**Table 5.1** Elemental analysis of PZ materials

| Catalyst             | Bulk P content <sup>a</sup> / wt% | Surface content <sup>b</sup> / wt% |       |       | Surface content <sup>b</sup> / at% |       |       |
|----------------------|-----------------------------------|------------------------------------|-------|-------|------------------------------------|-------|-------|
|                      |                                   | Zr±0.5                             | O±0.2 | P±0.1 | Zr±0.2                             | O±0.5 | P±0.1 |
| ZrO <sub>2</sub> 550 | 0                                 | 71                                 | 29    | 0     | 31                                 | 69    | 0     |
| PZ550 0.01           | 0.5±0.2                           | 70                                 | 29    | 0.5   | 30                                 | 69    | 0.6   |
| PZ550 0.05           | 2.3±0.2                           | 64                                 | 33    | 2.6   | 25                                 | 73    | 1.7   |
| PZ550 0.1            | 4.2±0.2                           | 61                                 | 35    | 4.1   | 24                                 | 74    | 2.9   |
| PZ550 0.25           | 6.1±0.2                           | 55                                 | 39    | 6.0   | 20                                 | 76    | 3.8   |
| PZ550 0.5            | 9.0±0.2                           | 48                                 | 46    | 6.6   | 15                                 | 79    | 6.0   |
| ZrO <sub>2</sub> 650 | 0                                 | 71                                 | 29    | 0     | 31                                 | 69    | 0     |
| PZ650 0.01           | 0.6±0.2                           | 69                                 | 29    | 1.7   | 29                                 | 71    | 0.8   |
| PZ650 0.05           | 2.3±0.2                           | 65                                 | 32    | 3.8   | 25                                 | 73    | 1.8   |
| PZ650 0.1            | 4.2±0.2                           | 60                                 | 33    | 6.3   | 23                                 | 74    | 2.9   |
| PZ650 0.25           | 5.8±0.2                           | 55                                 | 36    | 8.5   | 20                                 | 76    | 3.7   |
| PZ650 0.5            | 8.2±0.2                           | 44                                 | 41    | 14.3  | 15                                 | 79    | 5.9   |
| ZrO <sub>2</sub> 750 | 0                                 | 73                                 | 27    | 0     | 31                                 | 69    | 0     |
| PZ750 0.01           | 0.7±0.2                           | 69                                 | 29    | 1.9   | 29                                 | 70    | 1.0   |
| PZ750 0.05           | 2.7±0.2                           | 65                                 | 31    | 3.9   | 26                                 | 72    | 1.9   |
| PZ750 0.1            | 4.5±0.2                           | 62                                 | 33    | 5.4   | 24                                 | 73    | 2.6   |
| PZ750 0.25           | 6.1±0.2                           | 58                                 | 34    | 7.8   | 22                                 | 75    | 3.6   |
| PZ750 0.5            | 8.8±0.2                           | 47                                 | 40    | 13.4  | 16                                 | 78    | 5.6   |

From <sup>a</sup>ICP; <sup>b</sup>XPS

From now on, the catalysts will be referred to as  $x\text{-PZ}_y$ , where  $x$  is the bulk phosphorous loading obtained by ICP and  $y$  is the calcination temperature used after phosphate treatment. **Figure 5.3** shows the spectra of Zr 3d (left) and O 1s (right) of the PZ catalysts with different phosphate loading and pre-calcined at different temperatures, and **Figure 5.4** displays the spectra of P 2p (left) as well as the comparison between the surface and bulk P content obtained by XPS and ICP respectively.

The Zr 3d spectra of  $\text{ZrO}_2$  reveal the presence of a doublet at binding energy values of 181.8 and 184.2 eV, corresponding to Zr 3d<sub>5/2</sub> and Zr 3d<sub>3/2</sub> respectively, according to the values reported in the NIST database[50], which are associated with an oxidation state of tetravalent zirconium  $\text{Zr}^{4+}$ . The intensity ratio of the Zr 3d<sub>5/2</sub> and Zr 3d<sub>3/2</sub> peaks is fixed to 3 : 2 and the separation between the two Zr 3d peaks for all the series examined is 2.3- 2.4 eV. This peak separation is in good agreement with the Zr 3d peak separation in other reports for similar materials[51, 52]. With increasing phosphate content the signal is shifted up to 1.2 eV for the highest phosphate loading. This phenomenon has been previously reported for PZ materials[8, 40, 53], and can be attributed to the decrease in electron density after the introduction of the phosphate group, which makes the metal centre more electron deficient, thus shifting its binding energy[10].

The O 1s spectra of  $\text{ZrO}_2$  present two peaks at 529.7 and 531.6 eV which correspond to Zr-O-Zr and Zr-O-H respectively[54]. With the introduction of phosphate groups two new peaks arise at 531.6 eV and 533.5 eV corresponding to Zr-O-P (in coexistence with contributions from P=O and Zr-OH[55]) and P-O-H species respectively[56, 57], whose intensity increase steadily with the incorporation of phosphates. With increasing phosphate content, the Zr-O-P bond becomes the predominant signal, indicating that the main coordination modes transformed from Zr-O-Zr to Zr-O-P with the introduction of phosphorus. At the same time, the Zr-O-Zr signal experiences a 0.8 eV shift towards higher binding energy due to the change in electron density mentioned before. The P 2p signal is comprised by two peaks at 133.5 and 134.4 corresponding to P 2p<sub>5/2</sub> and P 2p<sub>3/2</sub>, which is characteristic of  $\text{P}^{5+}$ [56] and whose intensity increases with phosphate content.

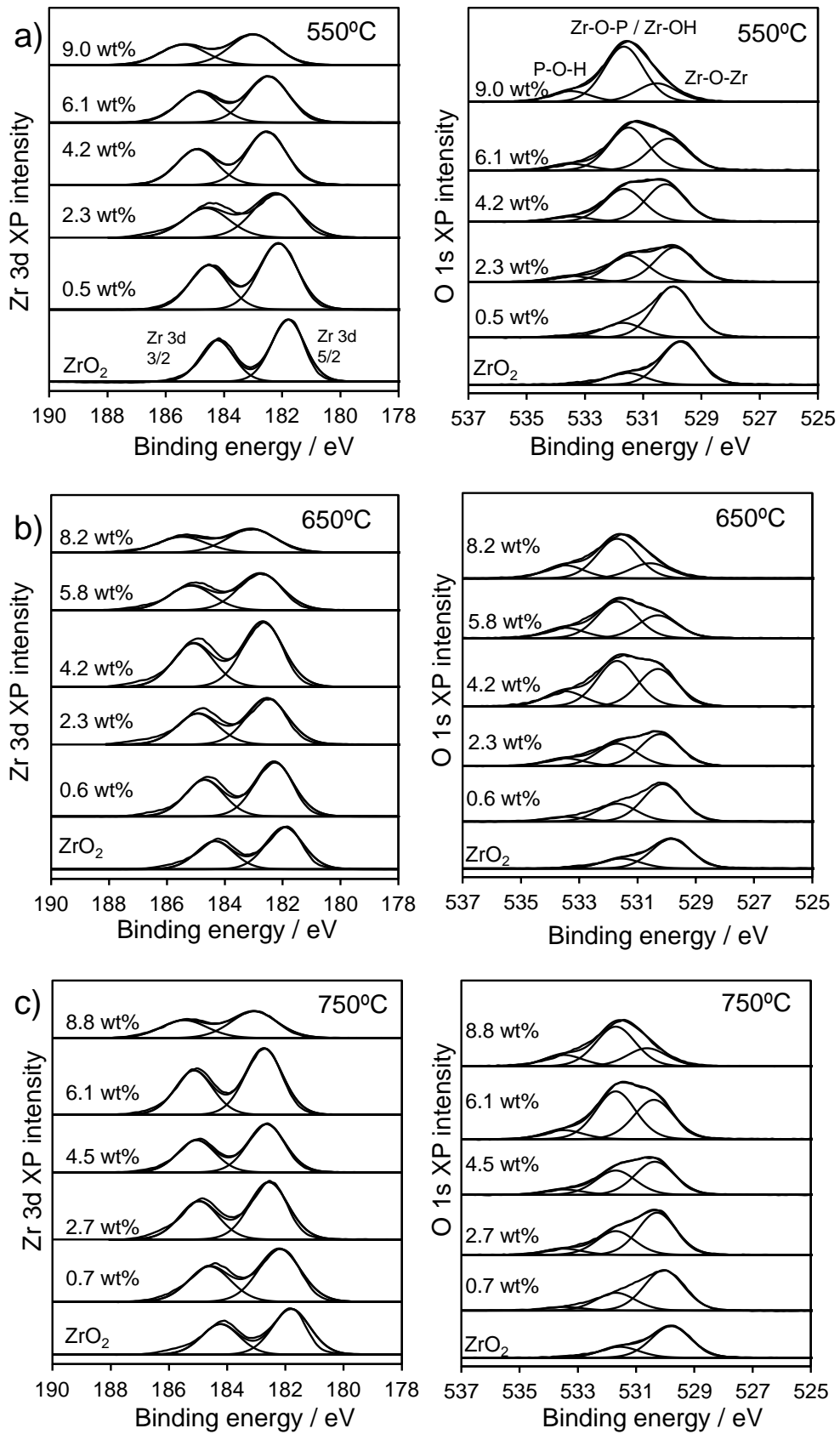


**Figure 5.3** XPS of the Zr 3d (left) and O 1s (right) regions for the PZ materials calcined at a) 550°C, b) 650°C and c) 750°C

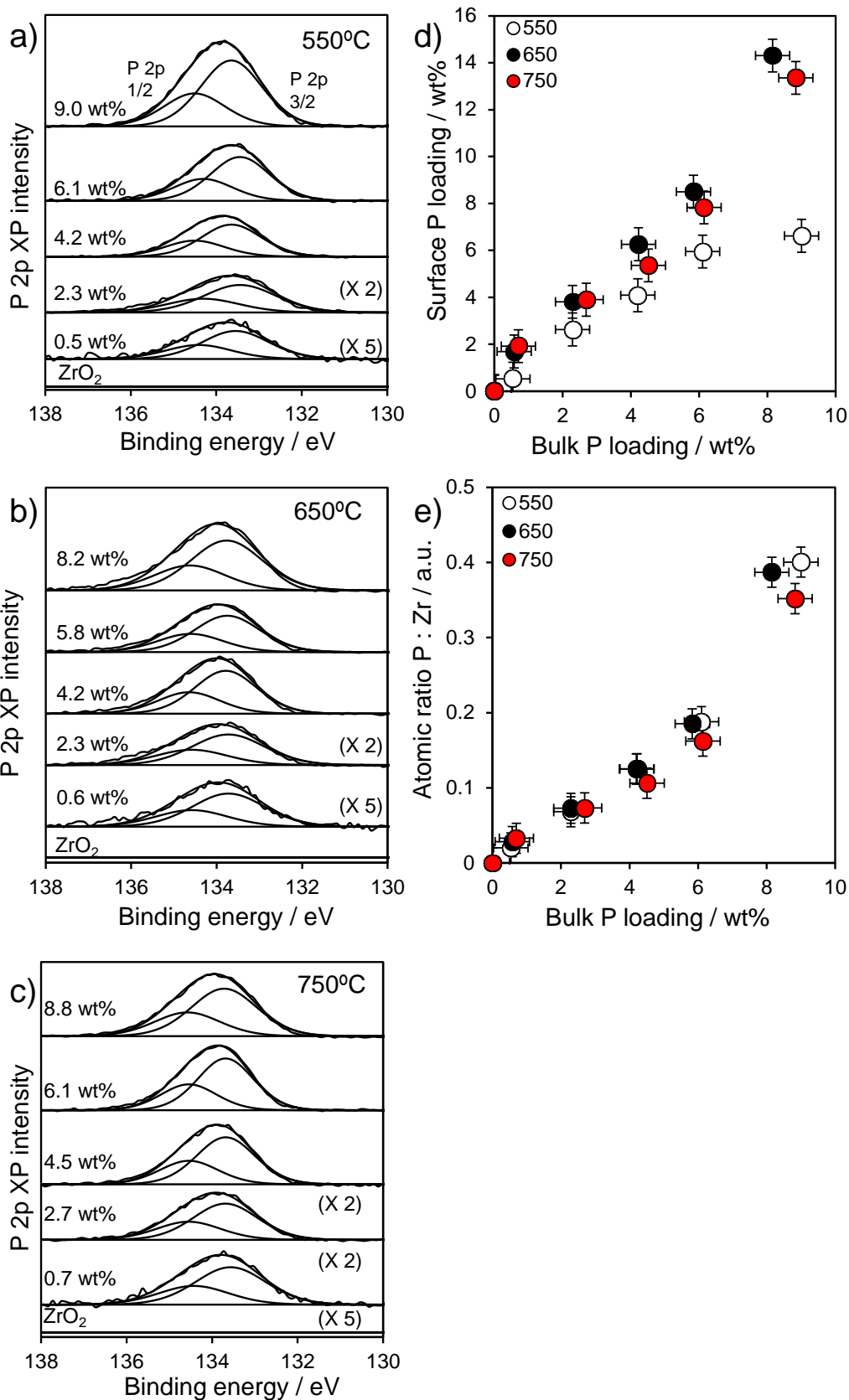


**Figure 5.4** XPS of the P 2p region for the PZ materials calcined at a) 550°C, b) 650°C and c) 750°C; d) comparative of bulk and surface P content and e) P:Zr ratio with P content for the series of catalysts calcined at 550°C (white), 650°C (black) and 750°C (red)

**Figure 5.4** also depicts the variation of bulk and surface P content with increasing phosphate loading. The series calcined at 550°C shows a linear correlation between bulk and surface species, but higher bulk P content is observed for the sample prepared with the highest concentration of phosphoric acid solution. This can be explained by the completion of a phosphate monolayer at this point, so that higher phosphate concentrations lead to agglomeration of phosphates on the surface of the zirconia support. This effect was also reported by Parida and Pattnayak at a similar phosphate concentration for materials prepared in a similar way[33]. Higher calcination temperatures seem to inhibit this phenomenon, since a higher surface P content is observed for all the samples, even at high phosphate concentrations. This can be explained by the disaggregation and redistribution of phosphates provoked by higher thermal treatment.

A similar trend is found for the effect of the P:Zr ratio with increasing phosphate content presented in **Figure 5.4**. Here in can be observed a linear increase in the P:Zr ratio up to the sample prepared with a  $\text{H}_3\text{PO}_4$  concentration of 0.25M equivalent to a P content of ~6 wt%. After this an exponential increase is detected for the highest P loading independent of the calcination temperature, which can be explained by the overshoot of the monolayer regime and polymerization of phosphate species.

#### **5.2.1.2 Textural properties**

**Figure 5.5** shows the porosimetry data for the three series of phosphated zirconia calcined at different temperatures. The parent  $\text{ZrO}_2$  data exhibit a type IV isotherm with hysteresis loops indicative of bottle-necked mesopores. Increasing phosphate content this characteristic slowly fades to give way to type II isotherms distinctive of non-porous materials. A broad pore size distribution is observed below 5nm for all the phosphated samples, however, since no directing agent was employed during the synthesis of these materials, the initial mesoporosity probably arises from interparticle voids between  $\text{ZrO}_2$  crystallites. No microporosity was detected on any of the samples, as it is indicated by the absence of a knee at low relative pressures. Absence of microporosity has been claimed before, using the same zirconium precursor[6].

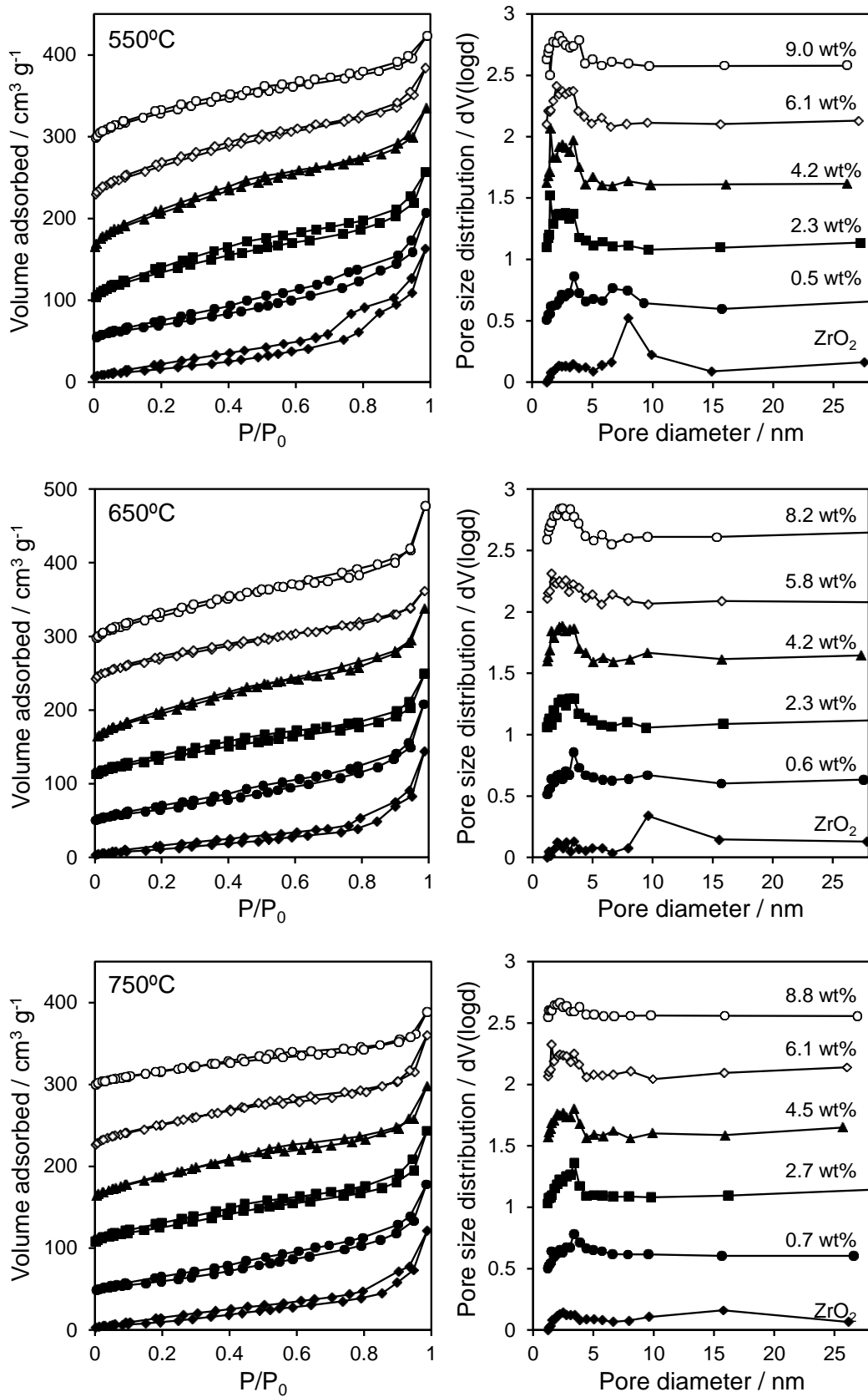


**Figure 5.5** N<sub>2</sub> porosimetry isotherms (left) and pore size distribution (right) of the series of PZ catalysts calcined at 550°C (top), 650°C (middle) and 750°C (bottom).

Textural properties of PZ materials are summarised in **Table 5.2**. Phosphate treatment induced a surface area increase for the three series of temperatures studied. As seen in **Figure 5.6**, both surface area and pore volume increase rapidly reaching a maximum for the catalysts prepared with 0.1M H<sub>3</sub>PO<sub>4</sub> concentration, to steadily decrease for higher concentrations in a volcano-like trend. For example, for catalysts calcined at 550°C the surface area increases from 61 m<sup>2</sup>/g for ZrO<sub>2</sub> to 260 m<sup>2</sup>/g for 4.2-PZ550, and decrease again down to 213 m<sup>2</sup>/g for 9.0-PZ550. This volcano shape was also reported by other groups for similar PZ materials, for example Parida and Pattnayak[33] obtained a maximum of 253 m<sup>2</sup>/g for a catalyst calcined at 400°C with 6.5 P wt%, and detected a steady decrease in surface area down to 88 m<sup>2</sup>/g for a P loading of 12.2 wt%. Other studies report maximum surface areas in the range of 150-280 m<sup>2</sup>/g depending on the precursor and calcination temperatures used[5, 6, 8, 12, 40]. The stabilization effect of surface area promoted by phosphate incorporation can be attributed to the higher resistance to sintering obtained by phosphate doping[5, 10].

**Table 5.2** Textural properties of PZ materials

| Catalyst             | Surface area <sup>a</sup> /<br>m <sup>2</sup> ·g <sup>-1</sup> | Pore diameter <sup>b</sup><br>/ nm | Pore volume <sup>c</sup><br>/ cm <sup>3</sup> ·g <sup>-1</sup> |
|----------------------|--|------------------------------------|--|
| ZrO <sub>2</sub> 550 | 61   | 8.0                                | 0.22   |
| 0.5-PZ550            | 108  | 3.4                                | 0.23   |
| 2.3-PZ550            | 214  | 1.5                                | 0.26   |
| 4.2-PZ550            | 260  | 1.5                                | 0.29   |
| 6.1-PZ550            | 231  | 2.0                                | 0.26   |
| 9.0-PZ550            | 213  | 1.7                                | 0.22   |
| ZrO <sub>2</sub> 650 | 41   | 2.0                                | 0.16   |
| 0.6-PZ650            | 62   | 3.4                                | 0.20   |
| 2.3-PZ650            | 141  | 2.2                                | 0.20   |
| 4.2-PZ650            | 219  | 1.5                                | 0.27   |
| 5.8-PZ650            | 180  | 1.5                                | 0.20   |
| 8.2-PZ650            | 169  | 1.8                                | 0.25   |
| ZrO <sub>2</sub> 750 | 40   | 2.5                                | 0.14   |
| 0.7-PZ750            | 42   | 1.5                                | 0.18   |
| 2.7-PZ750            | 110  | 3.4                                | 0.20   |
| 4.5-PZ750            | 155  | 2.0                                | 0.20   |
| 6.1-PZ750            | 146  | 1.5                                | 0.19   |
| 8.8-PZ750            | 95   | 1.8                                | 0.12   |

<sup>a</sup>N<sub>2</sub> BET; <sup>b</sup>BJH desorption branch of isotherm; <sup>c</sup>recorded at P/P<sub>0</sub>=0.98

The decrease in the surface area at high  $\text{H}_3\text{PO}_4$  concentrations has been attributed to the alteration of crystal structure and phosphate migration into the bulk phase of the solid, as previously observed for sulfated zirconia[58] and confirmed by the XPS results above presented.

Comparing materials with similar P loading calcined at different temperatures, it is possible to observe a considerable decrease in surface area when calcination temperature increases. Powers and Gray[59] demonstrated that there is a formation of oxo bridges at temperatures over  $80^\circ\text{C}$  due to the loss of water at the expense of double hydroxy bridges. Thus during the calcination of the phosphated materials, the presence of phosphates delays the formation of the oxo bonds, which may explain the observed loss of surface area as a function of temperature[4]. This effect can also be accompanied by the sintering of crystallites.

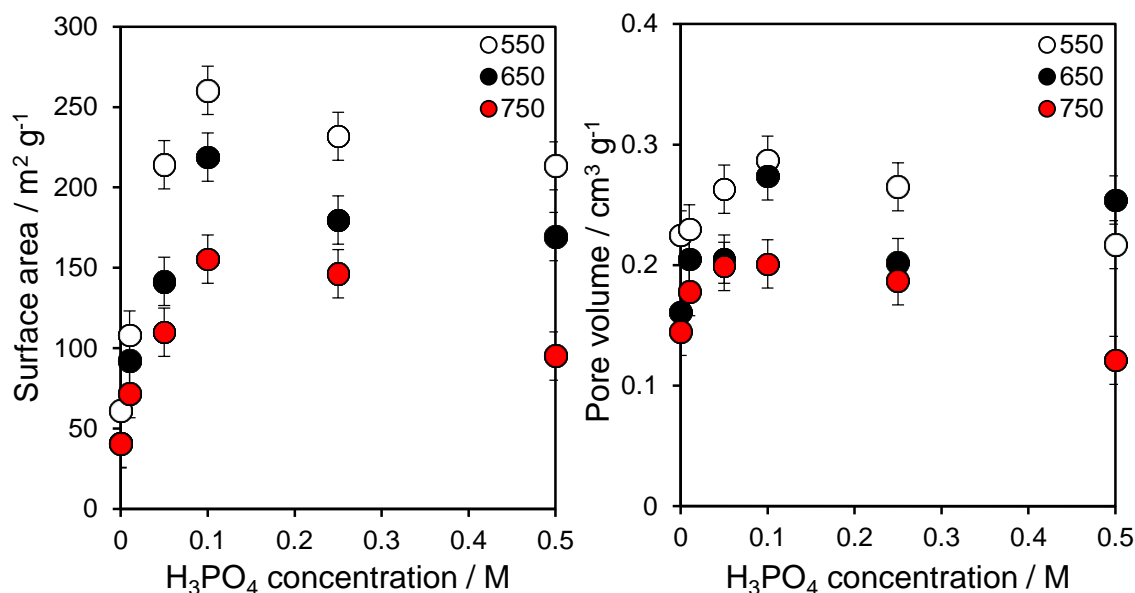


**Figure 5.6** Influence of  $[\text{H}_3\text{PO}_4]$  in surface area of PZ materials calcined at  $550^\circ\text{C}$  (white)  $650^\circ\text{C}$  (black) and  $750^\circ\text{C}$  (red)

### 5.2.1.3 Structure and morphology

Powder X-Ray diffraction was performed in order to assess the crystallinity and morphology of the zirconia materials with different phosphate loadings subjected to thermal treatment. Raman spectroscopy was performed to confirm the phosphated zirconia structure of the catalysts.

### 5.2.1.3.1 Powder X-Ray diffraction

The formation of crystalline species in calcined PZ samples was explored using powder XRD, and the diffractograms obtained are shown in **Figure 5.7**. Samples prepared without phosphate modification are well crystallized and contain mixtures of monoclinic and tetragonal phases, with a higher contribution of the former. Monoclinic phase shows reflections at  $2\theta = 24.7^\circ, 28.2^\circ, 31.5^\circ, 33.9^\circ$  and  $40.9^\circ$  which can be indexed as the (011), (-111), (111), (002) and (211) planes of the monoclinic phase of  $ZrO_2$  structure respectively and typical peaks for tetragonal phase are observed at  $30.3^\circ, 35.3^\circ, 50.3^\circ$  and  $59.9^\circ$  which can be indexed as the (111), (200), (220) and (311) planes[60]. With the incorporation of small amounts of phosphate species, the characteristic peaks of the monoclinic phase decrease their intensity, and those of tetragonal phase emerge, gaining intensity. This stabilization of tetragonal phase by the incorporation of phosphate groups has been previously reported for phosphated zirconia[33, 34] and also for sulfated zirconia[61, 62]. For samples prepared with higher concentrations of phosphoric acid during the impregnation process, the crystallinity of the materials decreases and an amorphous form arises[26]. The hindrance in the crystallization of the PZ samples at high phosphate loadings is probably due to the suppression of particle growth induced by the presence of phosphate species[10]. The presence of phosphate groups at the surface of the zirconia materials broadens the temperature range of existence of tetragonal phase, which delay the appearance of the amorphous phase at high phosphate loadings. This could happen because the inhibiting crystallization effect of the phosphate ions is weakened by the higher sintering potential attained at higher calcination temperatures.

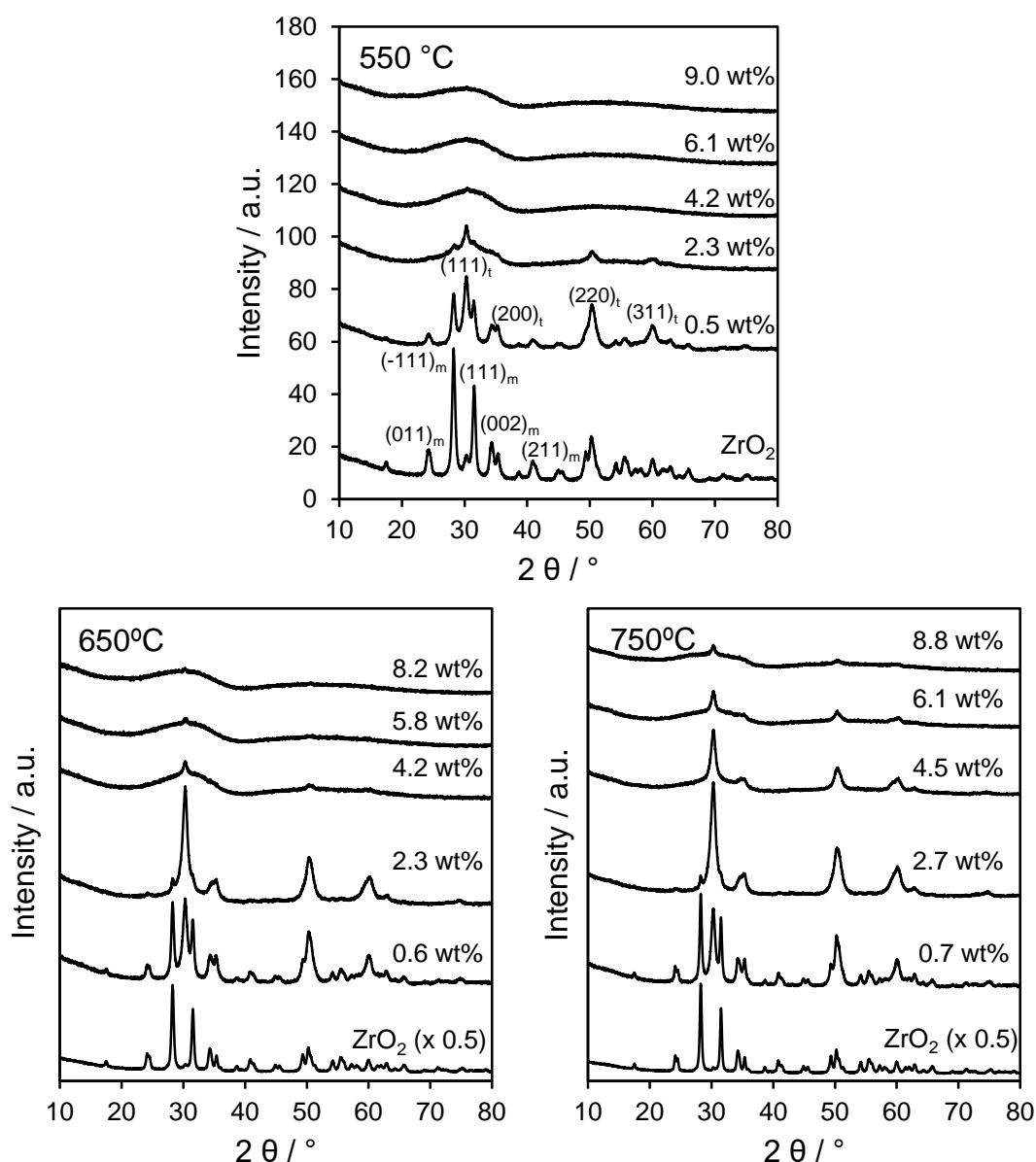


**Figure 5.7** X-Ray Powder diffractograms for phosphated zirconias series calcined at different temperatures

Based on the Scherrer equation (see **Chapter 2**), the monoclinic crystallite size in the pure zirconia sample is calculated to be 13.6 nm and increase to 17.3 and 20.9 nm at temperatures of 650°C and 750°C respectively due to sintering processes. Increasing phosphate content, the monoclinic phase is attenuated and the crystallite size calculated for the tetragonal signals is constant at a value of 10-12 nm for all crystalline samples independent of the phosphate loading or calcination temperature. This size of crystallite size is in accordance with reports published by Stojkovic *et al.* (13-19 nm for a PZ calcined at 600°C) [13] and Mercera *et al.*[63] (9-13 nm for a PZ calcined at 550 and 650°C). The lattice parameters for the monoclinic and tetragonal structures were calculated according to the combination of the lattice distance and Bragg's Law

equations displayed in **Chapter 2**. Thus, the monoclinic phase showed unit cell parameters of  $a = 5.32 \text{ \AA}$ ,  $b = 5.22 \text{ \AA}$ ,  $c = 5.15 \text{ \AA}$  calculated from the reflexions (111), (011) and (002) respectively, with  $\alpha = 90^\circ$ ,  $\beta = 99.11^\circ$  and  $\gamma = 90^\circ$ , in good agreement with the results obtained by Ali and Zaki[22, 64]. After transformation to the tetragonal phase, the lattice parameters obtained from the reflexions (200) and (111) were  $5.86 \text{ \AA}$  and  $4.19 \text{ \AA}$  respectively, whose structures were shown in **Figure 5.1** previously in this chapter.

#### 5.2.1.3.2 Thermogravimetric analysis and differential thermal analysis

Thermal stability of PZ materials was evaluated by thermogravimetric analysis and differential thermal analysis was used to further prove the consistency of desorption temperature across each family. **Figure 5.8** displays the decomposition steps as function of temperature for each PZ family calcined at 550, 650 and 750°C. The three families showed a common single decomposition step between 40 and 150°C, which is attributed to weakly bonded water molecules adsorbed on the materials surface. At higher temperatures  $>150^\circ\text{C}$ , no further mass loss was observed, revealing the absence of decomposition processes, and the high stability of materials, as confirmed also by other literature studies[10]. Differential thermal analysis further proved that physisorbed water desorption occurs at the same temperature for all the samples,  $64^\circ\text{C}$  suggesting that upon calcination PZ materials preserve the same physical properties. Additionally, differential scanning calorimetry analysis carried out for all the catalysts displayed no heat flow changes for temperatures  $>150^\circ\text{C}$ , indicating the absence of phase transition due to the pre-calcination over  $550^\circ\text{C}$ . To further investigate on the hydrophobicity-calcination temperature relationships of PZ materials, the mass loss % desorbed from each sample at  $64^\circ\text{C}$  was plotted against the molar concentration of phosphoric acid solution used for the impregnation of  $\text{ZrO}_2$ . As shown in **Figure 5.9**, the PZ series calcined at the lowest temperature possesses higher amount of physisorbed water than the 650 and 750 counterparts, which exhibit similar trends. Across the PZ550 family, the amount of physisorbed water rises rapidly from 0.3% to 2%, as observed for the parent  $\text{ZrO}_2$  and 0.05 M phosphoric acid solution respectively, at further phosphate loading the value plateaus at  $\sim 2.3\%$ . PZ650 and PZ750 series present similar trends than that obtained from PZ550 materials, where the amount of desorbed physisorbed water rises with increasing phosphate loadings, reaching a plateauing at  $\sim 1.7\%$  for catalysts with higher P content. Results evidence that the hydrophobic character is enhanced at higher calcination temperatures, as consequence of the major dihydroxylation of the surface.

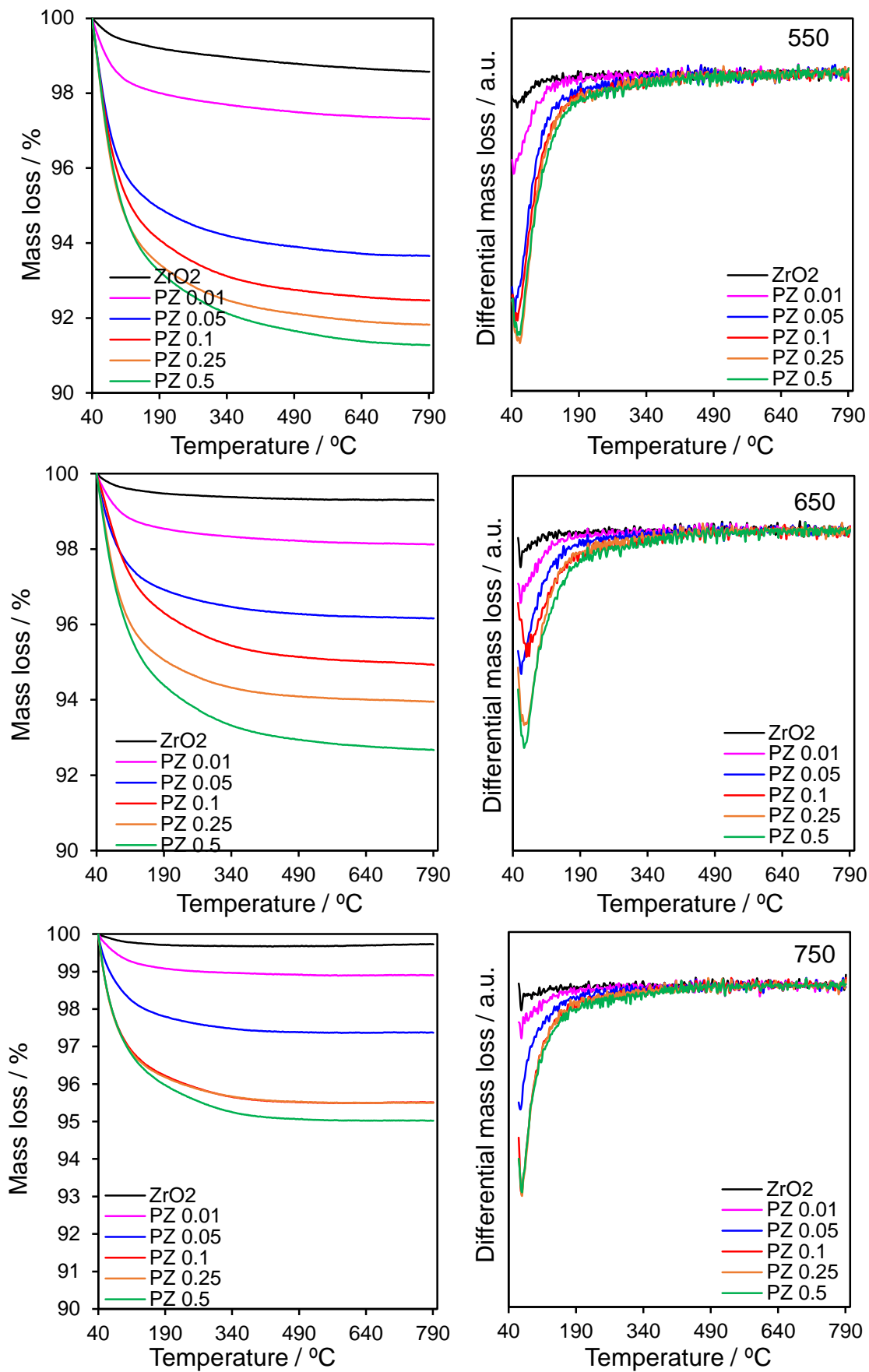


**Figure 5.8** – Thermal analysis reported as % mass loss as function of temperature, obtained for each PZ series (left); and differential thermal analysis (right).

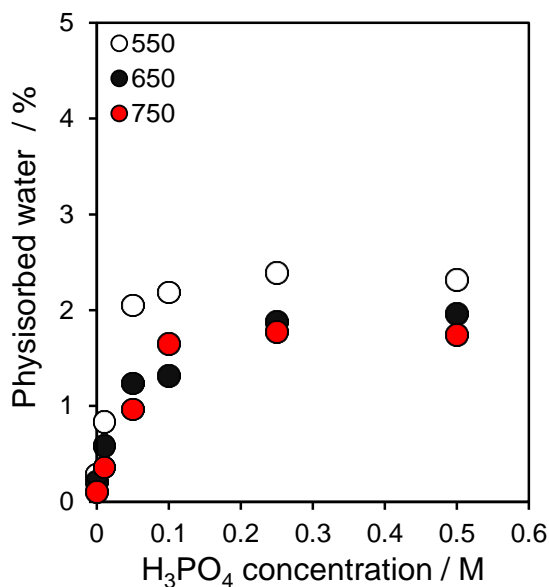


**Figure 5.9** – Physisorbed water mass loss for PZ materials calcined at different temperatures.

### 5.2.1.3.3 Raman spectroscopy

Raman spectroscopy allows the clear discrimination of the monoclinic and tetragonal phases of ZrO<sub>2</sub> (**Figure 5.10**). The tetragonal and the monoclinic phases of zirconia show intense bands of Zr-O vibrations up to 700 cm<sup>-1</sup> in the Raman spectra. The monoclinic phase of ZrO<sub>2</sub> exhibits bands at 140, 180, 216, 260, 301, 328, 342, 378, 471, 499, 533, 553, 610, and 632 cm<sup>-1</sup>, while the peaks observed at 148, 263, 325, 472, 608, and 640 cm<sup>-1</sup> are typical of the tetragonal phase[63, 65, 66]. ZrO<sub>2</sub> calcined at all temperatures studied presents a predominant signal from the monoclinic phase, as equally observed by XRD. For the samples calcined at 550°C the bands disappear at low phosphate loadings promoting the formation of an amorphous phase as observed by XRD. For higher calcination temperatures, the effect of phosphate incorporation is more obvious, represented by a decrease in band intensity at 180, 301, 328, 378, 471 and 632 belonging to the monoclinic phase signal, with a subsequent increase of the main tetragonal peaks at 263, 472 and 640 cm<sup>-1</sup>. As explained in the case of the XRD, the stability of the tetragonal phase increases with phosphate content and calcination temperature, as it was also observed by Mekhemer[4]. The broad peak centred around 1030 cm<sup>-1</sup> increasing its intensity with phosphate content is associated to P-O species.

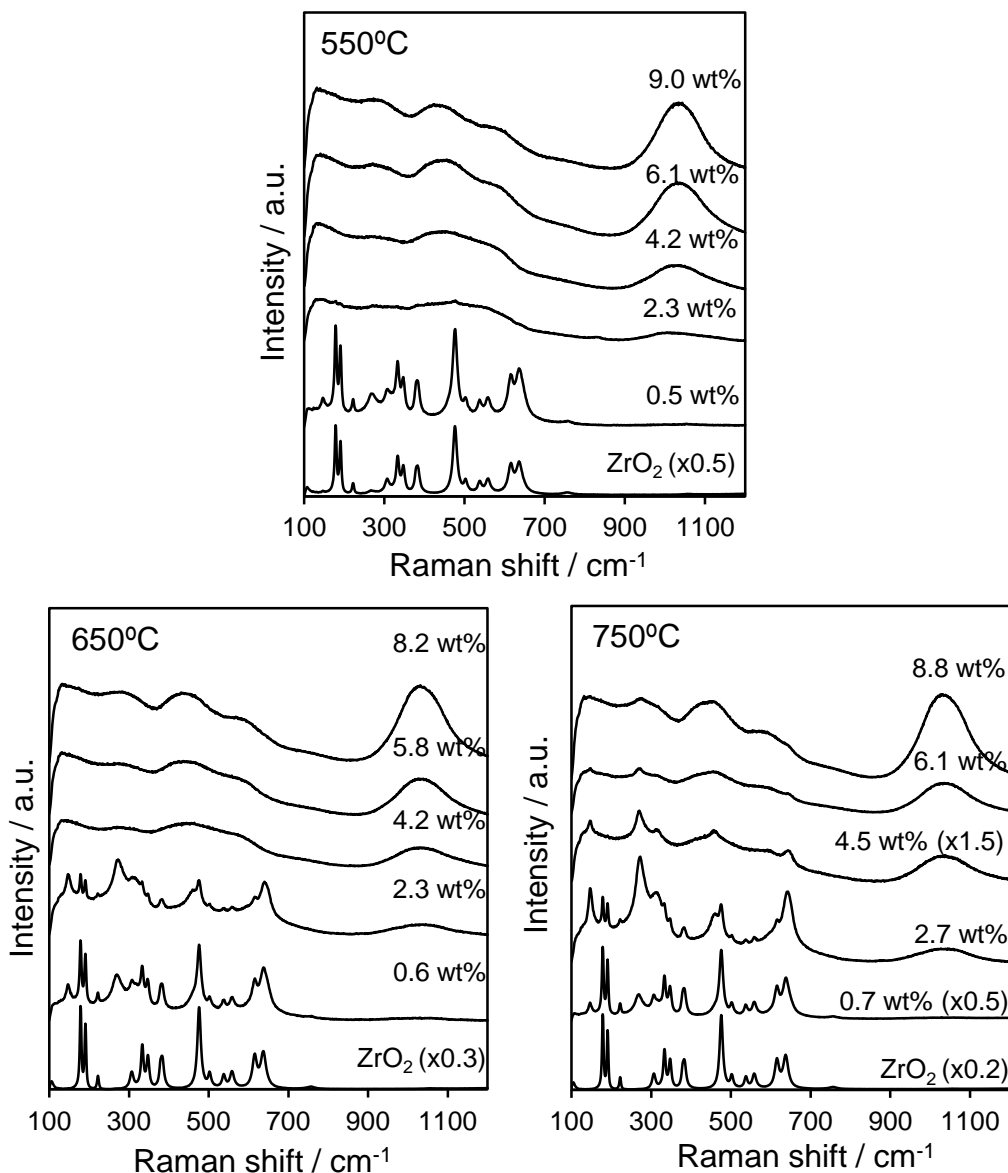


**Figure 5.10** Raman spectra of PZ series calcined at different temperatures

#### 5.2.1.4 Acid and base sites measurement

Surface acidity was probed by both pyridine and propylamine adsorption. The nature of acid sites was first examined through DRIFTS following pyridine treatment, and propylamine adsorption was used for the intrinsic acid site measurement of these catalysts. Zirconia catalysts also exhibit basic properties[67], so in order to calculate the total amount of basic sites as a function of phosphate loading and calcination temperature, CO<sub>2</sub> titrations were employed.

#### 5.2.1.4.1 Diffuse reflection infrared Fourier transform spectroscopy (DRIFTS) and in situ pyridine chemisorption

The presence of  $\text{PO}_4^{3-}$  species is supported by DRIFTS measurements shown in **Figure 5.11** (left). The IR spectra in the range of  $1000\text{-}1200\text{ cm}^{-1}$  exhibit a broad band growing in intensity with increasing phosphate loading and absent in the case of pure zirconia, with main vibrational bands at  $1043\text{ cm}^{-1}$  and a shoulder at  $1132\text{ cm}^{-1}$ . This band probably contains several overlapped bands which can be assigned to the P-O stretching and bending vibrations of the  $\text{PO}_4^{3-}$  anion[14, 38]. The band near  $1620\text{ cm}^{-1}$  shown in **Figure 5.11** (right) denotes the bending vibrational modes of -OH, which can be assigned to molecularly adsorbed water, Zr-OH and/or P-OH[10, 33]. The intensity of this band constantly increased with phosphate loading at all calcination temperatures studied. These results indicate the successful incorporation of the phosphate groups onto the surface of zirconia, and their permanence even at higher calcination temperatures, which is in good agreement with the Raman results above reported.

Zirconia is a solid acid material with the potential to exhibit both Lewis and Brønsted acidity depending on the crystalline phase. In order to measure the evolution of Lewis-Brønsted acidic properties of the PZ materials, analyses using pyridine as a probe molecule were conducted (**Figure 5.12**). Although monoclinic zirconia generated via calcination has been reported to exhibit predominantly Lewis acidity[68], the band related to both Lewis and Brønsted acid sites were very weak for the untreated  $\text{ZrO}_2$ , probably due to the low acidity of Zr-O-H groups, being unable to protonate pyridine at room temperature [14]. After the phosphate impregnation treatment, three bands arise gaining intensity with phosphate loading. The band at  $1448\text{ cm}^{-1}$  is attributed to pyridine adsorbed on Lewis acid sites, which include Lewis acid sites formed by metal attached to the phosphate group (Zr-O-P) and coordinatively unsaturated zirconium ions[5]. The band at  $1540\text{ cm}^{-1}$  is assigned to pyridine adsorbed on Brønsted acid sites of  $-\text{P}(\text{OH})_n$  ( $n=1, 2$ ) and the peak at  $1488\text{ cm}^{-1}$  is due to pyridine adsorbed on both Brønsted and Lewis acid sites[69]. Increase in phosphate loading gradually increases Brønsted acidity independently of the calcination temperature employed, due to a higher concentration of P-OH groups, which are responsible for the Brønsted acidity of the materials[11].

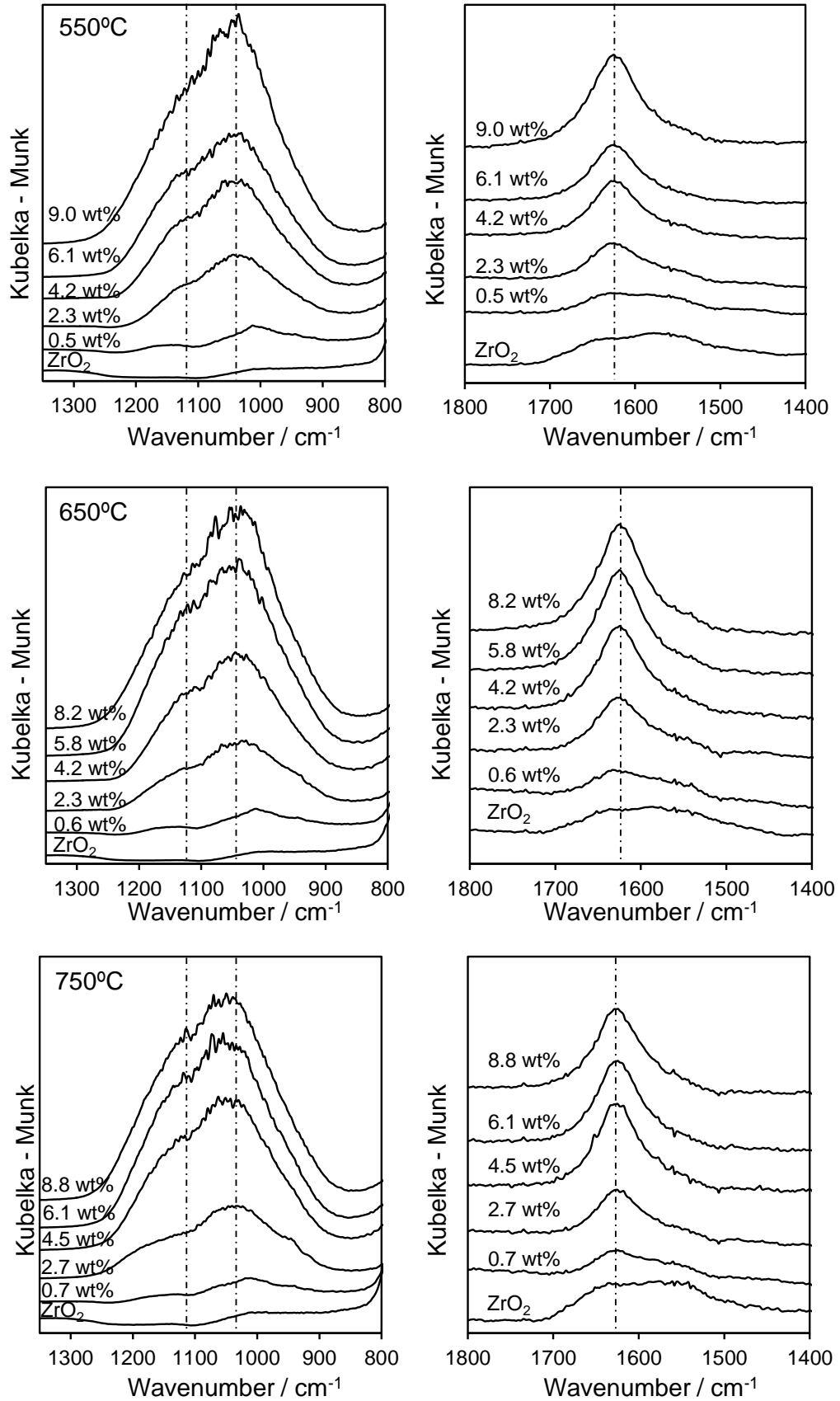


**Figure 5.11** In-vacuo DRIFT spectra of PZ as a function of bulk P content

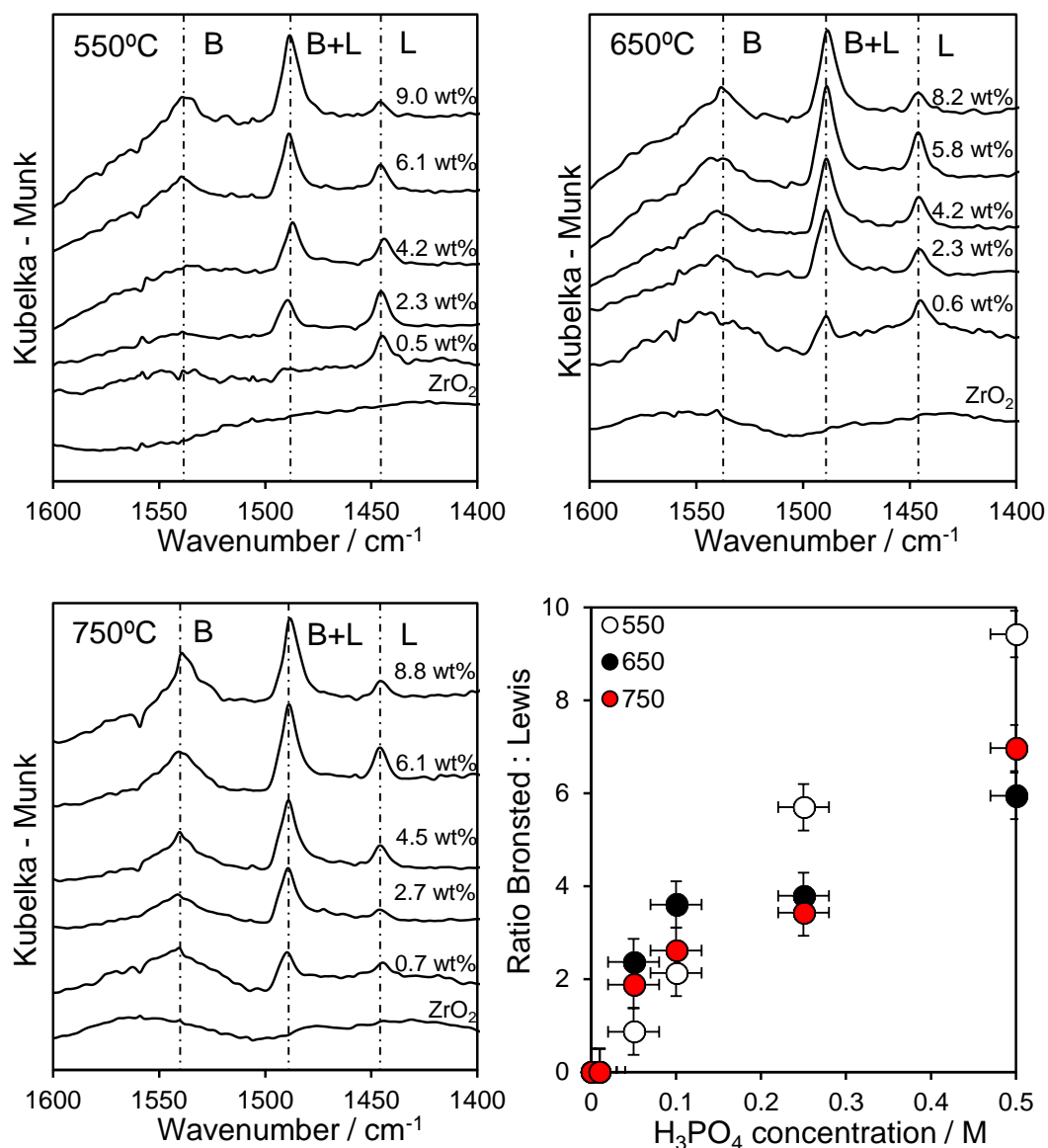


**Figure 5.12** In-vacuo DRIFT spectra of pyridine treated PZ materials at different calcination temperatures and their Brønsted : Lewis character as a function of acid concentration used during the impregnation procedure

The appearance of Lewis acidity after phosphate treatment as indicated by the emergence of the signal at  $1448\text{ cm}^{-1}$  is due to the aforementioned displacement of the electron density of the zirconia centre provoked by the introduction of the phosphate group. This phenomenon was responsible for the increase in binding energy of the Zr 3d signal in XPS, as well as for an increase in Lewis acid strength which makes Zr centre able to protonate the pyridine molecule, giving rise to the Lewis acid site related vibrational band. **Figure 5.12** also shows the Brønsted-Lewis ratio determined from the  $1448\text{ cm}^{-1}$  and  $1540\text{ cm}^{-1}$  peak areas. The increase in Brønsted acidity due to the higher concentration of P-OH, responsible for this type of acidity, leads to a monotonic

increase of the B/L ratio. The decrease in B/L ratio with increasing calcination temperature can be attributed to transformations of protonic sites to Lewis sites with elimination of water[70].

#### 5.2.1.4.2 Propylamine chemisorption and temperature programmed desorption

Acid site densities were evaluated by propylamine chemisorption and subsequent thermal analysis using thermogravimetric analysis. Propene reactively formed in the presence of acid sites was monitored by MS and used for the quantification of acid site density[71] as explained in **Chapter 2**. Determination of Brønsted acid sites (BAS) and Lewis acid sites (LAS) was carried out by means of the number of total acid sites in conjunction with the B/L ratio obtained from pyridine chemisorption. **Table 5.3** shows the acid loadings found for all the prepared materials, together with the B/L ratio obtained from pyridine adsorption and the calculation of BAS and LAS.

**Table 5.3** Acid properties of thermally treated PZ materials

| Catalyst             | Acid loading/<br>mmol·g <sup>-1</sup> | B/L ratio | BAS /<br>mmol·g <sup>-1</sup> | LAS /<br>mmol·g <sup>-1</sup> |
|----------------------|---------------------------------------|-----------|-------------------------------|-------------------------------|
| ZrO <sub>2</sub> 550 | 0.05                                  | N/A       | 0                             | 0.05                          |
| 0.5-PZ550            | 0.15                                  | N/A       | 0                             | 0.15                          |
| 2.3-PZ550            | 0.30                                  | 0.86      | 0.14                          | 0.16                          |
| 4.2-PZ550            | 0.38                                  | 2.13      | 0.26                          | 0.12                          |
| 6.1-PZ550            | 0.39                                  | 5.70      | 0.33                          | 0.06                          |
| 9.0-PZ550            | 0.42                                  | 9.43      | 0.38                          | 0.04                          |
| ZrO <sub>2</sub> 650 | 0.05                                  | N/A       | 0                             | 0.05                          |
| 0.6-PZ650            | 0.14                                  | N/A       | 0                             | 0.14                          |
| 2.3-PZ650            | 0.25                                  | 2.37      | 0.18                          | 0.07                          |
| 4.2-PZ650            | 0.31                                  | 3.60      | 0.24                          | 0.07                          |
| 5.8-PZ650            | 0.27                                  | 3.79      | 0.21                          | 0.06                          |
| 8.2-PZ650            | 0.30                                  | 5.94      | 0.26                          | 0.04                          |
| ZrO <sub>2</sub> 750 | 0.05                                  | N/A       | 0                             | 0.05                          |
| 0.7-PZ750            | 0.10                                  | N/A       | 0                             | 0.10                          |
| 2.7-PZ750            | 0.20                                  | 1.88      | 0.13                          | 0.07                          |
| 4.5-PZ750            | 0.25                                  | 2.61      | 0.18                          | 0.07                          |
| 6.1-PZ750            | 0.24                                  | 3.43      | 0.19                          | 0.05                          |
| 8.8-PZ750            | 0.18                                  | 6.97      | 0.16                          | 0.02                          |

The influence of the concentration of phosphoric acid used during impregnation on the total amount of acid sites is presented in **Figure 5.13** together with the propene signal obtained in the MS for all the catalysts. Equal acid strength can be accredited to all the catalysts, indicated by the propene detected at the same temperature ( $\sim 420^\circ\text{C}$ ).

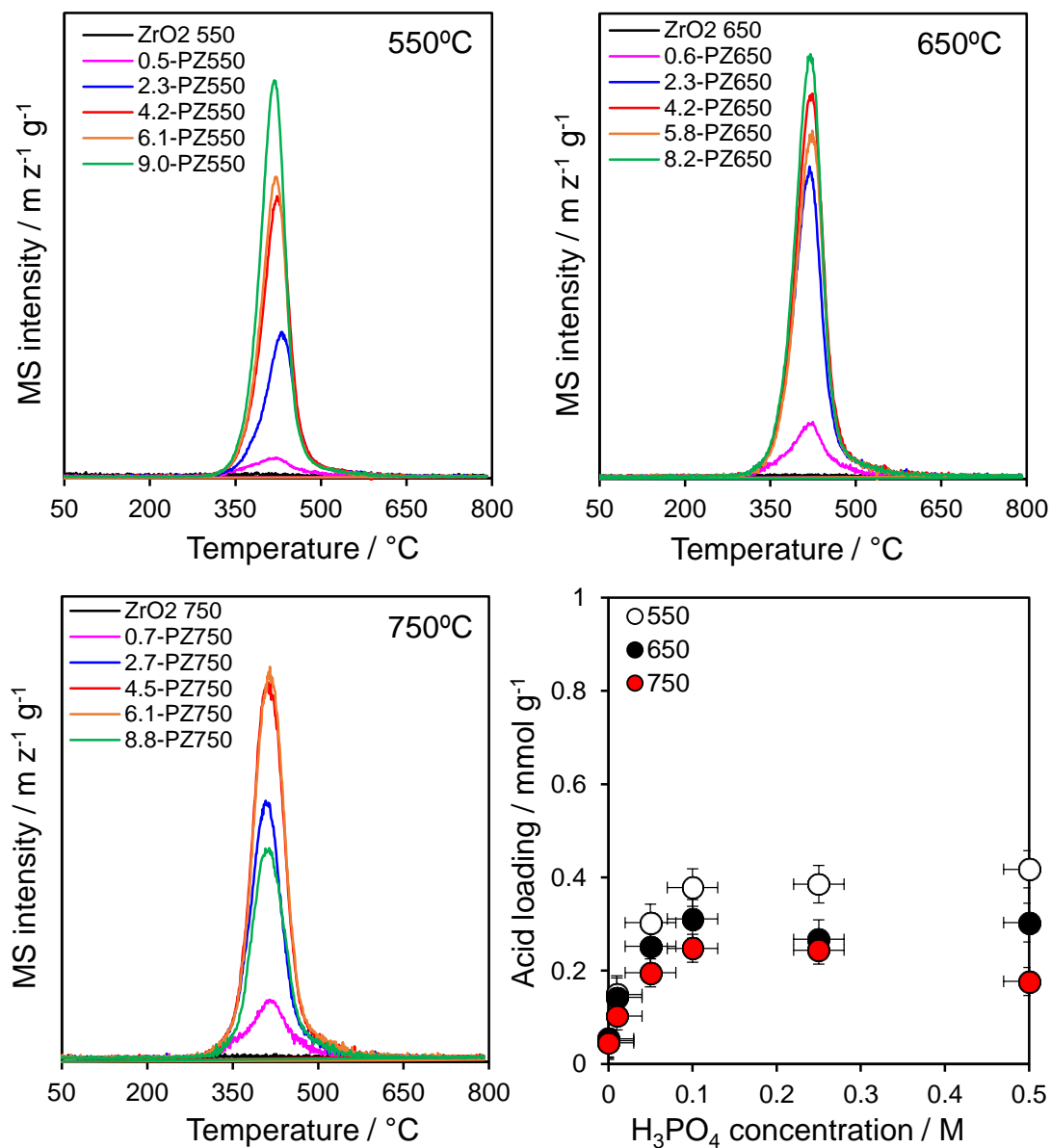


**Figure 5.13** Propene desorption for the PZ series at different calcination temperatures and variation of acid loading with acid concentration used during impregnation

Little acidity was detected for the unphosphated zirconia materials, which according to Bolis *et al.* is attributed to the mild Lewis acidity of the parent material[68]. Acid loading increases rapidly with phosphate addition for the three calcination temperatures studied, and then plateaus after acid concentration of 0.1M for the PZ series calcined at 550°C and 650°C and slightly decreases for the 750°C series. This volcano-shaped

curve was also observed for the surface area of the materials, and in fact, the calculation of the acid densities by normalization of the acid loading with the surface area of the materials, provides a constant value in the range of 1.4-2  $\mu\text{mol}/\text{m}^2$  for all the catalysts, evidencing the linear correlation between number of acid sites and surface area. This value of acid density is close to the 2.7  $\mu\text{mol}/\text{m}^2$  found by Kuwahara *et al.* for a sulfated zirconia sample prepared from a nitrate precursor[72]. Moreover, there is a clear effect of calcination temperature on the total acidity of the phosphate materials, with a progressive decrease of acid centres at higher temperatures. This effect must be related to the decrease in surface area of the catalysts as it is proved by the constant acid density. Additionally, during the TPD analysis the possible removal of acidic groups was studied by monitoring desorption of  $\text{PO}_3^{3-}$  and  $\text{PO}_4^{3-}$  ions. However, no signal was detected for the aforementioned ions, demonstrating the high thermal stability of the PZ materials.

#### 5.2.1.4.3 CO<sub>2</sub> titration

Basic properties of PZ materials were probed by CO<sub>2</sub> titration, with **Table 5.4** showing the dependence of basic sites with increasing phosphate coverage and calcination temperature. For the 550°C calcined series, whilst the parent ZrO<sub>2</sub> exhibits the highest basic loading, 60  $\mu\text{mol}\cdot\text{g}^{-1}$ , values drop dramatically with the increase of the phosphate content, being negligible for the materials impregnated with 0.25 and 0.5 M phosphoric solutions. For the 650 and 750°C calcined families, similar trend of basic loading across the PZ materials were observed, whereby for both series, the parent ZrO<sub>2</sub> possesses the most appreciable basic sites densities, 45 and 28  $\mu\text{mol}\cdot\text{g}^{-1}$  respectively, while it decreases at increased phosphate loadings.

**Table 5.4** Basic site loadings and densities (in brackets) as a function of P content and calcination temperature

|                              |     | Basic loading / $\mu\text{mol}\cdot\text{g}^{-1}$ (basic density / $\mu\text{mol}\cdot\text{g}^{-1}\cdot\text{m}^{-2}$ ) |              |              |              |             |      |     |
|------------------------------|-----|--|--------------|--------------|--------------|-------------|------|-----|
|                              |     | [H <sub>3</sub> PO <sub>4</sub> ] / M  | 0            | 0.01         | 0.05         | 0.1         | 0.25 | 0.5 |
| Calcination temperature / °C |     |  |              |              |              |             |      |     |
|                              | 550 |  | 60<br>(0.98) | 56<br>(0.52) | 12<br>(0.06) | 4<br>(0.02) | 0    | 0   |
|                              | 650 |  | 45<br>(1.10) | 29<br>(0.47) | 3<br>(0.02)  | 1<br>(0.01) | 0    | 0   |
|                              | 750 |  | 28<br>(0.71) | 9<br>(0.20)  | 0            | 0           | 0    | 0   |

According to the literature, the density of CO<sub>2</sub> adsorption sites on ZrO<sub>2</sub> based materials is strongly influenced by its crystallographic structure. Bachiller-Baeza *et al.*[73] proved via CO<sub>2</sub> IR spectroscopy, adsorption microcalorimetry and temperature programmed desorption (TPD) that in general the monoclinic ZrO<sub>2</sub> structure has higher CO<sub>2</sub> adsorption sites compared to the tetragonal structure, and ZrO<sub>2</sub> calcined at 500°C, which exhibits a mixture of the two phases, possesses the strongest basic centers among all the samples studied. Pokrovski *et al.*[74] reported that on the monoclinic zirconia the adsorption of CO<sub>2</sub> occurs forming both bicarbonate and mono-/ bidentate carbonate, while on the tetragonal phase bi-/ polydentate carbonates are formed, thus, suggesting that the crystalline structure highly influence the coordination mode. Results also indicate that the monoclinic phase, compared to the tetragonal, is able to adsorb more CO<sub>2</sub> thanks to the higher concentration of OH groups and stronger Lewis acid-base pairs.

For PZ materials, the decrease of basic sites is the result of both calcination temperature, which enhance the tetragonal character of undoped zirconia (as shown by XRD analysis), and phosphate loadings, which cover the basic centres of the parent ZrO<sub>2</sub> with the progressively formed PO<sub>4</sub> monolayer, as observed from XPS.

## 5.2.2 Catalytic results

Glucose and fructose dehydration reaction to HMF was subsequently conducted over the series of phosphated zirconia. Full reaction conditions are described in **Chapter 2**. Both Brønsted and Lewis acid sites as well as basic sites have been identified on the phosphate-treated materials. As seen in previous chapters of this thesis, glucose transformation to HMF takes place via isomerization of glucose to fructose over Lewis acid sites or basic sites, followed by dehydration of fructose to HMF over Brønsted acid sites. Herein we investigate the effect of phosphate loading and calcination temperature at the optimized reaction conditions found in **Chapter 4** for the niobia-based catalysts.

### 5.2.2.1 Effect of phosphate loading

#### 5.2.2.1.1 Glucose conversion

**Figure 5.14** shows the glucose dehydration reactions profiles over the series of PZ catalysts with different phosphate loading and calcined at 550°C. Production of HMF is observed only after 2 h of reaction, and after this time, only a small amount of product ~1 wt% is observed. A fast production of fructose is revealed within the first hour of the

reaction, with higher amounts obtained for the catalysts with lower phosphate loading, and after the second hour it remains stable. No other peaks related to other sugars or rehydration products of HMF were observed in the chromatogram.

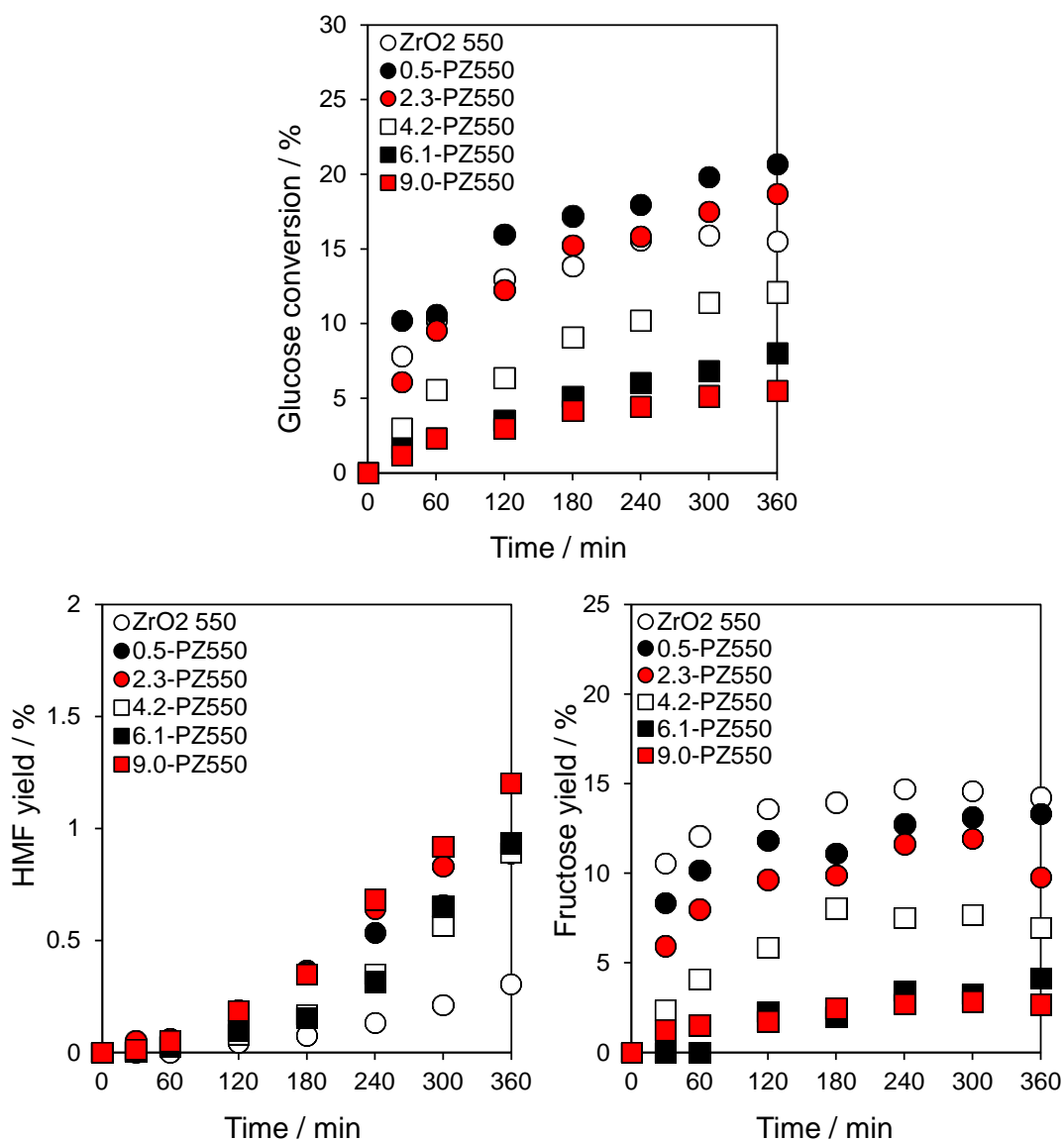


**Figure 5.14** Profiles of glucose conversion and yield of HMF, fructose and other sugars for glucose dehydration reactions at 100°C over PZ calcined at 550°C

**Figure 5.15** shows the resulting variations in glucose conversions and the yield and selectivity of main products of glucose dehydration reaction, fructose and HMF, after 6 h over phosphated zirconia catalysts calcined at 550°C as a function of phosphorous loading. A volcano-shaped curve is observed for glucose conversion, and HMF yield remains stable at ~1% for phosphated catalysts, while the parent ZrO<sub>2</sub> exhibited relatively lower HMF production. Moreover, the yield of fructose decreases consistently with increasing P loading due to the decrease in Lewis acidity and basic sites. The catalyst with the lowest phosphate loading showed the highest glucose conversion with

a value of 20.7% to progressively decrease down to 5.5 wt% for the highest phosphate loading. This behaviour is intrinsically related to the amount of Lewis acid sites found in the acidity study, as well as the total loading of basic sites, i.e. highest glucose conversion is achieved at lower B/L ratio. Glucose conversion is catalysed by Lewis acid sites and base sites, and the introduction of Brønsted phosphate groups hampers the isomerization of glucose to fructose. The decrease in glucose conversion is accompanied by a linear decrease in fructose yield due to the fewer amount of Lewis acidity and basicity at higher phosphate loadings. Likewise, a maximum fructose yield of 14.2% is observed for the 0.5 wt% catalyst decreasing down to 2.7% for the 9 wt% sample. In all cases the HMF yield is very low, unable to be produced over 0.7% yield. The low HMF yield can be explained because at low B/L ratio fructose is preferably formed, but the dehydration to HMF over LAS is unselective, while at high B/L ratio there are more active sites able to perform the dehydration from fructose, but little fructose is formed due to the decrease in Lewis acidity.

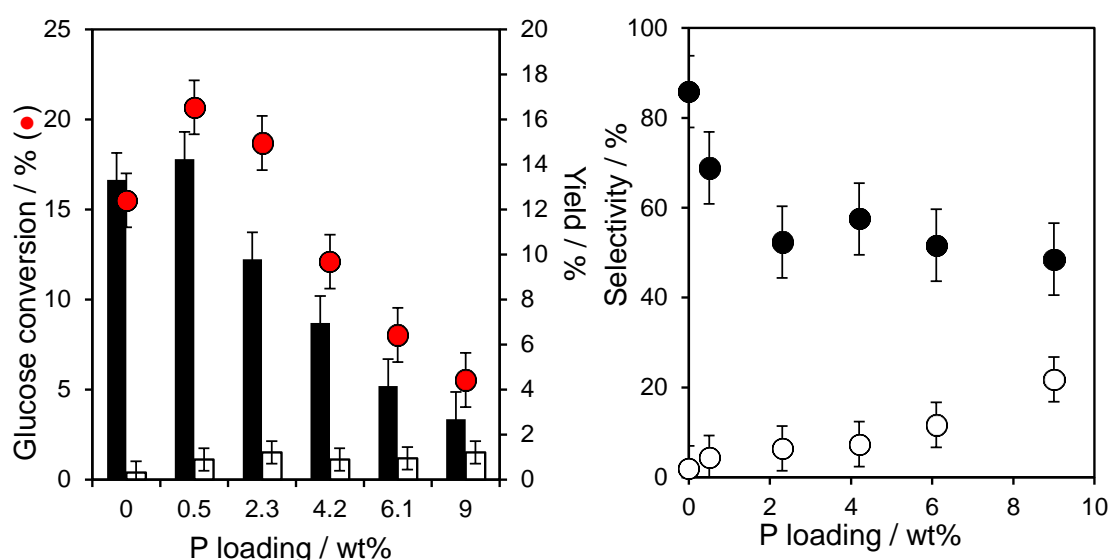


**Figure 5.15** Conversion of glucose over PZ550 catalysts and corresponding yield (left) and selectivity (right) of fructose (black) and HMF (white) as a function of phosphate loading after 6 h reaction at 100°C

These findings are in agreement with the results from the study on glucose dehydration over phosphate catalysts reported by Ordonsky *et al.*[12]. In this study it was reported that phosphated zirconia is more active than its aluminium and titanium counterparts, and exhibits a similar performance than phosphated niobium materials. They also found a more intensive glucose isomerization into fructose for oxides than that obtained by phosphates materials due to the higher Lewis acidity of the former, while aluminium and titanium phosphates proved to be inactive for glucose conversion. Weingarten *et*

*al.*[40] also reported a decrease in fructose selectivity at higher glucose conversion. Thereby, a phosphated zirconia catalyst attained 37% HMF selectivity at a glucose conversion of 40% in an aqueous reaction carried out at 160°C. In their study on the effect of B/L ratio on this reaction, they observed that glucose isomerization to fructose is favoured by higher Lewis acid concentrations. However, predominance of Lewis acidity also leads to the formation of more humin species due to the unselective dehydration of fructose on this type of acid sites. Consequently, a higher rate of glucose disappearance and lower selectivities to HMF are observed for catalysts with increased Lewis sites. This trend is also observed in **Figure 5.15**, where a considerable increase in HMF selectivity up to 21.8% is achieved at high phosphate loadings due to the presence of a high amount of BAS, which are able to dehydrate the scarce amount of fructose produced.

The only detected products of glucose dehydration in water were fructose and HMF. Fructose is the main product, especially for catalysts with low or none phosphate loading, reaching selectivity values as high as 85% for the parent ZrO<sub>2</sub>, and stabilizing at ~50% for the highest phosphate loadings studied. The absence of other sugars in the HPLC chromatogram leads to the conclusion that the missing carbon balance can be attributed to the formation of humins in the form of unidentified soluble and insoluble compounds. From the reaction profiles, the rates of glucose conversion and HMF formation and consequently glucose turnover frequency and HMF productivity were calculated. **Figure 5.16** shows glucose TOF and HMF productivity normalized to the total number of acid sites, after the subtraction of the background contribution observed in the stoichiometric reaction.

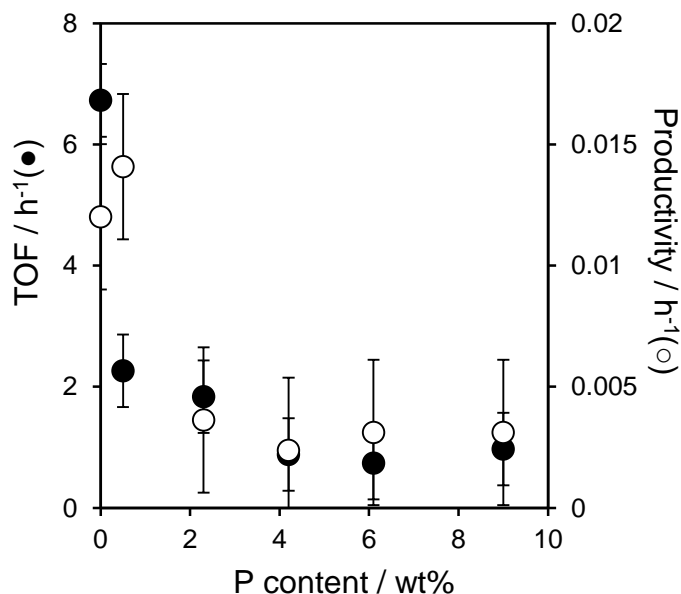


**Figure 5.16** Turnover frequencies for the aqueous phase conversion of glucose and associated HMF productivity normalised to total acid loading as a function of bulk phosphorous content

As seen in this figure, glucose TOF is higher for the catalyst with low B/L ratio, with  $6.7 \text{ h}^{-1}$  and  $2.3 \text{ h}^{-1}$  for  $\text{ZrO}_2$  and 0.5-PZ550 respectively, and reaches a plateau at  $\sim 0.9 \text{ h}^{-1}$  for the rest of the catalysts. It is worth mentioning that the initial rate can also be affected by the basic sites loading of the catalysts, but it is difficult to distinguish the contribution of each active site, either Lewis acid or basic, on the total rate of glucose conversion. On the other hand, HMF productivity experiments a slight increase for the lowest phosphate loading, reaching  $0.014 \text{ h}^{-1}$  to then mirror the TOF trend at lower productivity values. Osatiashtiani *et al.*[62] reported similar volcano-like HMF productivity at identical reaction conditions over sulfated zirconia catalysts. These results express the necessary collaboration of both Brønsted and Lewis acid sites or/and basicity for an optimum glucose conversion and HMF selectivity.

### 5.2.2.1.2 Fructose conversion

In **Chapter 4** higher catalytic performance of niobic acid catalysts was obtained when fructose was used as starting material. Fructose dehydration reactions were realized in order to test the reactivity of phosphated zirconia catalysts in the absence of the isomerization rate determining step.

The profile of fructose conversion and yields of glucose, HMF and other sugars over the PZ550 catalysts are shown in **Figure 5.17**. Other sugars refer to unidentified peaks in the HPLC chromatogram in the region where saccharides tend to appear as

explained in **Chapter 2**. An almost linear conversion of fructose is observed in the studied time of reaction for all the catalysts used for the dehydration reaction, thus, the absence of a plateau or its beginning indicates that higher conversions could have been achieved at longer reaction periods. The same linear increasing trend is observed for HMF yield obtained from every catalyst studied. Contrarily to glucose dehydration reactions, a considerable amount of other sugars were obtained from fructose due to the greater ease of fructose to react in the presence of acid catalysts, proving at the same time the higher stability of the glucose ring structure.

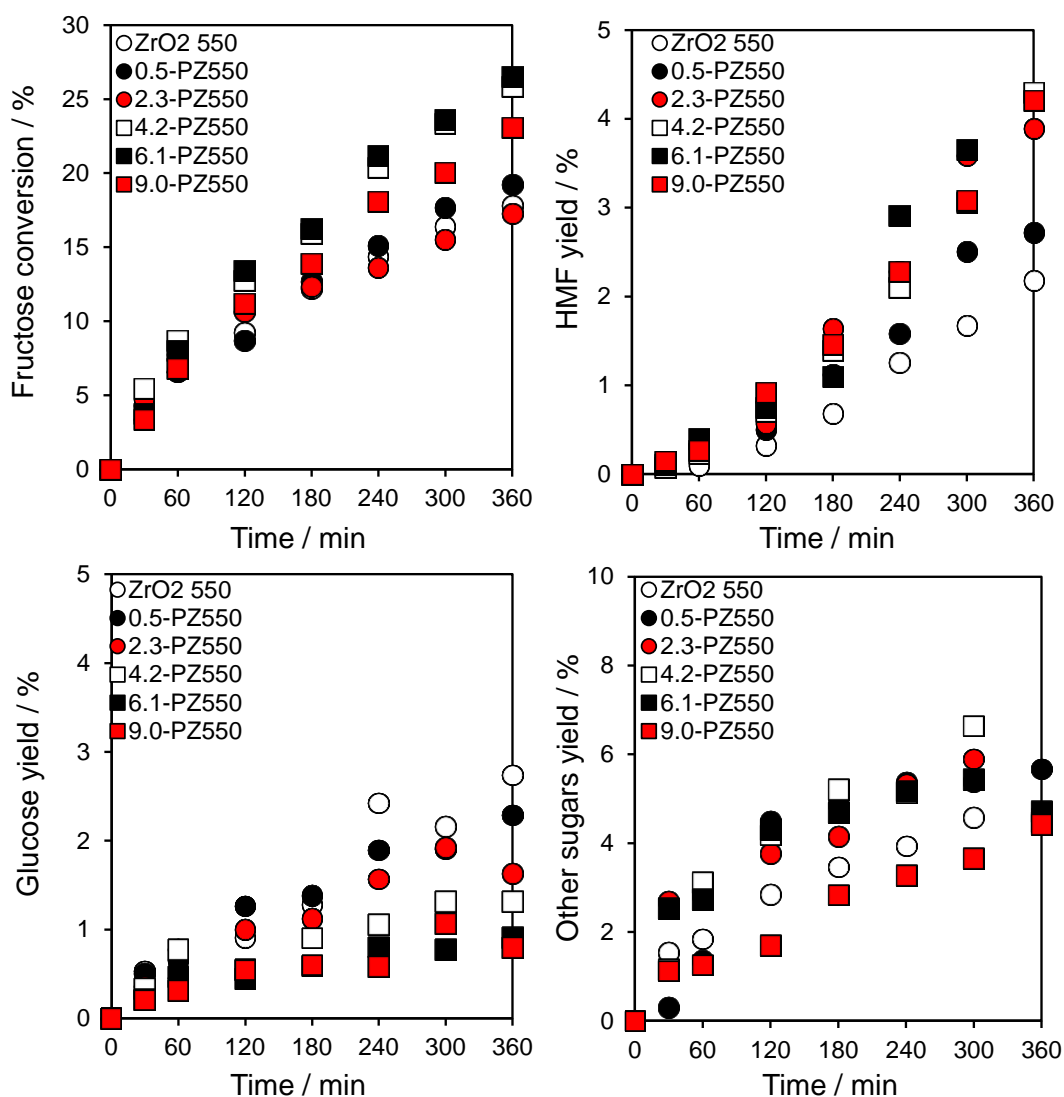


**Figure 5.17** Profiles of fructose conversion and yield of HMF, glucose and other sugars for fructose dehydration reactions at 100°C over PZ calcined at 550°C

Fructose dehydration results are displayed in **Figure 5.18**, where slightly higher activity of the phosphated materials for the dehydration of fructose compared to the glucose results is observed. Increased conversion from 17.7% to 26.5% was observed for ZrO<sub>2</sub>

and 6.1-PZ550 respectively, although further phosphorous content increase to 9 wt% causes a decrease in fructose conversion. This is consistent with a linear increase in Brønsted acidity in a monolayer regime. As inferred from XPS results, phosphate loadings over 6.1 wt% commence the agglomeration of acidic groups in the surface of the catalysts. Although higher amount of acid sites were obtained for 9.0-PZ550 it is possible that an overestimation of BAS occurred due to the ability of propylamine to intercalate into the phosphate conglomerate, giving information not only about the surface P-OH groups which participate in the reaction with fructose, as suggested by Clearfield and Tindwa[75].

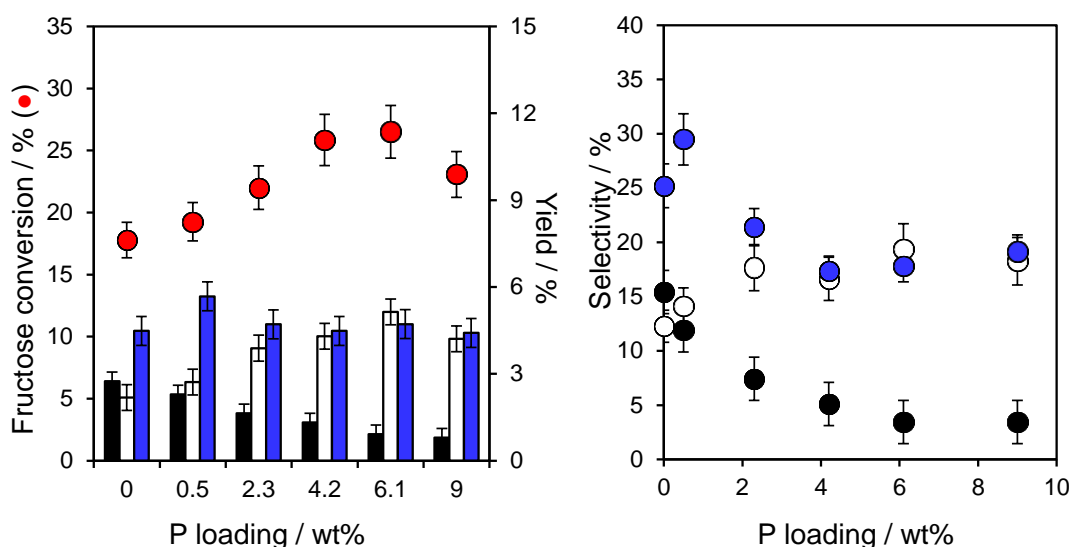


**Figure 5.18** Conversion of fructose over PZ catalysts calcined at 550°C and corresponding yields (left) and selectivity (right) of glucose (black), HMF (white) and other sugars (blue) as a function of phosphorous content after 6 h reaction at 100°C.

Thus, the over-concentrated acid sites no longer work as catalytically active sites probably due to inefficient accessibility of the reactants, but rather limit the reaction rates. Modest HMF yields with a volcano shape trend were observed for all the catalysts, with the highest being 5.1% achieved by 6.1-PZ550, while 19.4% HMF selectivity was attained for the same catalyst. The low B/L ratio present in the low or none phosphate loading is consistent with the ability of LAS to convert fructose back to glucose. For higher phosphate loadings, glucose yield and selectivity systematically decrease to values under 1% due to the disappearance of LAS and inherent basicity. The drop in activity over the monolayer regime after impregnation with acid species has been also reported for sulfated zirconia in this same reaction[62] and for the esterification of levulinic acid[72], while phosphated zirconia showed the same volcano-shaped trend for the acid catalysed conversion of 2-propanol to propene[26].

Similar to reactions of glucose, the rate of fructose conversion and HMF formation was measured, and consequently the fructose TOF and HMF productivity were calculated by normalizing the rate to both the mass of catalyst and the number of total acid sites. As depicted in **Figure 5.19**, fructose TOF rapidly decreases from 2.7 to 1.2 h<sup>-1</sup> over ZrO<sub>2</sub> and 0.5-PZ550 respectively and then remains stable at ~0.9 h<sup>-1</sup> for higher phosphate coverage. Additionally, HMF productivity mirrors the TOF values with a higher value of 0.07 h<sup>-1</sup> which stabilizes at ~0.03 h<sup>-1</sup> at high phosphate coverage. The fall in fructose TOF can be due to the inability of the phosphated materials to perform the isomerization of fructose to glucose due to the disappearance of LAS as the phosphate content increases. These TOF values are similar to those obtained by Benvenuti *et al.*[46] during the fructose dehydration aqueous reaction at 110°C, who reported 1.6 h<sup>-1</sup> and 1.1 h<sup>-1</sup> over zirconium and titanium phosphate salts respectively.

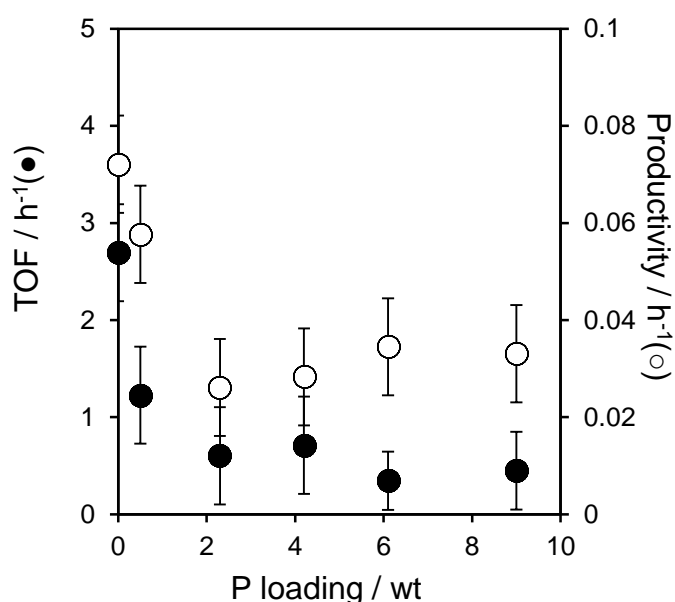


**Figure 5.19** Turnover frequencies for the aqueous phase conversion of fructose and associated HMF productivity normalised to total acid loading as a function of calcination temperature

It is worth mentioning that while HMF yields obtained in this thesis are lower than those reported in the literature, generally they are obtained at higher reaction temperatures (140-200°C), and/or promoted by biphasic systems and ionic liquids. For example, in 1980 Nakamura patented the production of HMF from hexoses in DMSO with PZ catalysts, obtaining a maximum HMF yield of 81% after 3 h of reaction at 140°C[45]. In a water/diglyme solvent system at 150°C, Jain *et al.* observed 80% HMF yield from fructose in 1 h using mesoporous zirconium phosphate catalysts[48]. Wang *et al.*[76] reported the use of mesoscopically assembled sulfated zirconia for the catalytic dehydration of fructose to HMF in DMSO at 110°C, even if in **Chapter 4** has been

proved the high catalytic effect of this solvent at the mentioned temperature, and they obtained HMF yield as high as 92% in 2 h.

### **5.2.2.2 Effect of calcination temperature**

The effect of the catalyst calcination temperature post-phosphation treatment was examined for glucose and fructose dehydration reactions under the same reaction conditions previously chosen. In each case, only the most selective material towards HMF was tested for comparative reasons.

#### **5.2.2.2.1 Glucose conversion**

PZ catalysts prepared from a 0.5M solution of phosphoric acid were used in this study, since they provided the highest selectivity to HMF in the phosphate loading influence study when glucose was used as a reagent, even if the lowest conversion was obtained compared to other phosphate loadings. The profile of glucose conversion and yields of fructose and HMF over the PZ catalysts prepared from a 0.5 M solution of phosphoric acid and calcined at different temperatures are shown in **Figure 5.20**. Here it can be seen that PZ calcined at 550°C performs slightly better at glucose conversion and HMF yield than catalysts calcined at higher temperatures, while PZ calcined at 650°C and 750°C behave almost identically.

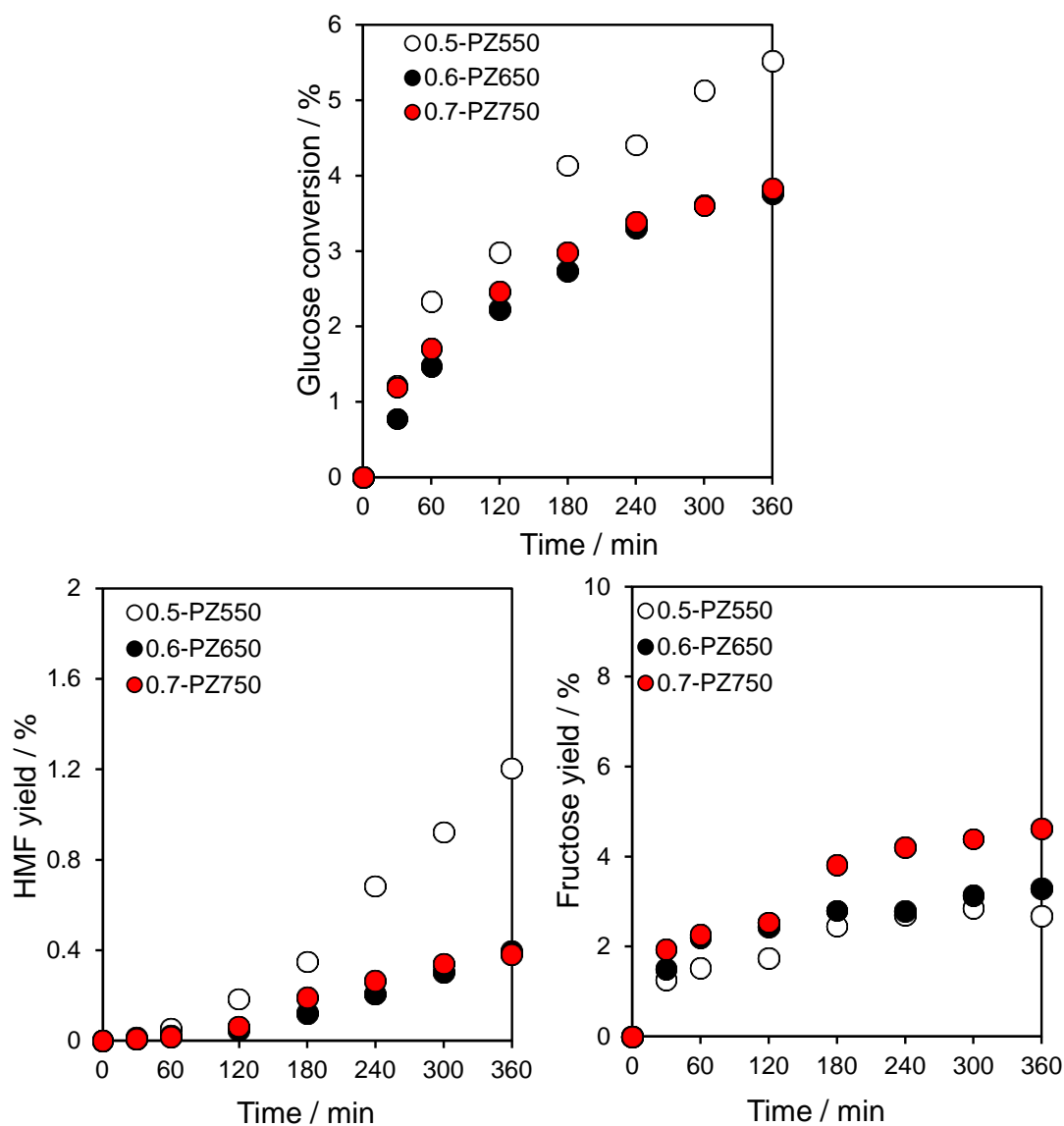


**Figure 5.20** Glucose conversion and yield of HMF and fructose profiles for glucose dehydration reactions at 100°C over PZ catalysts prepared from a 0.5 M solution of phosphoric acid calcined at different temperatures

**Figure 5.21** shows the resulting variations in glucose conversions and the yield and selectivity of main products of glucose dehydration reaction, fructose and HMF, after 6 h as a function of calcination temperature after phosphate impregnation, using PZ catalysts prepared from a 0.5M solution of phosphoric acid. A decrease in conversion and fructose yield is observe with increasing calcination temperature, consistent with the higher sintering effect provoked by the thermal treatment which leads to loss in surface area and acidity of the materials. The HMF selectivity is between 10-20%, while fructose selectivity is around 45-55% for all temperatures studied. In general, no significant activity variations are observed for glucose dehydration reactions when higher calcination temperatures were studied, apart from a slight decrease in glucose

conversion. Jiménez-Morales *et al.*[44] also observed a decrease in glucose conversion from 81% to 70% and HMF yield from 23% to 19% in the conversion of glucose in aqueous system at 175°C over zirconia catalysts supported on a mesoporous silica framework, when the catalyst was calcined at 550°C and 750°C respectively.

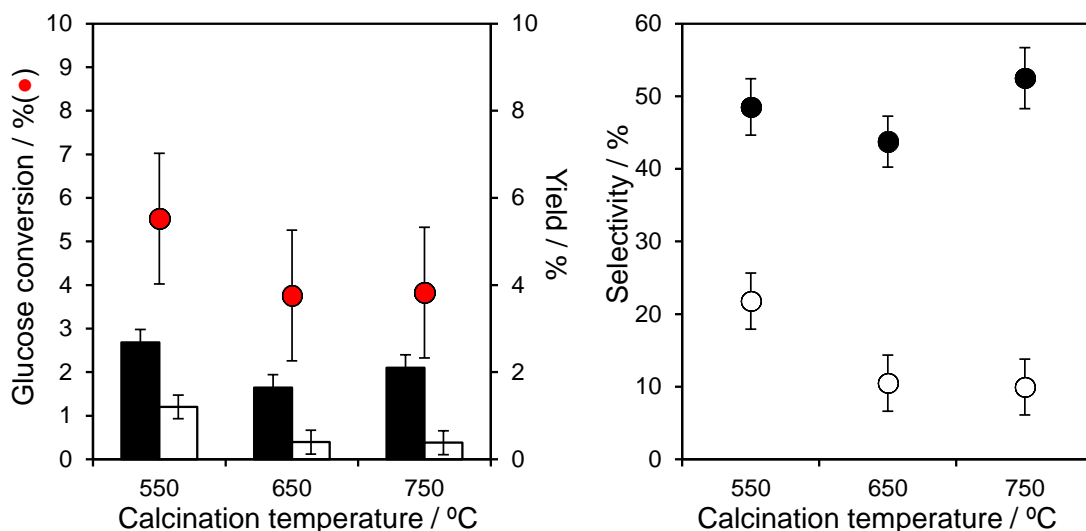


**Figure 5.21** Conversion of glucose over PZ catalysts prepared from a 0.5 M solution of phosphoric acid and corresponding yield (left) and selectivity (right) of fructose (black) and HMF (white) after 6 h reaction at 100°C as a function of calcination temperature

From the reaction profiles, the rates of glucose conversion and HMF formation and consequently glucose turnover frequency and HMF productivity were calculated and are shown in **Figure 5.22**. After normalization to total amount of acid sites, constant TOF of  $\sim 0.1 \text{ h}^{-1}$  and HMF productivity of  $\sim 0.0035 \text{ h}^{-1}$  are found independent of calcination temperature. These results indicate that the variations observed in glucose conversion and HMF yield with increasing calcination temperature are intrinsically related to the decrease in surface area and acidity of the catalysts.

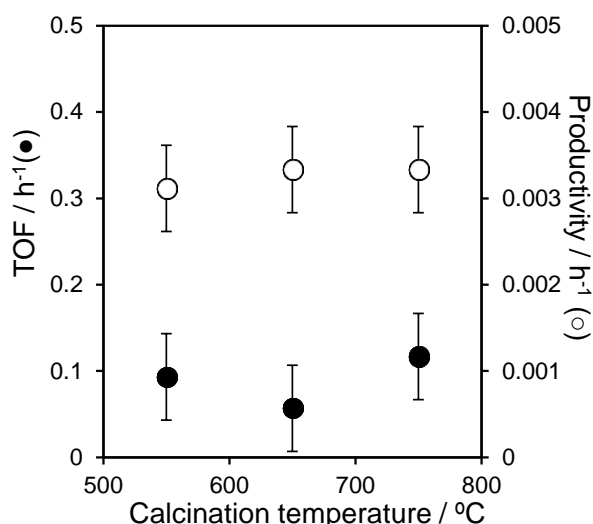


**Figure 5.22** Turnover frequencies for the aqueous phase conversion of glucose normalised to total acid loadings over PZ catalysts prepared from a 0.01M solution of phosphoric acid as a function of calcination temperature

#### 5.2.2.2.2 Fructose conversion

**Figure 5.23** shows the fructose dehydration reactions profiles over the PZ catalysts prepared from a 0.25M solution of phosphoric acid and calcined at different temperatures, since they provided the highest fructose conversion and selectivity to HMF in the phosphate loading influence study. Similar fructose conversion is observed within the first hour of reaction, but after that point, the PZ calcined at 550°C performs slightly better, probably due to the higher amount of BAS together with its higher surface area. A constant glucose production below 1.5% is observed after a plateau is reached within the first two hours of reaction. Significant formation of other sugars is also observed during the first two hours, and follows the same trend than glucose, plateauing after this period with values between 3-5%. It is at this moment when an increase in the rate of HMF formation is observed after an initial dormant period, commencing a steady increase during the reaction time studied.

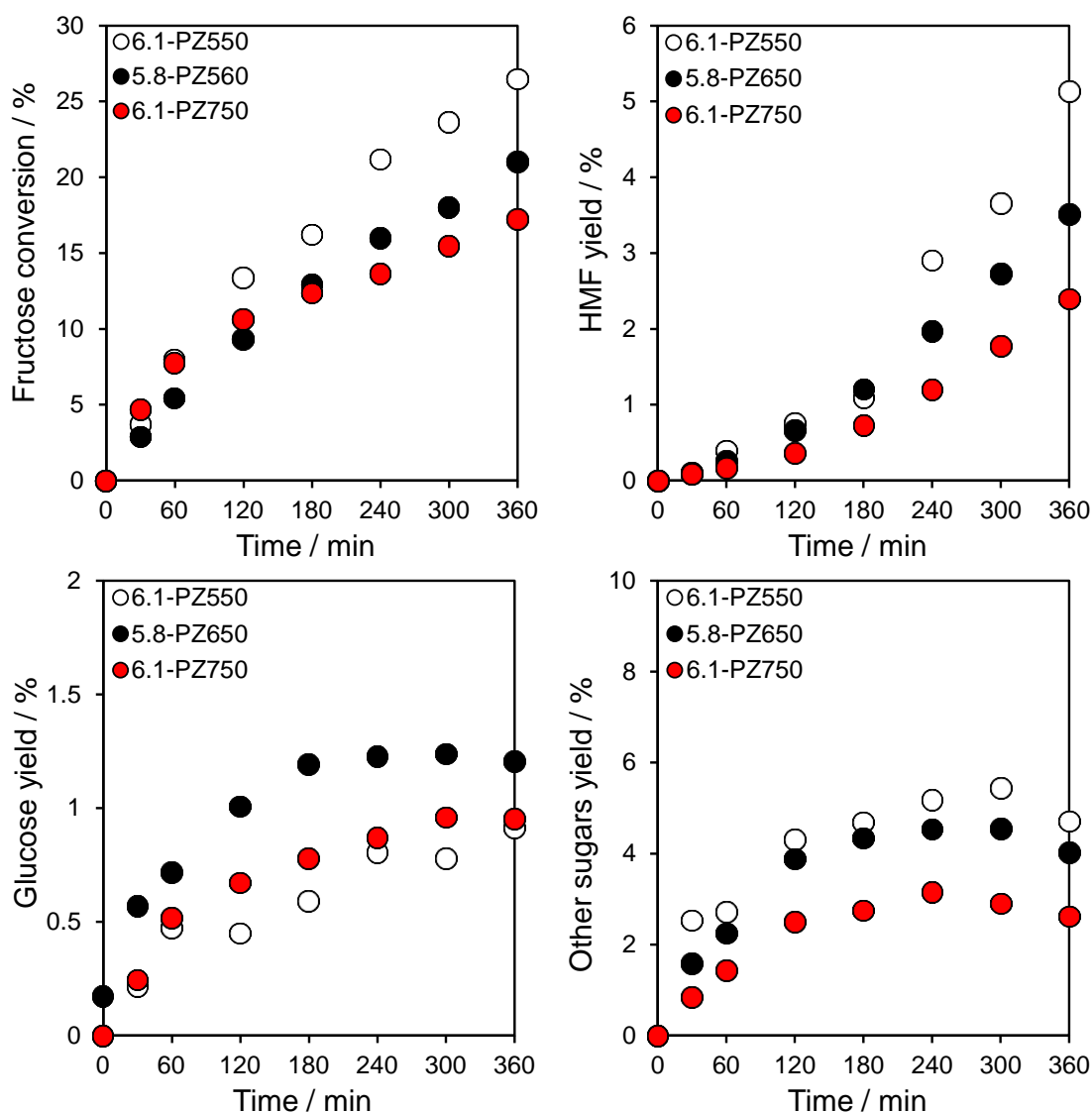


**Figure 5.23** Fructose conversion and yield of HMF and glucose profiles for fructose dehydration reactions at 100°C over PZ catalysts prepared from a 0.25M solution of phosphoric acid calcined at different temperatures

**Figure 5.24** shows the resulting variations in fructose conversions and the yield and selectivity of main products of fructose dehydration reaction, glucose and HMF, after 6 h as a function of calcination temperature after phosphate impregnation, using PZ catalysts prepared from a 0.25M solution of phosphoric acid. Similar results than those obtained from glucose are observe here. A steady decrease in fructose conversion and HMF yield is attained, while glucose yield remains constant at a value of ~1%. As in the case of glucose conversion, this steady decrease in fructose conversion with calcination temperature can be assigned to the sintering of zirconia crystallites producing a diminishing in surface area and acidity. Selectivity values remain somewhat stable, with values between 15-20%, 3-7% and 17-19% for HMF, glucose and other sugars respectively.

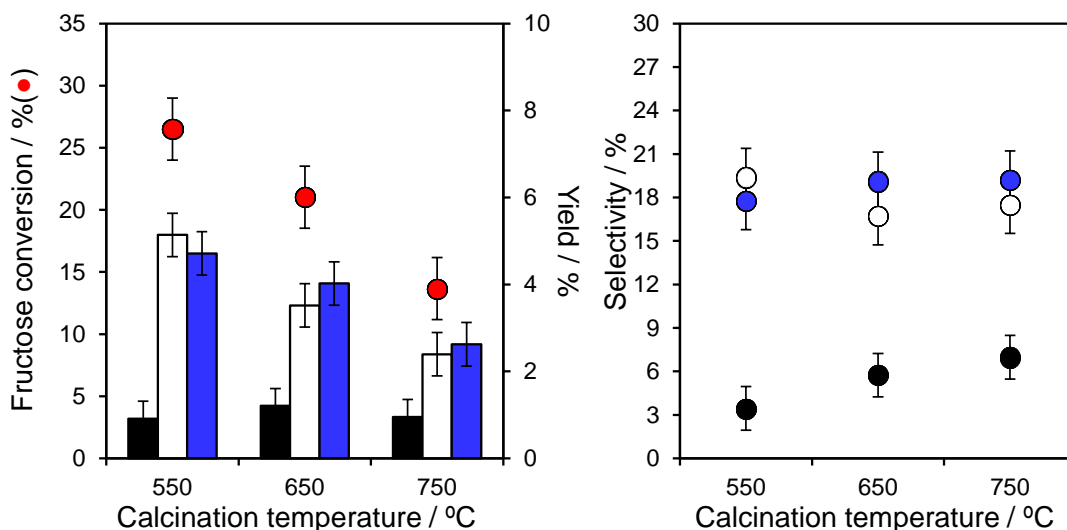


**Figure 5.24** Conversion of fructose over PZ catalysts prepared from a 0.25M solution of phosphoric acid and corresponding yield (left) and selectivity (right) of glucose (black), HMF (white) and other sugars (blue) after 6 h reaction at 100°C as a function of calcination temperature

**Figure 5.25** shows the turnover frequency for the three reactions studied. It was calculated from the initial rate of fructose conversion measured within the first hour of reaction and normalised to the total amount of acid sites, while HMF productivity was calculated from the rate of production of HMF in the same time and normalised to the amount of total acid sites. As in the case of the reactions performed using glucose as starting material, a constant TOF and HMF productivity are observed, being constant at  $0.5 \text{ h}^{-1}$  and  $0.045 \text{ h}^{-1}$  respectively. This TOF come near to the one reported by Benvenuti *et al.*[46] ( $1 \text{ h}^{-1}$ ) for the fructose dehydration to HMF at 100°C, using different phosphated zirconium-based catalysts.

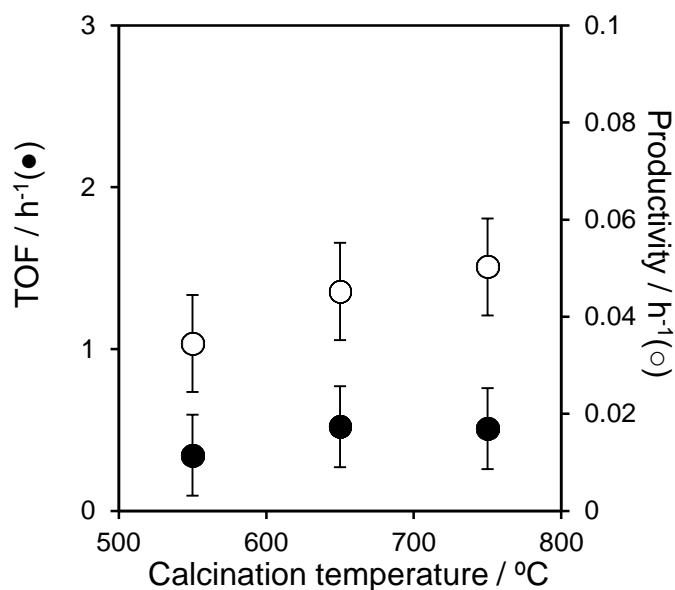


**Figure 5.25** Turnover frequencies for the aqueous phase conversion of fructose and associated HMF productivity normalised to total acid loading as a function of calcination temperature

### 5.3 Conclusions

The impact of phosphate addition upon the physicochemical properties of  $Zr(OH)_4$  calcined at different temperatures has been systematically investigated by a wide range of characterization techniques, including textural, structural and acidity measurements. The unphosphated precursor develops mainly a monoclinic structure with very weak acid sites, predominantly Lewis-type. The presence of phosphate ions was found to stabilize the tetragonal phase at low phosphate loadings when the catalysts are calcined at 550°C, although an amorphous phase was observed when higher calcination temperatures are used. Moreover, higher calcination temperatures assist in the preservation of the tetragonal phase even at high phosphate coverages. The phosphate impregnation leads to a remarkable increase in the surface area and acidity of the catalysts, with a striking increase in Brønsted acidity due to the P-OH groups in the surface of the catalyst acquired during the impregnation treatment with phosphoric acid, while the intrinsic basicity of the catalysts is rapidly lost upon phosphate treatment.

The prepared catalysts were tested in the glucose and fructose dehydration reaction to HMF at 100°C, and the effect of phosphate loading and calcination temperature were measured. Catalysts with low B/L ratio such as pure  $ZrO_2$  and PZ catalysts with low

phosphate loading, achieved higher glucose conversion, which correlates with high fructose yields and rate of formation due to the preferential isomerization of glucose to fructose over LAS and basic sites, but low selectivity to HMF is observed due to the few BAS able to catalyse the dehydration of fructose to HMF. In contrast, high phosphate loadings suppress glucose isomerisation to fructose in favour of a slight increase in HMF production associated with enhanced dehydration of the fructose intermediate. When fructose was used as the starting reactant, a progressive increase in conversion was observed with the increase of B/L ratio, although high phosphate loadings over 6 wt% of phosphorous lead to a decrease in the activity of the materials, coincident with the overshoot of a phosphate monolayer. In general, it was found that high phosphate loadings close to the monolayer regime and low calcination temperatures lead to a higher fructose conversion. Moreover, the activity of the active sites was found to be the same independent of phosphate loading or calcination temperature as indicated by constant turnover frequencies found in the catalytic studies. Constant acid densities indicate that the variation in surface area of the catalysts is the critical factor when determining the conversion of the hexoses analysed in this study.

## 5.4 References

- [1] K. Tanabe, *Materials Chemistry and Physics* 13 (1985) 347-364.
- [2] A. Clearfield, J. Stynes, *Journal of Inorganic and Nuclear Chemistry* 26 (1964) 117-129.
- [3] F. Abbattista, A. Delmastro, G. Gozzelino, D. Mazza, M. Vallino, V. Lorenzelli, *Journal of the Chemical Society, Faraday Transactions* 86 (1990) 3653-3658.
- [4] G.A. Mekhemer, *Colloids and Surfaces A: Physicochemical and Engineering Aspects* 141 (1998) 227-235.
- [5] D. Spielbauer, G. Mekhemer, T. Riemer, M. Zaki, H. Knözinger, *The Journal of Physical Chemistry B* 101 (1997) 4681-4688.
- [6] G.A. Mekhemer, H.M. Ismail, *Colloids and Surfaces A: Physicochemical and Engineering Aspects* 164 (2000) 227-235.
- [7] M.I. Zaki, A.A. Ali, *Colloids and Surfaces A: Physicochemical and Engineering Aspects* 119 (1996) 39-50.
- [8] F. Li, L.J. France, Z. Cai, Y. Li, S. Liu, H. Lou, J. Long, X. Li, *Applied Catalysis B: Environmental* 214 (2017) 67-77.
- [9] M.S. Wong, D.M. Antonelli, J.Y. Ying, *Nanostructured Materials* 9 (1997) 165-168.
- [10] V. Smitha, H. Suja, J. Jacob, S. Sugunan, *INDIAN JOURNAL OF CHEMISTRY SECTION A* 42 (2003) 300-304.
- [11] E. Zhao, Y. Isaev, A. Sklyarov, J. Fripiat, *Catalysis letters* 60 (1999) 173-181.
- [12] V. Ordonsky, V. Sushkevich, J. Schouten, J. van der Schaaf, T. Nijhuis, *Journal of Catalysis* 300 (2013) 37-46.
- [13] N. Stojkovic, M. Vasic, M. Marinkovic, M. Randjelovic, M. Purenovic, P. Putanov, A. Zarubica, *Chemical Industry and Chemical Engineering Quarterly* 18 (2012) 209-220.
- [14] V. Lorenzelli, P. Galli, A. La Ginestra, P. Patrono, *Journal of the Chemical Society, Faraday Transactions 1: Physical Chemistry in Condensed Phases* 83 (1987) 853-864.
- [15] A. La Ginestra, P. Patrono, *Materials chemistry and physics* 17 (1987) 161-179.
- [16] F.S. Asghari, H. Yoshida, *Carbohydrate research* 341 (2006) 2379-2387.
- [17] M. Watanabe, Y. Aizawa, T. Iida, R. Nishimura, H. Inomata, *Applied Catalysis A: General* 295 (2005) 150-156.
- [18] T.E. Mohan Kumar, S.Z. Mohamed Shamsuddin, *International Journal of Scientific Research* 2 (2012) 39-43.

- [19] T. Hattori, A. Ishiguro, Y. Murakami, *Journal of Inorganic and Nuclear Chemistry* 40 (1978) 1107-1111.
- [20] M.Y.M. Sulaiman, *Journal of Nuclear and Related Technologies* 2 (2005) 11-18.
- [21] M. Cutrufello, I. Ferino, R. Monaci, E. Rombi, V. Solinas, *Topics in catalysis* 19 (2002) 225-240.
- [22] A. Ali, M. Zaki, *Thermochimica acta* 336 (1999) 17-25.
- [23] S. Bogdanov, E. Valiev, Y.A. Dorofeev, A. Pirogov, L. Sharygin, V. Moisseev, V. Galkin, *Journal of Physics: Condensed Matter* 9 (1997) 4031.
- [24] A. La Ginestra, P. Patrono, M. Berardelli, P. Galli, C. Ferragina, M. Massucci, *Journal of Catalysis* 103 (1987) 346-356.
- [25] K. Segawa, T. Ozawa, *Journal of Molecular Catalysis A: Chemical* 141 (1999) 249-255.
- [26] P. Pattnayak, K. Parida, *Journal of colloid and interface science* 226 (2000) 340-345.
- [27] L. Cheng, X. Guo, C. Song, G. Yu, Y. Cui, N. Xue, L. Peng, X. Guo, W. Ding, *RSC Advances* 3 (2013) 23228-23235.
- [28] M. Pica, *Catalysts* 7 (2017) 190.
- [29] K. Yardley, *Mineralogical Magazine* 21 (1926) 169-175.
- [30] Temperature-Dependent Phase Transitions of ZrO<sub>2</sub>, Materials Design Inc, <http://www.materialsdesign.com/appnote/temperature-dependent-phase-transitions-zro2>, 2017.
- [31] D.A. Ward, E.I. Ko, *Journal of Catalysis* 157 (1995) 321-333.
- [32] C. Antonetti, M. Melloni, D. Licursi, S. Fulignati, E. Ribechini, S. Rivas, J.C. Parajó, F. Cavani, A.M.R. Galletti, *Applied Catalysis B: Environmental* 206 (2017) 364-377.
- [33] K. Parida, P. Pattnayak, *Journal of colloid and interface science* 182 (1996) 381-387.
- [34] Y. Ikeda, T. Sakaihorii, K. Tomishige, K. Fujimoto, *Catalysis letters* 66 (2000) 59-62.
- [35] A. Clearfield, D.S. Thakur, *Journal of Catalysis* 65 (1980) 185-194.
- [36] A. Clearfield, D.S. Thakur, *Applied Catalysis* 26 (1986) 1-26.
- [37] A. Sinhamahapatra, N. Sutradhar, B. Roy, A. Tarafdar, H.C. Bajaj, A.B. Panda, *Applied Catalysis A: General* 385 (2010) 22-30.
- [38] P. Wu, Y. Liu, M. He, M. Iwamoto, *Chemistry of materials* 17 (2005) 3921-3928.
- [39] Zirchrom.com, Why choose zirconia for the analysis of positional isomers? , <https://www.zirchrom.com/newsletter.asp>, 2017.

- [40] R. Weingarten, Y.T. Kim, G.A. Tompsett, A. Fernández, K.S. Han, E.W. Hagaman, W.C. Conner, J.A. Dumesic, G.W. Huber, *Journal of catalysis* 304 (2013) 123-134.
- [41] F. Chen, G. Coudurier, J.-F. Joly, J. Védrine, *Journal of Catalysis* 143 (1993) 616-626.
- [42] D. Spielbauer, G.A. Mekhemer, M. Zaki, H. Knözinger, *Catalysis letters* 40 (1996) 71-79.
- [43] X. Qi, M. Watanabe, T.M. Aida, R.L. Smith, *Catalysis Communications* 9 (2008) 2244-2249.
- [44] I. Jiménez-Morales, J. Santamaría-González, A. Jiménez-López, P. Maireles-Torres, *Fuel* 118 (2014) 265-271.
- [45] T. Nakamura, N. Aoi, Pat 55013243 (1980).
- [46] F. Benvenuti, C. Carlini, P. Patrono, A.M.R. Galletti, G. Sbrana, M.A. Massucci, P. Galli, *Applied Catalysis A: General* 193 (2000) 147-153.
- [47] H. Xu, Z. Miao, H. Zhao, J. Yang, J. Zhao, H. Song, N. Liang, L. Chou, *Fuel* 145 (2015) 234-240.
- [48] A. Jain, A.M. Shore, S.C. Jonnalagadda, K.V. Ramanujachary, A. Mugweru, *Applied Catalysis A: General* 489 (2015) 72-76.
- [49] A. Osatiashtiani, *Clean catalytic technologies for converting renewable feedstocks to chemicals and fuels*, Cardiff University, 2014.
- [50] NIST Standard Reference Database 20, Version 3.4 (web version).
- [51] J.L. Colón, D.S. Thakur, C.-Y. Yang, A. Clearfield, C.R. Martini, *Journal of Catalysis* 124 (1990) 148-159.
- [52] G. Alberti, U. Costantino, G. Marletta, O. Puglisi, S. Pignataro, *Journal of Inorganic and Nuclear Chemistry* 43 (1981) 3329-3334.
- [53] Z. Miao, L. Xu, H. Song, H. Zhao, L. Chou, *Catalysis Science & Technology* 3 (2013) 1942-1954.
- [54] M.-S. Kim, Y.-D. Ko, J.-H. Hong, M.-C. Jeong, J.-M. Myoung, I. Yun, *Applied surface science* 227 (2004) 387-398.
- [55] X. Tang, H. Chen, L. Hu, W. Hao, Y. Sun, X. Zeng, L. Lin, S. Liu, *Applied Catalysis B: Environmental* 147 (2014) 827-834.
- [56] Z.-Y. Yuan, T.-Z. Ren, A. Azioune, J.-J. Pireaux, B.-L. Su, *Catalysis today* 105 (2005) 647-654.
- [57] X.Z. Lin, Z.Y. Yuan, *European Journal of Inorganic Chemistry* 2012 (2012) 2661-2664.
- [58] D. Fa, J.Q. Li, S. Cameron, *Applied Catalysis A: General* 154 (1997) 173-184.
- [59] D. Powers, H.B. Gray, *Inorganic Chemistry* 12 (1973) 2721-2726.

- [60] V.G. Keramidas, W.B. White, *Journal of the American Ceramic Society* 57 (1974) 22-24.
- [61] X. Qi, M. Watanabe, T.M. Aida, R.L. Smith, *Catalysis Communications* 10 (2009) 1771-1775.
- [62] A. Osatiashtiani, A.F. Lee, D.R. Brown, J.A. Melero, G. Morales, K. Wilson, *Catalysis Science & Technology* 4 (2014) 333-342.
- [63] P. Mercera, J. Van Ommen, E. Doesburg, A. Burggraaf, J. Ross, *Applied catalysis* 57 (1990) 127-148.
- [64] A.A. Ali, M.I. Zaki, *Colloids and Surfaces A: Physicochemical and Engineering Aspects* 139 (1998) 81-89.
- [65] K. Tomishige, Y. Ikeda, T. Sakaihorii, K. Fujimoto, *Journal of Catalysis* 192 (2000) 355-362.
- [66] C. Phillippi, K. Mazdiyasnii, *Journal of the American Ceramic Society* 54 (1971) 254-258.
- [67] T. Viinikainen, H. Rönkkönen, H. Bradshaw, H. Stephenson, S. Airaksinen, M. Reinikainen, P. Simell, O. Krause, *Applied Catalysis A: General* 362 (2009) 169-177.
- [68] V. Bolis, C. Morterra, M. Volante, L. Orio, B. Fubini, *Langmuir* 6 (1990) 695-701.
- [69] J. Jiménez-Jiménez, P. Maireles-Torres, P. Olivera-Pastor, E. Rodríguez-Castellón, A. Jiménez-López, D.J. Jones, J. Rozière, *Advanced Materials* 10 (1998) 812-815.
- [70] A. Florentino, P. Cartraud, P. Magnoux, M. Guisnet, *Applied Catalysis A: General* 89 (1992) 143-153.
- [71] O. Kresnawahjuesa, R.J. Gorte, D. De Oliveira, L. Lau, *Catalysis letters* 82 (2002) 155-160.
- [72] Y. Kuwahara, W. Kaburagi, K. Nemoto, T. Fujitani, *Applied Catalysis A: General* 476 (2014) 186-196.
- [73] B. Bachiller-Baeza, I. Rodriguez-Ramos, A. Guerrero-Ruiz, *Langmuir* 14 (1998) 3556-3564.
- [74] K. Pokrovski, K.T. Jung, A.T. Bell, *Langmuir* 17 (2001) 4297-4303.
- [75] A. Clearfield, R.M. Tindwa, *Journal of Inorganic and Nuclear Chemistry* 41 (1979) 871-878.
- [76] N. Wang, Y. Yao, W. Li, Y. Yang, Z. Song, W. Liu, H. Wang, X.-F. Xia, H. Gao, *RSC Advances* 4 (2014) 57164-57172.

## ***Chapter 6***

### ***Concluding remarks and future work***

## 6.1 Conclusions

The goal at the beginning of this project was to investigate the use of water-tolerant solid acids for the conversion of sugars to 5-HMF which is an important platform chemical for the production of potential biofuels, polymers and fine chemicals. To fulfil this purpose, several materials were synthesised, characterized and tested in the aqueous dehydration reactions of glucose and fructose at mild conditions of temperature and pressure.

Hydrated niobium oxide (niobic acid) possesses high surface acidity which has been compared to the acid strength of 70% H<sub>2</sub>SO<sub>4</sub>[1], and its synthesis by soft chemical route employing a peptized niobic acid sol-gel grants the materials with both Lewis and Brønsted acidity, necessary for the isomerization and subsequent dehydration of glucose to HMF. Drastic changes on the physicochemical properties of niobic acid were found upon thermal treatment of the as-prepared niobic acid. Thermal treatment at 700°C led to the phase change of amorphous niobic acid observed by XRD and Raman, accompanied by the elimination of hydroxyl groups and sintering of nanoparticles after crystallization phenomenon occurs. The disappearance of hydroxyls was proved by XPS and a decrease in the Brønsted-Lewis ratio studied by infrared analysis, while growth of crystallite size was observable by TEM and XRD. Sintering effects lead to a significant decrease in surface area observed by nitrogen porosimetry, also inducing the loss of surface acidity as studied by pyridine adsorption and propylamine chemisorption.

Nanoparticulate niobic acid with different Brønsted-Lewis ratio due to pre-calcination at different temperatures was tested for the aqueous phase isomerisation of glucose to fructose, and subsequent fructose dehydration to 5-HMF under mild reaction conditions. Niobia crystallisation and the concomitant loss of (particularly Brønsted) acid sites notably lowers activity, for both glucose and fructose dehydration. Moreover, the impact of reaction temperature, reactant concentration and solvent used was also investigated. Reaction temperature was found to be a crucial parameter for the conversion of reactants and formation of HMF, showing a linear dependence with increasing reaction temperature. When DMSO was used as reaction media, an important background contribution was observed at 100°C, especially when fructose was used as the reagent. Albeit HMF yields and selectivities reported in this thesis are more moderate compared to those reported in the literature, it is noteworthy that those are usually performed at harsher conditions, usually at temperatures between 120-140°C and/or in the presence of ionic liquids or biphasic systems, promoting the

stoichiometric contribution of the reaction, and thus not considering solely the potential of the catalyst. In order to explore the full potential of niobic acid in DMSO, reaction temperature was decrease until no contribution from the non-catalytic reaction was observed (75°C). Isomerization of glucose could not be performed effectively, probably due to deactivation of Lewis acid sites by the Lewis base properties of DMSO. However, dehydration of fructose was found to be very efficient, even at such low temperature, attaining the same conversion of fructose than in aqueous system at 100°C, but with a two-fold increase in HMF selectivity due to the ability of this organic solvent to prevent rehydration of HMF and the formation of humin species.

Enhancement on the textural properties of these materials was sought and achieved by the introduction of mesoporosity by the precipitation of niobia nanoparticles onto a high surface area silica support such as SBA-15. The incorporation of different niobia loadings was assured by compositional analysis (ICP, XRD) and Raman analysis. The peptization of niobia nanoparticles in ethanolic solution containing previously synthesised SBA-15 allowed the high dispersion of niobic acid onto the support, as ascertained by TEM and compositional analysis techniques. The increased niobia loading on the mesoporous support induced a decrease in surface area as discovered by nitrogen adsorption desorption analysis, consistent with uniform dispersion throughout the pore network. Surface acidity was probed by both pyridine and propylamine adsorption. Total acid densities for the PNA/SBA-15 materials increased almost linearly with bulk niobia loading, consistent with the evolution of a conformal niobic acid adlayer. While good Brønsted character was observed independently of the loading used, Lewis acidity was only observed for higher loadings consistent with an increased amount of niobia centres with increasing loading, which arise due to coordinatively unsaturated niobium ions in the form of tetrahedral NbO<sub>4</sub>, providing the Lewis acidity. On the other hand Brønsted acidity arises from the distorted NbO<sub>6</sub> octahedral, so that a part of the surface OH groups function as Brønsted acid sites.

The catalytic performance of this series of catalysts was tested on the dehydration of glucose and fructose to HMF. Glucose isomerization could not be accomplished effectively because of the few Lewis centres present in the supported niobia samples. Lewis acidity could also be lost due to the coordination of Lewis acid sites in the precipitated niobic acid nanoparticles with surface hydroxyls on the SBA-15. Contrarily, a constant increase in the activity of fructose dehydration was observed with increasing niobium loading (**Figure 6.1** left) due to the aggregation of isolated species in two dimensional polymerised species, which induce the formation of bridged hydroxyl

groups (Nb-OH-Nb) able to generate additional Brønsted acidity. Nevertheless, the superior performance of highly dispersed niobic acid (per acid site/mass of niobium) is illustrated in **Figure 6.1** (right), indicating that lower amount of niobium is able to transform more substrate per gram of niobium compared to higher loadings.

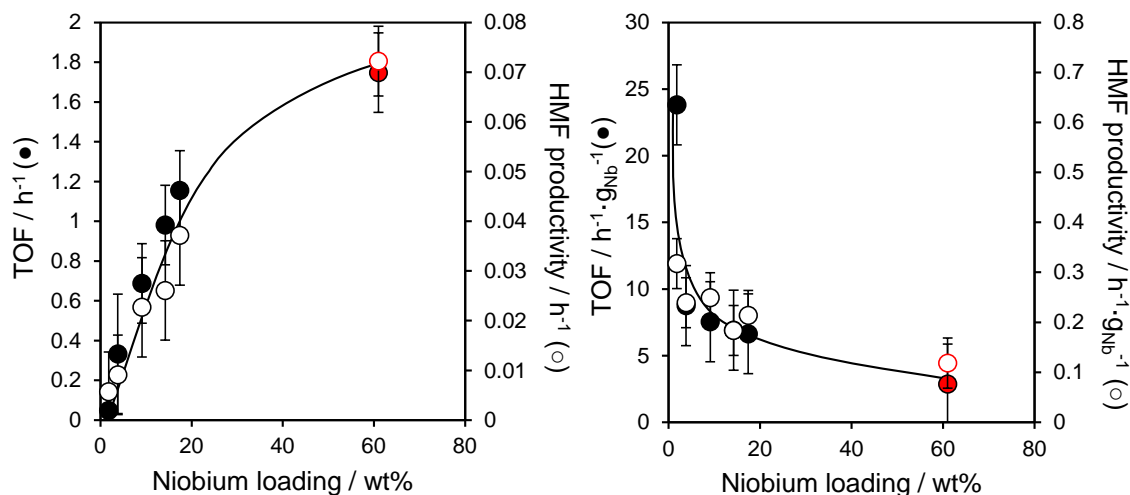


**Figure 6.1** Turnover frequencies for the aqueous phase conversion of fructose and associated 5-HMF productivity normalised to total acid loading (left) and to total acid loading and mass of niobium (right) as a function of niobium loading. Red circles refer to bulk PNA and black circles to PNA/SBA-15

Strong Brønsted acidity like that observed in the niobic acid materials is believed to promote side reactions, for this reason the synthesis of a series of catalysts with weaker Brønsted acidity such as phosphated zirconia was carried out. Moreover, zirconium also possesses inherent basicity which can assist the glucose to fructose isomerization step. Thus, a series of bifunctional phosphated zirconia catalysts were prepared by the impregnation of  $Zr(OH)_4$  with different concentrations of phosphoric acid solution, calcined at different temperatures and analysed by several characterization techniques.

The successful incorporation of phosphate species onto the zirconia surface was proved by XPS and ICP compositional analyses, especially the increase in the Zr-O-P signal from XPS. The crystalline phase of these materials was successfully examined by XRD and Raman spectroscopy. The parent zirconia catalysts showed a mixture of monoclinic and tetragonal phases, with a higher contribution of the former, while the incorporation of small amounts of phosphate species provoked the stabilization of tetragonal phase. High phosphates loadings promoted the formation of an amorphous phase due to the suppression of particle growth induced by the presence of phosphate species. The higher resistance to sintering obtained by phosphate doping was also reflected in the increase in surface area, reaching a maximum for catalysts with  $\sim 4$

Pwt%. Higher loadings alter the crystal structure of zirconia and experience a decrease in surface area. Pyridine and carbon dioxide adsorption revealed the presence of both acid and basic properties respectively, which varied systematically with concentration of impregnating phosphoric acid solution. The parent zirconia exhibited mixed Lewis acid and basicity, making it an effective catalyst for glucose isomerisation to fructose but poor towards fructose dehydration to HMF. Increasing phosphate loading led to the neutralisation of the basic properties and the concomitant increase in (especially Brønsted) acidity, making catalysts with high phosphate loading suitable materials for the dehydration of fructose to HMF, but poorly active for the isomerization reaction of glucose to fructose.

These hypotheses were verified by the catalytic tests regarding the glucose and fructose dehydration reactions. Higher glucose conversion and fructose selectivity were attained by the catalysts with a lower B/L ratio, proving the higher performance of combined Lewis acid and basic sites. While increasing the phosphate content results in reduction in glucose conversion due to loss of Lewis acid sites in favour of Brønsted acidity, HMF selectivity monotonically increased with phosphate loading, demonstrating the catalytic effect of this type of acid sites on the dehydration step. The study on catalyst calcination temperature showed that the sintering of zirconia crystallites producing a diminishing in surface area and acidity of the catalysts due to higher calcination temperatures, led to a decrease in reagent conversion, either glucose or fructose, and HMF selectivity.

## 6.2 Future work

- In this thesis, the application of water-tolerant solid acid catalysts for the production of HMF at mild conditions of temperature and atmospheric pressure were studied. However, comparison with literature results is difficult due to the harsher conditions there found, so testing these catalysts under conditions similar to the literature such as hot compressed water[2] or subcritical water[3] can provide a better understanding of the full catalytic potential of these materials.
- For the catalytic tests herein studied, it was usual the presence of unidentified by-products, such as insoluble humins and multiple compounds labelled as “other sugars”. For a better understanding of product formation, a more detailed analysis of by-products by NMR and infrared could serve as a mean to identify these unknown compounds[4].

- Although the activity of the studied catalysts was relatively good considering the mild conditions used, selectivity values are quite modest. Therefore, a way to improve the selectivity to HMF would be the use of biphasic systems or ionic liquids to study the stability of HMF in the presence of these solid acid catalysts.
- Also, the stability of these materials has not been tested in this work, so it would be sensible to explore the performance of these catalysts in continuous system in a similar manner to that reported by Carniti *et al.*[5] to study catalyst deactivation effects.
- Enhancement of the physicochemical properties of SBA-15 supported materials by tuning their Bronsted:Lewis acidic properties, hydrophobicity, etc. Besides, a different support such as KIT-6 can provide a better dispersion at high metal loadings and improve diffusional effects due to its interconnected pore network.
- Furthermore, phosphate treatment of niobic acid as means to decrease the acid strength and thus enhance selectivity to HMF could be studied, as well as other classes of catalysts with acid-base properties such as metal-organic framework materials[6].

### 6.3 References

- [1] K. Tanabe, *Catalysis Today* 8 (1990) 1-11.
- [2] M. Watanabe, Y. Aizawa, T. Iida, T.M. Aida, C. Levy, K. Sue, H. Inomata, *Carbohydrate research* 340 (2005) 1925-1930.
- [3] F. Salak Asghari, H. Yoshida, *Industrial & Engineering Chemistry Research* 45 (2006) 2163-2173.
- [4] I. van Zandvoort, Y. Wang, C.B. Rasrendra, E.R. van Eck, P.C. Bruijninx, H.J. Heeres, B.M. Weckhuysen, *ChemSusChem* 6 (2013) 1745-1758.
- [5] P. Carniti, A. Gervasini, M. Marzo, *Catalysis Today* 152 (2010) 42-47.
- [6] V.N. Panchenko, M.N. Timofeeva, S.H. Jung, *Catalysis Reviews* 58 (2016) 209-307.